# Dynamic Analysis of a Two-spool Aero-engine Model Undergoing Multi-disk Rub-impact using a Semi-analytical Method

*A Thesis submitted*

*in partial fulfilment for the degree of*

**Doctor of Philosophy**

*by*


## Prabith K




**Department of Aerospace Engineering**

**INDIAN INSTITUTE OF SPACE SCIENCE AND TECHNOLOGY**

**THIRUVANANTHAPURAM - 695 547**



**May 2022**

# CERTIFICATE

This is to certify that the thesis titled ***Dynamic analysis of a two-spool aero-engine model undergoing multi-disk rub-impact using a semi-analytical method*** submitted by **Prabith. K**, to the Indian Institute of Space Science and Technology, Thiruvananthapuram, in partial fulfillment for the award of the degree of **Doctor of Philosophy**, is a bonafide record of the original work carried out by him under my supervision. The contents of this thesis, in full or in parts, have not been submitted to any other Institute or University for the award of any degree or diploma.

**Dr. Praveen Krishna. I. R**
Research Supervisor
Associate Professor
Department of Aerospace Engineering

**Dr. Aravind Vaidyanathan**
Head of the Department
Department of Aerospace Engineering
IIST

**Place:** IIST, Thiruvanathapuram
**Date**: $30^{th}$ May 2022

# Declaration

I declare that this thesis titled ***Dynamic analysis of a two-spool aero-engine model undergoing multi-disk rub-impact using a semi-analytical method*** submitted in partial fulfillment for the award of the degree of **Doctor of Philosophy** is a record of the original work carried out by me under the supervision of **Dr. Praveen Krishna. I. R** and has not formed the basis for the award of any degree, diploma, associateship, fellowship, or other titles in this or any other Institution or University of higher learning. In keeping with the ethical practice in reporting scientific information, due acknowledgements have been made wherever the findings of others have been cited.

**Place:** IIST, Thiruvanathapuram
**Date**: $30^{th}$ May 2022

**Prabith. K**
SC16D021

# Acknowledgements

Firstly I would like to express my sincere gratitude towards my research advisor, Dr. Praveen Krishna I R., for giving me the opportunity to work under his guidance. I am very thankful to him for his continuous support, motivation, and guidance throughout my Ph.D. research in moulding me into a better researcher and also helping me to complete this project successfully.

I am very grateful to all my doctoral committee members, Dr. Chandramouli Padmanabhan (Professor, Department of Mechanical Engineering, IIT Madras), Dr. Aravind Vaidyanathan (DC Chairman, HOD, Dept. of Aerospace Engineering, IIST), Dr. Kurien Issac K. (Senior Professor, Dept. of Aerospace Engineering, IIST), Dr. Bijudas C R. (Associate Professor, Dept. of Aerospace Engineering, IIST), Dr. Harsha Simha M S. (Associate Professor, Dept. of Avionics, IIST), and Dr. Manoj T. Nair (Former HOD, Associate Professor, Dept. of Aerospace Engineering, IIST), for their valuable suggestions, guidance, and constructive criticisms in each phase of my research work, which helped me a lot in improving the quality of the research outputs.

I also express my gratitude and thanks to the Director of IIST, the Dean Academics, and the Dean R&D for providing an excellent research ambience during my tenure in IIST.

I would like to thank Mr. Prakash R S., Mr. Sathish Kumar, Mr. Muhammed Rijas A., Mr. Dinesh D., Mr. Bipin Davidson, and Mr. John Thomas for all their help in carrying out the research work smoothly.

I cannot express enough thanks to my colleagues, Dr. Aravind G P., Dr. Arun D I., Dr. Aryadutt Oamjee, Dr. Nitesh Verma, Mr. Muhammed Shiyas K M., Mr. Dhanesh A., Mr. Sarath K P., Mr. Prasoon C M., Mr. Renjith A R., Mr. Gaurab Khanra, Mr. Renjith Thomas, Mr. Manu K Sukesan, Mr. Rithwik Sankar A., Mr. Pavanam Thomas, Mr. Abhijith Ajayakumar, Ms. Sreelekshmi Mohan, Ms. Resmi V L., Ms. Soumya S, Ms. Anjuna Dileep, Ms. Aswathy M, and Ms. Lekshmi S R for all their support in many initiatives we have taken, both academic and non-academic, during these years, and also for all the wonderful memories we had as a student family.

I am extremely grateful to my parents, my siblings, my in-laws, and my fiancée Prajisha for all their love and unconditional support throughout my years of study. Without them, this thesis would not have been possible.

# Abstract

Fan blade-out event and windmilling of the turbofan engine, generated as a consequence of bird strike, is a potential threat to the aircraft during its flight. The tight clearance between the blades and casing can cause the multi-disk rub-impact in the engine whenever the rotor deflection exceeds the clearance. As a result, the Federal Aviation Administration has introduced some stringent rules and regulations in testing aircraft engines so that the engine can contain damages without catching fire. However, the conduction of tests to prove the engine's safety is costly and sometimes leads to severe injuries to the test personnel. In this work, a numerical model of the aero-engine dual-rotor similar to the CFM56-5B engine is utilized to analyze the response characteristics of the engine under multi-disk rub-impact. The rotor system is modelled using the tapered Timoshenko beam elements, including rotary inertia, gyroscopic moments and shearing effects. A modified model reduction technique based on component mode synthesis is utilized to reduce the size of the finite element model in which the whole model is divided into primary and secondary components. The primary component consists of all the nonlinear degrees of freedoms, while the secondary component is reduced using the Craig-Bampton substructuring technique based on the quadratic eigenvalue decomposition. The proposed method is effective in the model reduction of systems involving asymmetric global matrices. The steady-state response of the model under multi-disk rub impact is investigated using a semi-analytic technique called the approximate time variational method. It is a time-domain method and is suitable for solving multi-frequency excitation problems. Moreover, a hypersphere based continuation technique is also incorporated to trace the solution branches beyond bifurcation points. The type of bifurcations is determined by monitoring the Floquet exponents. While analyzing the results, it is observed that the nonlinearities are intensified, and the rightward bending of the response curve is increased during the multi-disk rub-impact. Limit point and Neimark-Sacker bifurcations are observed, and their onset points are dependent on the multi-disk rub-impact. The responses such as period-5, quasi-periodic, and dry friction backward whirl motions are noticed for different values of the rub parameters. As a result, a parametric analysis is also performed to understand the effects of rub and squeeze film damper parameters.

# Table of contents

# List of figures

# List of tables

# Nomenclature

### English Letters

| | |
|---|---|
| $\mathbf{C}$ | Damping matrix of the model |
| $c$ | Squeeze film damper clearance, mm |
| $c_0$ | Rolling contact bearing clearance, $\mu m$ |
| $C_b$ | Hertz contact stiffness, N/m$^n$ |
| $E_{Ni}$ | Young's modulus of nickel alloy, GPa |
| $E_{Ti}$ | Young's modulus of titanium alloy, GPa |
| $\mathbf{F}$ | External force vector |
| $\mathbf{F}_b$ | Rolling contact bearing force vector |
| $\mathbf{F}_{nl}$ | Nonlinear force vector |
| $\mathbf{F}_{rub}$ | Rub-impact force vector |
| $\mathbf{F}_{sfd}$ | Squeeze film damper force vector |
| $\mathbf{G}$ | Gyroscopic matrix of the model |
| $I_d$ | Diametral moment of inertia of the disk, kg.m$^2$ |
| $I_p$ | Polar moment of inertia of the disk, kg.m$^2$ |
| $\mathbf{K}$ | Stiffness matrix of the model |
| $K_a$ | Squirrel-cage elastic support stiffness, N/m |
| $k_c$ | Rotor-stator contact stiffness, N/m |

| | |
|---|---|
| $L$ | Width of damper, mm |
| $\mathbf{M}$ | Mass matrix of the model |
| $N$ | Degree of freedom of the complete model |
| $n$ | Nonlinear index of Hertz contact deformation |
| $N_b$ | Number of rollers in the bearing |
| $N_h$ | Number of harmonics selected for the MHBM |
| $N_{pt}$ | Number of time points selected for the TVM |
| $N_r$ | Degree of freedom of the reduced model |
| $\mathbf{q}$ | Displacement vector |
| $R$ | Journal radius, mm |
| $R_b$ | Outer ring radius of the bearing, mm |
| $r_b$ | Inner ring radius of the bearing, mm |

**Greek symbols**

| | |
|---|---|
| $\alpha$ | Nonlinear stiffness of the model |
| $\delta$ | Rotor-stator clearance, mm |
| $\eta$ | Dynamic Viscosity, Pa.s |
| $\mu$ | Co-efficient of friction |
| $\nu$ | Poisson's ratio |
| $\omega$ | Angular velocity of rotor, rad/s |
| $\rho$ | Density, Kg/m$^3$ |

**Abbreviations**

| | |
|---|---|
| AFT | Alternating Frequency Time |
| ATVM | Approximate Time Variational Method |
| CMS | Component Mode Synthesis |

| | |
|---|---|
| DOF | Degree of Freedom |
| FAA | Federal Aviation Administration |
| FE | Finite Element |
| FFT | Fast Fourier Transform |
| HBM | Harmonic Balance Method |
| HPC | High Pressure Compressor |
| HPT | High Pressure Turbine |
| LPC | Low Pressure Compressor |
| LP | Limit Point |
| LPT | Low Pressure Turbine |
| MHBM | Multi-Harmonic Balance Method |
| NI | Numerical Integration |
| NS | Neimark-Sacker |
| SFD | Squeeze Film Damper |
| TVM | Time Variational Method |

# Chapter 1

# Introduction

## 1.1 Background

The fan blade-out (FBO) in a turbofan engine is one of the most critical failures that will threaten the integrity of the aircraft engine and the safety of passengers. The loss of blades may occur due to several reasons such as corrosion/erosion, high cycle fatigue, foreign body ingestion, manufacturing and material defects, etc. An FBO event can create a lot of complexities in the aircraft engine, such as sudden imbalance, asymmetry of rotors, and blade-casing interactions. Several aircraft accidents have been reported worldwide regarding blade loss and subsequent blade-casing rubbing within the past few decades. On November 3, 1973, National Airlines Flight 27 was subjected to an emergency landing because of an uncontained engine failure resulting from the disintegration of fan assembly from the engine (John et al. (1975)). As a result, the fragments of the fan penetrated the fuselage and caused decompression of the aircraft cabin and loss of certain electrical and hydraulic services. The accident caused the death of a passenger, and 24 persons were treated for smoke inhalation, ear problems, and minor injuries. On February 3, 2007, a Boeing 747-438 aircraft had a compressor blade failure that happened due to the distortion of its casing and subsequent tip rubbing (ATSB (2008)). The released blade damaged the engine's high-pressure compressor, causing loud noise and vibrations in the aircraft. On May 13, 2014, a Beechcraft Beechjet 400A suffered a bird strike to its right engine, resulting in the cracking of fan blades at the root. During the examination, it was found that the engine cowling had multiple penetrations, indicating severe blade-stator interactions. After the inspection, the National Transportation Safety Board (NTSB) recommended modifying all JT15D-5 engines installed on Raytheon/Hawker Beechjet 400A aeroplanes to dampen the rub-induced excitation that can happen between the engine fan and casing during the FBO event (Christopher et al. (2017)).

As a consequence of several accidents in the past, the Federal Aviation Administration imposes strict rules and regulations in the design, construction, and testing of aircraft engines. As per 14 CFR § 33.94a, the manufacturers have to conduct an engine test demonstration to prove that the engine can contain damages without catching fire and shut it off within 15 seconds. Such certified engines are used in modern aircraft, and they will shut off rapidly when an FBO event occurs during a flight. However, the aircraft has to fly for some more hours before it lands at an en-route alternate airport. During this diversion flight, the engine fan rotates because of the aerodynamic forces called windmilling. It is observed through certain field events that the windmilling of the damaged rotor resulted in severe blade-casing interactions in the aircraft engines (Christie (1996)). Fortunately, in all the incidents, the aircraft was landed safely without any severe injuries to the passengers or damage to itself. As a result, the FAA made the rules and regulations more stringent by introducing 14 CFR § 33.74. According to this rule, the engine manufacturers must show that the continued rotation after blade loss doesn't create unwanted circumstances in the aircraft during its diversion flight. However, conducting the tests to prove the engine's safety during FBO and continued rotation is extremely expensive and sometimes leads to severe problems for the rig and the test personnel. As a result, developing analytical and numerical models of the rotor-stator rubbing is essential for predicting the response characteristics of the engine. During the past few decades, several research works have been conducted to understand the mechanism of rub-impact happening in rotor systems (Muszynska (2005)). A review of how the rotor-stator interaction studies are evolved during the past few decades is described as follows.

## 1.2 Literature review

The rotor-stator rubbing was first observed in steam turbines around the 1920s; since then, it has become a challenging topic for many researchers. Initially, Taylor (1924) and Newkirk (1927) noticed that when a rotor rubs the stator below its first critical speed, the shaft gets bowed due to the uneven temperature distribution. As a result, its lateral vibrations are amplified with time. Dimarogonas (1973, 1974) provided a quantitative explanation for this phenomenon and is termed as the Newkirk effect. Meantime, Black (1966) studied the influence of rotor-stator rub on the global dynamics of the system using an experimental setup. The test rig consisted of a long mild steel shaft carrying a disk at the centre. Mass unbalance is adjusted by attaching small amounts of plasticine to the central mass. A clearance bush made up of brass is used as the annulus. Due to the flexibility of the shaft, whirling took place, and the rotor touched the annular surface when the rotating speed was very close to the critical speed and altered its high-speed behaviour. A forward-leaning of the critical peak

is observed and is termed as super whirling. When the bush is made sufficiently dry and clean, counter-whirling is observed in the response with its amplitude greater than that of forward whirling (Black (1968)). Ehrich and O'Connor (1967) included the stator dynamics in the model and observed a stator motion showing some resemblance to the hula hoop and is termed as stator whirl. The stator whirl attained a considerable amplitude when the rotating speed became equal to the stator's natural frequency.

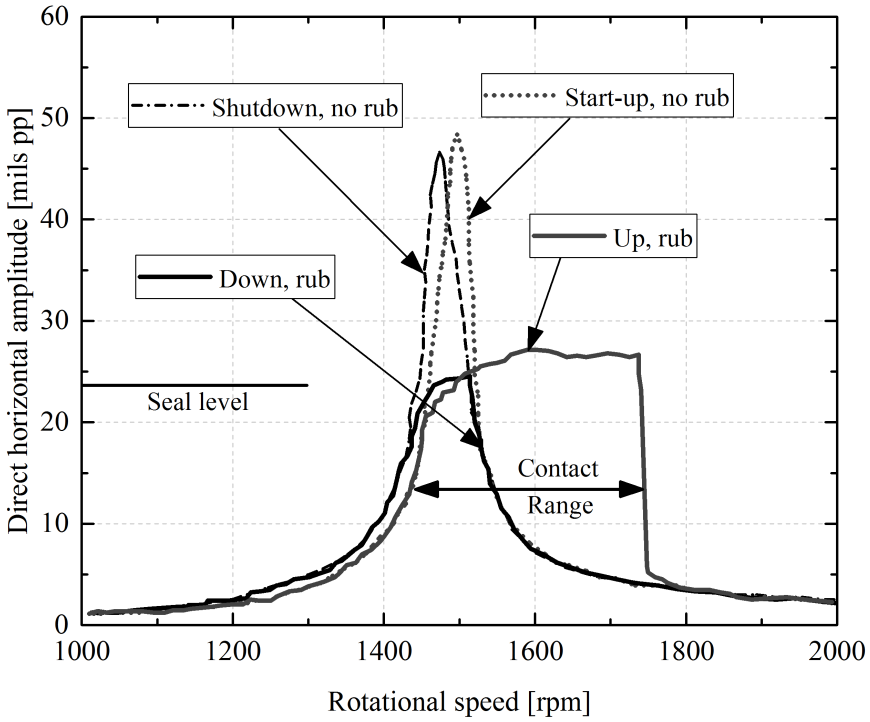


Fig. 1.1 Comparison of the rotor lateral responses during the start-up and shut down tests with and without seal rubbing (Yu et al. (2002)).

Later, Yu et al. (1998, 2002) provided a clear picture of the rotor-stator interaction using an experimental test rig consisting of a two-disk rotor model in which the shaft is made to rub against seals made up of Teflon and bronze. Mainly, two types of steady-state vibration regimes are observed in the rotor response depending upon the system parameters, such as rotor-stator friction coefficient, rotor unbalance and support stiffness. They are i) unbalance-excited synchronous rub and ii) self-excited dry whip. Compared to dry whip, the synchronous rub is less dangerous and occurs when the rotor contacts a properly lubricated stator due to mass unbalance effect (Zhang et al. (2009)). Sometimes, the accidental presence of some tiny materials in the radial clearance may also be a reason for the light synchronous rub (Vania et al. (2018)). During the contact, the seal acts as an additional bearing and

increases the stiffness of the model. As a result, the response changes in the range of original resonance and a forward-leaning can be observed as explained by Black (1966). After passing a certain rotational speed, the amplitude of whirling decreases rapidly, and a jump-down phenomenon happens to the no-rub response. However, the behaviour of the rotor during run-down is entirely different from that of run-up. The range of forward-leaning is shortened, and a jump-up phenomenon is observed during run-down, as shown in Fig. 1.1. Generally, the synchronous full annular rub is identified by the occurrence of a single point in the Poincaré map, one peak amplitude in the frequency spectrum, and one closed circle in phase portrait. It is a stable, periodic response with a very low vibration amplitude. The abradable coating on the casing may be slightly ground during the synchronous full annular rub, avoiding metal to metal contact. It doesn't lead to any unwanted situations that may affect the engine's integrity. Therefore, the synchronous full annular rub is the ideal operation status during the rubbing event.

The dry whip is the most destructive rotor motion in which the rotor continuously contacts the stator while orbiting in the backward direction. The whirling amplitude and frequency of the dry whip are so high that they can destroy the integrity of the rotor system. To determine the excitation mechanism that initiates the dry whip, Bartha (2000) built a test rig with realistic parameters to mimic the rubbing in a small turbo-compressor. A magnetic exciter is used to trigger the backward whirl, and different excitation levels are applied to determine the critical excitation force. After the analysis, it is concluded that an outside disturbance (hitting the shaft) is required to initiate the dry whip. However, contradictory to Bartha's conclusion, Bently et al. (2002) experimentally proved that dry whip could occur without any outside disturbance. Sufficiently high mass unbalance with a high coefficient of friction can initiate the dry whip. In addition, the rotor foundation had a substantial effect on the occurrence of the dry whip. For the same test rig, backward whirl could quickly occur for a foundation made up of stiff concrete, while only synchronous forward whirling could be generated for a flexible foundation.

In 2005, Jiang and Ulbrich (2005) explained the physical reason for the onset of dry whip analytically. According to their study, the onset of dry whip occurs when the rotor speed becomes equal to the negative natural frequency of the coupled nonlinear rotor-stator system, and no external mechanism is necessary, underlying the conclusion of Bently et al. (2002). Moreover, the rotor maintains continuous contact with the stator and whirls backwards with a super-synchronous frequency which is lower than the rotor-stator coupled linear natural frequency (Jiang (2007); Jiang et al. (2010)). As a result, the abradable coating may be wholly removed, and direct contact of blade tip with casing material occurs. This will induce localized thermal heating and disturb the thermal equilibrium of the model. The shaft will

undergo considerable deformations and be prone to high-frequency stresses, which may cause fatigue damage in the shaft and eventually lead to the complete failure of the machinery.

In addition to synchronous rub and dry whip, sub and super-harmonic responses are also observed in the rotating machinery. Sub-harmonic response refers to the bouncing of the rotor at exactly or nearly its natural frequency when the rotor rotates at a speed that is exactly or nearly a whole number (N) multiples of its natural frequency. Ehrich (1966) first identified the second-order sub-harmonics in the rotor response which is confirmed by Bently (1974) through experimental observations. According to Bently (1974), this kind of vibration occurs mainly due to the asymmetry in radial flexibility induced as a result of partial rubbing. Later, Childs (1979, 1982) analytically explained the occurrence of 1/2$\times$ and 1/3$\times$ sub-harmonics in the response using linear parametric analysis of a rotor system. Sub-harmonics are indicated by multiple closed circles in phase portrait, multiple peaks in the frequency spectrum, and multiple points in the Poincaré map (Chu and Lu (2005)). The presence of higher-order sub-harmonics (Ehrich (1988, 1991)) and super-harmonics (Ehrich (1992)) are also observed, depending on the model parameters. Super-harmonics is the mirror image of sub-harmonics, i.e. the rotor will bounce at exactly or nearly its natural frequency when the rotor rotates at a speed which is exactly or nearly $1/N$ times of its natural frequency (Ehrich (1992)). Sub and super-harmonic responses have all the characteristics of the critical response of the system, and they can excite the components of a turbomachine, such as a turbine disk, bearings, fastenings, couplings, etc. This may lead to the failure of such components and affect machinery's integrity.

It has been observed through different experiments and numerical studies that the transition zones between successive orders of the sub and super-harmonic responses have all the characteristics of chaotic nature (Muszynska and Goldman (1995)). They are characterized by irregular and non-repetitive multiple orbits (Gonsalves et al. (1995)). A fractal structure of points in the Poincaré map indicates the occurrence of chaotic behaviour in rotor responses (Khanlo et al. (2011)). The presence of nonlinearities in the rotor system, such as piecewise discontinuous stiffness, surface friction, and local impact, are the primary sources of chaotic responses (Goldman and Muszynska (1994); Karpenko et al. (2002)). In addition, the constant external excitations due to gravity load also induce complex nonlinear behaviours such as sub-harmonic, quasi-periodic, and chaotic motions (Hou et al. (2019)). Detailed post-processing analysis of rubbing reveals that the rotor motion alternates between periodic, quasi-periodic, and chaotic behaviours through different bifurcation points such as Neimark-Sacker bifurcation, quasi-periodic Hopf bifurcation, saddle-node bifurcation, and pitchfork bifurcation. The quasi-periodic vibration is generally indicated by the presence of incommensurate frequency components in the frequency spectrum and a closed curve in the

Poincaré map (Peletan et al. (2014)). Moreover, the entry and exit to chaos have different kinds of routes, i) a sudden transition from periodic response to the chaos, ii) through period-doubling bifurcation, and iii) through grazing bifurcation in which the period increases by a value of one, after each region of chaos (Chu and Zhang (1998)). The appearance of chaotic vibrations in the rotor response is a possible threat to aerospace structures because of their unpredictable time histories. Proper control of the design parameters and the construction of active controllers are the two practical measures for displacing the structure from chaotic regimes or stopping the chaos from occurring. As a result, the development of efficient numerical models is necessary for conducting the detailed rub-impact analysis, thereby reducing the possibilities of machinery failure.

### 1.2.1 Numerical models of rotor-stator rub

Numerical modelling of the rotor-stator rub was started in the late sixties using simple two degrees of freedom (DOF) models. Later, many modifications were applied incrementally to the basic models and developed complex rotor models for simulating the rub phenomenon. Establishing a numerical model mainly includes two steps: i) constructing a mechanical model for analyzing the vibrational behaviour of the system and ii) developing a proper contact model for determining the rubbing forces. A detailed review of different numerical models used for simulating the rub-impact is presented in the article by Ma et al. (2016b).

#### Mechanical models

The main task in the numerical modelling of rotor-stator rub is constructing a mechanical model for simulating the global response characteristics of the rotor system. The ability of a rotor model in predicting the complete response characteristics is mainly dependent on how well the system is modelled. The majority of the previous research works on the rotor-stator interactions utilized the modified Jeffcott rotor model, which is a 2 DOF rotor consisting of a thin, rigid disk mounted at the midspan of a flexible massless shaft, supported at the ends on bearings (Choi and Noah (1987); Jiang and Ulbrich (2001); Karpenko et al. (2003)). The schematic diagram of a modified Jeffcott rotor model is shown in Fig. 1.2. The structure of the Jeffcott rotor model is far away from the actual turbomachine. However, the researchers have utilized this model for investigating the response characteristics, stability ranges, and bifurcation pattern during rub-impact. Later, more modified Jeffcott rotor models are introduced by the researchers, incorporating oil film bearings, flexible disks, torsion and thermal bow. They are explained as follows.

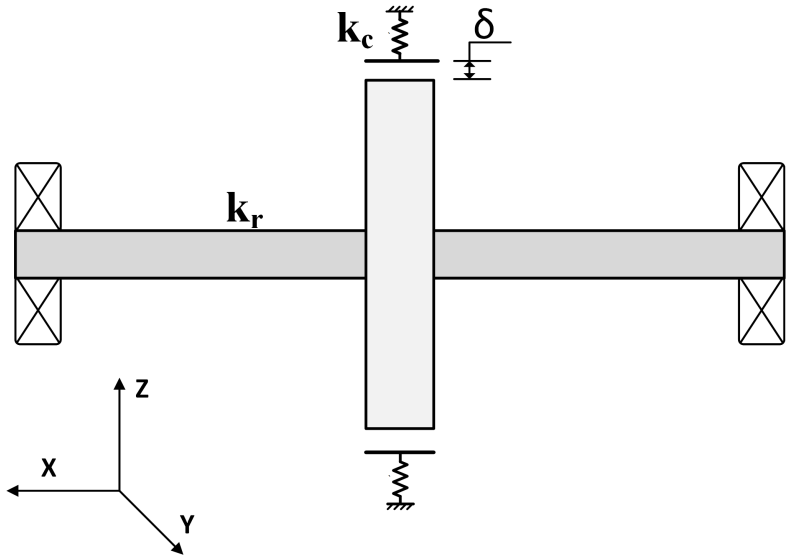


Fig. 1.2 Schematic diagram of a modified Jeffcott rotor model consisting of a thin, rigid disk mounted at the midspan of a flexible massless shaft, supported at the ends on bearings.

In a simple Jeffcott rotor model, the bearing is assumed to have linearized damping and stiffness applied at the rotor geometric centre. But, in most rotating machines, the rotor is supported on oil film bearings. The oil film bearings are the main source of nonlinear excitation forces that are self-exciting in nature. They can be calculated using the Reynolds equation assuming the short bearing approximation (Ghosh et al. (1979), Chu and Zhang (1997), Balaji and Krishna (2018)). It is observed that the unbalance response of the rotor can be significantly reduced by optimizing the bearing parameters such as the diameter, clearance, and the oil viscosity (Bhat et al. (1982)). Tiwari et al. (2004) presented a detailed review of different experimental techniques for the identification of dynamic parameters of bearings and similar components. Mainly vibration-based identification methods such as impulse and random response measurements are used (Tiwari (2017); Tiwari and Chakravarthy (2006, 2009); Tiwari and Vyas (1995)). Through the theoretical analysis, the direct and cross-coupled coefficients of stiffness and damping can be calculated and are applied at the bearing location during the analysis (Rao et al. (1980)). Depending on the values of the cross-coupled stiffness, backward whirling can be noticed in the rotor response (Rao (1982)). Moreover, the rotor becomes unstable when one of the cross-coupled stiffness coefficients is negative (Rao (1983, 1985); Sharan and Rao (1985)). As a result, oil whirl and oil whip appear in the rotor response. Oil whip is the main fluid film instability observed at a rotor speed far above the linearized first critical. It is one of the main sources of rub-impact and leads to quasi-periodic and chaotic vibrations of the rotor.

A very few researchers (Flowers and Ryan (1991); Flowers and Wu (1996, 1993); Kumar et al. (1997)) analyzed the modified Jeffcott rotor with flexible disks. Most often, a model consisting of a rigid ring elastically connected to a rigid hub is utilized for studying the effects of disk flexibility (Flowers and Wu (1993)). In the mathematical formulation, additional equations corresponding to the disk vibration are appended to the equations of shaft vibration. The studies demonstrated that super-harmonic vibrations produced as a result of rub-impact could excite the disk vibrations considerably, leading to increased bearing loads.

Most of the past research on rotor-stator interactions avoided the torsional vibrations, assuming the rotor is torsionally rigid. But, the presence of friction and tangential forces due to contact may induce torsional vibrations in the response. The addition of the torsional DOF to the Jeffcott model provides an efficient way for the analysis of lateral-torsional vibrations ( Al-bedoor (2000); Lu and Chu (2014); Mokhtar et al. (2017); Patel and Darpe (2009); Patel et al. (2012); Yang et al. (2019)). It forms a 6 DOF model with two lateral and one torsional motion for both rotor and stator. The results from this model showed a substantial amount of variations in the response from a model without torsional effects (Popprath and Ecker (2007)). Each contact with the stator excited torsional vibrations in the rotor with its amplitude decaying at a frequency equal to the torsional natural frequency of the model. During each contact, localized heating happens at the contact point, and it leads to a non-uniform heat distribution in the rotor (Newkirk (1927)). It induces a thermal bow in the shaft, and the stability of the model is highly dependent on the phase angle between static and dynamic bow (Goldman and Muszynska (1995); Goldman et al. (2000)).

In the past, there have been many studies that happened using the modified Jeffcott rotor. However, the excessive simplification of these lumped parameter models restricts them in the qualitative analysis only. In recent years, the finite element (FE) models of rotating machinery have been extensively used for the nonlinear dynamic analysis of the rub phenomenon (Rao (1996, 2011)). Most of the researchers have utilized one-dimensional beam elements for the FE modelling, based on Nelson and McVaugh (1976) rotor model. In this model, a rotor system is considered as an interconnection of different components made up of rigid disks, shaft elements, and linear bearings. The shaft elements have distributed mass and elasticity and are modelled using the Euler-Bernoulli or Timoshenko beam formulations, whereas the bearings are simplified as a linear spring-damper model. The rigid disks are included in the model by adding their inertial properties to the corresponding nodal properties of the shaft. Compared to the Jeffcott rotor, the FE models of the rotor system provide more accurate results quantitatively. In literature, most of the rotor FE models are developed in a single-spool configuration, consisting of a single rotor mounted on bearing supports (Mokhtar et al. (2017); Pennacchi et al. (2009); Torkhani et al. (2012)). However, the information

received from a single-spool rotor model won't be sufficient enough to predict the response behaviour of a modern aircraft engine since most of them have a two-spool configuration. For the analysis of such machines, a dual-rotor model will be appropriate.

***Dual-rotor model***: The aircraft engines are composed of two-spool rotors that will induce multiple excitations when they are subjected to unbalanced forces and external excitations. During the analysis, the aircraft engine is modelled as a dual-rotor consisting of two co-axial rotors connected using inter-shaft bearings. The presence of inter-shaft bearing makes the model's behaviour unique and results in the coupling of both rotor vibrations. As a result, the dynamic behaviour of such machines appears to be more complicated in the presence of rub-impact. The detailed studies on rub-impact in dual-rotor models have been started recently. Xu et al. (2016) performed an experimental research for understanding the dynamic characteristics of a two-spool rotor with rub-impact fault. The experimentation consisted of a dual-rotor model with a single-stage compressor and a turbine disk in each rotor. While observing the spectrums of rotor vibration, it is seen that the response of the dual-rotor model under rub-impact not only contains the excitation frequency components but also includes their linear combinations. Similar results are obtained for Yang et al. (2016) when the analysis is performed numerically. In their model, the fixed point rub happening in the dual-rotor is studied by considering the effects of coatings applied on the disks and casing. The Lankarani and Nikravesh (1990) model is used to determine the contact force generated between coated casing and disks. Later, Yang et al. (2017) investigated a two-disk rub-impact problem by assuming the contact occurring at compressor and turbine positions. A linear interpolation method is used to predict the instant of contact. Due to the two-disk rub-impact, the nonlinearities are intensified, and a rich mixture of nonlinear vibrations are observed in the response.

Recently, the researchers have introduced more complexities to the basic dual-rotor model. Rao (2013) studied the dynamics of a dual-rotor model by including stress stiffening and spin softening effects. The shafts with variable cross-sections were used to build a dual-rotor model (Rao and Sreenivas (2003)). Hou et al. (2017) and Wang et al. (2017) modified the dual-rotor model by incorporating ball bearings in place of inter-shaft bearing and studied the effects of bearing clearance and contact stiffness on the primary resonance of the model. Later, Gao et al. (2019) introduced a local defect on the bearing outer race and investigated its effects on the nonlinear dynamic characteristics of the dual-rotor model. Four abnormal resonances are observed in the frequency response curve due to the local defect, apart from the primary resonances. Moreover, a steady-state heat transfer model is also incorporated in the inter-shaft bearing using Palmgren's empirical formula (Gao et al. (2020)). It is observed that the thermal behaviour of the dual-rotor model became much

more complex due to the nonlinear dynamic characteristics of the inter-shaft ball bearing. Liu et al. (2020a,b, 2021) modelled the inter-shaft bearings based on the nonlinear spring characteristics of the rotor deflections and observed subharmonic resonances and internal resonances. The nonlinear spring characteristics are expressed in terms of power series as mentioned in the study of Yamamoto and Ishida (1977).

In recent time, Lu et al. (2021) investigated the nonlinear dynamic characteristics of a dual-rotor model when the ball bearing is located at a position other than the inter-shaft bearing. A resonance hysteresis phenomenon is observed in the frequency-response curve when the clearance of the ball bearing is increased. It is found that the performance of ball bearings highly influences the dynamic response of the rotor model. The performance can be improved by conducting a multi-objective optimization procedure during the design (Gupta et al. (2007)) of ball bearings. The dynamic capacity, the static capacity and the minimum film thickness can be optimized separately, pair-wise and simultaneously using a genetic algorithm. The design parameters include the rolling element diameter, the bearing pitch diameter, the number of rolling elements and inner and outer-race groove curvature radii (Rao and Tiwari (2007)). As a result of design optimization, the ball bearings deliver excellent performance, high reliability and maximum fatigue life (Verma and Tiwari (2021)).

Xinxing et al. (2021) included the squeeze film dampers (SFD) in the dual-rotor model and analyzed its nonlinear dynamic characteristics when supported by rolling contact bearings. The steady-state vibration responses of the model with or without SFD are solved by the numerical integration method. The influences of the ball bearing clearance, unbalance, centralizing spring stiffness and oil film clearance of SFD on the nonlinear steady-state vibration responses of the dual-rotor model are analyzed. Results show that SFD can effectively suppress the amplitude jump of the dual rotor model sustaining two rotors unbalance excitations. Even though this arrangement is for reducing the amplitude of vibration, it acts as an additional source of nonlinearity (Mohan and Hahn (1974)). The oil-film forces produced as a result of wedging action introduce nonlinearities in the model and results in the nonlinear dynamic responses (Gunter et al. (1977)). Reynold's equation with a short bearing approximation is employed to determine the oil-film forces (Chen et al. (2020); Humes and Holmes (1978)). A change in the SFD static eccentricity ratio and supply pressure can produce enough damping in the model, and it affects the rotor responses significantly. Inayat-Hussain (2009) performed the stability analysis of a rotor model with the SFD and observed different types of bifurcations in the response. Some researchers have designed the inter-shaft ball bearings in combination with the SFDs and observed remarkable variations in the response of dual-rotor models (El-Shafei (1991); Li et al. (1986); Luo et al. (2019); Wang et al. (2018)).

Recently, Wang et al. (2019) introduced a dual-rotor-blade-casing (DRBC) model by incorporating blades and thin-walled casing in the simple dual-rotor model. The vibration signals are measured from the casing surface, and certain periodic impact characteristics are observed in the signal with its frequency equal to the product of the rotational frequency and the number of blades. Yang et al. (2020) modelled a dual-rotor-bearing-double casing system (DRBDC) consisting of multilayered casings. It consisted of two separate casings for inner and outer rotors with a soft coating applied on the outer casing while a hard coating was applied on the inner casing. The local interaction between rotating blades and casing generates stresses and thermal loads on the blades (Bahree et al. (1989); Rao and Vyas (1990)). As a result, a coupled bending-torsional analysis of rotating blades is required to obtain the localized effects of rub-impact (Banerjee and Rao (1976); Rao and Banerjee (1977); Rao and Carnegie (1970); Subrahmanyam et al. (1981)). Yu et al. (2018) developed a complex aero-engine dual-rotor model consisting of multi-stage compressors and turbines. The model analyses the transient response during fan blade-out and steady-state response during windmilling. One-dimensional FE modelling is utilized to obtain the dynamic model of the system. Jin et al. (2019) constructed the FE model by combining cylindrical and conical beam elements. The total size of the FE model is reduced by a two-level model reduction method, including component mode synthesis (Hurty (1960)) and proper orthogonal decomposition (Lu et al. (2019)) technique. Recently, Ivanov et al. (2019) and Sun et al. (2018) proposed 3D finite element models of a turbofan engine using FE software packages. An eight-node hexahedral element is utilized to discretize the rotors. The model consisted of a 4-stage low-pressure compressor and a 9-stage high-pressure compressor. The main problem with the FE analysis is that it consumes more time during the nonlinear analysis because of the large DOF of the FE model. In such circumstances, a proper model reduction technique has to be used.

***Model reduction techniques***: Model reduction techniques are intended to reduce the size of FE models without losing the completeness of the information. The main idea of these techniques is to obtain a lower-order model such that it effectively captures the dynamics of the original high-order model. There are different techniques available in the literature that efficiently perform the reduction procedure (Besselink et al. (2013); Friswell et al. (2010); Koutsovasilis and Beitelschmidt (2008); Qu (2004)). In most of the reduction techniques, a master-slave substructuring is utilized. Guyan (1965) developed a reduction technique based on static condensation. In this technique, the stiffness terms are only included in the transformation matrix by omitting the inertia and damping terms. As a result, the method is ineffective in the higher frequency ranges, even though it is efficient in the lower frequency ranges.

Leung (1978) developed a dynamic condensation technique including the inertia term in the model. The method reduced the model accurately over the whole frequency range. Later, O'Callahan (1989a) modified the Guyan condensation method and included the inertia term partially in the formulation. The new technique is called the improved reduced system (IRS) method. In this technique, the transformation matrix is perturbed from the static case by including the inertia terms as pseudo-static forces. The method results in a reduced model that ideally matches the full model at low-frequency resonance regions. However, the reduced stiffness matrix resulting from the IRS method is stiffer than that of the Guyan reduction method and is less suitable for orthogonality checks. As a result, Friswell et al. (1995) extended the IRS method in two ways: by performing the basic transformation on dynamic reduction rather than static reduction and by introducing an iterative scheme in which the corrective term is generated iteratively using the current best estimate of the reduced model. The convergence of the iterated IRS scheme is dependent on the choice of the master coordinates, and it is found that the lower modes converge more quickly than the higher modes (Friswell et al. (1998)). To prove the accuracy of the method in the reduction process, a linear structure with local nonlinearities is analyzed (Friswell et al. (1996). Two cantilever beams joined with a cubic spring are utilized, and the coordinates corresponding to the nonlinearities are chosen as the master DOF during the analysis. Better quality results are obtained when the master coordinates are selected accurately.

Meantime, O'Callahan (1989b) introduced another method called system equivalent reduction expansion process (SEREP), in which an eigenvalue decomposition process is utilized to get a low dimensional subspace through a set of selected modes and a set of master DOFs. Friswell and Inman (1999) used this method for the reduction of structures with viscoelastic components. The damping of the viscoelastic material is incorporated into the method by utilizing the complex eigenvectors. It is found that the SEREP method can approximate the high-frequency responses perfectly.

Another commonly used reduction technique is the component mode synthesis (CMS) method, in which different components of a model, either in the experimental or numerical form, are coupled together to predict the response of the whole model. Generally, the Craig-Bampton substructuring (Craig Jr and Bampton (1968)) technique is employed to achieve coupling of the different components. In this technique, the interior coordinates of the substructures are reduced using modal truncation while the boundary coordinates are kept as such. The transformation matrix includes the eigenvectors of the interior DOFs and a constraint matrix obtained using the geometric compatibility conditions of the boundary DOFs. The CMS technique and Craig-Bampton substructuring are implemented in some of the commercial FEM software.

There are some reduction techniques that are based on projection methods (Gildin (2006)). One of them is the proper orthogonal decomposition (POD), in which the response function is projected onto an orthonormal basis (Lu et al. (2019)). In this technique, the relevant POD modes are selected in such a way that they capture the complete characteristics of the original higher-order model accurately. The POD technique is equivalent to the singular value decomposition (SVD) and principal component analysis (PCA) (Chatterjee (2000)). The advantage of the POD over eigenvalue decomposition is that it can also handle the non-square matrices. Another reduction technique is based on the Krylov subspace method in which the response function is projected onto the Krylov subspace (Liesen and Strakos (2013)). It is an iterative approach, avoiding the matrix-matrix multiplications but using the matrix-vector multiplications (Saad (2003)). Bai (2002) employed a Lanczos process-based Krylov subspace technique for reducing the dynamical systems arising from circuit simulation, structural dynamics, and microelectromechanical systems. Xiang et al. (2018) utilized the Krylov subspace-based scheme for the reduced-order modelling of piezoelectric energy harvesters with complicated mechanical geometries and nonlinear circuits. It is observed that the method has improved the simulation efficiency by several orders of magnitude. Recently, Haller and Ponsioen (2016) utilized the spectral submanifold (SSM) theory for performing the model reduction. In this technique, the relevant normal modes are determined using the SSM theory, which facilitates a reliable projection of the governing nonlinear equations onto modal subspaces (Buza et al. (2021)). Ponsioen et al. (2020) demonstrated this technique using high-dimensional damped-forced beam models.

In the field of rotordynamics, the use of model reduction techniques are very significant since their dynamic models include asymmetric stiffness, localized nonproportional damping and frequency-dependent gyroscopic effects (Wagner et al. (2010)). Rouch and Kao (1980) used the Guyan reduction technique for predicting the forced response and stability of an unbalanced rotor model. Later, Kim and Noah (1991) utilized the dynamic condensation technique for reducing the rotor model undergoing rub-impact at the bearing clearance. However, the CMS technique with Craig-Bampton substructuring is widely used in rotordynamic systems since it is very effective in handling the mechanical systems with localized nonlinearities (Krishna and Padmanabhan (2011)). In this technique, the nodes containing the nonlinearities are included in the master component, while the linear nodes are assembled in the slave component. Based on the CMS technique, Zuo and Wang (2015) developed the reduced model of an aero-engine rotor system for proving the accuracy and efficiency of the technique. As a result, a reduction efficiency of 99.83% is obtained with an error of 0.81%. Later, Sun et al. (2018) reduced the three-dimensional FE model of a complicated aero-engine dual-rotor system using the CMS method and studied the effects

of rub-impact on the global response of the model. Recently, Jin et al. (2019) proposed a two-level model reduction method combining the CMS and POD techniques. According to their results, the proposed method has higher computational efficiency and accuracy in terms of mode expansion than the direct model reduction by using the POD method alone.

**Contact models**

Once the mechanical model is defined, the next task is to develop a contact model for determining the interacting forces during the rotor-stator rub. The contact models are mainly intended to describe the momentum exchange happening during rotor-stator interactions and to establish an explicit functional relationship between the contact force and the corresponding indentation. Mainly, there are two different approaches for performing the contact analysis. In the first approach, referred to as *discrete methods*, the contact occurs for a very short interval of time, and a sudden change in the momentum happens for each contacting body. In the second approach, referred to as *continuous methods*, the impact forces act continuously during the contact period, and the analysis is performed in a usual way, by adding the impact forces to the governing equations during their action period (Gilardi and Sharf (2002)). In literature, most of the researchers have used the continuous contact models, especially the piecewise linear force model (Jiang (2009); Krishna and Padmanabhan (2018); Shang et al. (2011)) and the Lankarani and Nikravesh model (Lankarani and Nikravesh (1990)). The appropriate choice of the contact model decides its capability in simulating the complex rub-impact phenomenon. The loads generated by the contact models are incorporated in the mechanical model. Then, the overall vibration behaviour of the rotating machine can be determined accurately using the different solution techniques as explained as follows.

### 1.2.2 Solution techniques

The time integration method is the most commonly used solution technique for solving the governing equations of a nonlinear mechanical system. In this technique, the solution process starts with an initial guess and then marches in the time domain. Two types of numerical integration schemes exist; they are explicit and implicit schemes. In explicit schemes, the future of a system is calculated from its current state. The Fourth-order Runge-Kutta method is an explicit scheme, based on the Taylor series expansion with a local truncation error of the order $O(h^5)$. Many researchers have used this technique to obtain the rotor response under rub-impact and found it suitable for contact problems (Moreira and Paiva (2018); Wang et al. (2020a); Yang et al. (2016)). The main drawback of explicit schemes is that they require impractically tiny time steps to solve stiff differential equations to keep the numerical stability, which will consume a lot of computational power. On the other hand, the implicit

schemes are ideally suited for solving stiff differential equations with less computational time. It uses the current state and the future state of a system for calculating the state later. The Newmark-beta method is a popular implicit scheme that is used for solving nonlinear differential equations (Ma et al. (2016a); Xu et al. (2016)). It can use large time steps even for stiff differential equations without losing its stability and accuracy. However, the time integration methods are computationally expensive and time-consuming because one has to wait until the attenuation of the transient to obtain the steady-state response.

To get the steady-state solutions of a nonlinear differential equation fastly, a frequency domain method called harmonic balance method (HBM) is introduced by Urabe and Reiter (1966). It is a special version of Galerkin's method in which the response is assumed in terms of truncated Fourier series of $N_h$ harmonics. The method is found to be accurate with less than 5% error and efficient compared to time integration methods (Kim et al. (1991)). In literature, many researchers have used the HBM for finding the steady-state solutions of the rubbing phenomenon (Petrov (2012, 2016); Zhao et al. (2015)). However, recent studies revealed that a simple HBM could not capture specific response characteristics of rotor models such as quasi-periodicity. The quasi-periodic response generally arises in a rotor when it undergoes certain fault conditions such as rub-impact, crack, misalignment, and pedestal looseness. It is observed that during the quasi-periodic response, the rotor whirls with a frequency, which is a linear combination of two incommensurable frequencies. Such a quasi-periodic nature of the response can be captured by introducing the concept of multi-dimensional time into the HBM. The modified method is called the multi-harmonic balance method (MHBM) or quasi-periodic harmonic balance method.

In addition to the application of capturing quasi-periodicity, the MHBM is also employed for analyzing the vibrations in self-excited aperiodic rotor systems, dual rotor systems in aircraft engines, and nonlinear dynamical systems subjected to multi-frequency excitations. Sun et al. (2016) developed an 8 DOF model of a dual-rotor system and investigated the effects of rub-impact using the MHBM technique. An alternating frequency-time (AFT) technique that uses a direct fast Fourier transform (FFT) is utilized for the determination of the Jacobian matrix and the nonlinear force vector (Cameron and Griffin (1989)). Later, Hou et al. (2017) continued the analysis by using the same method for determining the effects of bearing clearance at the inter-shaft ball bearing location. Bifurcation and stability analysis is also carried out when the rotor is subjected to constant excitation and rub-impact (Hou et al. (2019)). Since the MHBM-AFT is a frequency domain technique, Hsu's method is used to predict the stability and bifurcation nature of the model.

Even though the MHBM-AFT technique is formulated to solve multi-frequency excitation problems, most of the research works that presented the MHBM solved up to two-frequency

excitation problems. It is because the programming of the AFT procedure becomes cumbersome when higher dimensional FFTs need to be calculated. Complex matrix operations are required to be performed for obtaining the Fourier coefficients (Ju et al. (2017)). However, a multi-excitation problem can be transformed into a single excitation problem by expressing the excitation frequencies in terms of their common divisor (Guskov and Thouverez (2012)). Now, a simple HBM can solve the transformed equations of motion. But, a higher number of harmonic coefficients are required to capture the complete nonlinear phenomena. Moreover, the alternate transformation between time and frequency domains to calculate the nonlinear Jacobian becomes complex. One way to overcome the issue is by performing the complete analysis in the time domain.

A new time-domain technique called the time variational method (TVM) is introduced by Rook (2002) which didn't require the alternate transformation between the frequency and time domains during the calculation of the Jacobian and nonlinear forces. It is a semi-analytic technique generally employed to solve periodic and single excitation problems. Krishna and Padmanabhan (2011) used the TVM for investigating the response behaviour of nonlinear, multi DOF mechanical models subjected to external excitations. Later, the method is extended in the rotordynamic analysis as well (Krishna and Padmanabhan (2018)). However, in literature, there aren't many studies using the TVM in response analysis; hence, there is a vast area for future research, exploring the TVM in different problem scenarios.

## 1.3 Research gap

In aero-engines, the possibility for the multi-disk rub-impact is high during the FBO event and subsequent windmilling action. However, most of the researchers in this area developed a simplified dual-rotor model of the aero-engine, consisting of a single-stage compressor and turbine, and analyzed single-disk rub-impact only. In their model, the nonlinearities are applied at a single-disk position only by assuming no contact at other disk positions. Such assumption won't be practical for a two-spool aero-engine, consisting of multi-disks that may undergo rub-impact simultaneously. As a result, the influence of multi-disk rub-impact on the dynamic characteristics of an aircraft engine needs to be appropriately studied to avoid the adverse effects of the FBO and windmilling actions.

Since the rotordynamic analysis includes asymmetric matrices and frequency-dependent gyroscopic effects, the model reduction techniques that are effective in structural dynamic problems won't be suitable for rotordynamic problems. In most of the previous works, the gyroscopic effects of the shaft elements were negligible; hence, no difficulties were observed during the reduction process as the skew-symmetric gyroscopic matrices are only at specific

disk locations. However, when the shaft gyroscopic effects are significant, the whole model becomes asymmetric, and the diagonalization is only possible by considering both the right and left eigenvectors. In such cases, the existing model reduction technique needs to be modified to reduce the rotor FE model efficiently even when the asymmetric matrices are present.

As mentioned earlier, the MHBM-AFT technique has certain limitations when more than two-frequency excitations come into the picture. In such circumstances, the AFT procedure is so complex that the determination of the nonlinear Jacobian matrix is cumbersome. The literature shows that the TVM is an appropriate solution technique for solving periodic excitation problems, and it operates without any transformation between time and frequency domains. Till now, the works that employed the TVM analyzed periodic and single excitation problems only. However, the TVM can also be extended to systems involving multiple-frequency excitations. This thesis attempts to address these issues and fill the research gap.

## 1.4 Objectives and Scope

The overall research objective of the current study is “to analyze the steady-state nonlinear response of a two-spool aero-engine model undergoing multi-disk rub-impact using a semi-analytical method." The major objectives of the present study can be summarized as:

1. To understand the nonlinear responses observed in the model during multi-disk rub-impact by:
    - Developing a modified model reduction technique capable of handling asymmetric matrices.
    - Developing an approximate TVM in effectively solving the multi-frequency excitation problems.
    - Validating the method with existing numerical techniques.
2. To evaluate the stability of the model when it experiences multi-disk rub-impact by:
    - Investigating the different steady-state rotor motions observed in the model.
    - Studying the different bifurcations noticed in the model when it undergoes multi-disk rub-impact.
3. To study the effects of parameter variations on the dynamic characteristics of the model by:

- Varying the coefficient of friction and the rotor-stator contact stiffness.
- Introducing the squeeze film damper to the dynamic model and varying the squeeze film clearance and oil viscosity.

## 1.5 Contributions of thesis

The major contributions of this thesis can be summarized as follows,

1. The importance of multi-disk rub-impact studies over single-disk rub-impact studies is well stated in this work. The comparison is performed using a two-spool aero-engine model similar to the CFM56-5B engine. This is the main contribution of the thesis, and there aren't any studies in the literature that analyze the multi-disk rub-impact in the aero-engine models. The proposed model reduction and solution techniques are utilized for this analysis and present the response and stability of the aero-engine model using different post-processing techniques.

2. A modified model reduction technique is developed to reduce the models having asymmetric global matrices. It is a generalized method that can be applied to all mechanical models. In this technique, the reduction is carried out using a method of quadratic eigenvalue decomposition, and it is validated with the existing results. The proposed technique is efficient in terms of accuracy and solution time. As a result, it is applied to reduce the aero-engine dual-rotor model consisting of skew-symmetric gyroscopic matrices.

3. An approximate TVM is introduced to solve the multi-frequency excitation problems. It is developed by transforming the multi-frequency excitation problem into a single-frequency excitation by expressing the frequencies in terms of their common divisor. An optimization procedure is also incorporated to minimize the error between the actual and approximated frequency ratios. The proposed ATVM technique is used to solve the aero-engine dual-rotor model undergoing multi-frequency excitations. The method accurately captures the model response when it undergoes multi-disk rub-impact.

4. The procedures for evaluating the stability and bifurcation nature of mechanical models are described using the ATVM. It is performed by determining the Floquet exponents of the perturbed model. The main advantage of this procedure is that it calculates the stability of the model along with the continuation technique, thereby reducing the evaluation time.

5. A parametric analysis is carried out to understand the effects of rub parameters on the multi-disk rub-impact. The parameters such as rotor-stator friction coefficient and contact stiffness are varied to study their impact on the stability of the aero-engine model. It is observed that the values of rub parameters significantly influence the stability of the model and lead to different kinds of bifurcations in the response. Moreover, the onset of quasi-periodic response and dry whip is dependent on the values of rub parameters.

6. A squeeze film damper is also incorporated into the aero-engine model to understand its influence on the multi-disk rub-impact. It is attached to a bearing near the fan disk, and it significantly reduces the vibration amplitudes of the engine fan. In addition, the effects of SFD parameters on multi-disk rub-impact are also determined. The parameters such as oil viscosity and SFD clearance are used for the analysis.

## 1.6 Organization of thesis

The thesis is organized as follows. After the introduction, Chapter 2 explains the methodology formulation in which the modified model reduction technique and the approximate TVM are described in detail. Moreover, the implementation of the hyper-sphere-based continuation technique and the stability theory are also discussed. In Chapter 3, the proposed model reduction technique and the ATVM are validated. Three different mechanical models are considered for the demonstration of the ATVM, while a Nelson and McVaugh (1976) rotor model is used to verify the model reduction technique. In Chapter 4, the proposed numerical methodology is applied in a simplified dual-rotor model to obtain steady-state, periodic responses under single-disk rub-impact. The model stability is also assessed, and the bifurcation types are determined. Chapter 5 provides the nonlinear dynamic responses of an aero-engine dual-rotor model under multi-disk rub-impact. The model consists of multi-stage compressors and single-stage turbines that undergo rubbing whenever their deflection exceeds the clearance. The frequency response, stability, and parametric analyses are performed to understand the significance of multi-disk rub-impact studies. In Chapter 6, the influence of SFD on the multi-disk rub-impact responses of the aero-engine model is investigated for different values of the SFD parameters. Finally, Chapter 7 summarizes the work and gives directions for future work.

# Chapter 2

# Formulation of Modified Model Reduction Technique & Approximate Time Variational Method

This chapter is mainly intended to formulate a modified model reduction technique and an approximate time variational method for obtaining the response characteristics of an aero-engine model. This is the main contribution of the thesis that makes the solution process efficient. The proposed model reduction technique can handle the models having asymmetric global matrices; hence, it can be used in the applications of rotor systems. The proposed ATVM can be employed to analyse multi-frequency excitation problems in the time domain, thereby reducing the effort of programming.

To carry out the analysis, an aero-engine model similar to CFM 56-5B engine is utilized and its schematic diagram is shown in Fig. 2.1. The CFM 56-5B engine comprises a sophisticated rotordynamic structure consisting of multi-stage bladed disks, hollow & conical shafts, thin-walled casing, rolling contact bearings, and dampers (CFMI (2000)). It consists of two rotors, namely low-pressure and high-pressure rotors which operate at two different speeds. The two rotors are connected using an inter-shaft bearing, which leads to the coupling of the dynamics of both rotors. The low-pressure rotor has a heavy fan, a four-stage compressor, and a four-stage turbine supported on three bearings, whereas the high-pressure rotor has a nine-stage compressor and a single-stage turbine supported on two bearings as shown in Fig. 2.1. However, in the present work, a single-stage turbine is considered at the low-pressure side according to the article by Jin et al. (2019). The dynamic modelling of the dual-rotor model is carried out using the FE method in which the shafts are discretized using the Timoshenko beam elements, including rotary inertia, shear factor, and gyroscopic effects. Based on the section type, cylindrical and conical beam elements are used for the FE

modelling. The dynamic equations of an aero-engine rotor model undergoing multi-frequency excitation can be formulated in the FE method as,

$$\mathbf{M}\ddot{\mathbf{q}} + \mathbf{C}\dot{\mathbf{q}} + \mathbf{G}(\omega_1, \omega_2)\dot{\mathbf{q}} + \mathbf{K}\mathbf{q} + \mathbf{F}_{nl}(\mathbf{q}, \dot{\mathbf{q}}, t) = \mathbf{F}(\omega_1, \omega_2, ..., \omega_n, t) \tag{2.1}$$

where $\omega_1, \omega_2.., \omega_n$ are the excitation frequencies that may be fractional multiples of each other; out of which $\omega_1$ and $\omega_2$ constitute the rotating speeds of low-pressure and high-pressure rotors respectively. The other excitation frequencies may be due to aerodynamic excitations and engine vibrations. **M**, **C**, **G**, and **K** represent the mass, damping, gyroscopic, and stiffness matrices of size $N \times N$. The mass matrix **M** is symmetric, while the damping matrix **C** may be symmetric or asymmetric depending upon the components of the model. The gyroscopic matrix **G** is always skew-symmetric, which includes the gyroscopic effects of the shaft as well as disk. In a dual-rotor model, the gyroscopic matrix is always a function of low-pressure and high-pressure rotor speeds $\omega_1$ and $\omega_2$. The stiffness matrix **K** is symmetric or asymmetric, depending upon the type of problem and material model. The vector **q** is of size $N \times 1$, representing the displacement vector while $\mathbf{F}_{nl}$ and **F** represent the nonlinear and external force vectors respectively. $\dot{\mathbf{q}}$ and $\ddot{\mathbf{q}}$ are the first and second derivatives of **q** with respect to time $t$. Equation 2.1 constitutes a multi-frequency excitation problem that is common in the engineering systems such as electronic circuits, vehicle suspensions, gears, and multi-spool gas turbine engines.

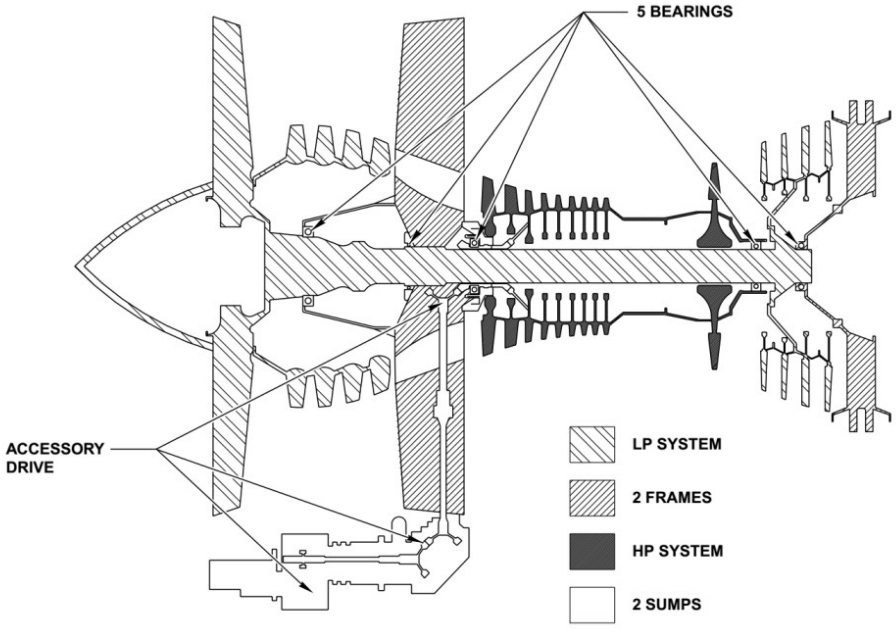


Fig. 2.1 The schematic diagram of a CFM 56-5B aero-engine model(CFMI (2000))

Figure 2.2 shows the flow chart of the present work. Once the FE modelling of the dual-rotor model is completed, a modified model reduction technique is introduced to reduce the size of the FE model. The proposed method is developed based on the quadratic eigenvalue decomposition, and it is validated using the existing numerical results. Later, the response characteristics of the model under multi-disk rub-impact are determined using the ATVM, whose performance is initially verified using existing numerical methods. The analyses such as modal, unbalance response, single-disk rub-impact and multi-disk rub-impact are performed to understand the dynamic characteristics of the aero-engine model. The post-processing of results is carried out using different tools such as Campbell diagrams, frequency response diagrams, orbit plots, FFT spectra and Poincaré maps. It can provide a clear picture of the aero-engine response characteristics under multi-disk rub-impact scenarios occurring due to FBO events.

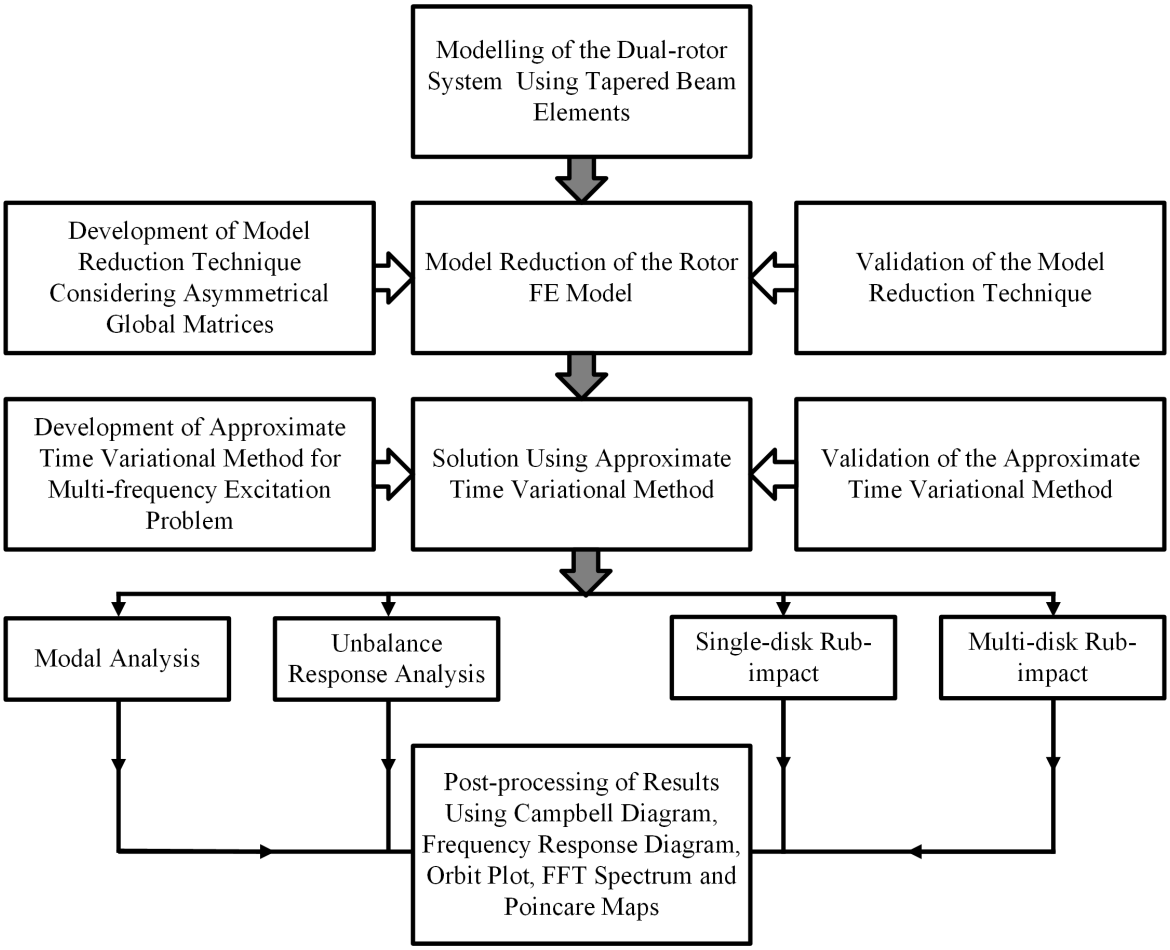


Fig. 2.2 Flow chart of the present work

## 2.1 Modified model reduction technique

In the majority of the mechanical systems, the nonlinearities are localized. Hence, it won't be advisable to use the nonlinear solution technique to all the DOFs, as it increases the computational expense and complexity of the solution process. In the proposed technique, the CMS method is employed for the model reduction in which the model is divided into two components, namely primary and secondary components (Krishna and Padmanabhan (2011)). The primary component consists of all the DOFs where the nonlinearity comes, whereas the secondary component includes all the remaining DOFs. During the reduction process, the secondary component is reduced using the Craig-Bampton substructuring technique (Craig Jr and Bampton (1968)), while the primary component is kept as it is. However, the Craig-Bampton substructuring becomes inefficient when the global matrices are asymmetric in nature. In such cases, the diagonalization of the global matrices using modal transformation won't work, resulting in an inefficient reduction process. The CMS method is modified in the proposed technique by utilizing the quadratic eigenvalue transformation that effectively diagonalizes the global matrices when expressed in the state-space form. The equation of motion for the secondary component is written as,

$$\mathbf{M}_s\,\ddot{\mathbf{q}}_s + (\mathbf{C}_s + \omega\mathbf{G}_s)\,\dot{\mathbf{q}}_s + \mathbf{K}_s\,\mathbf{q}_s = \mathbf{F}_s \tag{2.2}$$

where subscript 's' stands for the secondary component. The nonlinear term won't be there in the governing equations of the secondary component since it contains the linear nodes only. Unlike the existing reduction techniques, the complete damped equation of motion in its state-space form is utilized to perform the reduction procedure. It is written as follows,

$$\begin{bmatrix} \mathbf{C}_s + \omega\mathbf{G}_s & \mathbf{M}_s \\ \mathbf{M}_s & \mathbf{0} \end{bmatrix} \begin{Bmatrix} \dot{\mathbf{q}}_s \\ \ddot{\mathbf{q}}_s \end{Bmatrix} + \begin{bmatrix} \mathbf{K}_s & \mathbf{0} \\ \mathbf{0} & -\mathbf{M}_s \end{bmatrix} \begin{Bmatrix} \mathbf{q}_s \\ \dot{\mathbf{q}}_s \end{Bmatrix} = \begin{Bmatrix} \mathbf{F}_s \\ \mathbf{0} \end{Bmatrix} \tag{2.3}$$

According to the Craig-Bampton substructuring (Craig Jr and Bampton (1968)), the displacement vector in Eq. 2.3 is partitioned into the interior and boundary coordinates. The associated state vector is expressed as,

$$\mathbf{h}_s = \begin{Bmatrix} \mathbf{q}_s \\ \dot{\mathbf{q}}_s \end{Bmatrix} = \begin{Bmatrix} \mathbf{q}_s^i \\ \mathbf{q}_s^b \\ \dot{\mathbf{q}}_s^i \\ \dot{\mathbf{q}}_s^b \end{Bmatrix} \tag{2.4}$$

where $\mathbf{q}_s^i$ is the interior coordinate and $\mathbf{q}_s^b$ is the boundary coordinate.

For further simplicity of derivation, the state vector **h** is transformed using the relation,

$$\mathbf{h}_s = \mathbf{T}\,\mathbf{u}_s \tag{2.5}$$

where

$$\mathbf{T} = \begin{bmatrix} \mathbf{I} & 0 & 0 & 0 \\ 0 & 0 & \mathbf{I} & 0 \\ 0 & \mathbf{I} & 0 & 0 \\ 0 & 0 & 0 & \mathbf{I} \end{bmatrix} \qquad \mathbf{u}_s = \begin{Bmatrix} \mathbf{u}_s^i \\ \mathbf{u}_s^b \end{Bmatrix} = \begin{Bmatrix} \mathbf{q}_s^i \\ \dot{\mathbf{q}}_s^i \\ \mathbf{q}_s^b \\ \dot{\mathbf{q}}_s^b \end{Bmatrix} \tag{2.6}$$

Equation 2.5 is substituted in Eq. 2.3 and pre-multiplied with the transpose of transformation matrix, **T** to obtain the first order component equation as,

$$\begin{bmatrix} \mathbf{C}_s^{ii} + \omega\mathbf{G}_s^{ii} & \mathbf{M}_s^{ii} & \mathbf{C}_s^{ib} + \omega\mathbf{G}_s^{ib} & \mathbf{M}_s^{ib} \\ \mathbf{M}_s^{ii} & \mathbf{0} & \mathbf{M}_s^{ib} & \mathbf{0} \\ \mathbf{C}_s^{bi} + \omega\mathbf{G}_s^{bi} & \mathbf{M}_s^{bi} & \mathbf{C}_s^{bb} + \omega\mathbf{G}_s^{bb} & \mathbf{M}_s^{bb} \\ \mathbf{M}_s^{bi} & \mathbf{0} & \mathbf{M}_s^{bb} & \mathbf{0} \end{bmatrix} \begin{Bmatrix} \dot{\mathbf{q}}_s^i \\ \ddot{\mathbf{q}}_s^i \\ \dot{\mathbf{q}}_s^b \\ \ddot{\mathbf{q}}_s^b \end{Bmatrix} + \begin{bmatrix} \mathbf{K}_s^{ii} & \mathbf{0} & \mathbf{K}_s^{ib} & \mathbf{0} \\ \mathbf{0} & -\mathbf{M}_s^{ii} & \mathbf{0} & -\mathbf{M}_s^{ib} \\ \mathbf{K}_s^{bi} & \mathbf{0} & \mathbf{K}_s^{bb} & \mathbf{0} \\ \mathbf{0} & -\mathbf{M}_s^{bi} & \mathbf{0} & -\mathbf{M}_s^{bb} \end{bmatrix} \begin{Bmatrix} \mathbf{q}_s^i \\ \dot{\mathbf{q}}_s^i \\ \mathbf{q}_s^b \\ \dot{\mathbf{q}}_s^b \end{Bmatrix} = \begin{Bmatrix} \mathbf{F}_s^i \\ \mathbf{0} \\ \mathbf{0} \\ \mathbf{0} \end{Bmatrix} \tag{2.7}$$

Now, Eq. 2.7 can be re-written as,

$$\begin{bmatrix} \mathbf{A}_s^{ii} & \mathbf{A}_s^{ib} \\ \mathbf{A}_s^{bi} & \mathbf{A}_s^{bb} \end{bmatrix} \begin{Bmatrix} \dot{\mathbf{u}}_s^i \\ \dot{\mathbf{u}}_s^b \end{Bmatrix} + \begin{bmatrix} \mathbf{B}_s^{ii} & \mathbf{B}_s^{ib} \\ \mathbf{B}_s^{bi} & \mathbf{B}_s^{bb} \end{bmatrix} \begin{Bmatrix} \mathbf{u}_s^i \\ \mathbf{u}_s^b \end{Bmatrix} = \begin{Bmatrix} \mathbf{L}_s^i \\ \mathbf{0} \end{Bmatrix} \tag{2.8}$$

Subsequently, the state vector in Eq. 2.8 is transformed into a new set of coordinates using the relation given below.

$$\begin{Bmatrix} \mathbf{u}_s^i \\ \mathbf{u}_s^b \end{Bmatrix} = \begin{bmatrix} \mathbf{\Phi}_R & \mathbf{\Psi} \\ \mathbf{0} & \boldsymbol{I} \end{bmatrix} \begin{Bmatrix} \mathbf{q}_{mod} \\ \mathbf{u}_s^b \end{Bmatrix} = \mathbf{V_R}\,\mathbf{z}_s \tag{2.9}$$

The associated left transformation matrix is written as,

$$\mathbf{V_L} = \begin{bmatrix} \mathbf{\Phi}_L & \mathbf{\Psi} \\ \mathbf{0} & \boldsymbol{I} \end{bmatrix} \tag{2.10}$$

where $\mathbf{\Phi}_R$ and $\mathbf{\Phi}_L$ are the retained right and left modal matrices and $\mathbf{q}_{mod}$ is the retained modal coordinate such that,

$$\begin{aligned} \mathbf{\Phi}_L^T\,\mathbf{A_s^{ii}}\,\mathbf{\Phi}_R &= \mathbf{D} \\ \mathbf{\Phi}_L^T\,\mathbf{B_s^{ii}}\,\mathbf{\Phi}_R &= -\Lambda\mathbf{D} \end{aligned} \tag{2.11}$$

where **D** is the diagonal matrix of normalization constants and $\Lambda$ is the diagonal matrix

of retained eigenvalues, both are of size $m \times m$. The number of retained modes is selected based on the convergence study. The value of $m$ is far less than the total DOF of the model, facilitating the model reduction. $\mathbf{\Psi}$ is the constraint mode function which is determined using the relation,

$$\mathbf{\Psi} = \begin{bmatrix} -(\mathbf{K}_s^{ii})^{-1}\mathbf{K}_s^{ib} & 0 \\ 0 & -(\mathbf{K}_s^{ii})^{-1}\mathbf{K}_s^{ib} \end{bmatrix} \tag{2.12}$$

The substitution of Eq. 2.9 into Eq. 2.8 and pre-multiplying with the transpose of $\mathbf{V_L}$ yields the reduced equation of the secondary component as,

$$\mathbf{P}_s\, \dot{\mathbf{z}}_s + \mathbf{Q}_s\, \mathbf{z}_s = \mathbf{L}_s \tag{2.13}$$

where

$$\begin{aligned} \mathbf{P}_s &= \begin{bmatrix} \mathbf{\Phi}_L & \mathbf{\Psi} \\ \mathbf{0} & \boldsymbol{I} \end{bmatrix}^T \begin{bmatrix} \mathbf{A}_s^{ii} & \mathbf{A}_s^{ib} \\ \mathbf{A}_s^{bi} & \mathbf{A}_s^{bb} \end{bmatrix} \begin{bmatrix} \mathbf{\Phi_R} & \mathbf{\Psi} \\ \mathbf{0} & \boldsymbol{I} \end{bmatrix} \\ \mathbf{Q}_s &= \begin{bmatrix} \mathbf{\Phi}_L & \mathbf{\Psi} \\ \mathbf{0} & \boldsymbol{I} \end{bmatrix}^T \begin{bmatrix} \mathbf{B}_s^{ii} & \mathbf{B}_s^{ib} \\ \mathbf{B}_s^{bi} & \mathbf{B}_s^{bb} \end{bmatrix} \begin{bmatrix} \mathbf{\Phi_R} & \mathbf{\Psi} \\ \mathbf{0} & \boldsymbol{I} \end{bmatrix} \\ \mathbf{L}_s &= \begin{bmatrix} \mathbf{\Phi}_L & \mathbf{\Psi} \\ \mathbf{0} & \boldsymbol{I} \end{bmatrix}^T \begin{Bmatrix} \mathbf{L}_s^i \\ \mathbf{0} \end{Bmatrix} \end{aligned} \tag{2.14}$$

The size of the reduced secondary component is equal to the sum of the number of retained normal modes and twice the number of the boundary coordinates (i.e. $N_s = m + 2n_b$). It is very small compared to that of the complete model. For the primary component, all the DOFs are retained in physical coordinates due to the presence of nonlinearity. The state-space form of the primary component is written as,

$$\begin{bmatrix} \mathbf{C}_p + \omega\mathbf{G}_p & \mathbf{M}_p \\ \mathbf{M}_p & \mathbf{0} \end{bmatrix} \begin{Bmatrix} \dot{\mathbf{q}}_p \\ \ddot{\mathbf{q}}_p \end{Bmatrix} + \begin{bmatrix} \mathbf{K}_p & \mathbf{0} \\ \mathbf{0} & -\mathbf{M}_p \end{bmatrix} \begin{Bmatrix} \mathbf{q}_p \\ \dot{\mathbf{q}}_p \end{Bmatrix} + \begin{Bmatrix} \mathbf{F}_{nlp} \\ \mathbf{0} \end{Bmatrix} = \begin{Bmatrix} \mathbf{F}_p \\ \mathbf{0} \end{Bmatrix} \tag{2.15}$$

The state vector in the Eq. 2.15 is transformed as in Eq. 2.5 and pre-multiplied with the transpose of $\mathbf{T}$ to get the equation of motion as,

$$\begin{bmatrix} \mathbf{A}_p^{ii} & \mathbf{A}_p^{ib} \\ \mathbf{A}_p^{bi} & \mathbf{A}_p^{bb} \end{bmatrix} \begin{Bmatrix} \dot{\mathbf{u}}_p^i \\ \dot{\mathbf{u}}_p^b \end{Bmatrix} + \begin{bmatrix} \mathbf{B}_p^{ii} & \mathbf{B}_p^{ib} \\ \mathbf{B}_p^{bi} & \mathbf{B}_p^{bb} \end{bmatrix} \begin{Bmatrix} \mathbf{u}_p^i \\ \mathbf{u}_p^b \end{Bmatrix} + \begin{Bmatrix} \mathbf{E}_{nlp}^i \\ \mathbf{0} \end{Bmatrix} = \begin{Bmatrix} \mathbf{L}_p^i \\ \mathbf{0} \end{Bmatrix} \tag{2.16}$$

In order to keep the component mode procedure the same as that of the secondary component, an identity matrix transformation is used instead of $\mathbf{V_R}$ and $\mathbf{V_L}$, leading to the governing

equation of the primary component as,

$$\mathbf{P}_p\,\dot{\mathbf{z}}_p + \mathbf{Q}_p\,\mathbf{z}_p + \mathbf{E}_{nlp} = \mathbf{L}_p \tag{2.17}$$

Finally, the reduced dynamic equations of the model can be obtained by assembling Eq. 2.13 and Eq. 2.17 and can be written as,

$$\mathbf{P}\dot{\mathbf{z}} + \mathbf{Q}\mathbf{z} + \mathbf{E}_{nl} = \mathbf{L}(\omega_1, \omega_2, ..., \omega_n, t) \tag{2.18}$$

The total DOF of the reduced model expressed in Eq. 2.18 is $N_r = N_s + (N_p - 2n_s.n_{nod})$, where $N_s$ is the DOF of the reduced secondary component, $N_p$ is the DOF of the primary component, $n_s$ is the number of secondary components and $n_{nod}$ is the nodal DOF. It should be noted that the value of $N_r$ is very much less than that of the total DOF. The use of the state-space form of the governing equation and the quadratic eigenvalue transformation facilitates the efficient reduction of the models containing asymmetric global matrices, especially in rotordynamic systems.

## 2.2 Solution techniques

As mentioned earlier, multi-frequency excitation problems are common in specific mechanical systems such as articulated loading platforms, vehicle suspensions, gears, and multi-spool gas turbine engines. The model response becomes very complex when the ratios of the excitation frequencies are fractional, besides the existence of localized nonlinearities. Generally, the time integration methods are used for solving the nonlinear systems undergoing multi-frequency excitations. However, the time integration methods are computationally expensive and time-consuming since one has to wait until the attenuation of the transient to obtain the steady-state response. As a result, semi-analytic techniques such as the multi-harmonic balance method and time variational method are required to get the steady-state responses at a faster rate.

### 2.2.1 Multi-harmonic balance method

The multi-harmonic balance method is an extension of the basic HBM in which the concept of hyper-time is utilized. The main assumptions in generating the governing equations of the MHBM are stated as follows.

- Since there are ‘n’ excitation frequencies, the hyper-time is n-dimensional, and the solution is supposed to be periodic for each dimension.

- The response vector, external force vector and the nonlinear function are assumed to contain the linear combinations of excitation frequencies. Hence, they all are expressed in a similar form in the governing equations.

- The Fourier coefficients are assumed to be constant numbers.

As a result, the response vector, external force vector and the nonlinear function are expressed as a truncated Fourier series (Sun et al. (2016)) as given,

$$\mathbf{z}(t) = \sum_{i_1=-N_h}^{N_h} .. \sum_{i_n=-N_h}^{N_h} [\mathbf{a}_{i_1..i_n} \cos(i_1\omega_1 + .. + i_n\omega_n)t + \mathbf{b}_{i_1..i_n} \sin(i_1\omega_1 + .. + i_n\omega_n)t] \quad (2.19)$$

$$\mathbf{E}_{nl}(t) = \sum_{i_1=-N_h}^{N_h} .. \sum_{i_n=-N_h}^{N_h} [\mathbf{c}_{i_1..i_n} \cos(i_1\omega_1 + .. + i_n\omega_n)t + \mathbf{d}_{i_1..i_n} \sin(i_1\omega_1 + .. + i_n\omega_n)t] \quad (2.20)$$

$$\mathbf{L}(t) = \sum_{i_1=-N_h}^{N_h} .. \sum_{i_n=-N_h}^{N_h} [\mathbf{e}_{i_1..i_n} \cos(i_1\omega_1 + .. + i_n\omega_n)t + \mathbf{f}_{i_1..i_n} \sin(i_1\omega_1 + .. + i_n\omega_n)t] \quad (2.21)$$

where $N_h$ represents the number of harmonics selected for the analysis. $(\mathbf{a}_{i_1..i_n}, \mathbf{b}_{i_1..i_n})$, $(\mathbf{c}_{i_1..i_n}, \mathbf{d}_{i_1..i_n})$ and $(\mathbf{e}_{i_1..i_n}, \mathbf{f}_{i_1..i_n})$ are the Fourier coefficients of the response, nonlinear force and external force vectors respectively. By substituting these equations in the governing equation of the reduced model and applying the Galerkin procedure, the algebraic expression for the residual can be obtained as,

$$\mathbf{R}(\tilde{\mathbf{z}}) = \mathbf{Y}\,\tilde{\mathbf{z}} + \tilde{\mathbf{e}}_{nl} - \tilde{\mathbf{f}} \quad (2.22)$$

where $\tilde{\mathbf{e}}_{nl}$ and $\tilde{\mathbf{f}}$ are the vectors containing the Fourier coefficients of the nonlinear force and external force of size $2N_t \times 1$ in which $N_t = (2N_h + 1)^n$. The matrix $\mathbf{Y}$ can be expressed as,

$$\mathbf{Y} = \begin{bmatrix} \mathbf{Y}^0 & 0 & \cdots & 0 & 0 & 0 \\ 0 & \mathbf{Y}^1 & \cdots & 0 & 0 & 0 \\ \vdots & \vdots & \ddots & \vdots & \vdots & \vdots \\ 0 & 0 & \cdots & \mathbf{Y}^k & 0 & 0 \\ \vdots & \vdots & \ldots & \ldots & \ddots & \vdots \\ 0 & 0 & \cdots & 0 & \ldots & \mathbf{Y}^{N_t} \end{bmatrix} \quad \mathbf{Y}^k = \begin{bmatrix} \mathbf{Q} & \mathbf{P}(i_1\omega_1 + .. + i_n\omega_n) \\ -\mathbf{P}(i_1\omega_1 + .. + i_n\omega_n) & \mathbf{Q} \end{bmatrix} \quad (2.23)$$

Equation 2.22 can be solved using the Newton-Raphson method. The initial value of $\tilde{\mathbf{z}}$ is determined by neglecting the nonlinear term and performing the linear response analysis alone. The obtained linear solution will be in the frequency domain, which is transformed

into the time domain using the inverse FFT. Later, the nonlinear function is calculated by substituting the linear solution into the nonlinear equation. Then, the corresponding nonlinear vector is calculated in the frequency domain using the direct FFT. It indicates that an alternate transformation between the frequency and time domains is always required to calculate the nonlinear vector $\tilde{\mathbf{e}}_{nl}$ in Eq. 2.22. A similar procedure is required to calculate the nonlinear Jacobian as well. Generally, an AFT technique is employed to perform the transformation between the frequency and time domains. However, the AFT technique has limitations when dealing with more than two-frequency excitation problems. In such problems, the AFT procedure becomes cumbersome since it involves complex matrix operations while calculating the higher dimensional FFT. This limitation of the AFT technique makes the MHBM technique complicated in more than two-frequency excitation problems.

### 2.2.2 Approximate time variational method

The TVM is a periodic solution methodology generally employed to solve single excitation problems (Krishna and Padmanabhan (2011)). However, in a multi-frequency excitation problem such as in aero-engines, the TVM becomes ineffective when the frequency ratios are fractional or irrational multiples of each other. In such situations, the TVM can be extended to the multi-frequency excitation problems by introducing an approximate time variational method (ATVM). In this study, the ATVM is formulated by expressing the frequencies in terms of a fundamental frequency that is the common divisor of the excitation frequencies. In case the frequency ratio is irrational, it is approximated to the nearest rational number, and then, the greatest common divisor of the approximated frequency components are obtained as given,

$$\omega_0 = \frac{\tilde{\omega}_j}{p_j}, \qquad j = 1,2,..,n \qquad p_j \in \mathbb{N} \tag{2.24}$$

where $\tilde{\omega}_j$ is the approximated value of $\omega_j$ obtained by approximating the irrational excitation frequencies to rational ones. As a result, the response will be approximate, and its accuracy is highly dependent on how close the approximated ratios are with the actual ones. An optimization procedure can achieve the optimum frequency ratio that minimizes the error between the actual and approximated responses. The objective function can be written as,

$$\textit{Minimize} \quad \mathbf{Z}_{obj} = \sum \frac{\left| r_j - \tilde{r}_j \right|}{r_j}, \qquad j = 1,2,..,n \tag{2.25}$$

where $r_j$ and $\tilde{r}_j$ are the actual and approximated values of the frequency ratios, such that $r_j = \frac{\omega_1}{\omega_j}$ and $\tilde{r}_j = \frac{\tilde{\omega}_1}{\tilde{\omega}_j} = \frac{p_1}{p_j}$. $p_1$, $p_2$,...., $p_n$ are the integers that represent the decision variables of the optimization. The constraint equation is written as,

$$\gamma_{min} < p_j < \gamma_{max} \quad \text{and} \quad p_j \geq 0, \qquad j = 1,2,..,n \tag{2.26}$$

where $\gamma_{min}$ and $\gamma_{max}$ are the integers chosen by the user. The stepwise procedure to implement the optimization algorithm is explained as follows.

- Initially, the values of $\gamma_{min}$ and $\gamma_{max}$ are chosen based on the computation requirements. They need to be integer numbers with values greater than zero.
- Different combinations of $p_j$'s are determined by satisfying the constraint equations. The values of $p_j$'s are connected to each other using the expression, $p_j = round\left(\frac{p_1}{r_j}\right)$ where *round* ( ) is a function that rounds off the decimal points.
- The optimization is carried out by determining the global minima of the objective function. The values of $p_j$'s for which the objective function is minimum are used to calculate the optimized frequency ratio.

Once the optimized frequency ratios are obtained, the greatest common divisor can be calculated using Eq. 2.24. Now, the transformed form of Eq. 2.18 can be expressed as,

$$\omega_0 \mathbf{P}\mathbf{z}' + \mathbf{Q}\mathbf{z} + \mathbf{E}_{nl} = \mathbf{L}(\tau) \tag{2.27}$$

where $\mathbf{z}'$ is the first derivative of $\mathbf{z}$ with respect to $\tau$. Fortunately, Eq. 2.27 is equivalent to a periodic, single excitation problem with a fundamental frequency $\omega_0$, and it can be solved using the TVM. More information about the TVM can be obtained from the article by Rook (2002). In this method, the response, nonlinear function, and external force vectors can be expressed in terms of a basis function as follows,

$$\mathbf{z}(\tau) = \hat{\mathbf{Z}} \,.\, \chi(\tau) \qquad \mathbf{E}_{nl}(\tau) = \hat{\mathbf{E}}_{nl} \,.\, \chi(\tau) \qquad \mathbf{L}(\tau) = \hat{\mathbf{L}} \,.\, \chi(\tau) \tag{2.28}$$

where $\chi(\tau)$ maybe a wavelet scaling function or a finite element shape function. This approximation helps to discretize the periodic response function into several time points. The discretized response function is determined using the Newton-Raphson method and the complete analysis is performed in the time domain. In Eq. 2.28, $\hat{\mathbf{Z}}$ represents a matrix whose $i$th row denotes the $i$th DOF value calculated at discrete time points. Its column size is equal to the number of discrete time points $N_{pt}$ taken for the analysis. Similarly, $\hat{\mathbf{L}}$ and $\hat{\mathbf{E}}_{nl}$ are the external and nonlinear force matrices calculated at discrete time points respectively. The substitution of Eq. 2.28 in Eq. 2.27 and then, applying the Galerkin method, a weak residual form of Eq. 2.27 is obtained as,

$$\mathbf{R}(\hat{\mathbf{z}}) = \left[\omega_0\left(\mathbf{P}\otimes\mathbf{D}^{(1)}\right) + \left(\mathbf{Q}\otimes\mathbf{D}^{(0)}\right)\right]\hat{\mathbf{z}} + \left(\mathbf{I}\otimes\mathbf{D}^{(0)}\right)\left(\hat{\mathbf{e}}_{nl} - \hat{\mathbf{f}}\right) = 0 \tag{2.29}$$

where $\hat{\mathbf{z}} = \text{vec}\,(\hat{\mathbf{Z}}^T)$, $\hat{\mathbf{e}}_{nl} = \text{vec}\,(\hat{\mathbf{E}}_{nl}^T)$ and $\hat{\mathbf{f}} = \text{vec}\,(\hat{\mathbf{L}}^T)$. vec ( ) is the vectorize operator that stacks the columns of the matrix operated upon and $\otimes$ is the Kronecker product. $D^{(0)}$ and $D^{(1)}$ are the differentiation matrices of order 0 and 1 respectively. Equation 2.29 is a set of nonlinear algebraic equations of size $N_{pt}\,N_r$ and are solved using the Newton-Raphson method. The modified method is called the approximate time variational method.

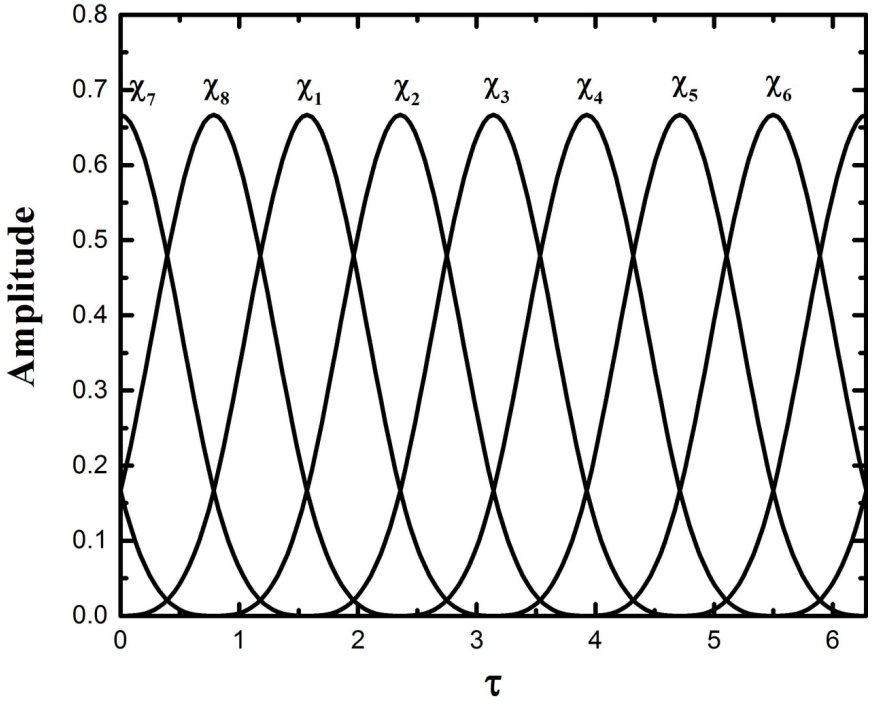


Fig. 2.3 A group of cubic splines translated to each other representing a basis function

The main step in the formulation of the ATVM is the determination of differentiation matrices. It is mainly dependent on the type of basis function chosen for the analysis. A cubic spline function has a good convergence rate compared to the other functions due to the narrow banded structure of the differentiation matrices (Rook (2002)). A cubic spline is a type of B-spline of order three which passes through a set of control points. Fig 2.3 shows a group of cubic splines that are translated to each other, together which represents the basis function $\chi(\tau)$. In Fig 2.3, $\chi_1$ is the representation of $\chi_{3,4}$ and the other splines are its translated forms. The basis function of a B-spline can be written in general form as,

$$\chi_{i,k}(\tau) = \frac{(\tau - t_i)\chi_{i,k-1}}{(t_{i+k-1} - t_i)} + \frac{(t_{i+k} - \tau)\chi_{i+1,k-1}}{t_{i+k} - t_{i+1}} \tag{2.30}$$

where $t_i$'s are called knot values and are obtained as,

$$t_i = \begin{cases} 0 & \text{for } \; i < k \\ i-k+1 & \text{for } \; k \leq i \leq N_p \\ N_p - k + 2 & \text{for } \; i > N_p \end{cases} \tag{2.31}$$

where $i = 0$ to $N_p + k$. The value of $k$ decides the spline type, whether it is linear, quadratic or cubic. For cubic spline, the value of $k$ is 4. Now, the differentiation matrices can be determined as in Eq. 2.32.

$$\begin{aligned} D^{(0)} &= \frac{1}{2\pi} \int_0^{2\pi} \chi(\tau) \cdot \chi^T(\tau) \, d\tau \\ D^{(1)} &= \frac{1}{2\pi} \int_0^{2\pi} \chi(\tau) \cdot \chi(\tau)'^T \, d\tau \end{aligned} \tag{2.32}$$

### 2.2.3 Parametric continuation

The presence of strong nonlinearities in the system leads to the occurrence of different solution branches for a certain set of system parameters. The point at which the new solution branches are originated is called the bifurcation point. A proper understanding of bifurcation is essential in nonlinear dynamic analyses, and all the possible vibration regimes need to be included in the design stages to avoid undesirable events. The occurrence of a particular vibration regime is mainly dependent on the initial conditions of the system. Generally, a continuation algorithm is employed for the tracing of solution branches by incorporating an additional tracing equation in Eq. 2.29 as,

$$\mathbf{R}_1(\hat{\mathbf{z}}, \omega_0) = \begin{Bmatrix} \mathbf{R}(\hat{\mathbf{z}}, \omega_0) \\ \mathbf{r}(\hat{\mathbf{z}}, \omega_0) \end{Bmatrix} = 0 \tag{2.33}$$

where $\mathbf{r}(\hat{\mathbf{z}}, \omega_0) = 0$ is the tracing equation which may take the form of arc-length continuation, pseudo-arc-length continuation or hypersphere continuation (Krishna and Padmanabhan (2011)). The tracing equation of the hyper-sphere based continuation algorithm is written as,

$$\mathbf{r}(\hat{\mathbf{z}}, \omega_0) = (\hat{\mathbf{z}}^2 - \hat{\mathbf{z}}_c^2) + (\omega_0^2 - \omega_{0c}^2) - \bar{r}^2 = 0 \tag{2.34}$$

where $\bar{r}$ is the radius of the hypersphere, and the variables with subscript $c$ are the previous steady-state points representing the centre of the hypersphere. Now, the Newton-Raphson equation can be expressed as,

$$\begin{bmatrix} \mathbf{J} & \mathbf{R}_{\omega_0} \\ \frac{\partial \mathbf{r}}{\partial \hat{\mathbf{z}}} & \frac{\partial \mathbf{r}}{\partial \omega_0} \end{bmatrix} \begin{Bmatrix} \Delta\hat{\mathbf{z}} \\ \Delta\omega_0 \end{Bmatrix} = \mathbf{J_1}(\hat{\mathbf{z}}, \omega_0) \begin{Bmatrix} \Delta\hat{\mathbf{z}} \\ \Delta\omega_0 \end{Bmatrix} = \begin{Bmatrix} \mathbf{R}(\hat{\mathbf{z}}, \omega_0) \\ \mathbf{r}(\hat{\mathbf{z}}, \omega_0) \end{Bmatrix} \tag{2.35}$$

where $\mathbf{J} = \frac{\partial \mathbf{R}}{\partial \hat{\mathbf{z}}}$ and $\mathbf{R}_{\omega_0} = \frac{\partial \mathbf{R}}{\partial \omega_0}$. The increments, determined using Eq. 2.35 are added to the current solution point to obtain the future solution point and eventually, traces the complete solution branch.

### 2.2.4 Stability theory

Once the complete solution branches are determined, it is necessary to assess the stability of the solution points. It is achieved by introducing a small perturbation $\varepsilon$ in the steady-state solution point $\mathbf{z}^*$ to obtain the modified equation as,

$$\omega_0 \ \mathbf{P} \ (\mathbf{z}^* + \varepsilon)' + \mathbf{Q} \ (\mathbf{z}^* + \varepsilon) + \mathbf{E}_{nl}(\mathbf{z}^* + \varepsilon) = \mathbf{L} \tag{2.36}$$

By linearizing the nonlinear force $\mathbf{E}_{nl}$ around $\mathbf{z}^*$ using the Taylor series expansion, Eq. 2.36 is changed as,

$$\omega_0 \ \mathbf{P} \ (\mathbf{z}^* + \varepsilon)' + \mathbf{Q} \ (\mathbf{z}^* + \varepsilon) + \mathbf{E}_{nl}(\mathbf{z}^*) + \frac{\partial \mathbf{E}_{nl}(\mathbf{z}^*)}{\partial \mathbf{z}} \varepsilon = \mathbf{L} \tag{2.37}$$

Since $\mathbf{z}^*$ is an equillibrium point,

$$\omega_0 \ \mathbf{P} \ \mathbf{z}^{*'} + \mathbf{Q} \ \mathbf{z}^* + \mathbf{E}_{nl}(\mathbf{z}^*) - \mathbf{L} = 0 \tag{2.38}$$

Hence, the remaining perturbation equation is written as,

$$\omega_0 \ \mathbf{P} \ \varepsilon' + \mathbf{Q} \ \varepsilon + \frac{\partial \mathbf{E}_{nl}(\mathbf{z}^*)}{\partial \mathbf{z}} \varepsilon = 0 \tag{2.39}$$

According to the Floquet theory, $\varepsilon(\tau) = e^{\lambda \tau} \phi(\tau)$, where $\lambda$ is the eigenvalue and $\phi(\tau)$ is a periodic function. By substituting the expression of $\varepsilon(\tau)$ and its derivatives into Eq. 2.39, the modified equation is written as,

$$\left\{ [\omega_0 \mathbf{P} \phi] \lambda + [\omega_0 \mathbf{P} \phi' + \mathbf{Q} \phi + \frac{\partial \mathbf{E}_{nl}(\mathbf{z}^*)}{\partial \mathbf{z}} \phi] \right\} e^{\lambda \tau} = 0 \tag{2.40}$$

Now, the periodic function $\phi(\tau)$ is expressed in terms of the basis function as $\phi(\tau) = \hat{\Phi} \ . \ \chi(\tau)$. Substitution of this expression into Eq. 2.40 and following the Galerkin procedure, an eigenvalue problem is obtained as (Rook (2002)),

$$
\begin{aligned}
&(\lambda\Xi_1+\Xi_0)\hat{\Phi}=0 \qquad \text{where}\\
&\quad \Xi_1=\omega_0\left(\mathbf{P}\otimes\mathbf{D}^{(0)}\right)\\
&\quad \Xi_0=\omega_0\left(\mathbf{P}\otimes\mathbf{D}^{(1)}\right)+\left(\mathbf{Q}\otimes\mathbf{D}^{(0)}\right)+\left(\mathbf{I}\otimes\mathbf{D}^{(0)}\right)\frac{\partial\hat{\mathbf{e}}_{nl}}{\partial\hat{\mathbf{z}}}
\end{aligned}
\tag{2.41}
$$

Even though, Eq. 2.41 provides $N_{pt}N_r$ eigenvalues, only $N_r$ eigenvalues have physical meaning. Hence, the first $N_r$ eigenvalues with the smallest imaginary part can be calculated instead of determining the complete set of eigenvalues. The system is stable when real parts of the first $N_r$ eigenvalues are negative, while it is unstable when at least one of them is positive. The advantage of this method is that all the terms in Eq. 2.41 are determined during each iteration of the continuation procedure. Hence, the stability analysis can be performed along with the continuation procedure, which saves time.

## 2.3 Post-processing techniques

Once the results are obtained using the ATVM, the next step is to present them properly for providing useful information to the readers. There are specific post-processing techniques available to extract information from the numerical response and to present them in various diagrams/plots. In this work, different techniques such as Campbell diagram, time response, frequency response, orbit plot, FFT spectrum and Poincaré maps are used and are explained as follows.

### 2.3.1 Campbell diagram

The Campbell diagrams are used to obtain the critical speeds of the rotor system by performing the modal analysis. Due to the presence of gyroscopic moments, the natural frequencies of the rotor will vary with the rotating speed. The plot showing the variation of natural frequency with respect to the rotating speed is called the Campbell diagram. The stepwise procedure to plot the Campbell diagram is explained as follows.

- Initially, the eigenvalue analysis of the rotor model is performed using the expression as given,

$$
\mathbf{AI}=\lambda\mathbf{I} \qquad \text{where} \qquad \mathbf{A}=\begin{bmatrix}\mathbf{0} & \mathbf{I}\\ -\mathbf{M}^{-1}\mathbf{K} & -\mathbf{M}^{-1}(\mathbf{C}+\omega\mathbf{G})\end{bmatrix} \tag{2.42}
$$

  In Eq. 2.42, the characteristic matrix $\mathbf{A}$ is a function of rotating speed $\omega$.

- Once the analysis is completed, the eigenvalues are obtained in the form of complex numbers due to damping and gyroscopic terms. The imaginary part of the complex eigenvalue gives the natural frequency of the model.

- Later, the natural frequency is plotted against the rotating speed to obtain the Campbell diagram. The critical speeds are calculated by noting the intersection points of frequency curves with the synchronous excitation line ($1\times$).

### 2.3.2 Time response signal

The time response signals are used to present the variations in rotor responses with respect to time. They provide the history of rotor motions during a period. Since the ATVM operates in the time domain, the numerical responses are obtained directly as a function of time. When they are plotted against time, the time response signals are received.

### 2.3.3 Frequency response diagram

The frequency response diagrams show the variations in rotor responses with respect to the frequency. They provide complete information about the system resonances within the operating range. To get the frequency response diagram, the rotating speed of the rotor is varied between certain frequency limits and the steady-state response signals are obtained at each frequency using the ATVM. Then, the maximum amplitude of the response signals is recorded and plotted against the frequencies to obtain a frequency response diagram.

### 2.3.4 Orbit plot

The orbit plots are used to present the trajectories of the rotor during its operation. It shows the whirling nature of the rotor within the clearance space. The direction of whirling, whether it is forward or backward, can also be understood from the orbit plot. Through ATVM, the rotor's horizontal and vertical (X and Y) displacements are received in the time domain. When they are plotted against each other, the orbit plots are obtained.

### 2.3.5 FFT spectrum

The FFT spectrum is used to understand the frequency contents in the response during its operation. It is obtained by performing the FFT of the time signal recorded using the ATVM. It is found that the FFT spectrum of a linear model always shows the excitation frequency

components alone. However, the FFT spectrum of the nonlinear model may show the other frequency components as well due to the nonlinearity.

### 2.3.6 Poincaré map

The Poincaré map is a collection of points obtained by storing a single point of the trajectory onto the phase space for each cycle of motion, with consistent timing (Moon (2008)). It helps to understand the type of motion, whether periodic or nonperiodic. If the Poincaré map contains a single point, then the motion is said to be periodic. If it includes closed curves, the motion is said to be quasi-periodic. Moreover, a fractal structure of points in the Poincaré map indicates the occurrence of chaotic behaviour. The stepwise procedure to obtain the Poincaré map from the numerical response is explained as follows.

- Initially, the rotor displacements and velocities are obtained in the time domain using the ATVM.
- Later, the displacements and velocities are recorded as points in the phase space with a consistent time gap. As a result, a plot showing the collection of points is received, which is called the Poincaré map.

## 2.4 Summary

In this chapter, the different numerical methods required for the analysis of aero-engine dual-rotor model are formulated for studying the multi-disk rub-impact. It involves the introduction of a modified model reduction technique and a semi-analytic solution technique called the approximate time variational method. The proposed reduction technique is based on the CMS method coupled with the Craig-Bampton substructuring. Using the quadratic eigenvalue decomposition, the proposed method can reduce the models having asymmetric global matrices. The MHBM-AFT technique is the most commonly used solution technique for the two-frequency excitation problem; however, it has limitations while dealing with more than two-frequency excitation problems. In such scenarios, the proposed ATVM technique will be useful that expresses the excitation frequencies in terms of a fundamental frequency which is the common divisor of the approximated frequency components. The proposed ATVM can capture the solution branches effectively even when the excitation frequency components are incommensurable. It has to be validated by comparing the results with the existing numerical methods, as discussed in the following chapter.

# Chapter 3

# Validation of Modified Model Reduction Technique & Approximate Time Variational Method

This chapter is mainly intended to validate the proposed model reduction technique and the ATVM using the existing numerical methods. The accuracy of results and the computation time are compared to evaluate the performances of the proposed methods. A Nelson and McVaugh (1976) rotor model is used to verify the performance of the modified model reduction technique, while three mechanical models are utilized for validating the ATVM.

## 3.1 Validation of the modified model reduction technique

Figure 3.1 shows the schematic diagram of a Nelson and McVaugh (1976) rotor model. In their paper, Nelson and McVaugh (1976) modelled the shaft as a six-element member with each element consisting of several sub-elements. A reduction technique based on static condensation was used to reduce the internal displacements into the element endpoint displacements. However, in the current work, in order to verify the proposed technique, the rotor-bearing system is modelled with 18 elements (equal to the total number of sub-elements) and are partitioned into primary and secondary components as shown in Fig. 3.2. The node containing the disk and its adjacent nodes are included in the primary component, while the remaining nodes are added to the secondary components.

The details of model reduction are given in Table 3.1. The complete model has a total DOF of 76. In the reduced model, the primary component contains three nodes and are kept in physical coordinates, whereas the secondary components are reduced using the

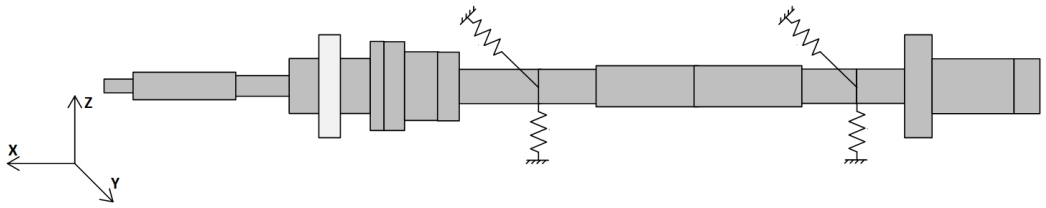


Fig. 3.1 Schematic diagram of the Nelson and McVaugh (1976) rotor model

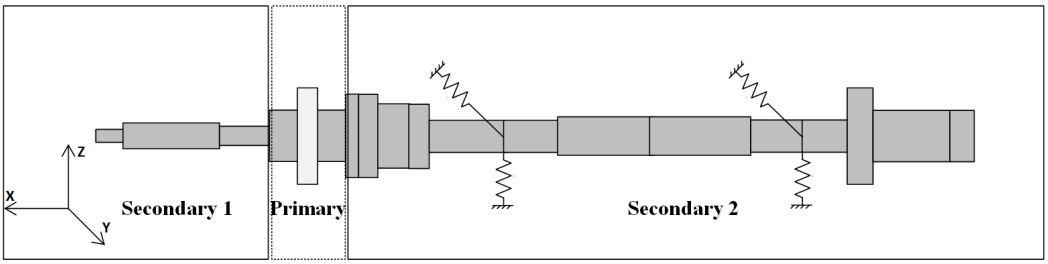


Fig. 3.2 Component mode partition of the Nelson and McVaugh (1976) rotor

Craig-Bampton substructuring. The Secondary 1 component has four nodes, and its interior DOFs are reduced using the modal transformation, with the first two modes are retained. The state-space form of the equation leads to 8 DOF in the boundary node resulting in 10 DOF at the Secondary 1 component against the actual DOF of 16. Similarly, the Secondary 2 component is reduced to 12 DOF against the actual DOF of 56. Finally, after assembling the primary and secondary components, the total DOF of the reduced model is obtained as 30 which is less than 50% of that of the complete model.

Table 3.1 The details of model reduction applied to the Nelson & McVaugh rotor

| System | # of nodes | Actual DOF | Retained modes | Physical DOF | State-space DOF | Total DOF |
|---|---|---|---|---|---|---|
| Complete model | 19 | 76 | 0 | 76 | – | 76 |
| Secondary 1 | 4 | 16 | 2 | 4 | 8 | 10 |
| Primary | 3 | 12 | 0 | 12 | 24 | 24 |
| Secondary 2 | 14 | 56 | 4 | 4 | 8 | 12 |
| Reduced model | | | After Assembly | | | 30 |

The Campbell diagram and the unbalance response of the given rotor-bearing model is obtained using the proposed methodology, and it is compared with the results from the paper of Nelson and McVaugh (1976) as shown in Fig. 3.3. The critical speeds are also compared and are listed in Tab. 3.2. The average error between the present results and the existing results are very small and they are in good agreement. For the reduced model, the computation time to obtain the unbalance response is 20 seconds, while the full model took 52 seconds. It indicates that the proposed model reduction technique is effective, and computation time is reduced by 50% of that of the complete model.

Table 3.2 Critical speed comparison: full and reduced models of Nelson & McVaugh rotor

| Spin speed (rpm) | Whirl natural frequency (rpm) | | | | | | Avg. error (%) |
|---|---|---|---|---|---|---|---|
| | Reduced model(30 DOF) | | Full model(76 DOF) | | Reference | | |
| | Forward | Backward | Forward | Backward | Forward | Backward | |
| 0 | 16276 | 16276 | 16276 | 16276 | 16267 | 16267 | 0.055 |
| | 49830 | 49830 | 49830 | 49830 | 48384 | 48384 | 2.98 |
| | 76522 | 76522 | 76522 | 76522 | 76382 | 76382 | 0.183 |
| 70000 | 19795 | 12872 | 19795 | 12872 | 19838 | 12815 | 0.33 |
| | 51960 | 47052 | 51960 | 47052 | 50555 | 45599 | 2.98 |
| | 91296 | 64171 | 91284 | 64171 | 91320 | 63990 | 0.15 |

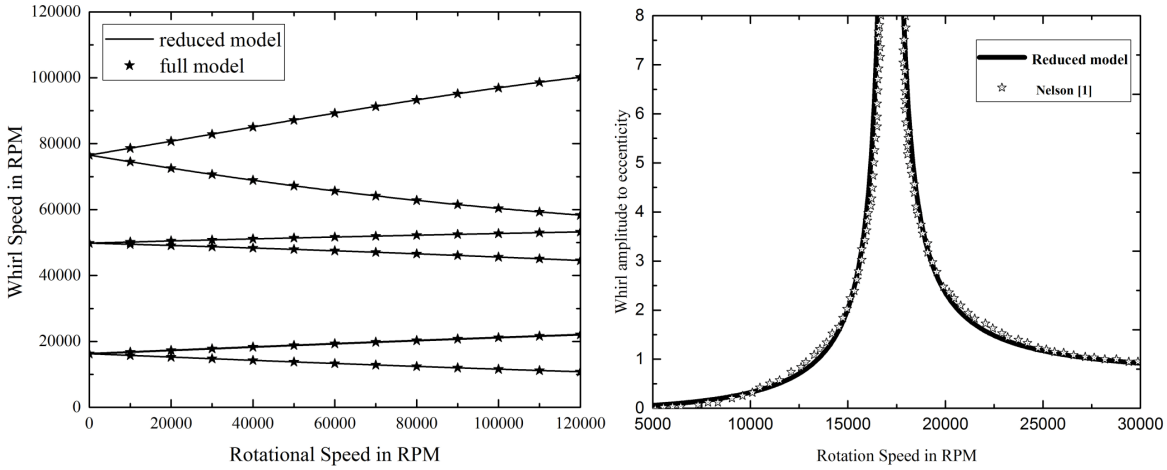


Fig. 3.3 Comparisons of the (a) Campbell and (b) unbalance response diagrams of the full and reduced models of the Nelson and McVaugh (1976) rotor

## 3.2 Validation of the ATVM

In order to demonstrate the ATVM, three different mechanical models are considered for the analysis. The first model consists of a spring-mass-damper system with cubic nonlinearity. It is a single DOF model subjected to multi-frequency quasi-periodic excitations. The second model consists of a cantilever beam undergoing bending vibrations with its tip motion constrained by a nonlinear spring. This is a multi-DOF model, and its size is effectively reduced using the model reduction technique. The beam is excited by a multi-frequency force applied at a point from the fixed end. The third one is a dual-rotor model undergoing rub-impact. It is an FE model subjected to two-frequency excitation. The parameters of this model are taken from a reference article (Yang et al. (2016))) and its results are reproduced using the ATVM. Utilizing the above-said models, the effectiveness of the ATVM is compared with the existing solution methodologies such as numerical integration and the MHBM-AFT technique.

### 3.2.1 Spring-mass-damper model

A nonlinear spring-mass-damper model undergoing multi-frequency quasi-periodic excitation is shown in Fig. 3.4. The model parameters are given in Table 3.3. In this model, three different cases of external forcing functions are analyzed for showing the applicability of the proposed method in the multiple-frequency excitation problems. Especially, the quasi-periodic nature of the responses is analyzed by taking appropriate excitation frequency ratios. The ratios of the excitation frequencies for the three cases can be expressed as given below,

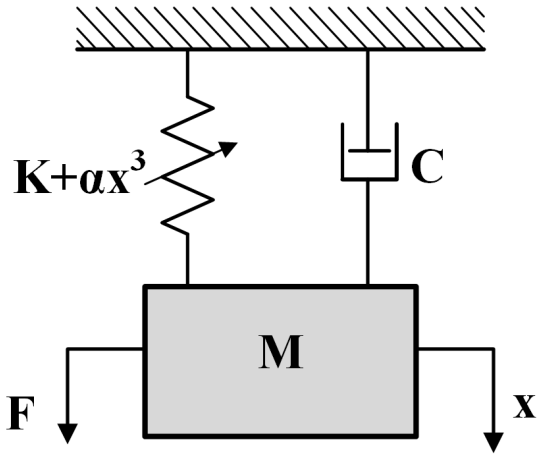


Fig. 3.4 A spring-mass-damper model with a cubic nonlinearity subjected to the multi-frequency excitation with their ratios are irrational numbers.

$$\begin{aligned} &\frac{\omega_1}{\omega_2} = \pi && && \text{for case 1} \\ &\frac{\omega_1}{\omega_2} = \sqrt{2}, && \frac{\omega_1}{\omega_3} = e && \text{for case 2} \\ &\frac{\omega_1}{\omega_2} = \sqrt{3}, && \frac{\omega_1}{\omega_3} = e, && \frac{\omega_1}{\omega_4} = \sqrt{2} \quad \text{for case 3} \end{aligned} \tag{3.1}$$

**Case 1 : Two-frequency excitation**

An external excitation consisting of two frequencies, namely $\omega_1$ and $\omega_2$, are applied at the mass centre. Its ratio is given in Eq. 3.1. In order to find the approximated frequency components, the optimization procedure is carried out by taking $\gamma_{min}$ and $\gamma_{max}$ as 10 and 100. As a result, the value of $p_1$ is obtained as 22, for which the objective function is minimum. Later, the value of $p_2$ is calculated and it is obtained as 7. The optimized frequency ratios and

Table 3.3 Properties of the spring-mass-damper model with a cubic nonlinearity

| Properties | Value |
|---|---|
| Mass (kg) | $\mathbf{M}$ = 10 |
| Damping (Ns/m) | $\mathbf{C}$ = 20 |
| Stiffness (N/m) | $\mathbf{K}$ = 4000 |
| Nonlinear function | |
| $\mathbf{F}_{nl} = \alpha x^3$ | $\alpha$ = 10000 |
| Excitation force | |
| $\mathbf{F} = f_1\cos(\omega_1 t) + f_2\cos(\omega_2 t)$ | $f_1$ = 1000, $f_2$ = 1000, |
| $\mathbf{F} = f_1\cos(\omega_1 t) + f_2\cos(\omega_2 t) + f_3\cos(\omega_3 t)$ | $f_1$ = 400, $f_2$ = 500, $f_3$ = 500 |
| $\mathbf{F} = f_1\cos(\omega_1 t) + f_2\cos(\omega_2 t) + f_3\cos(\omega_3 t) + f_4\cos(\omega_4 t)$ | $f_1$ = 100, $f_2$ = 200, $f_3$ = 200, $f_4$ = 100 |

the greatest common divisor of the approximated frequency components can be written as,

$$\tilde{r}_1 = \frac{\tilde{\omega}_1}{\tilde{\omega}_1} = \frac{22}{22} = 1 \qquad \tilde{r}_2 = \frac{\tilde{\omega}_1}{\tilde{\omega}_2} = \frac{22}{7} = 3.1428 \approx \pi \qquad \omega_0 = \frac{\tilde{\omega}_1}{22} = \frac{\tilde{\omega}_2}{7} \tag{3.2}$$

Now, it can be assumed that the spring-mass-damper model is undergoing a periodic excitation with fundamental frequency $\omega_0$. It is solved using the ATVM by taking $N_{pt}$ = 800. The accuracy of the proposed method is validated by comparing its results with that of the MHBM technique and numerical integration (NI), as shown in Fig. 3.5. The number of harmonics taken for the MHBM-AFT technique is $N_h$ = 5. Exact matching is obtained between the results of the proposed ATVM and the existing methods. The analysis is carried out using a Fujitsu CELSIUS R940 workstation with intel® Xeon® processor with a clock speed of 2.20 GHz. The computation time taken to complete the analysis using the ATVM, MHBM and NI (without continuation) techniques is 358, 105 and 132 seconds, respectively. Even though the computation time is more for the ATVM, its easiness of employing the method for the multi-DOF and multi-frequency excitation problems validates its usefulness.

The stability analysis of the model is performed using the theory as described in Sec. 2.2.4. Figure 3.6 shows the stability diagram of the response in which the stable part is represented using the continuous line, whereas the unstable part is represented using the dashed line. The bifurcations appearing in the model are determined by monitoring the Floquet exponents. The limit point (LP) and Neimark-Sacker (NS) bifurcations are observed in the response, and they are represented using the circle and triangle markers respectively in Fig. 3.6. Figure 3.7 shows the Floquet exponents in the vicinity of LP and NS bifurcations. As in Fig. 3.7a, an LP bifurcation is detected when at least one of the Floquet exponents crosses the imaginary axis along the real axis of the complex plane, whereas the NS bifurcation is identified when

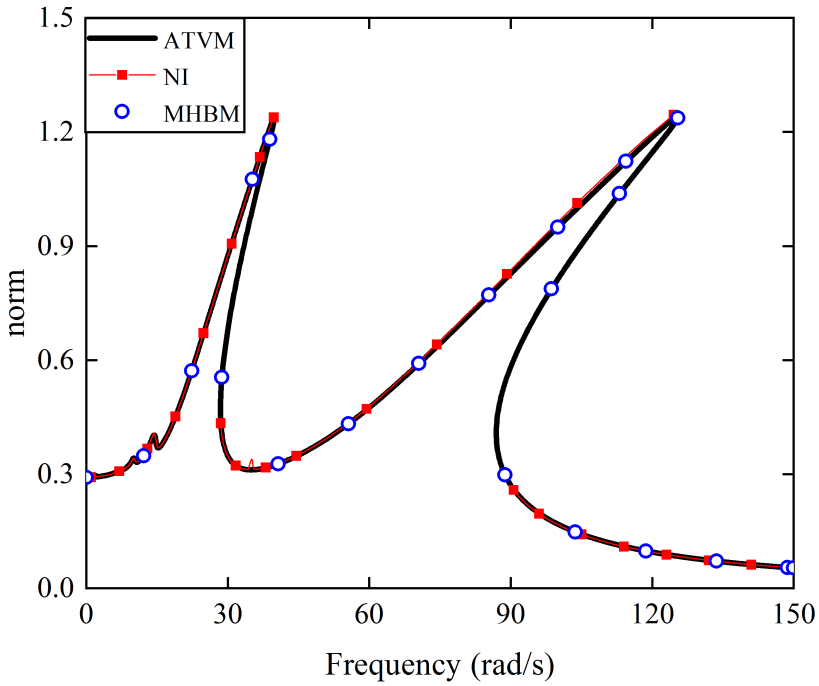


Fig. 3.5 Validation of the ATVM technique with the MHBM and numerical integration for the two-frequency quasi-periodic excitation problem. Exact matching is obtained between the proposed ATVM and the existing methods.

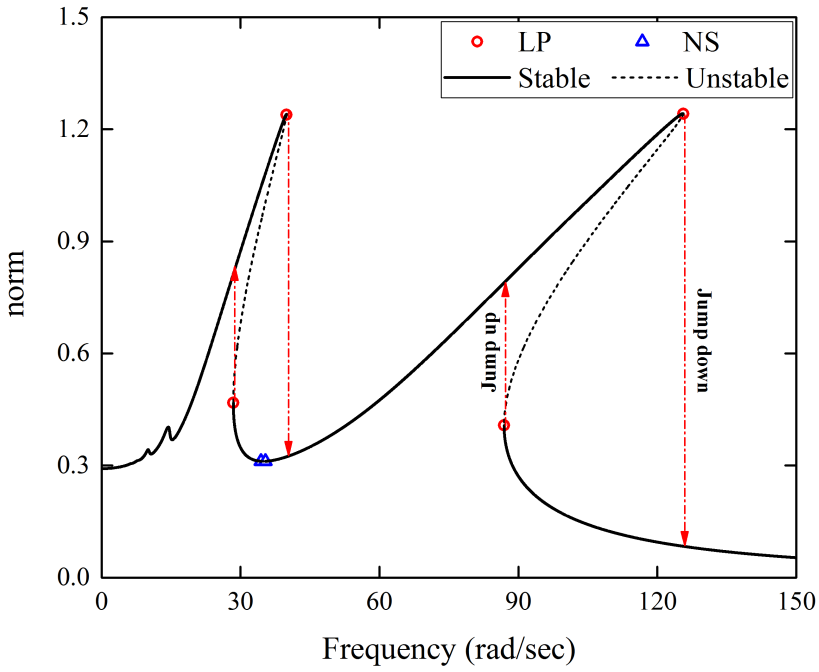


Fig. 3.6 Stability diagram of the two-frequency excitation problem showing the LP and NS bifurcations represented by circle and triangle markers, respectively.

a pair of Floquet exponents crosses the imaginary axis as a pair of complex conjugates as in Fig. 3.7b.

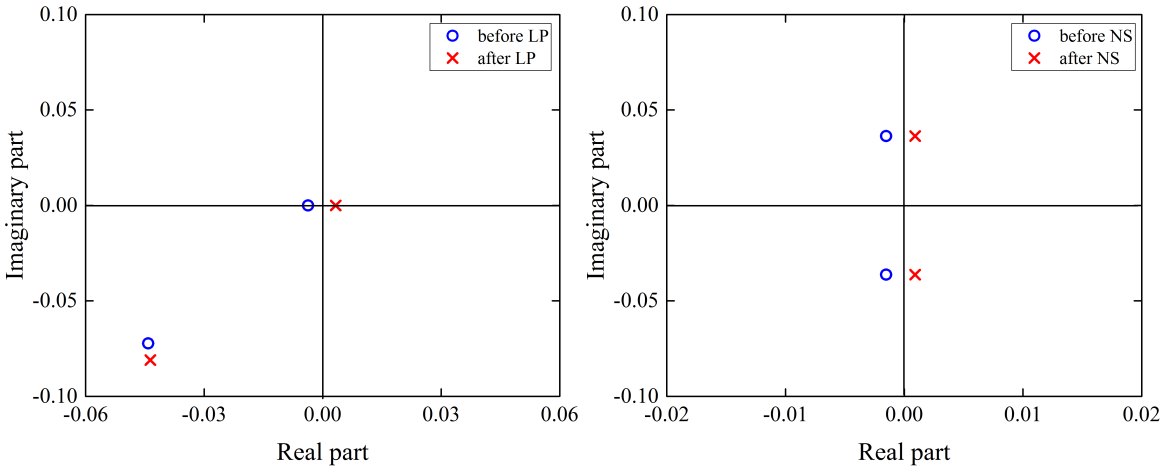


(a) LP at $\omega = 39.94$ rad/s (b) NS at $\omega = 34.42$ rad/s

Fig. 3.7 Floquet exponents in the vicinity of (a) LP and (b) NS bifurcations (for two-frequency excitation problem)

The LP bifurcation indicates a sudden jumping phenomenon in which a jump-down occurs during the run-up and a jump-up occurs during run-down, respectively. Generally, the NS bifurcation represents a transition from the periodic regime to the quasi-periodic regime. However, in the case of quasi-periodic excitation problems, the response is already quasi-periodic. Hence, in this study, the NS bifurcation represents a transition from one quasi-periodic to another quasi-periodic regime. The proposed ATVM technique cannot capture the quasi-periodic branches; hence it can be generated using numerical integration.

More information can be acquired by analyzing the Poincaré maps and FFT diagrams of the motions before and after the NS bifurcation, as shown in Fig. 3.8. Since the Poincaré maps of both motions are closed curves, the motions are said to be quasi-periodic. Now, the FFT of the responses are analyzed to determine the frequency contents. It is found that the motion before the NS bifurcation contains the frequency components that are the linear combinations of the excitation frequencies. Hence, this kind of motion is predictable using the current solution method. However, the motion after the NS bifurcation includes certain frequency components that aren't known before the methodology formulation, such as $0.614\omega_1$, $0.659\omega_1$ and $0.704\omega_1$. The determination of such a quasi-periodic branch is difficult using the proposed method since the frequency components are unknown initially. However, the main advantage of the proposed method is that it can detect the onset points of the quasi-periodic branches accurately with less computation time than numerical integration, especially for the MDOF models.

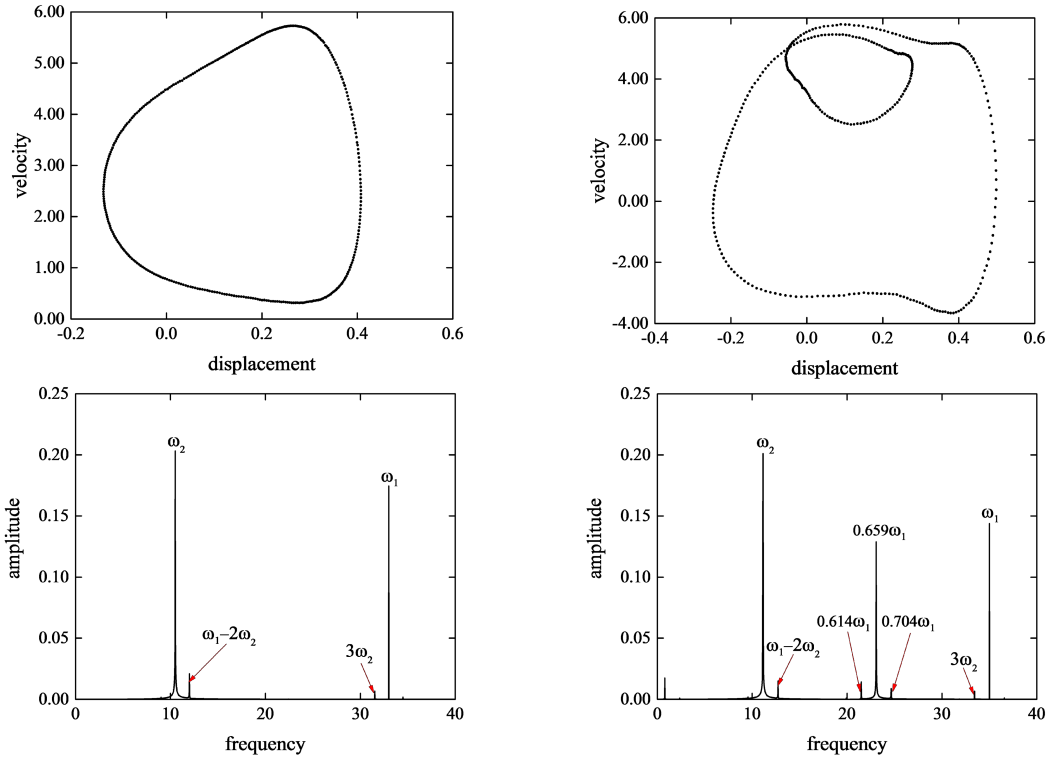


Fig. 3.8 Poincaré map and FFT spectra of the responses (a) before and (b) after NS bifurcation for two-frequency excitation problem (obtained using numerical integration). Both the responses are quasi-periodic in nature; however, some of the frequency components are a priori unknown in the responses after NS bifurcation.

### Case 2 : Three-frequency excitation

In order to validate the effectiveness of the ATVM in more than two-frequency excitation problems, a three-frequency excitation is applied at the mass centre with a ratio as given in Eq. 3.1. During the optimization procedure, the values of $\gamma_{min}$ and $\gamma_{max}$ are taken as 10 and 100. After the calculation, the value of $p_1$ is obtained as 68. Later, the value of $p_2$ and $p_3$ are found as 48 and 25 respectively. Since the excitation frequencies are expressed as the large multiples of $\omega_0$, more time points are required to approximate the time response. Hence, for the ATVM, the number of discrete time points $N_{pt}$ is taken as 1000. Now, $\tilde{r}_j$'s and $\omega_0$ can be expressed as,

$$\begin{aligned} \tilde{r}_1 &= \frac{\tilde{\omega}_1}{\tilde{\omega}_1} = \frac{68}{68} = 1 & \tilde{r}_2 &= \frac{\tilde{\omega}_1}{\tilde{\omega}_2} = \frac{68}{48} = 1.416 \approx \sqrt{2} \\ \tilde{r}_3 &= \frac{\tilde{\omega}_1}{\tilde{\omega}_3} = \frac{68}{25} = 2.72 \approx e & \omega_0 &= \frac{\tilde{\omega}_1}{68} = \frac{\tilde{\omega}_2}{48} = \frac{\tilde{\omega}_3}{25} \end{aligned} \tag{3.3}$$

The frequency response of the model undergoing three-frequency quasi-periodic excitation is shown in Fig. 3.9. In the case of the MHBM technique, the AFT method becomes cumbersome since calculating the three-dimensional FFT matrix is time-consuming. Hence, the results are compared with numerical integration (without continuation). Figure 3.9 shows the validation of the ATVM results with the numerical integration, and an excellent agreement is obtained. The stability analysis is also performed along with the parametric continuation, and the diagram is shown in Fig. 3.10. As seen in the previous section, an LP bifurcation is observed in the response, indicating the sudden jumping phenomenon. Since the number of time points $N_{pt}$ is increased, the computation time is also increased to 872 seconds leading to a slower solution process for the three-frequency excitation problem.

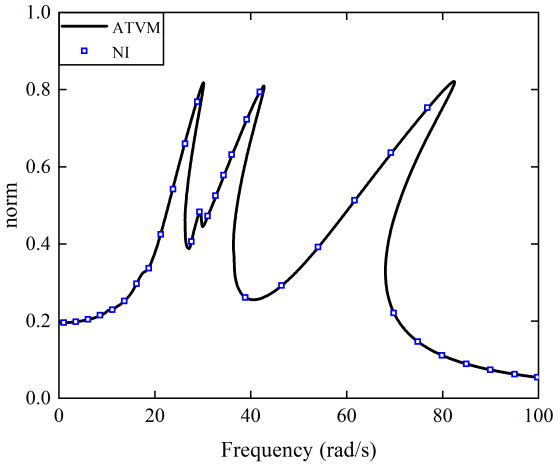


Fig. 3.9 Validation of the ATVM technique with numerical integration for the three-frequency quasi-periodic excitation.

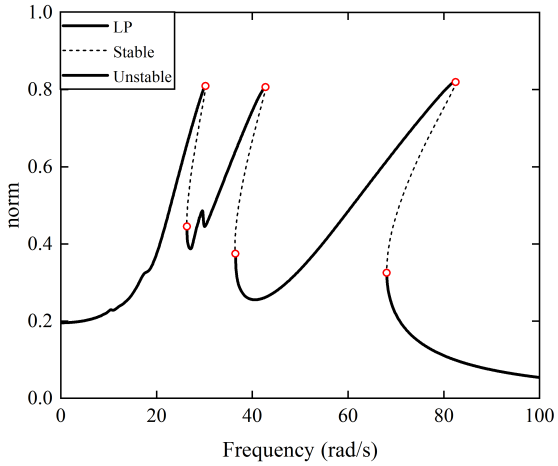


Fig. 3.10 Stability diagram of the three-frequency excitation problem showing the LP bifurcation.

**Case 3 : Four-frequency excitation**

In this case, the spring-mass-damper model is subjected to four-frequency excitation with their ratios as given in Eq. 3.1. The values of $\gamma_{min}$ and $\gamma_{max}$ are taken as 10 and 100. Hence, the values of $p_1$, $p_2$, $p_3$ and $p_4$ are obtained as 95, 55, 35 and 67 respectively. Now, the optimized frequency ratios and the greatest common divisor can be written as,

$$\begin{aligned} \tilde{r}_1 &= \frac{\tilde{\omega}_1}{\tilde{\omega}_1} = \frac{95}{95} = 1 & \tilde{r}_2 &= \frac{\tilde{\omega}_1}{\tilde{\omega}_2} = \frac{95}{55} = 1.72 \approx \sqrt{3} \\ \tilde{r}_3 &= \frac{\tilde{\omega}_1}{\tilde{\omega}_3} = \frac{95}{35} = 2.714 \approx e & \tilde{r}_4 &= \frac{\tilde{\omega}_1}{\tilde{\omega}_4} = \frac{95}{67} = 1.418 \approx \sqrt{2} \end{aligned} \tag{3.4}$$

$$\omega_0 = \frac{\tilde{\omega}_1}{95} = \frac{\tilde{\omega}_2}{55} = \frac{\tilde{\omega}_3}{35} = \frac{\tilde{\omega}_4}{67}$$

The response curve is plotted using the ATVM technique by taking $N_{pt}$ = 2000. The variation in the response with respect to nonlinear stiffness is also shown in Fig. 3.11. It is noticed that as the value of nonlinear stiffness increases, the forward-leaning of the response curve is increased, which is captured by the ATVM technique. The number of time points required for the analysis is also increased, which in turn increases the computation time. However, the formulation of the ATVM technique is simple compared to the MHBM-AFT, and the performance is good compared to numerical integration. From the above analysis, the effectiveness of the ATVM in multi-frequency quasi-periodic excitation problems is validated, though the results are approximate.

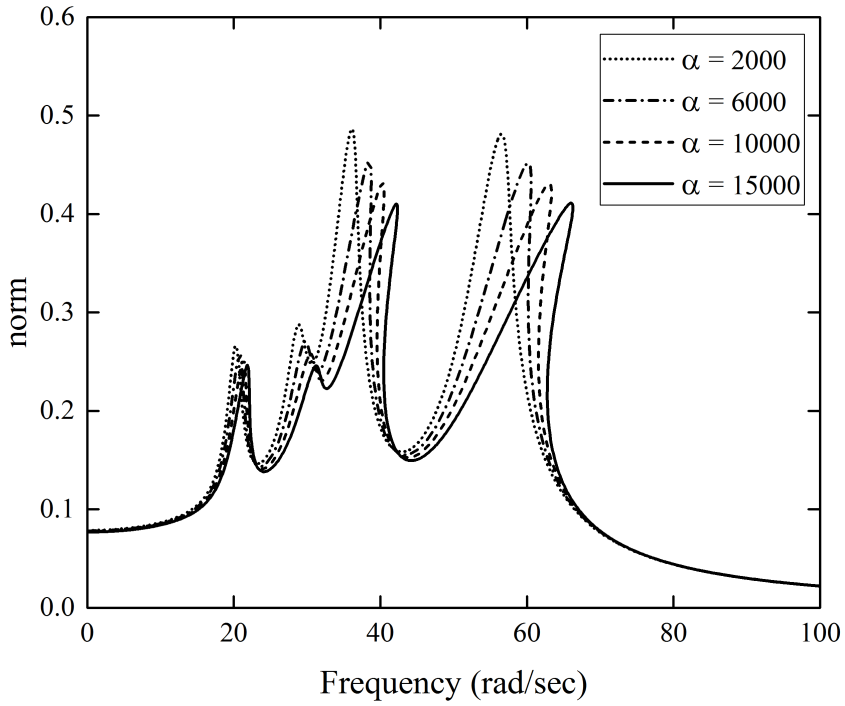


Fig. 3.11 Variations in the nonlinear responses of a four-frequency excitation problem for different values of $\alpha$

### 3.2.2 Cantilever beam supported by nonlinear spring

The majority of the engineering systems are treated as continuous systems while studying their dynamical behaviour. Such continuous systems are modelled using finite element formulations that discretize them into finite DOF models. Generally, suitable model reduction techniques are employed for reducing their model size. To understand the effectiveness of the ATVM in analyzing the reduced models, a cantilever beam with a nonlinear spring is studied as shown in Fig. 3.12. It is a multi-DOF model undergoing multi-frequency excitation.

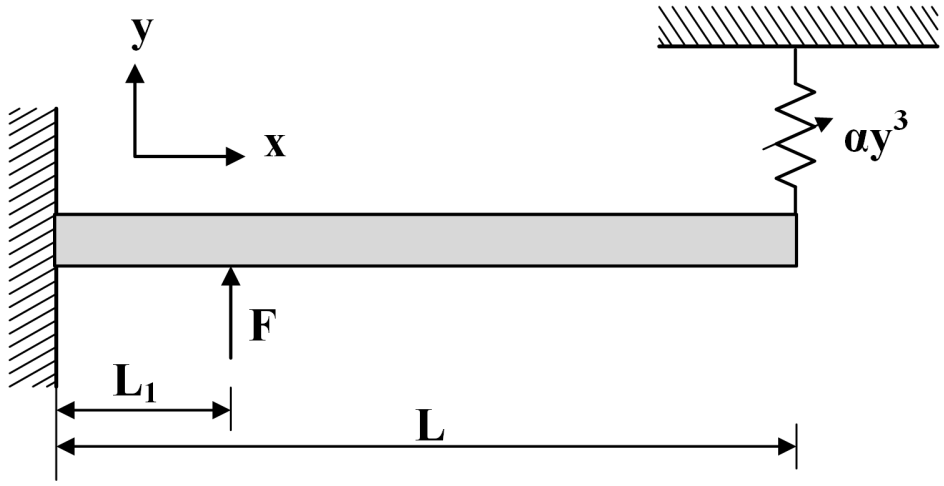


Fig. 3.12 Cantilever beam with a nonlinear spring undergoing bending vibrations

Table 3.4 Properties of the beam bending model

| Properties | |
|---|---|
| Density (kg/$m^3$) | 2700 |
| Young's Modulus (GPa) | 69 |
| Cross section (mm $\times$ mm) | 48 $\times$ 3 |
| Length of beam ($L$) (mm) | 370 |
| Distance of excited point from fixed end ($L_1$) (mm) | 74 |
| DOF per node | 2 |
| Number of Elements | 10 |
| Rayleigh damping coefficient (mass) | 2.45 |
| Rayleigh damping coefficient (Stiffness) | $1.75 \times 10^{-3}$ |
| Nonlinear force | $\alpha$ = 1300800$\times$10, $\alpha$ = 1300800$\times$20 |
| $\mathbf{F}_{nl}$= $\alpha y^3$ | $\alpha$ = 1300800$\times$30, $\alpha$ = 1300800$\times$40 |
| External force, | $f_1$ = 6, $f_2$ = 10 |
| **F**= $f_1\cos(\omega_1 t)+f_2\sin(\omega_2 t)+f_3\sin(\omega_3 t)+f_4\cos(\omega_4 t)$ | $f_3$ = 6, $f_4$ = 10 |

A four-frequency excitation is applied on the beam to determine its responses at the free end. The excitation frequencies are related to each other as follows,

$$\frac{\omega_2}{\omega_1} = 0.7, \quad \frac{\omega_3}{\omega_1} = 1.8, \quad \frac{\omega_4}{\omega_1} = 0.3 \tag{3.5}$$

The properties of the beam are reported in Table 3.4. The beam model is discretized into finite elements, and later, its size is reduced using the proposed model reduction technique. However, the system equations aren't converted into the state-space form since all the matrices are symmetric in nature. Figure 3.13 shows the component mode partition of the beam, and Table 3.5 gives the details of the model reduction. The approximated excitation

frequency components are given below,

$$\begin{aligned} \frac{\tilde{\omega}_2}{\tilde{\omega}_1} &= \frac{7}{10} = 0.7 \qquad & \frac{\tilde{\omega}_3}{\tilde{\omega}_1} &= \frac{18}{10} = 1.8 \\ \frac{\tilde{\omega}_4}{\tilde{\omega}_1} &= \frac{3}{10} = 0.3 \qquad & \omega_0 &= \frac{\tilde{\omega}_1}{10} = \frac{\tilde{\omega}_2}{7} = \frac{\tilde{\omega}_3}{18} = \frac{\tilde{\omega}_4}{3} \end{aligned} \tag{3.6}$$

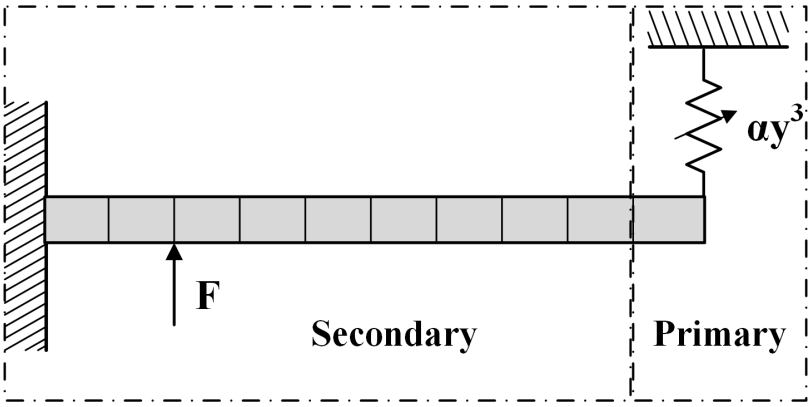


Fig. 3.13 Component mode partition of the beam model

Table 3.5 The details of model reduction of beam bending model

| System | No. of nodes | Actual DOF | Retained modes | Physical DOF | Total DOF |
|---|---|---|---|---|---|
| Complete model | 10 | 20 | 0 | 20 | 20 |
| Primary | 2 | 4 | 0 | 4 | 4 |
| Secondary | 9 | 18 | 2 | 2 | 4 |
| Assembled model | After component mode synthesis | | | | 6 |

In the model reduction technique, the number of retained modes for the secondary component is taken as 2. It is chosen based on a convergence study. Since the response near the first mode is mainly analyzed, increasing the number of modes beyond two does not affect the model response. The stiffness of the clamped-pinned beam ($\alpha$ = 1300800) is taken as the base nonlinear stiffness of the spring, and its multiples are taken for the study. To show the effectiveness of the model reduction technique, frequency responses of the full model and the reduced model are compared for $\alpha = 1300800 \times 20$. The comparison plot is shown in Fig. 3.14 and a good agreement is obtained.

The response curves of the reduced model for different values of nonlinear stiffnesses are shown in Fig. 3.15. It is observed that the forward-leaning of the response curves is increased as the values of nonlinear stiffness are increased. Table 3.6 gives the number of

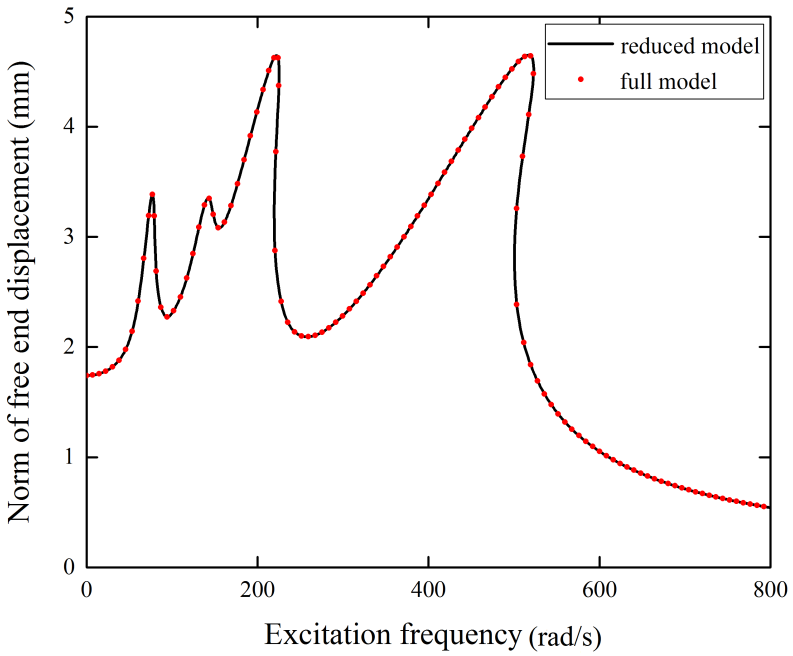


Fig. 3.14 Comparison of the responses of the reduced and full models of the cantilever beam ($\alpha = 1300800 \times 20$)

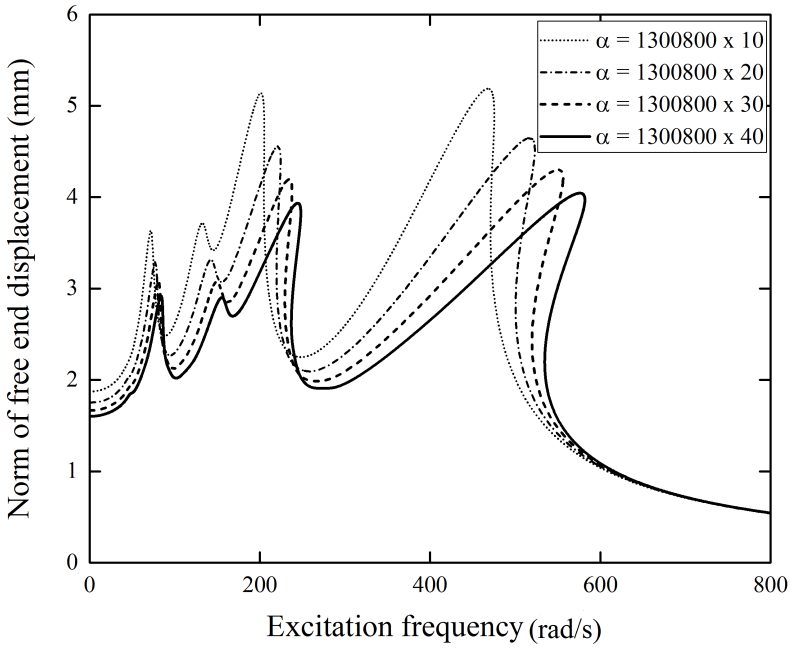


Fig. 3.15 The response curves of the reduced beam model for different values of nonlinear stiffnesses

time points required for obtaining each response along with the solution time consumed. It is seen that the number of time points is increased as the values of nonlinear stiffness are increased. This is because, as the model becomes more nonlinear, a large number of time points are required to capture the complete response signal. As a result, the size of governing equations ($N_{pt}$ $N_r$) is also increased, thereby increasing the solution time.

Table 3.6 Time points and solution time consumed for beam bending model

| Nonlinear stiffness $\alpha$ | No. of time points $N_p$ | Solution time (sec) |
|---|---|---|
| $\alpha = 1300800\times00$ | 75 | 2.3 |
| $\alpha = 1300800\times10$ | 400 | 2572 |
| $\alpha = 1300800\times20$ | 800 | 13672 |
| $\alpha = 1300800\times30$ | 900 | 20053 |
| $\alpha = 1300800\times40$ | 1200 | 30125 |

### 3.2.3 Simplified dual-rotor model undergoing rub-impact

In order to validate the proposed ATVM with existing numerical/experimental results, a dual-rotor model from the article of Yang et al. (2016) is analyzed. The details of model parameters are given in the article. The Timoshenko beam elements are utilized for developing the FE models of the low-pressure and high-pressure shafts. A fixed elastic limiter is used as the stator representing the convex protuberance on the casing. The disk and the fixed limiter are applied with softer coatings and several local contacts happen during the orbital motion. Hence, a Lankarani–Nikravesh model is employed to obtain the contact force generated between the rotor disk and the fixed limiter. In literature, Yang et al. (2016) used the numerical integration technique to acquire the rubbing response, whereas, in the present study, the ATVM is utilized. As a result, the computation time is significantly reduced since the ATVM provides the steady-state response directly.

Initially, the unbalance response of the model without rub-impact is studied. Figure 3.16 & 3.17 show the comparison of the results of the present study with the numerical/experimental results from the article of Yang et al. (2016). From Fig. 3.16 & 3.17, it is clear that the results of the present study are well-matched with numerical/ experimental results. Once rub-impact happens, the model response becomes nonlinear and different combinations of excitation frequencies can be seen in the frequency spectrum. Figure 3.18 shows the comparison of the frequency spectra obtained from the present study and the reference article. A clear agreement is obtained between both results. However, a slight variation is observed with the experimental results. The frequency dispersion that is observed in the experimental result is

not obtained in the numerical results. Still, the amplitudes and frequencies of both results have good matching.

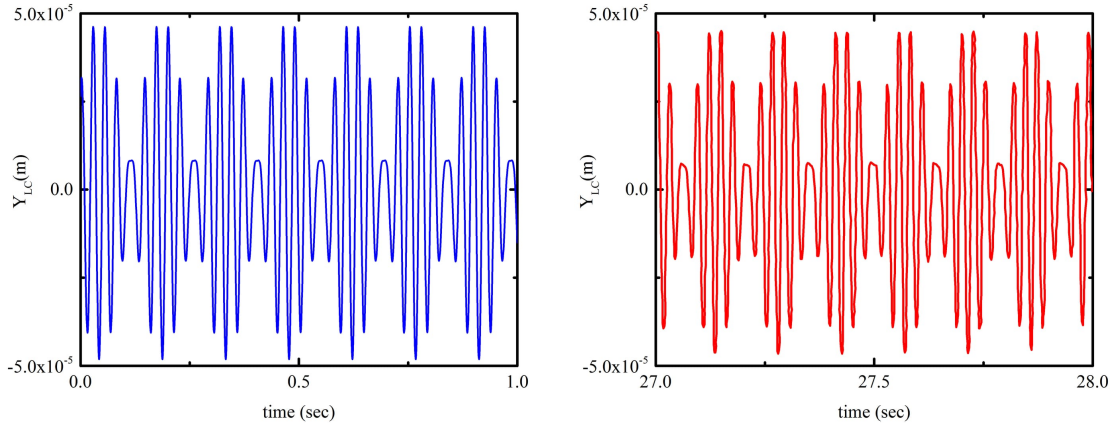


Fig. 3.16 Vertical vibration of the low-pressure compressor disk at $\omega_1 = 216.8$ rad/s and speed ratio = 1.2 (a) present study (b) numerical study from the article of Yang et al. (2016)

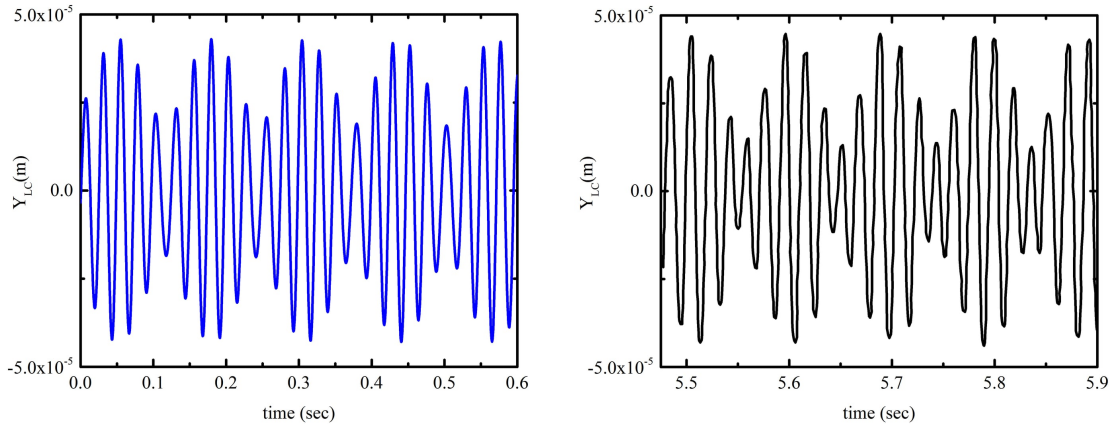


Fig. 3.17 Vertical vibration of the the low-pressure compressor disk at $\omega_1 = 252.6$ rad/s & $\omega_2 = 301.2$ rad/s (a) present study (b) experiment from the article of Yang et al. (2016)

The current analysis validates the use of the ATVM in the multi-DOF systems undergoing multi-frequency excitations. Now, the proposed technique needs to be applied in the stability analysis of rotor systems which will be explained in the following chapter.

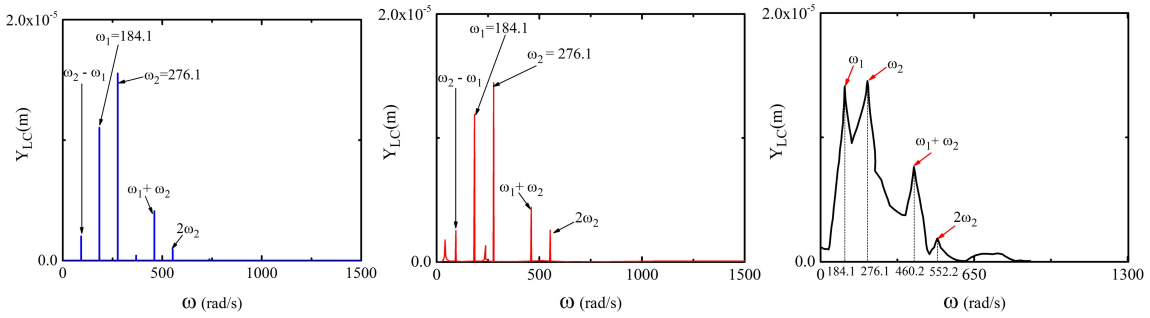


Fig. 3.18 Frequency spectra of the low-pressure compressor disk at $\omega_1 = 184.1$ rad/s after rub-impact (a) present study (b) numerical study from the article of Yang et al. (2016) (c) experimental study from the article of Yang et al. (2016)

## 3.3 Summary

In this chapter, the validations of the proposed model reduction technique and the ATVM are carried out using the existing numerical methods. A Nelson and McVaugh (1976) rotor model is used to verify the efficiency of the model reduction technique. It is observed that the computation time for the reduced model is decreased by 50% of that of the complete model with the results exactly matching to each other, underlining the efficiency of the reduction technique. The ATVM technique is validated using three nonlinear mechanical models, and the results are compared with that of the MHBM-AFT and numerical integration techniques. The results are exactly matching when proper approximated frequency ratios are taken after the optimization procedure. However, the time taken for obtaining the solution is large for the ATVM compared to the MHBM-AFT technique, and it increases with the extent of nonlinearity. But, the easiness of the ATVM in extending the analysis beyond two-frequency excitation problems validates its usefulness. Compared to the numerical integration technique, the ATVM determines the solution fastly, especially for the multi-DOF systems undergoing multi-frequency excitations.

# Chapter 4

# Stability of a simplified dual-rotor undergoing single-disk rub-impact

This chapter is mainly intended to perform the stability analysis of a simplified dual-rotor model undergoing a single-disk rub-impact. Mainly, the bifurcations occurring in the model are investigated using the proposed numerical procedure. It detects the onset points of the bifurcations at a faster rate compared to the existing numerical techniques. This is the main contribution of the work. The dual-rotor model is composed of a pair of co-axial rotors that are connected together using an inter-shaft bearing. In this model, the compressor and turbine units are simplified as four rigid disks without incorporating the blades. There are two modes of rotor operations possible in a dual-rotor model: **co-rotation** in which both the rotors spin in the same direction and **counter-rotation** in which one rotor spins in the opposite direction to the other. The effects of co-rotation and counter-rotation on the response behaviour must be investigated in detail.

## 4.1 Mechanical model of simplified dual-rotor

Figure 4.1 shows the schematic diagram of a simplified dual-rotor model. The inner rotor is made up of a long and slender shaft supported at the ends using two isotropic bearings. In contrast, the outer rotor consists of a hollow shaft whose one end is connected to the frame through an isotropic bearing while the other end is connected to the inner rotor through an inter-shaft bearing. The presence of inter-shaft bearing couples the rotor vibrations and leads to combined harmonic responses. The outer rotor is spinning at a speed that is 1.2 times the speed of the inner rotor (speed ratio $\kappa = 1.2$). The following assumptions are made to perform the nonlinear dynamic analysis,

1. All the bearings are modelled using linear springs and viscous dampers.
2. All the disks are rigid and are represented using lumped masses with symmetric moments of inertias in the XY plane.
3. No coatings are applied on the casing and disk surfaces
4. The axial and torsional vibrations are small, hence ignored.

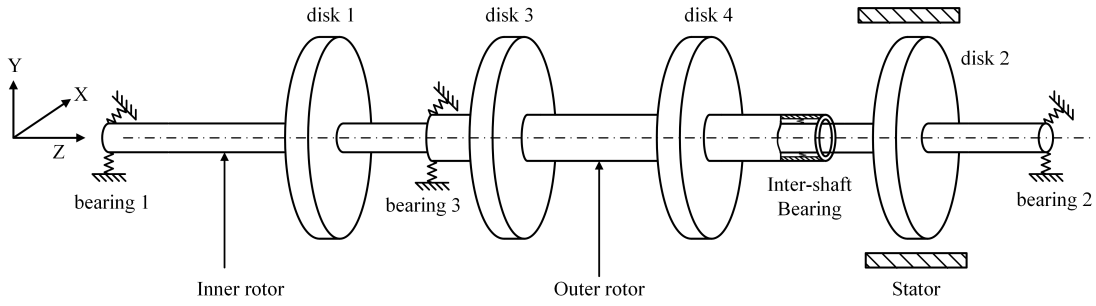


Fig. 4.1 The schematic diagram of a simplified dual-rotor model (Friswell et al. (2010))

Table 4.1 and 4.2 give the details of the bearings and disks used in the model. The complete rotor model is cyclically symmetric with the elastic modulus as 207 *GPa*, the Poisson's ratio as 0.3, and the mass density as 8300 $kg/m^3$. The geometric properties of the shafts are given in Table 4.3. Disk 1 and 3 have mass unbalances of magnitude 0.0001 *kgm* each that forces the rotors to whirl during their operation.

Table 4.1 Properties of the isotropic bearings used in the dual-rotor (Friswell et al. (2010))

| Properties | Bearing | | | |
|---|---|---|---|---|
| | 1 | 2 | 3 | Inter-shaft |
| Stiffness (N/m) | $52\times10^6$ | $36\times10^6$ | $36\times10^6$ | $9\times10^6$ |
| Damping (Ns/m) | 100 | 100 | 100 | 100 |
| Distance from left end bearing (m) | 0 | 0.508 | 0.152 | 0.406 |

Table 4.2 Properties of the disks used in the dual-rotor (Friswell et al. (2010))

| Properties | Disk | | | |
|---|---|---|---|---|
| | 1 | 2 | 3 | 4 |
| Mass (kg) | 10.5 | 7.0 | 7.0 | 3.5 |
| Polar inertia (kgm$^2$) | 0.086 | 0.068 | 0.042 | 0.026 |
| Diametral inertia (kgm$^2$) | 0.043 | 0.034 | 0.021 | 0.013 |
| Distance from left end bearing (m) | 0.076 | 0.457 | 0.203 | 0.356 |

Table 4.3 Geometric properties of the shafts used in the dual-rotor (Friswell et al. (2010))

| Shaft | Length (m) | Inner Dia (m) | Outer dia (m) |
|---|---|---|---|
| Outer Shaft | 0.254 | 0.05 | 0.06 |
| Inner Shaft | 0.508 | 0 | 0.03 |

The schematic diagram of the rub-impact is shown in Fig. 4.2. The stator is assumed as a rigid ring with its centre at 'O'. The XY coordinates are fixed at the stator centre, pointing to horizontal and vertical directions. The geometric centre of the rotor is located at 'o' that coincides with the stator centre at rest. The mass centre of the rotor is located at a distance 'e' from the geometric centre, generating an unbalance force during its operation. As a result, the rotor whirls with an amplitude 'r' as shown in Fig. 4.2.

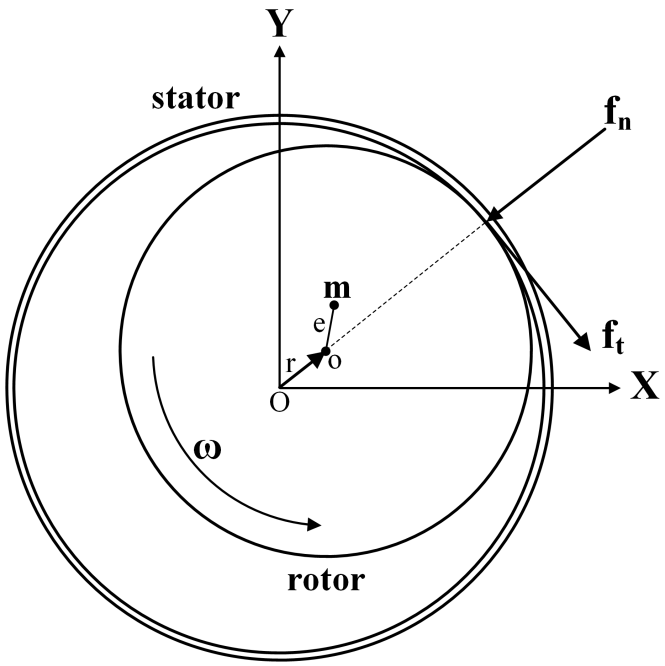


Fig. 4.2 Schematic diagram of the rub-impact model. Rotor-stator contact happens whenever the rotor displacement exceeds the clearance. As a result, a normal and tangential force acts on the rotor at the contact point (Jiang (2007)).

When the whirling amplitude of the rotor exceeds the clearance $\delta$, disk 2 impacts the stator. During the contact, a normal ($f_n$) and tangential ($f_t$) force acts on the rotor at the contact point, as shown in Fig. 4.2. They are determined using a piecewise contact modelling strategy as given,

$$f_n = \begin{cases} 0 & \text{for} \quad r < \delta \\ k_c(r-\delta) & \text{for} \quad r \geq \delta \end{cases} \quad ; \quad f_t = \mu f_n \tag{4.1}$$

where $k_c$ is the rotor-stator contact stiffness and $\mu$ is the coefficient of friction. The friction at the contact interface is modelled according to Coulomb's frictional law without considering the thermal effect and the material removal. Now, the normal and tangential forces are resolved along the X and Y directions as given (Jiang (2009)),

$$\begin{aligned} f_{nx} &= \Theta k_c \left[1 - \frac{\delta}{r}\right](x - \mu \ \text{sign}(v_{rel})\ y) \\ f_{ny} &= \Theta k_c \left[1 - \frac{\delta}{r}\right](\mu \ \text{sign}(v_{rel})\ x + y) \end{aligned} \tag{4.2}$$

where $v_{rel} = \omega r_{disk} + v_{tang}$ represents the relative velocity between the rotor and the stator at the contact point. $r_{disk}$ is the radius of the disk, $\omega$ is the angular velocity of the disk, and $v_{tang}$ is the instantaneous tangential velocity of whirling at the contact point. The relative velocity will be larger than the circumferential speed of the rotor at the contact point when the rotor whirls forward (with a positive $v_{tang}$). It will be less than the circumferential speed when the rotor whirls backward (with a negative $v_{tang}$). $\Theta$ is a switching function that is equal to one when contact occurs and equal to zero when no contact occurs.

## 4.2 Rotor FE modelling and dynamic analysis

The dual-rotor model is completely modelled using one-dimensional finite elements. Mainly, Timoshenko beam elements are used for discretizing the shafts with rotary inertia, shearing, and gyroscopic effects are taking into account. Each node has 4 DOFs: two translational and two rotational displacements. The complete model is discretized into 13 elements with a total of 52 DOFs. Later, its size is reduced using the proposed model reduction technique as described in Sec. 2.1. The component mode partition of the dual-rotor model is shown in Fig. 4.3 and its details are given in Table 4.4. The primary component includes all the nodes containing nonlinearity and their adjacent nodes, while the secondary component has the remaining linear nodes. This is the criteria for dividing a structure into primary and secondary components.

Table 4.4 The details of the model reduction of simplified dual-rotor model

| System | No. of nodes | Actual DOF | Retained modes | Physical DOF | Total DOF |
|---|---|---|---|---|---|
| Complete model | 13 | 52 | 0 | 52 | 52 |
| Primary | 3 | 12 | 0 | 12 | 12 |
| Secondary | 11 | 44 | 2 | 16 | 18 |
| Assembled model | | After component mode synthesis | | | 26 |

In this dual-rotor model, disk 2 undergoes rub-impact; hence, the node containing disk 2 is kept in the primary component along with its adjacent nodes. As a result, the primary component includes 3 nodes with 12 DOFs; all are held in physical coordinates. The secondary component has the remaining 11 linear nodes and is reduced using the Craig-Bampton substructuring to get 18 DOFs. After assembling the primary and secondary components, the reduced size of the dual-rotor model is obtained as 26, which is 50% of the complete model.

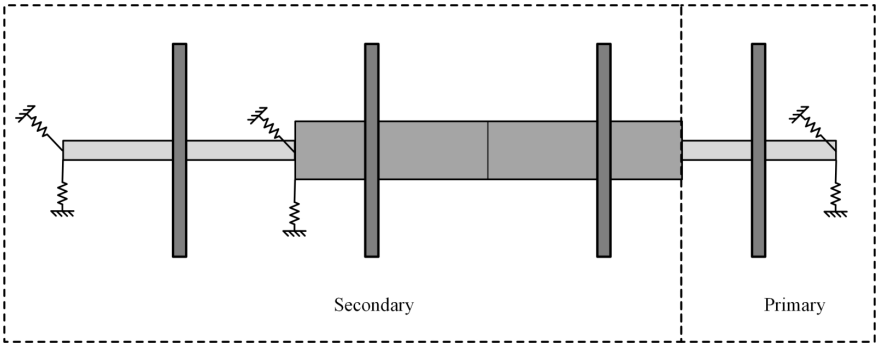


Fig. 4.3 Component mode partition of the simplified dual-rotor model

### 4.2.1 Co-Rotation

In this mode of rotor operation, the rotors are co-rotating with a speed ratio of $\kappa = 1.2$; hence the approximated excitation frequency components and their common divisor $\omega_0$ can be determined as,

$$\frac{\tilde{\omega}_2}{\tilde{\omega}_1} = \frac{6}{5} = 1.2 \qquad \omega_0 = \frac{\tilde{\omega}_1}{5} = \frac{\tilde{\omega}_2}{6} \tag{4.3}$$

Now, by expressing the external excitations in terms of $\omega_0$, the ATVM can be utilized for finding the responses. At first, the modal analysis is performed to determine the natural frequencies of the model. The first five natural frequencies of the model under the non-rotating condition are given in Table 4.5. However, for a rotating system, the natural frequencies vary with the rotor speed due to the presence of the gyroscopic effect. This variation is displayed through the Campbell diagram. Figure 4.4a and 4.4b show the Campbell diagrams of the two-spool rotor model when excited by the inner and outer rotors, respectively. Due to the gyroscopic effects, the frequencies split into forward and backward whirls. The critical speeds of the model are obtained by noting the rotational speeds at the crossing points of the frequency curves with the synchronous excitation line ($1\times$). They have listed in Table 4.6. For each vibration mode, there are two critical speeds corresponding to the forward and

the backward whirl motions as listed in Table 4.6. Figure 4.4 also gives a comparison of the Campbell diagrams of the complete and the reduced models. It shows the effectiveness of the model reduction technique. A perfect agreement is observed between the results of both models.

Table 4.5 Natural frequencies of the dual-rotor model under the non-rotating condition

| Two-spool rotor | Order | | | | |
|---|---|---|---|---|---|
| | 1st | 2nd | 3rd | 4th | 5th |
| Frequency (Hz) | 91.807 | 197.485 | 318.329 | 403.455 | 421.738 |

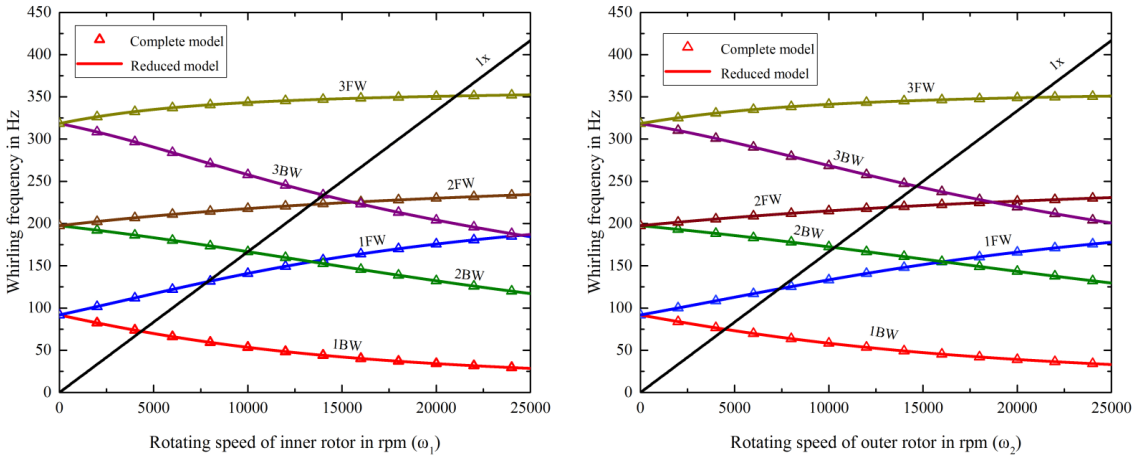


(a) excited by inner rotor (b) excited by outer rotor

Fig. 4.4 Campbell diagram of the simplified dual-rotor model (co-rotation)

Table 4.6 Critical speeds of the simplified dual-rotor model (co-rotation)

| Order | Excited by inner rotor (rpm) | | Excited by outer rotor (rpm) | |
|---|---|---|---|---|
| | backward | forward | backward | forward |
| 1 | 4346 | 7872 | 4493 | 7363 |
| 2 | 10003 | 13350 | 10300 | 13150 |
| 3 | 14020 | 21060 | 14650 | 20960 |

### 4.2.2 Counter-Rotation

In this mode of rotor operation, one rotor rotates in the opposite direction to the other with a speed ratio of $\kappa = -1.2$. The approximated excitation frequency components and their common divisor $\omega_0$ can be determined as,

$$\frac{\tilde{\omega}_2}{\tilde{\omega}_1} = -\frac{6}{5} = -1.2 \qquad \omega_0 = \frac{\tilde{\omega}_1}{5} = -\frac{\tilde{\omega}_2}{6} \tag{4.4}$$

The Campbell diagrams for this mode of operation are shown in Fig. 4.5 and the corresponding critical speeds are listed in Table 4.7. While comparing the critical speeds of the co & counter-rotating models, it is observed that the forward speeds are lower and backward speeds are higher for the counter-rotating model. It means that the separation between the forward and backward speeds are reduced. This behaviour can be seen in the Campbell diagrams as well. The forward and backward speeds are close to each other for the counter-rotating model. This happens mainly due to the cancellation of the gyroscopic moments of the two rotors during the counter-rotation.

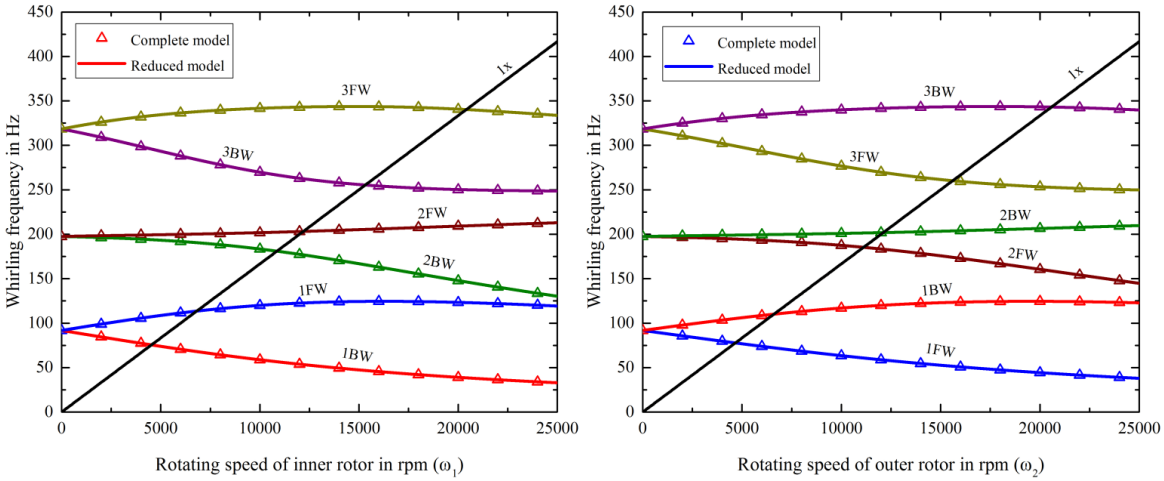


(a) excited by inner rotor (b) excited by outer rotor

Fig. 4.5 Campbell diagram of the simplified dual-rotor model (counter-rotation)

Table 4.7 Critical speeds of the simplified dual-rotor model (counter-rotation)

| Order | Excited by inner rotor (rpm) | | Excited by outer rotor (rpm) | |
|---|---|---|---|---|
| | backward | forward | backward | forward |
| 1 | 4533 | 6815 | 6609 | 4667 |
| 2 | 10860 | 12190 | 12110 | 11120 |
| 3 | 15320 | 20410 | 20590 | 15610 |

## 4.3 Unbalance response

The presence of mass unbalances in disks 1 and 3 produces centrifugal forces in the rotors, leading to rotor whirling during their operation. Initially, by assuming no stationary components in the model, it is possible to study the nature of whirling and the frequency contents. Since both the rotors are excited together, the model response will contain both frequency

components. The number of discrete-time points $N_{pt}$ is taken as 200 for the ATVM to capture the response completely. To validate its performance, the model response is compared with that of the MHBM-AFT. Figure 4.6 shows the unbalance responses of the inner rotor at disk 2 position under two-frequency excitations. Exact matching is observed between the results of the ATVM and the MHBM.

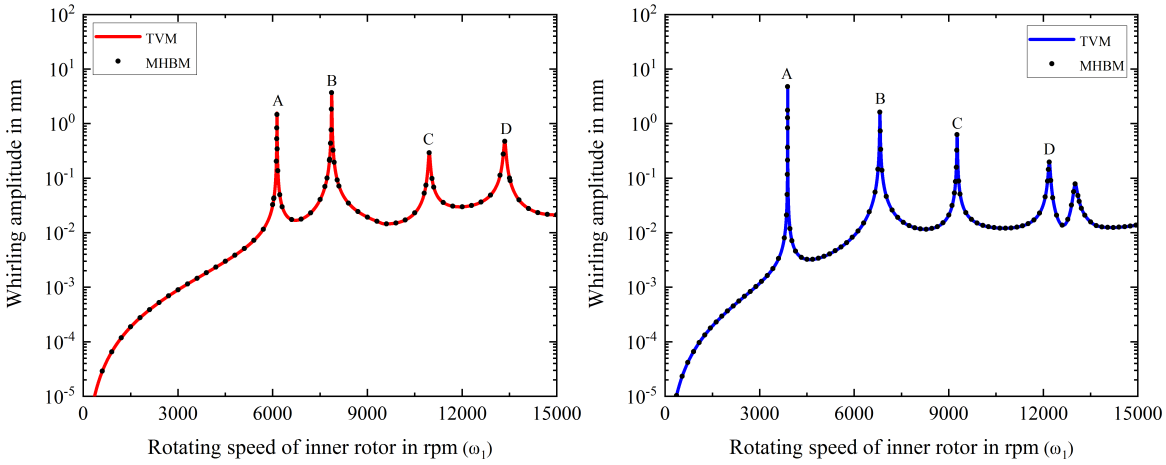


(a) co-rotation (b) counter-rotation

Fig. 4.6 Response of inner rotor at disk 2 position when mass unbalances are at disk 1 & 3

In Fig. 4.6, only forward whirling modes are excited since all the bearings used in the model are isotropic. The peaks A and C represent the resonance when the rotating speed is equal to $\frac{1}{1.2}$ times the critical speeds of the model with respect to the outer rotor excitations. The peaks B and D correspond to the resonance when the rotating speed becomes equal to the critical speeds of the model with respect to the inner rotor excitation. In order to analyze the whirling nature and the frequency content, the orbit plot and the frequency response plot are constructed for different rotating speeds of the rotors. Figure 4.7 and 4.8 show the orbit plots and the frequency response plot during the co & counter-rotation of the rotors respectively. In Fig. 4.7 and 4.8, the frequency response are plotted for the vertical responses measured at disk 2 position. It is observed that the rotor response contains the combinations of the inner and outer rotor excitations. Generally, the linear combinations of the inner and outer rotor excitations are expressed as $i\omega_1 + j\omega_2$. For simplicity, it can be denoted using $(i, j)$, where $i$ and $j$ are integers. Since, the unbalance response is linear, (1,0) and (0,1) components are observed in the rotor displacements as shown in Fig. 4.7 and 4.8.

The direction of the rotor whirl can be obtained from the orbit plot. It is seen that during co-rotation, the inner and outer rotors (disk 2 and disk 4) whirls in the same direction as the rotor rotation (in an anti-clockwise direction) for all the values of rotating speeds. However, during counter-rotation, the whirling nature of the rotors is different at different rotating

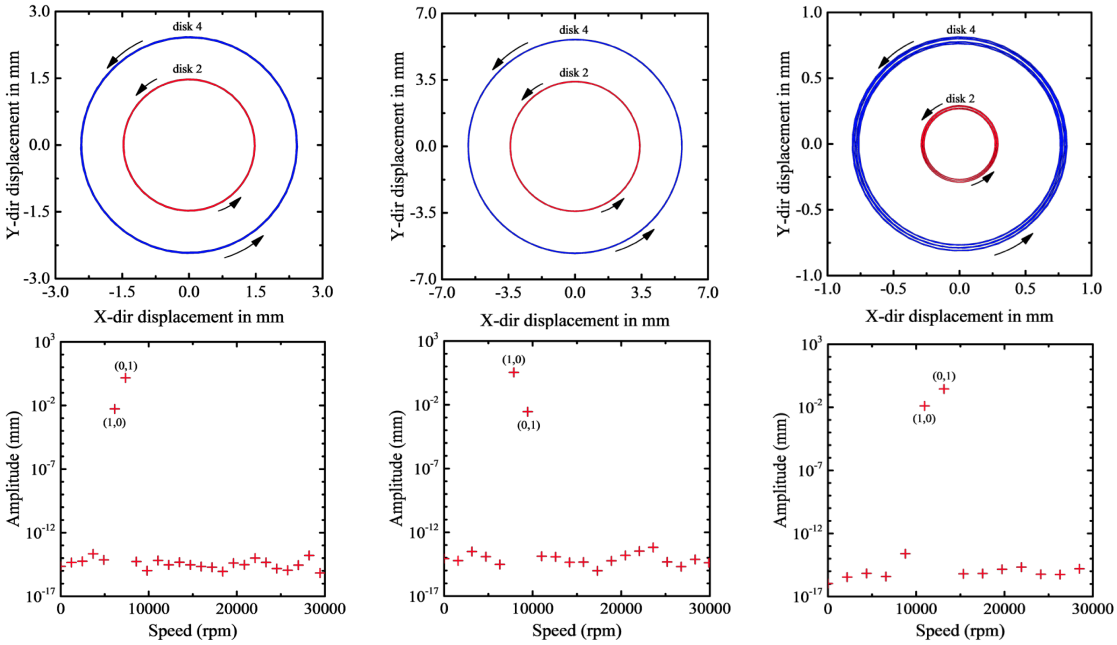


(a) $\omega_1$ = 6135 rpm (b) $\omega_1$ = 7872 rpm (c) $\omega_1$ = 10958 rpm

Fig. 4.7 Orbit plot and the frequency response plot of the rotor displacements during co-rotation of rotors

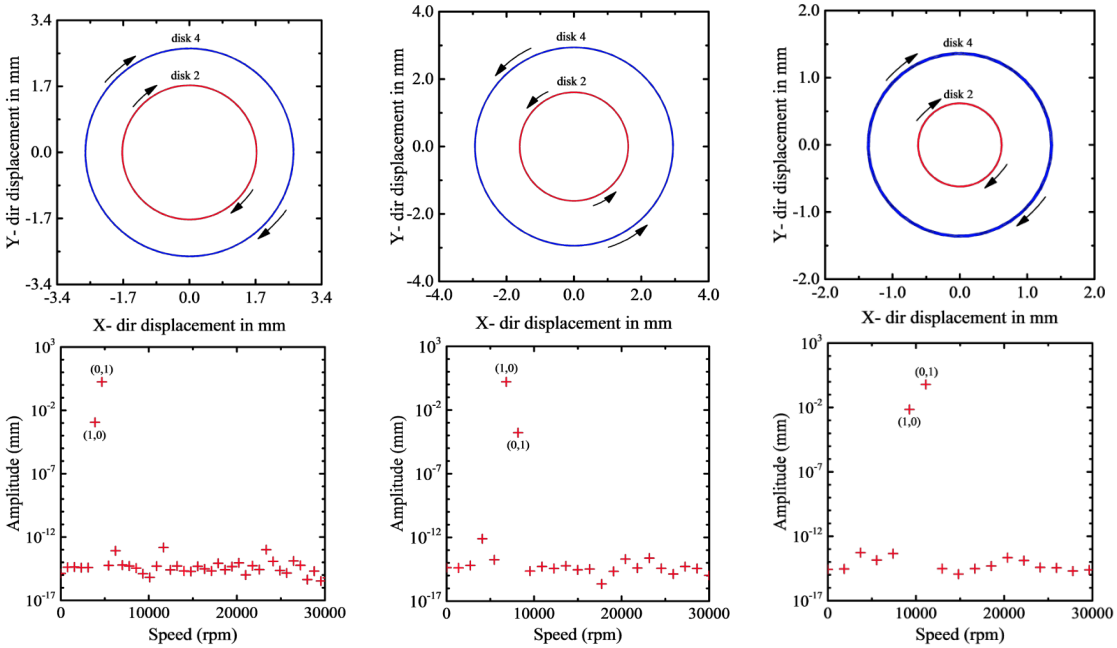


(a) $\omega_1$ = 3889 rpm (b) $\omega_1$ = 6815 rpm (c) $\omega_1$ = 9265 rpm

Fig. 4.8 Orbit plot and the frequency response plot of the rotor displacements during counter-rotation of rotors

speeds. It can be observed from Fig. 4.8a and Fig. 4.8c that when the rotating speed lies in the region of resonance with respect to the outer rotor excitation, both rotors whirl in the same spin direction as the outer rotor, i.e. in the clockwise direction. But, when the rotor speed is in the region of resonance with respect to the inner rotor excitation, both rotors whirl in the same spin direction as the inner rotor, i.e. in an anti-clockwise direction, as in Fig. 4.8b. It indicates that the direction of whirling is dependent on the value of rotating speed when the rotors are counter-rotating.

## 4.4 Rub-impact in the dual-rotor model

As the whirling amplitude of the rotor exceeds the clearance at disk 2 position, it contacts the stator during a rotor orbit. As a result, the nature of the rotor response changes significantly. To study this nonlinear behaviour, the ATVM is employed. The number of discrete-time points $N_{pt}$ is increased to 300. It is because a more number of time points are required to capture the complete nonlinearities arising due to rub-impact. Figure 4.9 and 4.10 show the rubbing responses of the rotor at disk 2 position when it is undergoing co-rotation and counter-rotation respectively. The model parameters are taken as $k_c = 5 \times 10^6$ N/m, $\delta = 0.1$ mm and $\mu = 0.01$. As the rotor touches the stator, a forward-leaning is observed along with a resonance shift which is happening mainly due to the addition of contact stiffness. In a speed range of [0,15000] rpm, four contact regions are noticed in the response which are zoomed in Fig. 4.9 and 4.10.

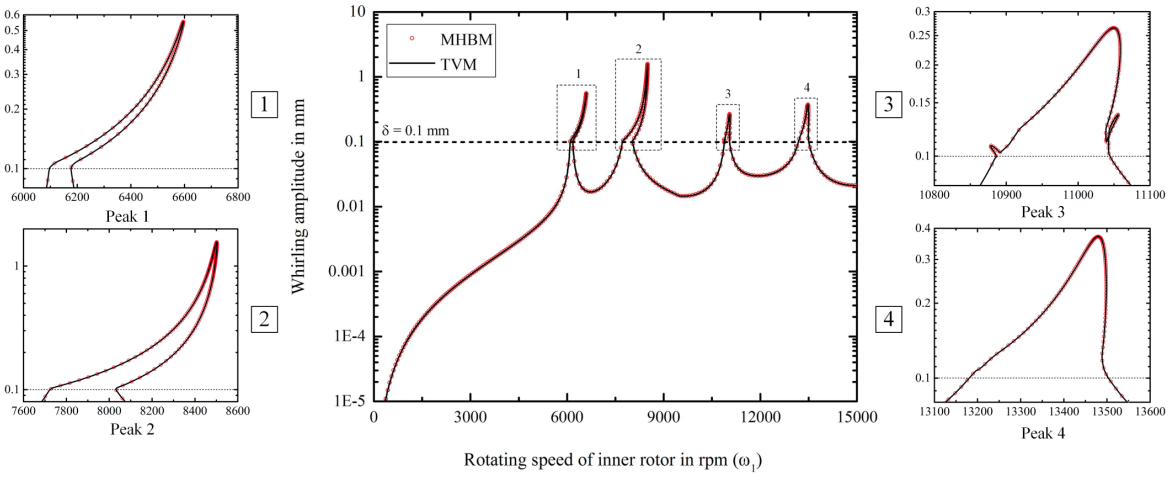


Fig. 4.9 Response at disk 2 position when rotors are co-rotating

When rotors are co-rotating, the initial contact happened at $\omega_1 = 6096.3$ rpm, whereas for the counter-rotation, it happened at $\omega_1 = 3882$ rpm. It shows that the counter-rotating

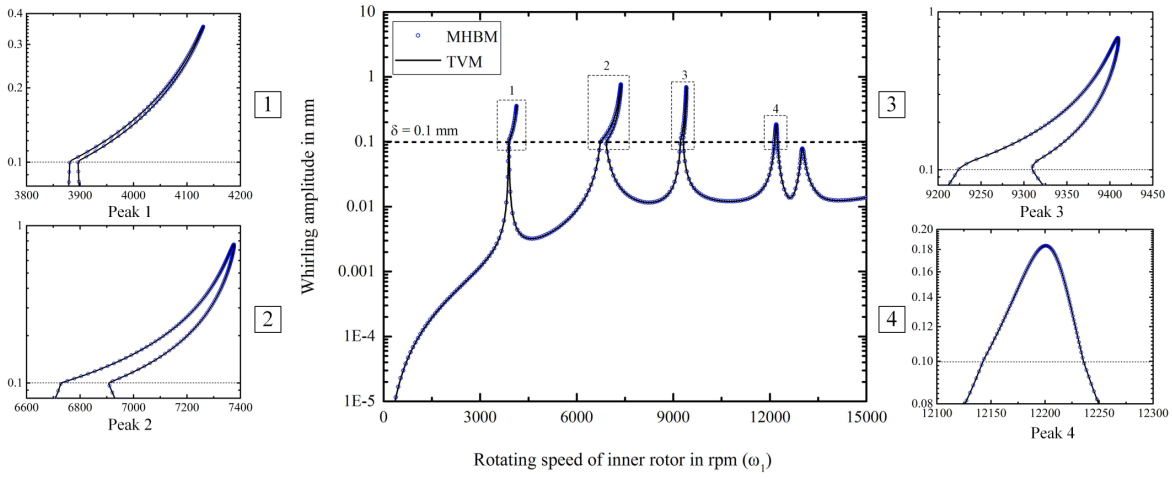


Fig. 4.10 Response at disk 2 position when rotors are counter-rotating

model undergoes early rub-impact for the same set of model parameters. This is due to the lower critical speeds of the counter-rotating model compared to the co-rotating model. The validation of the ATVM with the MHBM-AFT is also displayed in Fig. 4.9 and 4.10. The MHBM-AFT technique is utilized by taking the number of harmonics as 5. An exact agreement is obtained between the results of both methods. To verify the coupling of the inner and outer rotor vibrations, the responses are also determined at the disk 4 position. They are shown in Fig. 4.11 and 4.12. It is observed that the outer rotor also experiences a similar kind of forward-leaning as the inner rotor, even though it doesn't undergo any rub-impact. It shows the coupling of the inner and outer rotor vibrations, which is mainly occurring due to the presence of the inter-shaft bearing. Moreover, it is also noticed that the amplitude of the outer rotor response is slightly larger than that of the inner rotor.

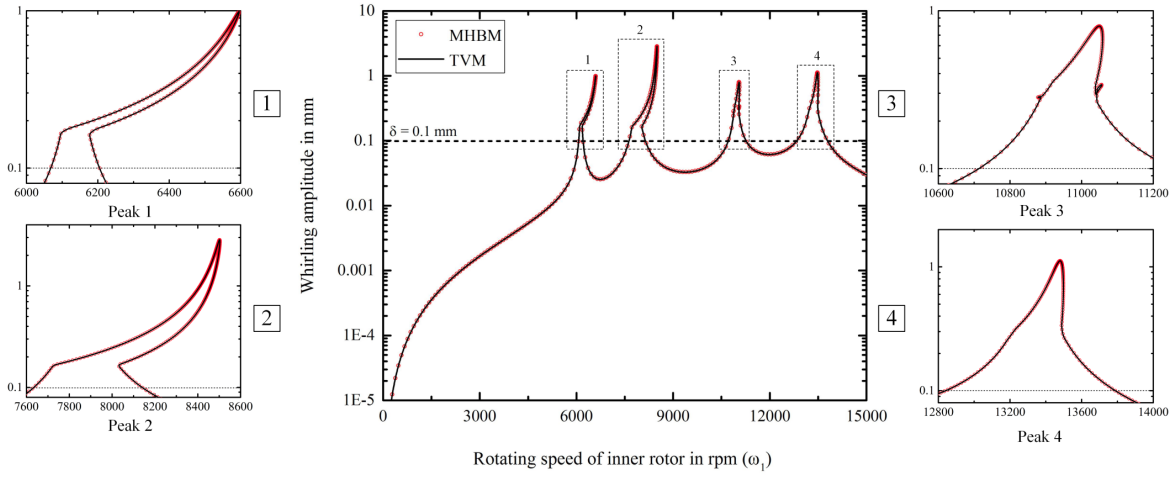


Fig. 4.11 Response at disk 4 position when rotors are co-rotating

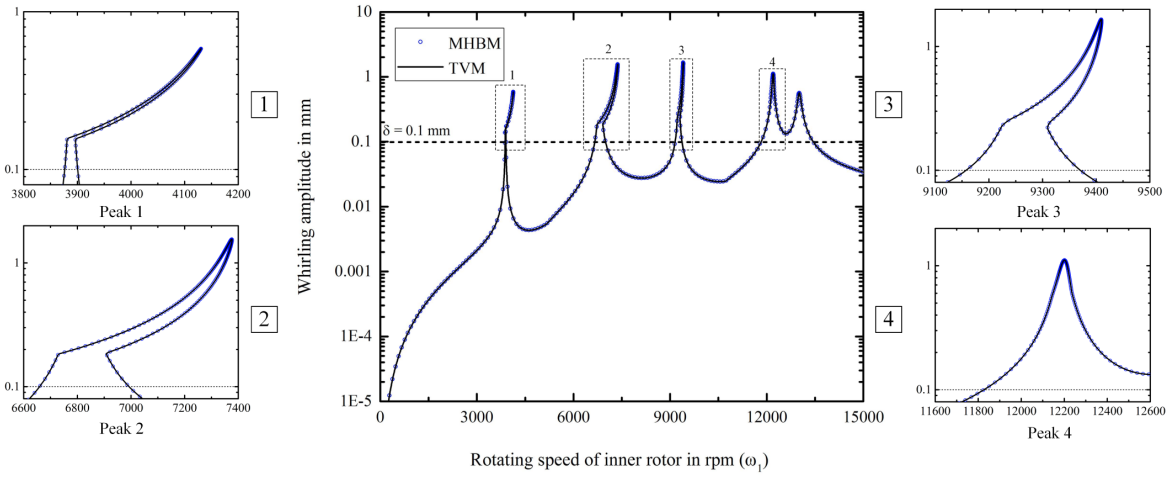


Fig. 4.12 Response at disk 4 position when rotors are counter-rotating

## 4.5 Stability analysis

**Co-rotation**: The stability analysis of the model is performed using the theory as described in Sec. 2.2.4. Figure 4.13 shows the stability diagrams of the model during co-rotation. The first four rub-impact regions are only displayed in the plot due to the lack of space. In Fig. 4.13, the stable part is represented using the continuous line, whereas the unstable part is represented using the dotted line. The LP and NS bifurcations are indicated using the circle and triangle markers respectively. The response is stable until the rotating speed $\omega_1$ = 6338.1 rpm. An NS bifurcation is detected at $\omega_1$ = 6338.1 rpm by monitoring the Floquet exponents of the model. Figure 4.14a shows the Floquet exponents of the model before and after NS bifurcation. It is seen that a pair of Floquet exponents crossed the imaginary axis as a pair of complex conjugates that confirms the occurrence of NS bifurcation at $\omega_1$ = 6338.1 rpm. As a result, a quasi-periodic regime can be initiated from this bifurcation point. The proposed methodology cannot capture the quasi-periodic regime since the quasi-periodicity contains the irrational frequency components that are unknown. However, the ATVM can detect the onset points of the quasi-periodic branches accurately with less computation time than numerical integration. It will help the designer in choosing the appropriate parameters to avoid the entry of the model into the quasi-periodic regime and dry friction backward whirl. Later, the numerical integration technique can get the quasi-periodic curve beyond the NS bifurcation point. It saves computation time since the numerical integration isn't required to run from the starting rotor speed. In future, the TVM will be modified to capture the quasi-periodic regime accurately by using the concept of hypertime as in the case of the MHBM.

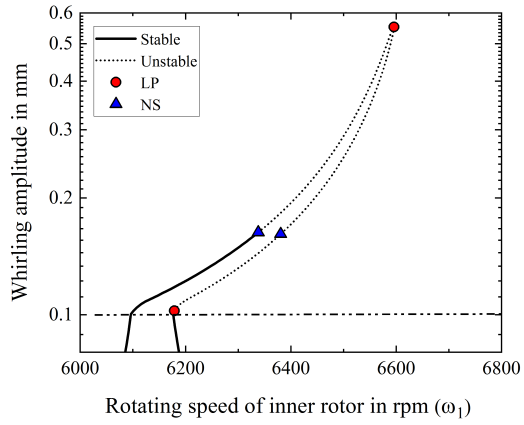


(a) Peak 1

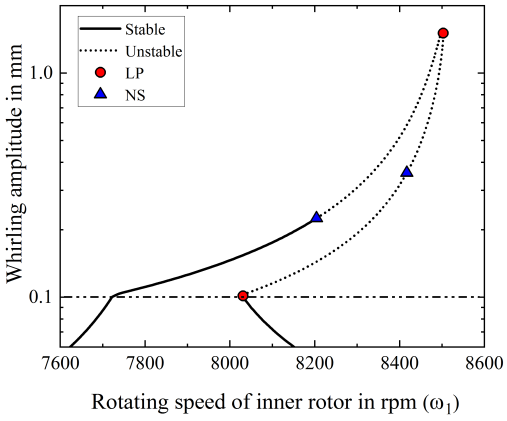


(b) Peak 2

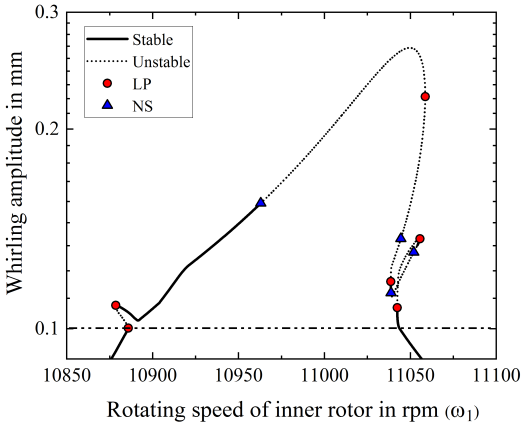


(c) Peak 3

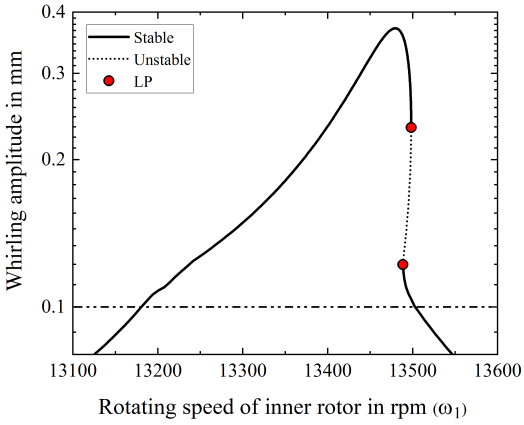


(d) Peak 4

Fig. 4.13 Stability analysis of the dual-rotor model when rotors are co-rotating

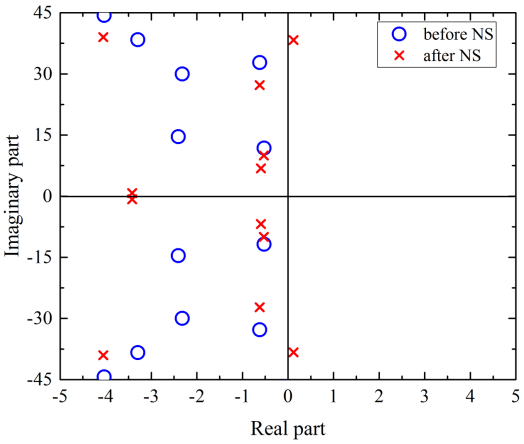


(a) NS at $\omega_1$ = 6338.1 rpm

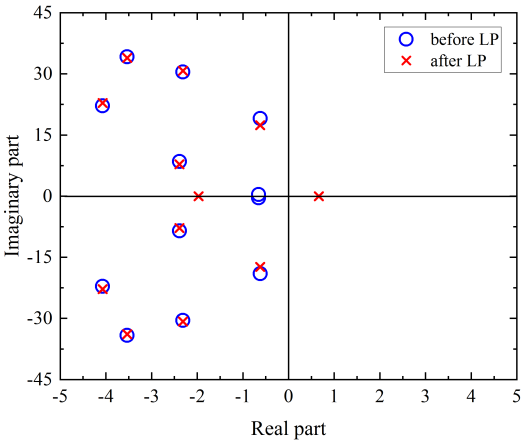


(b) LP at $\omega_1$ = 6596 rpm

Fig. 4.14 Floquet exponents in the vicinity of NS and LP bifurcations (co-rotation)

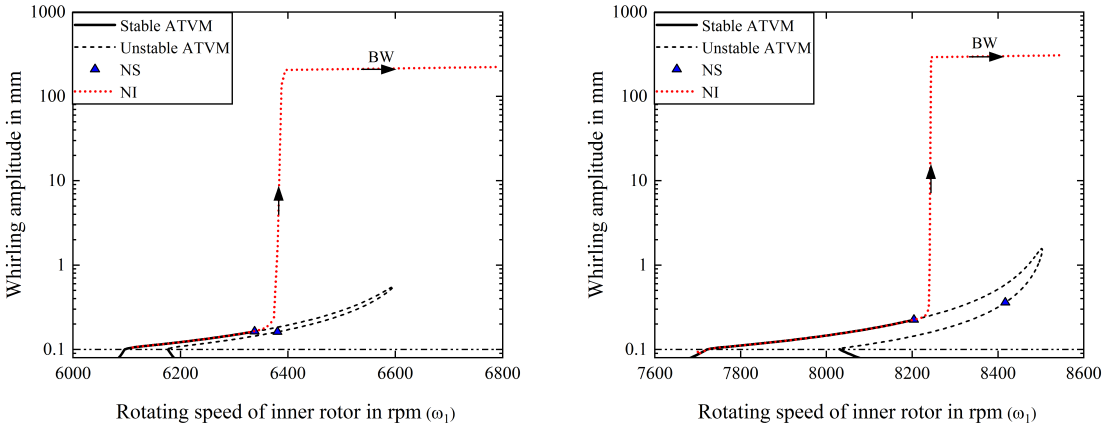


(a) Peak1 (b) Peak2

Fig. 4.15 Comparison of rub-impact responses determined using the ATVM and NI for the first two peaks (co-rotation)

Figure 4.15 shows the comparison of rub-impact responses determined using the ATVM and NI for the first two peaks. It is observed that the response is periodic until the NS bifurcation point; hence, the results obtained using the ATVM and NI match each other during this period of motion. While analyzing the orbit plot, a period-5 motion is observed in the response before the NS bifurcation point, indicating the full annular rub. It is shown in Fig. 4.16a at a speed of 6250 rpm.

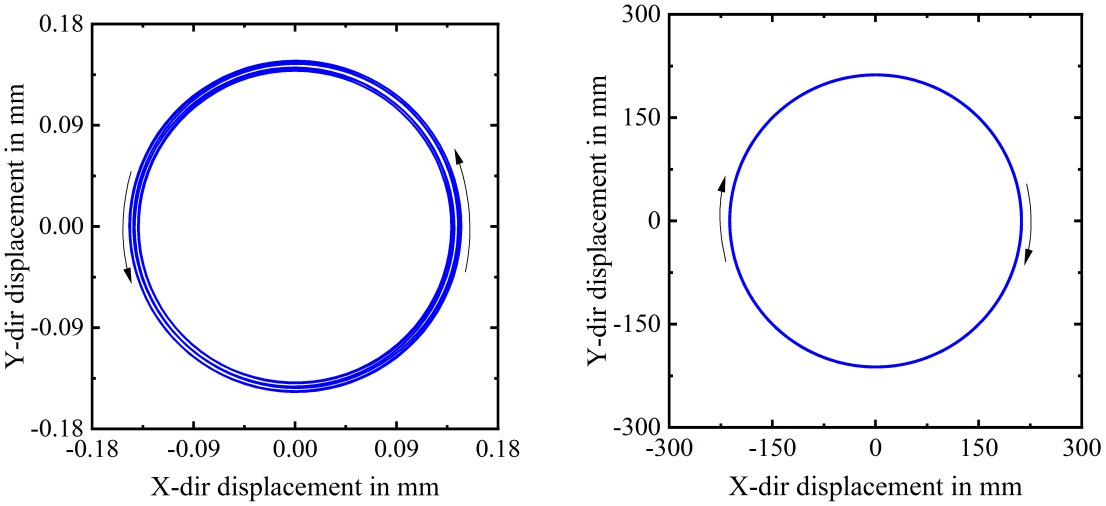


(a) Speed = 6250 rpm (b) Speed = 6550 rpm

Fig. 4.16 Orbit plots of the rotor at disk 2 position (a) before and (b) after the NS bifurcation (co-rotation), obtained using numerical integration. Forward whirl is noticed before the NS bifurcation, while dry friction backward whirl is observed beyond the NS bifurcation.

The direction of the whirl is the same as that of the rotor rotation; hence, it is a forward whirl. While noticing the FFT diagram in Fig. 4.17a, it is found that in addition to (1,0) and (0,1) components, other components such as (1,-2) and (2,-1) are also seen in the response. However, their amplitudes are small compared to that of the excitation frequency components. The additional frequency components appear mainly due to nonlinearities induced by rub.

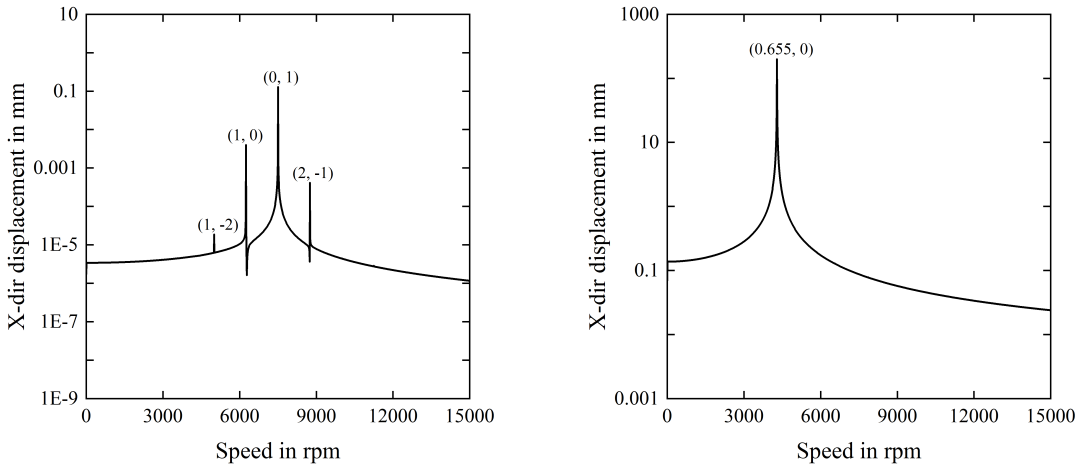


(a) Speed = 6250 rpm (b) Speed = 6550 rpm

Fig. 4.17 FFT diagram of the rotor response at disk 2 position (a) before and (b) after the NS bifurcation (co-rotation), obtained using numerical integration.

Beyond the NS bifurcation, the quasi-periodic regime starts, and it suddenly changes into the BW motion as shown in Fig. 4.15. During this period of motion, the results of the ATVM and NI don't match because the ATVM is unable to capture the quasi-periodic branch. However, the NI captures the quasi-periodic branch effectively. From Fig. 4.15, it is seen that the ATVM predicts the onset point of the quasi-periodic branch precisely. It saves a lot of time during the computation since the complete analysis doesn't require numerical integration. The NI is required only beyond the NS bifurcation. The orbit plot at $\omega_1 = 6550$ rpm is shown in Fig. 4.16b indicating the BW motion in which the direction of the whirl is opposite to that of the rotor rotation. From the FFT diagram in Fig. 4.17b, it is observed that a single frequency component is coming in the response with its amplitude being very high of the order of 2. This kind of motion is harmful to the rotor system and may lead to machinery failure.

Beyond $\omega_1 = 6338.1$ rpm, the periodic response obtained using the ATVM becomes unstable, and the dotted line shows it in Fig 4.13. At $\omega_1 = 6596$ rpm, an LP bifurcation is identified, which indicates the presence of a sudden jump phenomenon. To verify this, the Floquet exponents are determined and displayed in Fig. 4.14b. It is observed that one of the Floquet exponents crossed the imaginary axis along the real axis. It confirms the occurrence

of LP bifurcation at $\omega_1$ = 6596 rpm. Similar to the first peak, the NS and LP bifurcations are observed for the other peaks also.

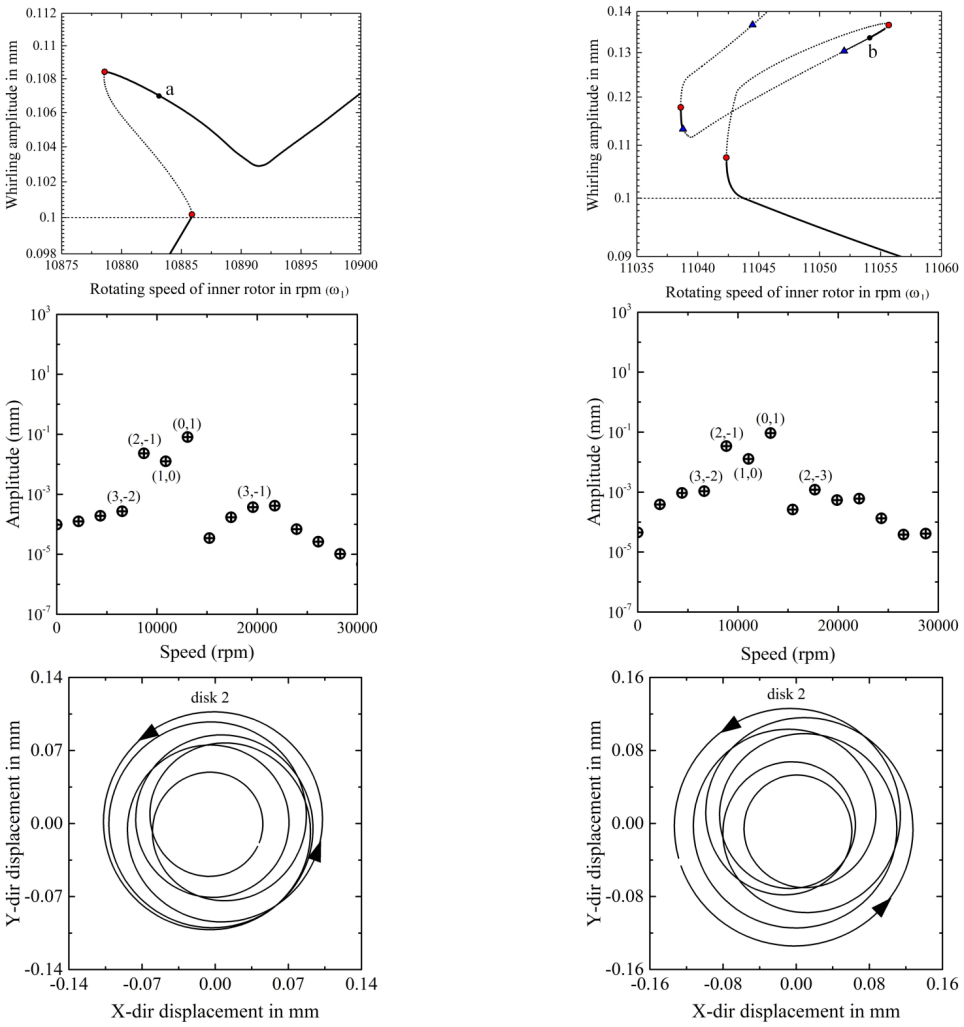


(a) 10882 rpm (b) 11055 rpm

Fig. 4.18 Stability diagram, FFT spectrum, and orbit plot of the two additional peaks. An additional (2,-1) component is also present in the response besides (1,0) and (0,1) components. As a result, the rub-impact happens occasionally, indicating the bouncing motion of rotor.

Two additional small peaks are also observed in the response between 10885-10892 rpm and 11038-11043 rpm. They are analyzed using the stability diagrams, FFT spectra, and orbit plots. In Fig. 4.18, the orbit plots and FFT diagrams are determined at the stable regions of the response, marked as points *a* and *b*. While observing the frequency components, it is seen that an additional (2,-1) component is also present in the response besides (1,0) and (0,1) components. Due to the presence of this frequency component, additional peaks appear in the response. Since the damping in the model is very low, the (2,-1) component also

dominates in the response along with the excitation frequency components. Some other frequency components also exist in the frequency spectrum; however, their effects are not visible due to their low amplitudes. From the orbit plots, it is seen that the rotors are whirling in multiple orbits, and they are moving in and out of the clearance space. It also indicates the presence of multiple frequency components in the response.

**Counter-rotation**: The stability analysis is performed for the counter-rotating model as well. It is shown in Fig. 4.19. The periodic response became unstable when the rotational speed reached $\omega_1$ = 3883.3 rpm. An NS bifurcation is detected at $\omega_1$ = 3883.3 rpm, and it is verified by comparing the results with that of NI as shown in Fig. 4.20.

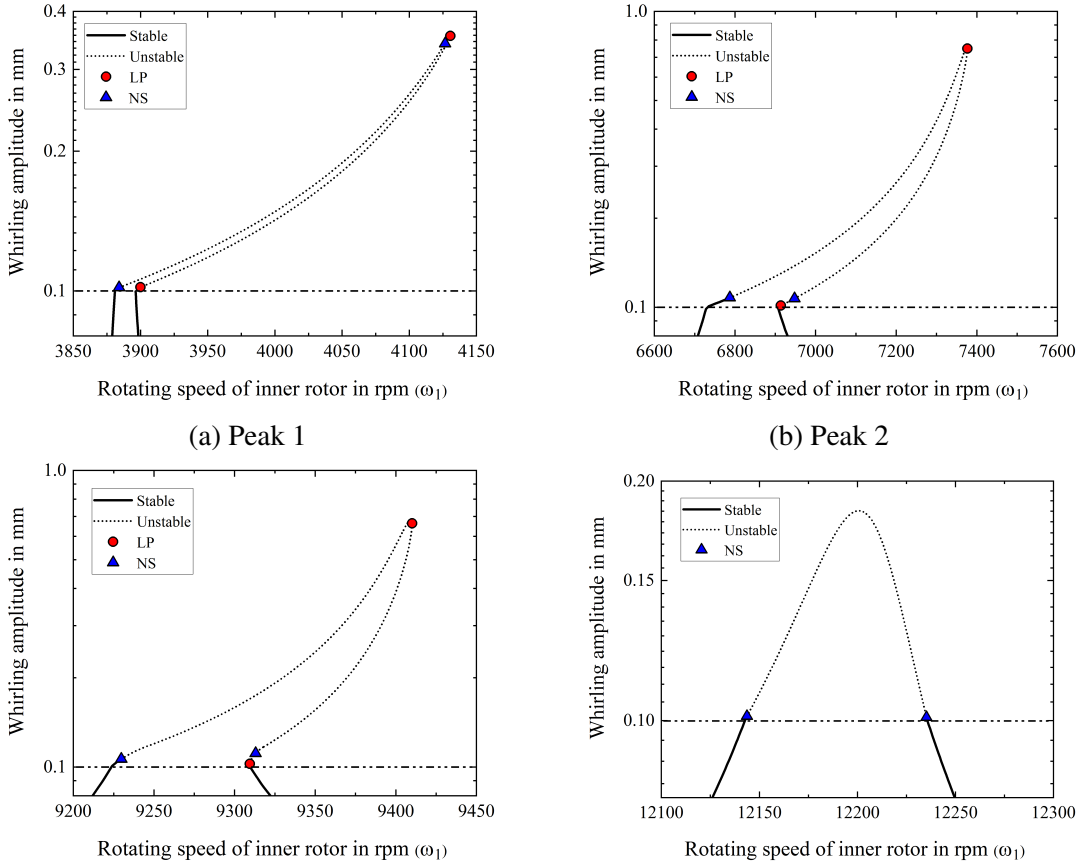


(a) Peak 1

(b) Peak 2

(c) Peak 3

(d) Peak 4

Fig. 4.19 Stability analysis of the model when rotors are counter-rotating

The rotor enters into the dry friction backward whirl very fastly and continues in this motion for a wide range of speed. The periodic response obtained using the ATVM becomes unstable during the remaining contact period, and an LP bifurcation is identified at $\omega_1$ = 4130.6 rpm as shown in Fig. 4.19a. The Floquet exponents in the vicinity of the NS and LP bifurcations are shown in Fig. 4.21, and it verifies the occurrence of the NS and LP

bifurcations. The model became unstable immediately after the contact for the other peaks as well. Hence, for the same set of model parameters, the NS bifurcation and the onset of the quasi-periodic regime are happening early for the counter-rotation. Therefore, a co-rotating system will be preferable in a dual-rotor model when considering the model stability during rub-impact.

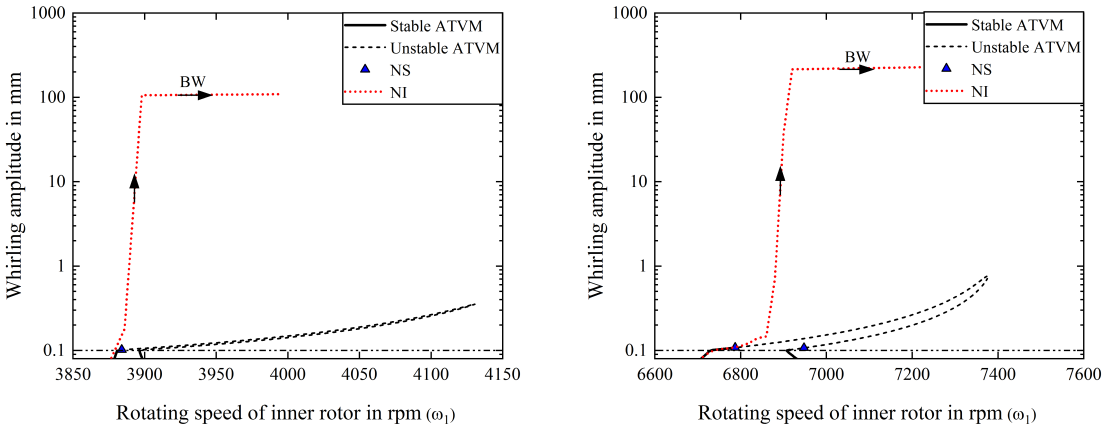


(a) Peak1 (b) Peak2

Fig. 4.20 comparison of rub-impact responses determined using the ATVM and NI for the first two peaks (counter-rotation)

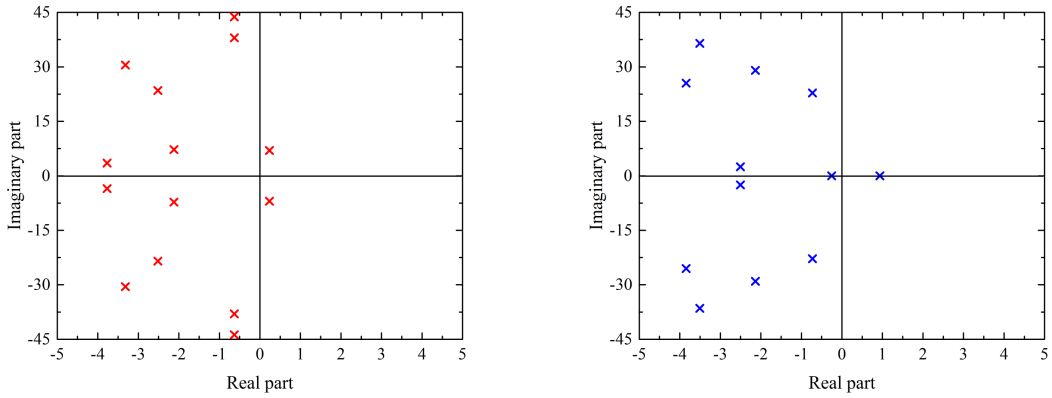


(a) NS at $\omega_1$ = 3883.3 rpm (b) LP at $\omega_1$ = 4130.6 rpm

Fig. 4.21 Floquet exponents in the vicinity of NS and LP bifurcations (counter-rotation)

The proposed method has to be applied in the complex aero-engine model consisting of multi-stage compressors and turbines to investigate the effects of multi-disk rub-impact. It will be explained in detail in the following chapter.

## 4.6 Summary

In this chapter, the stability analysis of a simplified dual-rotor model undergoing a single-disk rub-impact is performed using the proposed methodology. The study is carried out by developing a one dimensional FE model of a dual-rotor model using the Timoshenko beam elements. Later, its size is reduced using an efficient model reduction technique based on component mode synthesis. Two modes of rotor operations, namely co-rotation and counter-rotation, are included in the analysis to study their effects on the response behaviour. The Campbell diagrams and the unbalance responses of the dual-rotor model are determined for both modes of rotor operations. From the Campbell diagrams, it is observed that the critical speeds are different for both co and counter rotations. For counter-rotation, the forward critical speeds are smaller, and backward critical speeds are larger than that of co-rotation. This is mainly due to the cancellation of the gyroscopic moments in the case of counter-rotation. Moreover, during the counter-rotation, the whirling direction depends on the value of rotating speed. When the rotating speed is in the range of resonance with respect to the outer rotor excitation, both the rotors whirled in the same spin direction as the outer rotor. In contrast, when the speed is in the range of resonance with respect to the inner rotor excitation, both the rotors whirled in the same spin direction as the inner rotor. However, during the co-rotation, the whirling always happens in one direction irrespective of the rotating speed.

When contact is initiated, a rightward bending of the response curve is observed as it touches the stator. Due to the presence of inter-shaft bearing, the coupling of the inner and outer rotor vibrations have happened. As a result, the outer rotor also showed a similar rightward bending, although it didn't undergo any rub-impact. The stability of the model is assessed using a technique based on the Floquet theory. The Floquet exponents are monitored to detect the bifurcation points during the continuation procedure. Mainly, LP and NS bifurcations are observed in the responses when the rotor touches the stator. It is observed that the direction of rotor rotation has a significant effect on the onset of NS bifurcation. For the same model parameters, the onset of NS bifurcation happened earlier for the counter-rotating model than for the co-rotating model. As a result, a co-rotating model will be preferable in a dual-rotor when considering the stability of the model during rub-impact.

# Chapter 5

# Multi-disk rub-impact in the two-spool aero-engine model

This chapter is mainly intended to discuss the nonlinear dynamic characteristics of a two-spool aero-engine model undergoing multi-disk rub-impact using the proposed numerical procedure. This is the main contribution of the thesis, and there aren't any studies in the literature that analyze the multi-disk rub-impact in the aero-engine models. The two-spool rotor model consists of multi-stage compressors and single-stage turbines that experience rubbing whenever their deflection exceeds the clearance. In most of the previous works, rub-impact is studied by assuming the contact is happening at a single disk position only. However, in a multi-disk rotor model like an aircraft engine, the rotor-stator contacts may happen at more than one disk position under large unbalance forces. As a result, the model response may get complicated and sometimes lead to the machinery's failure. It necessitates the multi-disk rub-impact studies in the aero-engine rotor models.

## 5.1 Dynamic modelling of the two-spool aero-engine rotor

The real aero-engine comprises a sophisticated rotordynamic structure consisting of multi-stage bladed disks, hollow & conical shafts, thin-walled casing, rolling contact bearings, and dampers. The schematic diagram of a complex aero-engine model is shown in Fig. 5.1. The modelling of such a system is very complicated since it involves the dynamics of the different rotor components such as blades, disks, and drums. Hence, in this work, a simplified form of the aircraft engine is developed for analyzing its nonlinear responses under multi-disk rub-impact by referring to the model constructed by Jin et al. (2019). In this model, the rotor structure is built by combining the cylindrical and conical sections as shown in Fig.

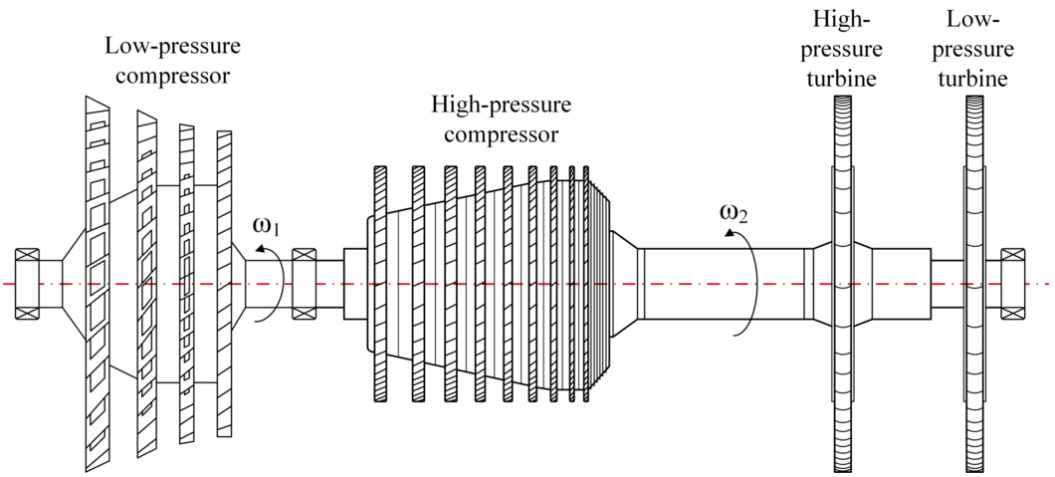


Fig. 5.1 Schematic diagram of an aero-engine dual-rotor model consisting of multi-stage compressors and single-stage turbines supported on bearings (Sun et al. (2018)). The low and high-pressure rotors operate at two different speeds, $\omega_1$ and $\omega_2$, and are connected using an inter-shaft bearing.

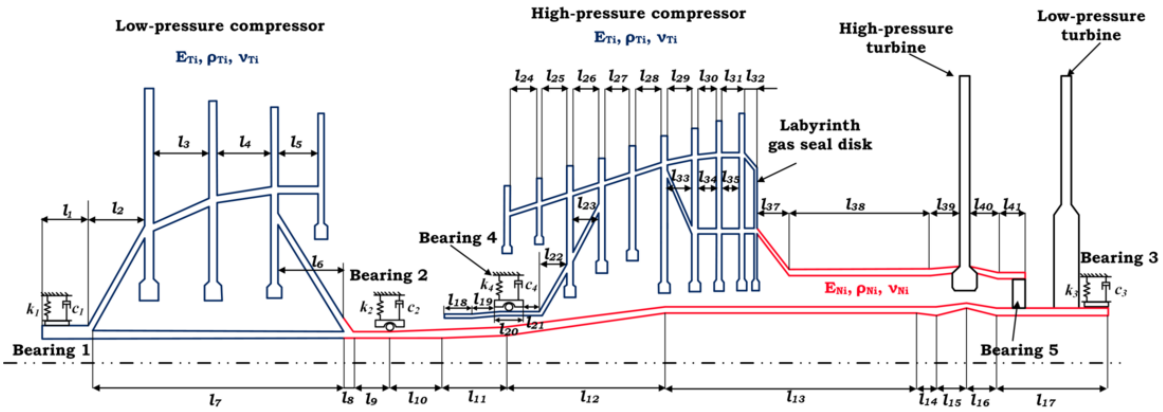


Fig. 5.2 The sectional view of the aero-engine dual-rotor model, which is made up of cylindrical and conical shaft sections, rigid disks, and rolling contact bearings (Jin et al. (2019)).

5.2. The model consists of two rotors, namely low-pressure and high-pressure rotors which operate at two different speeds, $\omega_1$, and $\omega_2$. As a result, the dual-rotor model undergoes two-frequency excitation with their ratio may not be an integer. The two rotors are connected using an inter-shaft bearing, leading to the coupling of low-pressure and high-pressure rotor dynamics. The inter-shaft bearing is replaced by a linear spring similar to a model presented in the paper by Sun et al. (2018). The bladed disks are assumed as rigid cylindrical disks, and the supporting pedestals are simplified as spring-damper models. The low-pressure rotor

has a four-stage compressor and a single-stage turbine supported on three bearings, whereas the high-pressure rotor has a nine-stage compressor and a single-stage turbine supported on two bearings. The compressors are made up of titanium alloy whose material properties such as the elastic modulus, density, and Poisson ratio are denoted as $E_{Ti}$, $\rho_{Ti}$ and $\nu_{Ti}$. They are connected to the corresponding turbines using inter-connecting shafts that are made up of nickel-based alloy with material properties $E_{Ni}$, $\rho_{Ni}$ and $\nu_{Ni}$. The geometrical dimensions and the physical properties of the aero-engine dual-rotor model are listed in Appendix A.

### 5.1.1 Finite element discretization of the model

The dynamic modelling of the dual-rotor model is carried out using the FE method. Mainly, the Timoshenko beam elements are used for discretizing the shafts, including the rotary inertia, shear factor, and gyroscopic effects in the formulation. Based on the section type, two kinds of beam elements are used for the FE modelling, such as cylindrical and conical elements.

#### Dynamic equations of a conical beam element

In this work, the lateral vibrations of the shaft element are only considered, ignoring the axial and torsional vibrations. Each element has two nodes with 4 DOFs in each node: two translations and two angular motions. Hence, the coordinate vector is given as, $\mathbf{q}_e = [x_A, y_A, \theta_{xA}, \theta_{yA}, x_B, y_B, \theta_{xB}, \theta_{yB}]^T$, where $A$ and $B$ are the two endpoints of a beam element. Now, the dynamic equation of a conical beam element can be written as,

$$\Big(\big[\mathbf{M}_e^t\big]_{con} + \big[\mathbf{M}_e^r\big]_{con}\Big)\ddot{\mathbf{q}}_e + \omega\big[\mathbf{G}_e\big]_{con}\dot{\mathbf{q}}_e + \big[\mathbf{K}_e\big]_{con}\mathbf{q}_e = \big[\mathbf{F}_e\big]_{con} \tag{5.1}$$

where $\big[\mathbf{M}_e^t\big]_{con}$, $\big[\mathbf{M}_e^r\big]_{con}$, $\big[\mathbf{G}_e\big]_{con}$ and $\big[\mathbf{K}_e\big]_{con}$ are the mass, rotary inertia, gyroscopic and stiffness matrices of a conical beam element respectively. $\big[\mathbf{F}_e\big]_{con}$ is the genaralized force vector of the element. The expansion of these matrices are given in Appendix B.

#### Dynamic equations of a cylindrical beam element

The cross-section parameters of a cylindrical beam element are constant throughout the section. Hence, its dynamic matrices can be obtained by substituting the cross-section parameters in the dynamic matrices of a conical beam element. Let, $\big[\mathbf{M}_e^t\big]_{cyl}$, $\big[\mathbf{M}_e^r\big]_{cyl}$, $\big[\mathbf{G}_e\big]_{cyl}$ and $\big[\mathbf{K}_e\big]_{cyl}$ represent the mass, rotary inertia, gyroscopic and stiffness matrices of a cylindrical beam element respectively. Then, its dynamic equation can be expressed as,

$$\left(\left[\mathbf{M}_e^t\right]_{cyl}+\left[\mathbf{M}_e^r\right]_{cyl}\right)\ddot{\mathbf{q}}_e+\omega\left[\mathbf{G}_e\right]_{cyl}\dot{\mathbf{q}}_e+\left[\mathbf{K}_e\right]_{cyl}\mathbf{q}_e=\left[\mathbf{F}_e\right]_{cyl} \tag{5.2}$$

**Dynamic equations of a rigid disk**

Rigid disk is a single-noded element with the coordinate vector, $\mathbf{q}_d=[x,y,\theta_x,\theta_y]^T$. Its dynamic equation can be written as,

$$\left[\mathbf{M}_d\right]\ddot{\mathbf{q}}_d+\omega\left[\mathbf{G}_d\right]\dot{\mathbf{q}}_d=\left[\mathbf{F}_d\right] \tag{5.3}$$

$$\left[\mathbf{M}_d\right]=\begin{bmatrix} m_d & 0 & 0 & 0\\ 0 & m_d & 0 & 0\\ 0 & 0 & I_d & 0\\ 0 & 0 & 0 & I_d\end{bmatrix},\quad \left[\mathbf{G}_d\right]=\begin{bmatrix} 0 & 0 & 0 & 0\\ 0 & 0 & 0 & 0\\ 0 & 0 & 0 & I_p\\ 0 & 0 & -I_p & 0\end{bmatrix}$$

where $m_d$, $I_d$, and $I_p$ are the mass, diametral moment of inertia, and polar moment of inertia of the disk respectively. $\left[\mathbf{F}_d\right]$ is the excitation force vector due to mass unbalances in the disks.

**Total dynamic equations of the aero-engine dual-rotor model**

The total dynamic equation of the aero-engine dual-rotor model is obtained by assembling the equations of disks, bearings, cylindrical, and conical shaft elements. In this study, the low-pressure rotor is discretized using 53 beam elements, whereas the high-pressure rotor is discretized using 31 beam elements. The compressor and turbine disks are assumed as rigid disks, and their inertial properties are added to the corresponding nodal positions. The final dynamic equation of the dual-rotor model is expressed as,

$$\mathbf{M}\ddot{\mathbf{q}}+\mathbf{C}\dot{\mathbf{q}}+\mathbf{G}(\omega_1,\omega_2)\dot{\mathbf{q}}+\mathbf{K}\mathbf{q}+\mathbf{F}_{nl}(\mathbf{q},t)=\mathbf{F}(\omega_1,\omega_2,t) \tag{5.4}$$

where $\mathbf{M}$, $\mathbf{C}$, $\mathbf{G}$ and $\mathbf{K}$ are the total mass, damping, gyroscopic and stiffness matrices of the aero-engine dual-rotor model. The damping matrix consists of two components, namely Rayleigh damping and support bearing damping. The Rayleigh damping coefficients are given in Tab. A.1. The vectors $\mathbf{q}$, $\mathbf{F}$ and $\mathbf{F}_{nl}$ represent the displacement vector, excitation force vector, and nonlinear force vector, respectively. The nonlinear force vector $\mathbf{F}_{nl}$ consists of the rolling contact bearing force and rub-impact force ($\mathbf{F}_{nl}=\mathbf{F}_b+\mathbf{F}_{rub}$). The details of rub-impact force are already discussed in Sec. 4.1 and the formulation of rolling contact bearing is discussed as follows.

**Rolling contact bearing model**: The schematic diagram of a rolling contact bearing model is shown in Fig. 5.3. In this model, the inner ring of the bearing is jointed to the rotor shaft while the outer ring is connected to the housing. During the operation, a point or line contact happens between the roller and the inner raceway. There exists a small clearance '$c_0$' between the rollers and outer raceway during the normal running conditions. When the deflection of the rollers exceeds the clearance, a nonlinear force is generated at the point of contact. It is derived using the Hertz contact theory, as explained (Hou et al. (2017)).

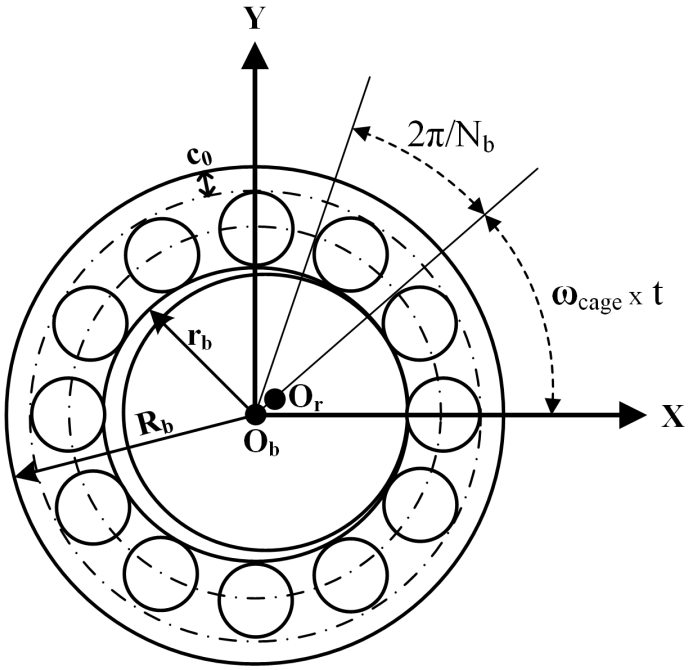


Fig. 5.3 Schematic diagram of a rolling contact bearing model (Hou et al. (2017))

$$
\begin{aligned}
f_{bx} &= \sum_{j=1}^{N_b} C_b(x\cos\beta_j + y\sin\beta_j - c_0)^n \, H(x\cos\beta_j + y\sin\beta_j - c_0)\cos\beta_j \\
f_{by} &= \sum_{j=1}^{N_b} C_b(x\cos\beta_j + y\sin\beta_j - c_0)^n \, H(x\cos\beta_j + y\sin\beta_j - c_0)\sin\beta_j
\end{aligned}
\tag{5.5}
$$

where $f_{bx}$ and $f_{by}$ are the bearing forces in X and Y directions respectively. $x$ and $y$ are the relative displacements of inner and outer rings. $n$ is the nonlinear index of Hertz contact deformation ($n = \frac{3}{2}$ for ball bearing and $n = \frac{10}{9}$ for cylindrical roller bearing). $H(.)$ is the heavy side function and $\beta_j$ is the angular position of the $j^{th}$ roller which is described as follows.

$$\begin{aligned} \beta_j &= \omega_{cage} \times t + \frac{2\pi}{N_b}(j-1), \qquad j = 1,2,...,N_b \\ \omega_{cage} &= \omega_i \times \frac{r_b}{R_b + r_b} \end{aligned} \tag{5.6}$$

where $\omega_i$ is the angular velocity of the inner ring, it is assumed to be equal to the angular velocity of the respective rotor. $r_b$ and $R_b$ are the radii of the inner and outer rings, respectively. The bearing force vector $\mathbf{F}_b$ is formed by inserting $f_{bx}$ and $f_{by}$ in the respective positions corresponding to each rolling contact bearing.

## 5.2 Verification of the model

This study assumes that both the low-pressure and high-pressure rotors are co-rotating with a speed ratio of 1.2. Initially, the natural frequencies and the mode shapes of the aero-engine dual-rotor model are determined and compared with the ANSYS model. In ANSYS, the beam 188 element is used to model the shaft, with the rotor being discretized into 94 elements. The tapered beam sections are utilized to represent the conical shafts. The disks are modelled using the mass21 element, while the linear bearings are modelled using the combin14 elements. The QR damped method is employed to determine the complex eigenvalues and it allows the processing of asymmetric matrices. Table 5.1 gives the first four natural frequencies of the model calculated using the present method and the ANSYS. The percentage of errors is calculated and listed in Tab. 5.1. It is observed that the variation is under 1 %. Later, the mode shapes of the aero-engine dual-rotor model are determined and compared with that of the ANSYS model as shown in Fig. 5.4.

Table 5.1 Natural frequencies of the aero-engine model under non-rotating condition

| dual-rotor | Order | | | |
|---|---|---|---|---|
| | 1st | 2nd | 3rd | 4th |
| Present model Frequency (Hz) | 121.75 | 249.80 | 361.56 | 514.37 |
| ANSYS model Frequency (Hz) | 121.12 | 250.85 | 360.19 | 511.52 |
| Percentage of error (%) | 0.52 | -0.42 | 0.38 | 0.55 |

The first two modes are only presented since the rubbing responses at the first two vibration modes are mainly analyzed in this work. From Fig. 5.4, it is noticed that the results obtained using the present method are well-matched with that of the ANSYS model. While analyzing the first two modes, it is seen that the deformation of the low-pressure compressor (LPC) is very low compared to that of the high-pressure compressor (HPC) and turbines

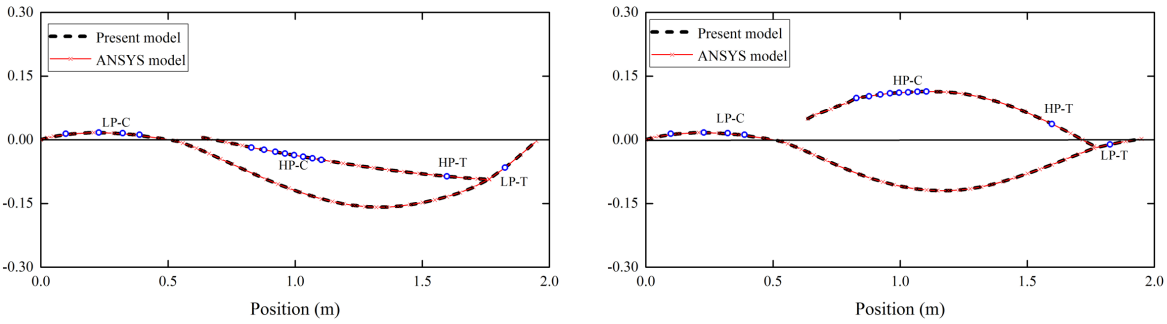


Fig. 5.4 Mode shapes of the aero-engine model at (a) 121.75 Hz (first mode) and (b) 249.8 Hz (second mode). They are well-matched with the ANSYS model, proving the effectiveness of the dynamic modelling method. Blue circles show the location of mass points.

(HPT). Hence, the LPC disks cannot rub against the casing surface. All the nodes containing disks and bearings are included in the primary component during the model reduction process. To verify the effectiveness of the model reduction technique, the Campbell diagrams of the full and reduced models are compared. It is shown in Fig. 5.5. Good matching is obtained between the results of the full and reduced models up to a frequency of 1000 Hz. The critical speeds of the aero-engine dual-rotor model are listed in Tab. 5.2.

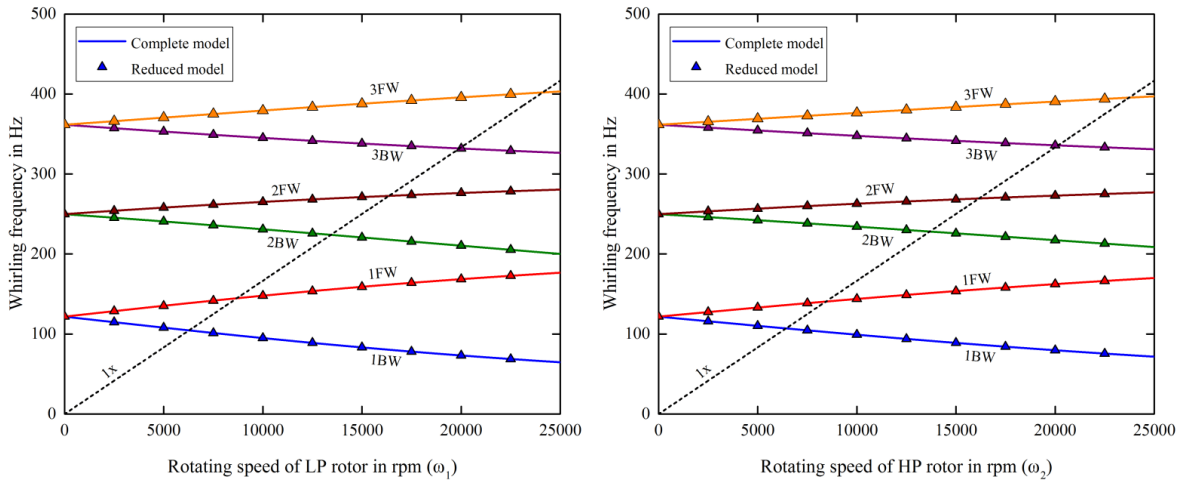


Fig. 5.5 Campbell diagrams of the aero-engine model when excited by (a) low-pressure rotor and (b) high-pressure rotor. The Campbell diagrams of the full and reduced models are well-matched, proving the effectiveness of the model reduction technique.

Later, the unbalance responses of the model are determined without considering the rub-impact. The mass unbalances are applied at LPC-3, HPC-7, LPT, and HPT disks with

Table 5.2 Critical speeds of the aero-engine model

| Order | Excited by low-pressure rotor (rpm) | | Excited by high-pressure rotor (rpm) | |
|---|---|---|---|---|
| | (BW) | (FW) | (BW) | (FW) |
| 1 | 6275 | 8685 | 6425 | 8435 |
| 2 | 13440 | 16360 | 13690 | 16170 |
| 3 | 19920 | 24110 | 20150 | 23730 |

their eccentricities are given in Tab. A.1. The ATVM is used to calculate the steady-state responses of the model by taking the number of time points, $N_{pt}$ as 150.

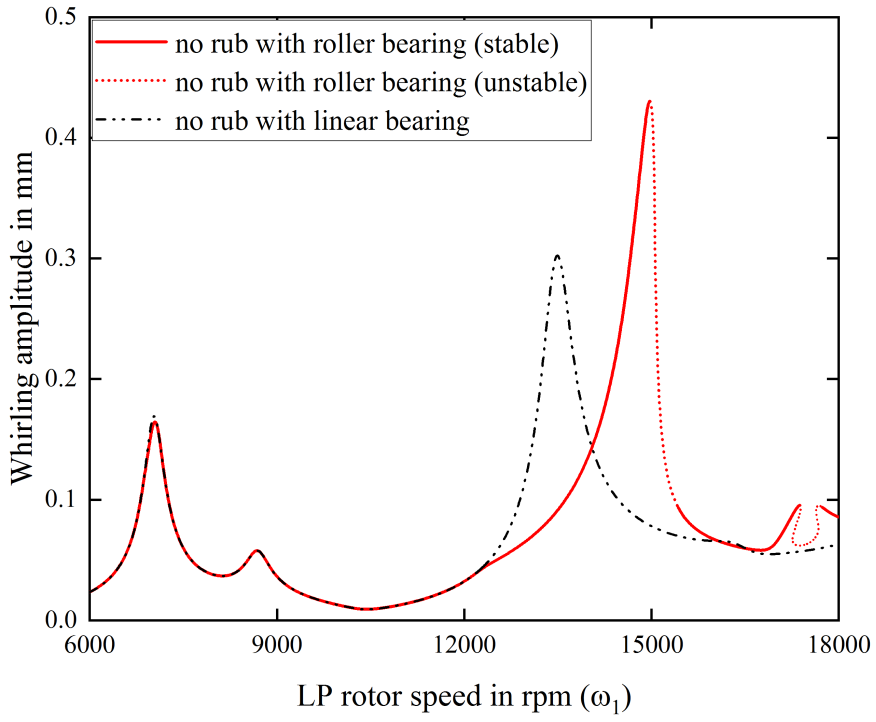


Fig. 5.6 Comparison of the frequency responses of the models supported on linear bearings and rolling contact bearings. A rightward shifting of the resonant curve is observed for the model with rolling contact bearings. It is mainly due to the hard spring characteristics of the rolling contact bearings.

In Fig. 5.6, the unbalances response of the aero-engine dual-rotor model with and without rolling contact bearings are compared. Four resonance peaks are observed in the response in which the first two corresponds to the first vibration mode, and the last two corresponds to the second vibration mode. In the first vibration mode, the displacements at the bearing locations are negligible, which is evident from Fig. 5.4. As a result, there aren't many variations in the response of both models. However, for the second mode of vibration, the displacement at

bearing 4 is so significant that a rightward shifting of the resonant curve is noticed. The first resonant curve of the second mode is shifted from 13490 rpm to 14980 rpm, while the second curve is shifted from 16360 rpm to 17380 rpm. In addition, a mode splitting is observed at the second vibration mode due to the hard spring characteristics of the rolling contact bearings.

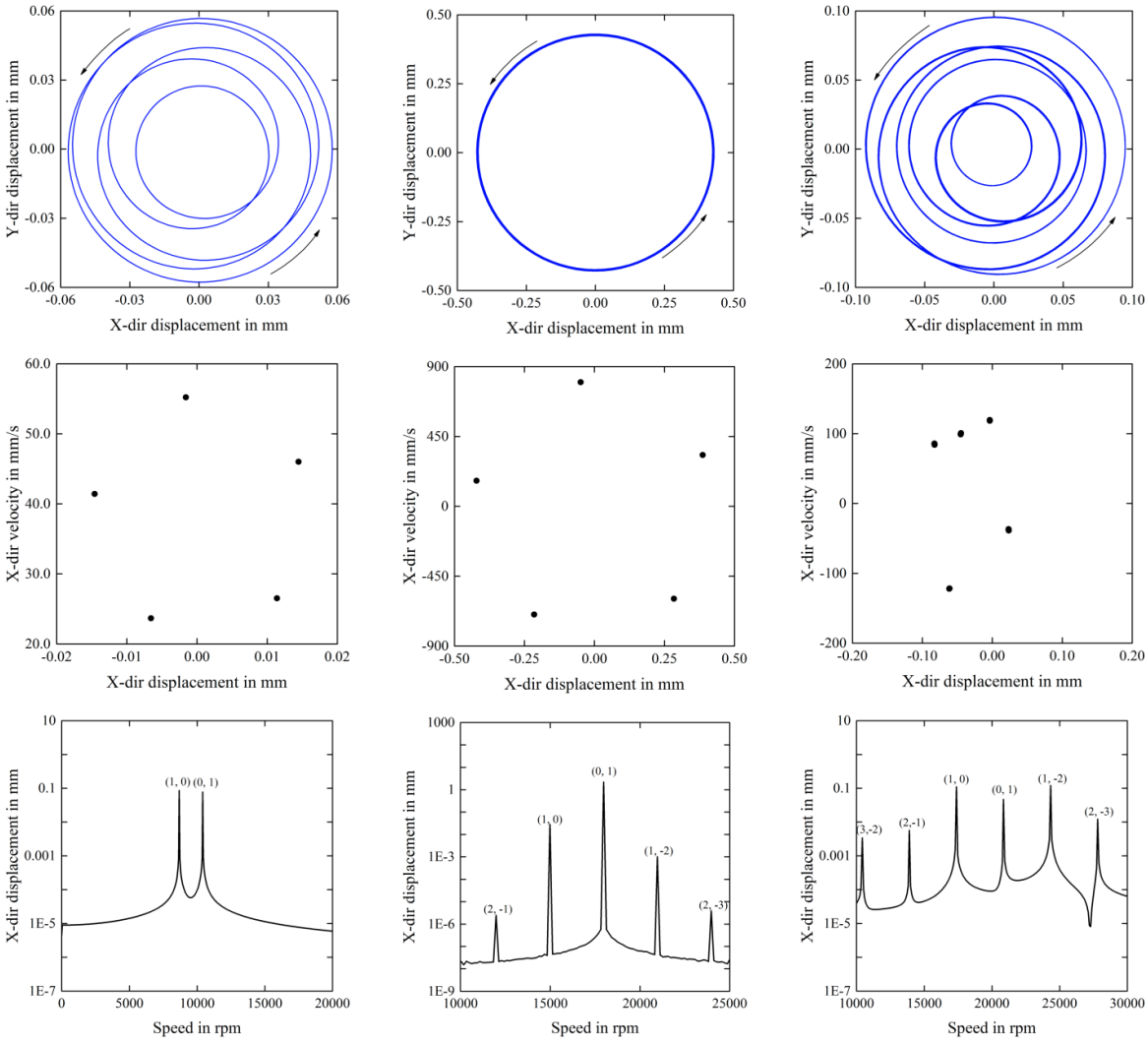


Fig. 5.7 Orbit plots, Poincaré maps, and FFT spectrum calculated at HPC-7 position when the rotor speed is (a) 8680 rpm, (b) 14980 rpm, and (c) 17380 rpm. For all speeds, the orbit plots show five closed circles, and the Poincaré maps show five points, indicating a period-5 motion. Due to the presence of ball bearing nonlinearity, some additional frequency components are appearing in the FFT spectrum.

Figure 5.7 shows the orbit plots, Poincaré maps, and FFT spectra of the response at resonant speeds. Five closed circles are observed in the orbit plots, while five points are seen

in the Poincaré maps, indicating a period-5 motion. While analyzing the FFT spectrum, it is observed that only excitation frequency components such as $\omega_1$ and $\omega_2$ are seen in the first mode regions [0 - 10370 rpm], indicating that the effects of rolling contact bearings are negligible within this speed range. However, additional frequency components such as $(\omega_1 - 2\omega_2)$, $(2\omega_1 - \omega_2)$, $(2\omega_1 - 3\omega_2)$ and $(3\omega_1 - 2\omega_2)$ are noticed in the second mode regions [10370 - 18000 rpm]. They are denoted as (1,-2), (2,-1), (2,-3) and (3,-2) in the FFT diagrams displayed in this report. The additional frequency components appear mainly due to the nonlinearity in the rolling contact bearings, and it is more visible during the second resonant region as shown in Fig. 5.7c.

Meanwhile, the time response signals obtained using the ATVM are verified with the numerical integration results. Fig. 5.8 shows the validation of the ATVM with the numerical integration (NI) method. As per Fig. 5.8, the results of the ATVM are well-matched with that of the NI method.

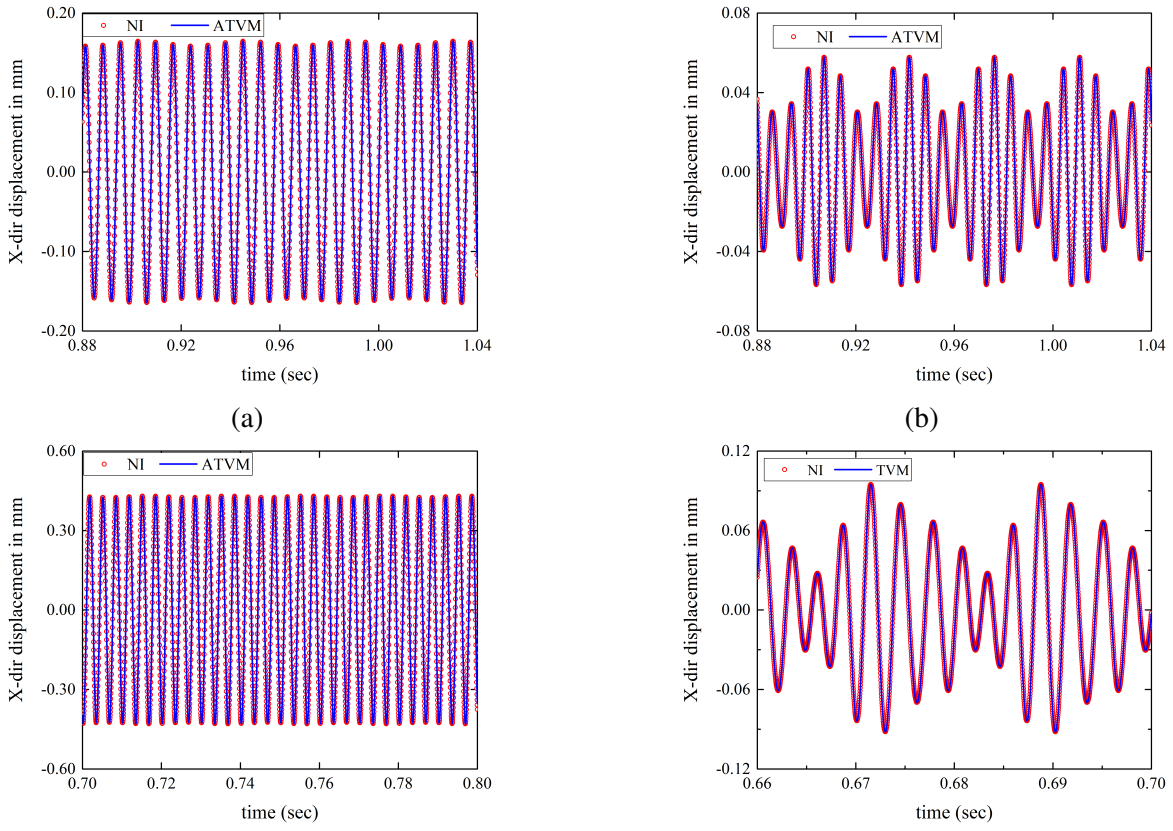


Fig. 5.8 X-dir displacements calculated at HPC-7 disk position when the rotor speed is (a) 7050 rpm, (b) 8680 rpm, (c) 14980 rpm, and (d) 17380 rpm under the no-rub condition using the ATVM and numerical integration. In ATVM, the number of time points $N_{pt}$ is taken as 150. A good agreement in the results of both methods is obtained.

## 5.3 Response of the model under multi-disk rub-impact

Once the whirling amplitudes of the rotors exceed the clearance, it contacts the stator. As a result, the response of the model changes significantly, and it becomes nonlinear. The nonlinear forces are determined by taking the parameters $k_c = 0.3\times10^8$, $\mu = 0.2$ and $\delta = 0.1$. The rub-impact responses are obtained using the ATVM by taking $N_{pt}$ as 180.

### 5.3.1 Significance of multi-disk rub-impact studies

As mentioned earlier, most of the research works in the past analyzed the single-disk rub-impact problems in which the rub is considered at a single disk position only. However, in a multi-disk rotor, there is a possibility for more than one disk in the rotor to undergo rubbing.

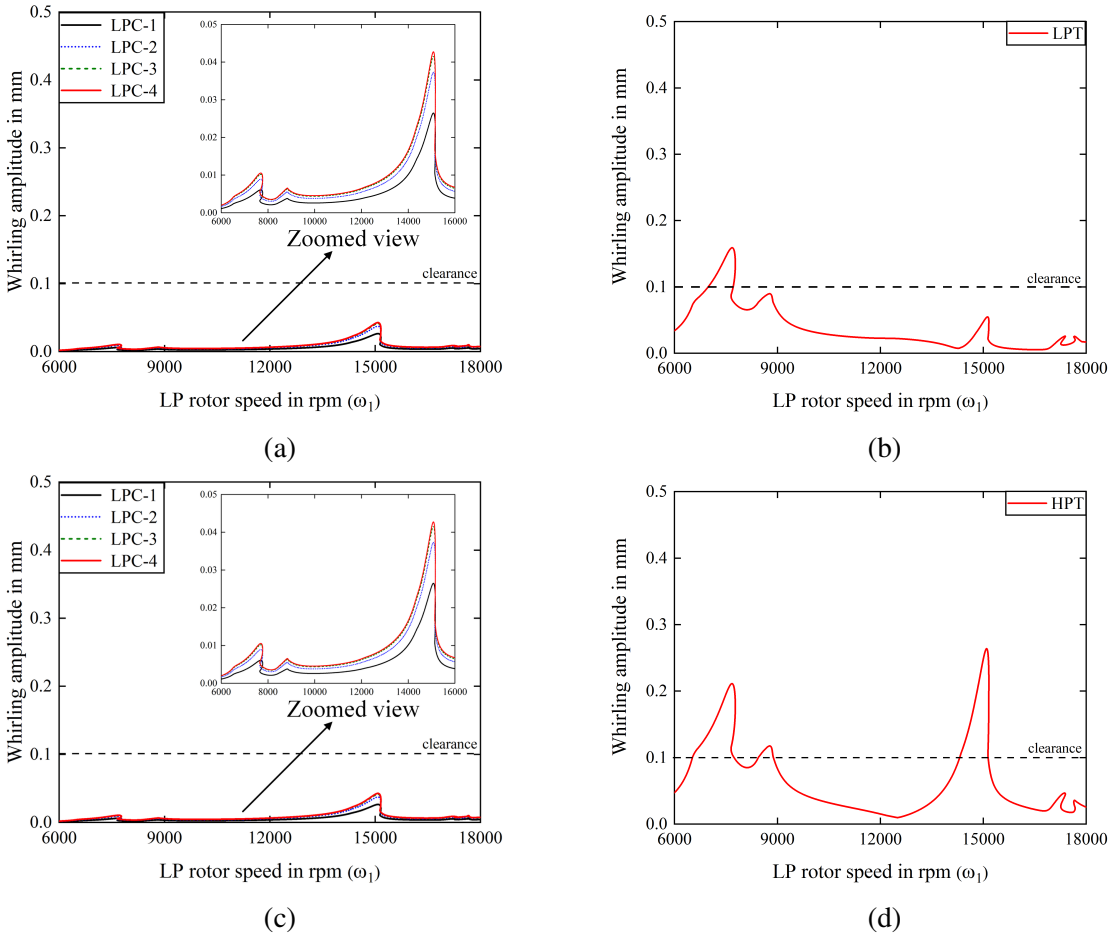


Fig. 5.9 Frequency response diagram calculated at (a) LPC (b) LPT (c) HPC and (d) HPT disk positions when rub-impact nonlinearity is assumed at HPT disk position alone. Due to the coupling of rotors, similar behaviour is observed for other disks as well, even though they didn't undergo any rub-impact.

To verify this, a single-disk rub-impact is applied to the present model, and the response curves are obtained as shown in Fig. 5.9. Referring to the papers by Sun et al. (2016); Wang et al. (2017, 2020b), the contact is assumed to happen at the HPT disk position alone. During the analysis, the rotor-stator clearance is considered constant for all the disks. Until the point of contact, the response is similar to that of the no-rub response. At 6523 rpm, the HPT disk initiates the contact, and a rightward bending is observed due to the modification of the model stiffness. Even though the rub nonlinearities aren't assigned for the other disks, a similar kind of rightward bending is noticed. It is due to the coupling of rotors. While analyzing Fig. 5.9b & 5.9c, it is seen that the deflections of LPT, HPC-8, and HPC-9 disks are exceeding the clearance for the first peak; still, no changes are observed in the response since the nonlinearity is applied at the HPT disk position alone. Similarly, for the third resonance peak, all the HPC disks are exceeding the clearance, but no variations are observed, as shown in Fig. 5.9c. It proves the limitations of the single-disk rub-impact studies and underlines the importance of multi-disk rub-impact studies.

Figure 5.10 shows the frequency response curves of the aero-engine dual-rotor model determined at different disk positions during multi-disk rub-impact. Once the engine is started, the rotors begin to whirl within the clearance space till 6522 rpm, representing the no-rub response. At 6522 rpm, the HPT disk initiates the contact, and a rightward bending occurs due to the modifications in the model stiffness. Due to the coupling of rotors, all other disks also show a similar trend in the response characteristics. The sequence in which the disks are rubbing can be understood by monitoring the nonlinear function, as shown in Fig. 5.11. The rub nonlinearity in X-direction, $f_{nx}$ is plotted in Fig. 5.11 to find the status of contact at a particular speed. Initially, the HPT disk alone rubs the stator within a speed range of $6522 \leq N_{speed} \leq 6985$ rpm. It can be validated by checking the nonlinear function at a speed of 6640 rpm within this range, as shown in Fig. 5.11a. The nonlinear function corresponding to the HPT disk is only existing in Fig. 5.11a, indicating the HPT disk rubbing alone. It means that the multi-disk rub response is similar to that of the single-disk rub-impact till this rotating speed of 6985 rpm.

At 6985 rpm, the LPT disk as well starts to contact the stator, and the corresponding rub-impact happens in the range of $6985 \leq N_{speed} \leq 7465$ rpm. It is verified by checking the nonlinear function at a speed of 7350 rpm where the rub nonlinearity corresponding to the HPT and LPT disks are coming as shown in Fig. 5.11b. As a result, the extend of rightward bending is increased in comparison to the single-disk rub-impact, which is evident from Fig. 5.10b & 5.10d. As the speed is increased beyond 7465 rpm, the deflection of the HPC-9 disk also exceeds the clearance, and it commences to participate in the rub, followed by the contact of the HPC-8 disk at 7710 rpm. It is confirmed by monitoring the rub nonlinearity

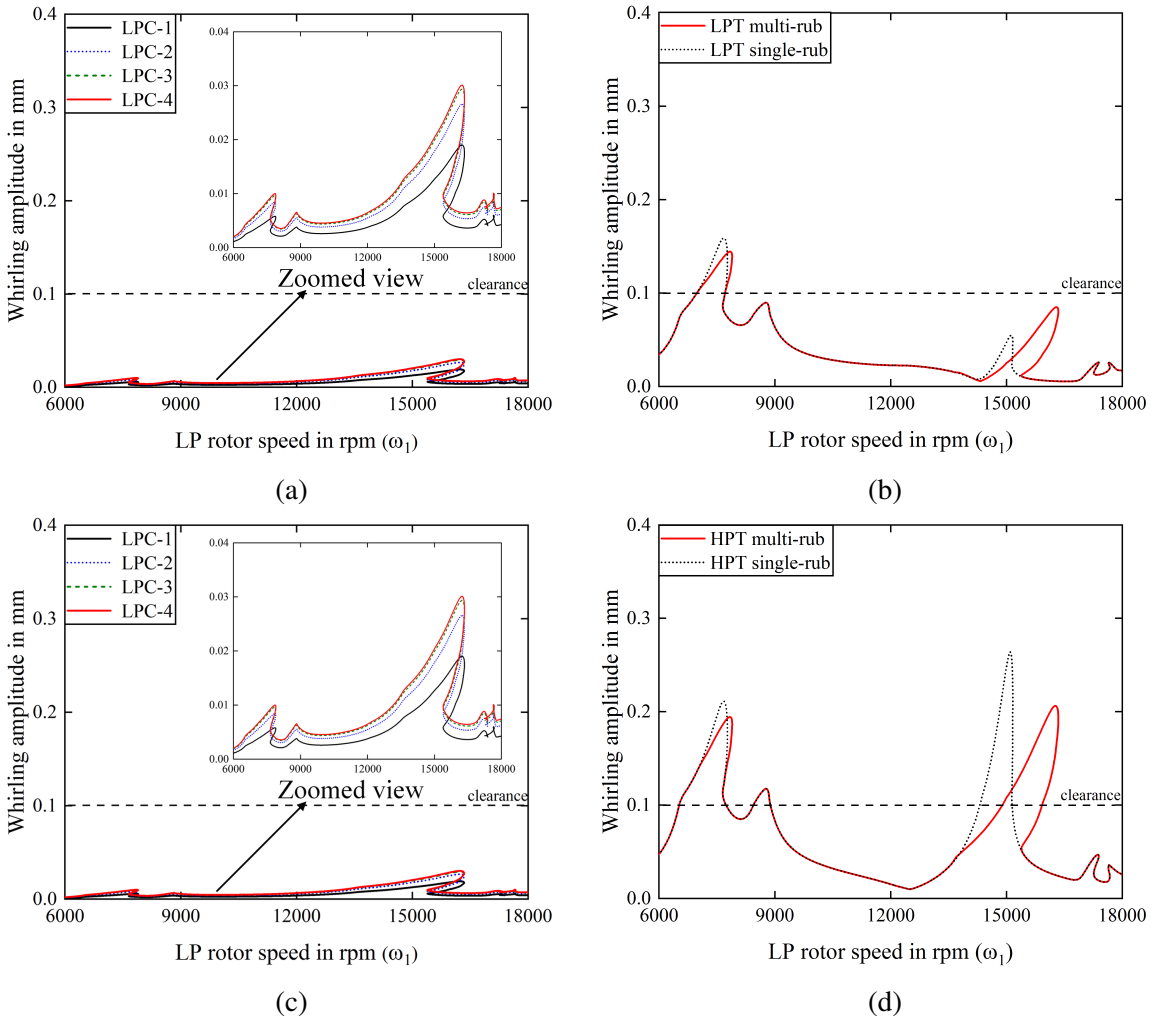


Fig. 5.10 Frequency response diagram calculated at (a) LPC (b) LPT (c) HPC and (d) HPT positions when the multi-disk rub-impact is analyzed. The extend of rightward bending is increased for multi-disk rub-impact since more disks undergo rub-impact simultaneously.

function at a speed of 7836 rpm. The nonlinearities of HPT, LPT, HPC-9 and HPC-8 have nonzero values, as shown in Fig. 5.11c.

For the second resonance peak, the initial contact has happened at 8443 rpm. The HPT disk started the contact, and it alone rubs the stator in the whole frequency range of 8443-8890 rpm, which is verified by checking the nonlinear function at a speed of 8600 rpm, as shown in Fig. 5.11d. Within this speed range, both the single and multi-disk rub-impact responses coincide with each other. During the third resonance peak, the HPC-9 disk initiated the contact at a speed of 13574 rpm, followed by the HPC-8 disk at 13600 rpm. Later on, all the HPC disks start to contact the stator one by one. Beyond 14897 rpm, the HPT disk as well begins to rub the stator along with the HPC disks. It can be validated by checking

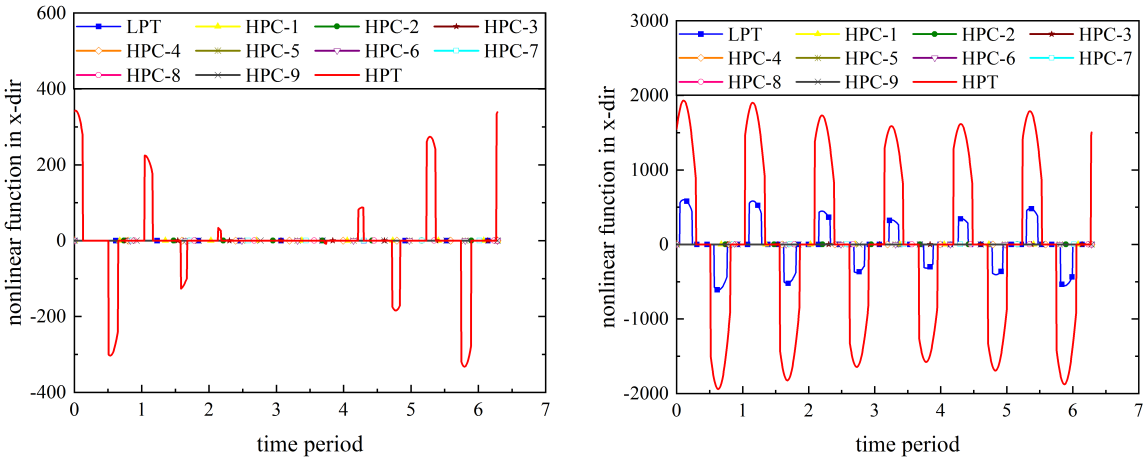


(a) Speed = 6640 rpm




(b) Speed = 7350 rpm

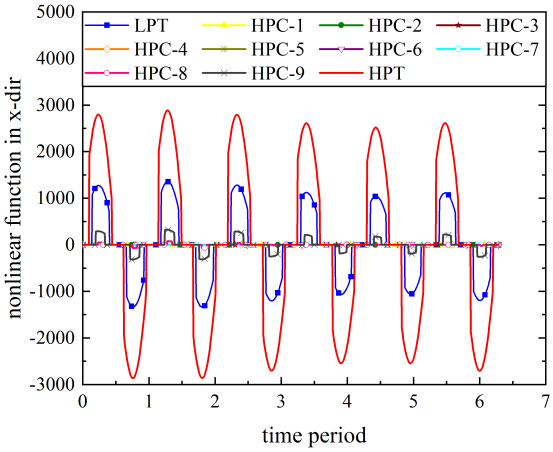


(c) Speed = 7836 rpm

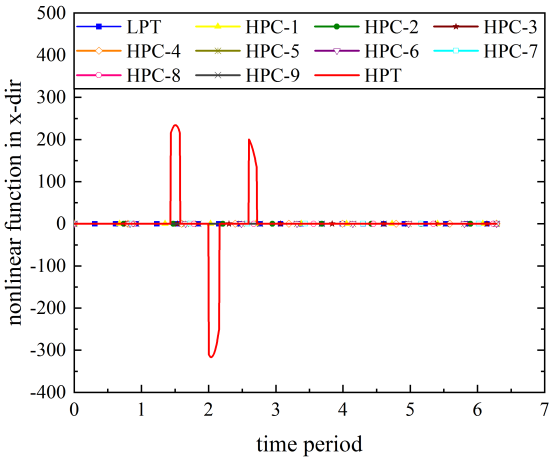


(d) Speed = 8600 rpm

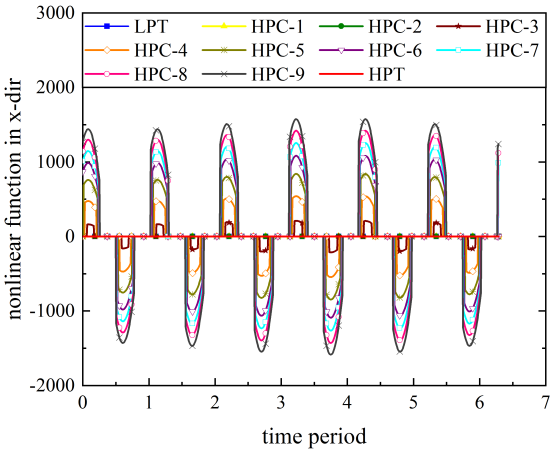


(e) Speed = 14852 rpm

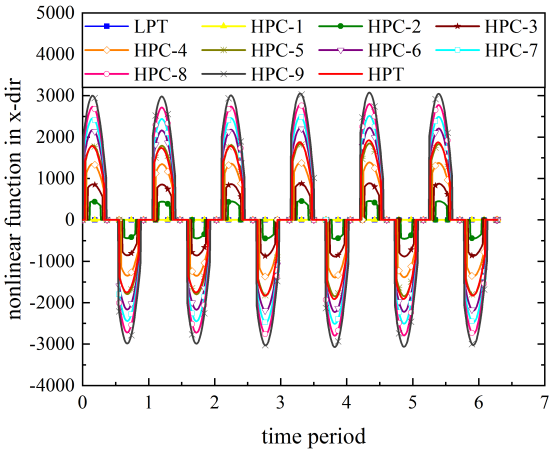


(f) Speed = 15717 rpm

Fig. 5.11 Rub-impact nonlinearity in X-direction ($f_{nx}$) at different rotating speeds for identifying the sequence of disk's rub.

Fig. 5.11e & 5.11f. In order to find the time lag between the different disks during contact, time response plots are obtained in the X direction as shown in Fig. 5.12. They are plotted between the two extreme disks undergoing rub-impact. Figure 5.12a gives the time lag between HPC-9 & LPT disks measured at a speed of 7680 rpm. The time lag is obtained as 0.0485 milliseconds which is equal to an angular deviation of 2.23 degrees. At 16110 rpm, the time lag is measured as 0.054 milliseconds which is equal to an angular deviation of 5.216 degrees between the HPC-2 & HPT disks. Hence, it can be noted that at any particular rotating speed, the disks start contacting the stator one by one with certain angular deviations to each other.

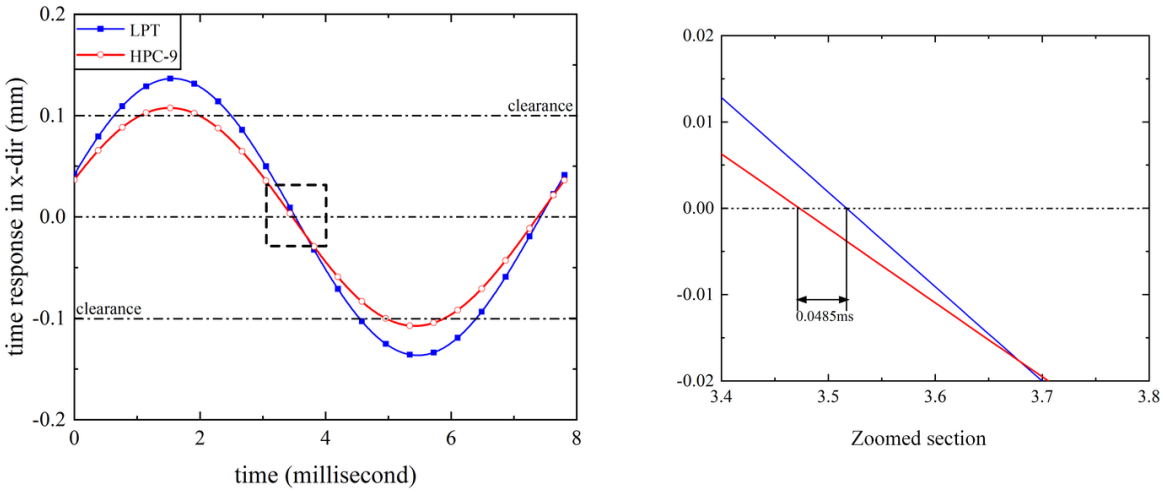


(a) X-dir response at speed = 7680 rpm

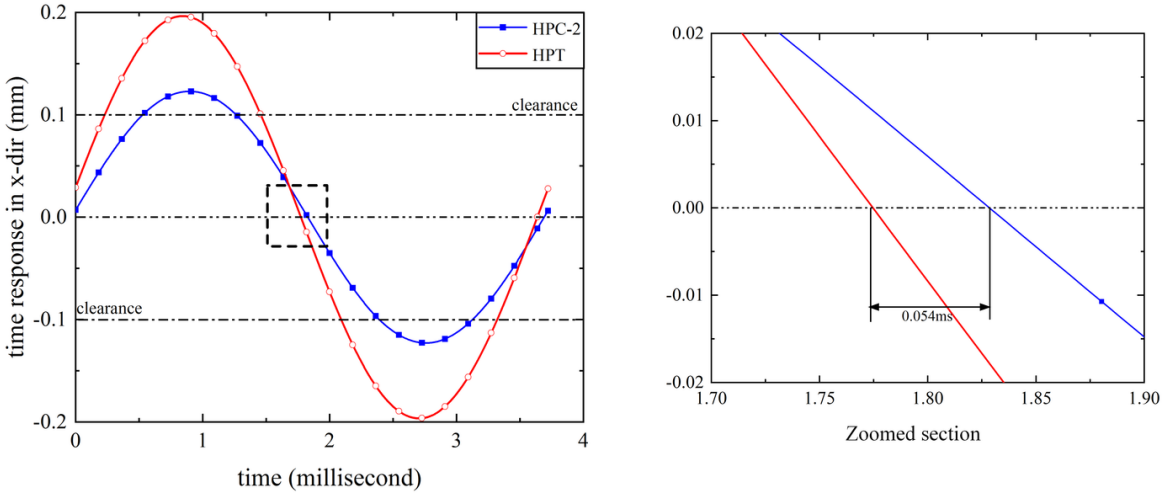


(b) X-dir response at speed = 16110 rpm

Fig. 5.12 Time response plot in X direction for finding the time lag between different disks.

Whenever, new disk contacts the stator, the extend of rightward bending is increased, and it is reflected in the responses of other disks also as shown in Fig. 5.10. In addition,

the deflections of rotors are significantly reduced due to the constraint effect of the stators. However, the deflection of the LPT disk is slowly exceeding the no-rub deflection during the third resonance peak, indicating that the dynamics of the LPT disk are significantly affected by the rub-impact at the HPC disks. These observations prove the importance of multi-disk rub-impact studies in dual-rotor models.

### 5.3.2 Stability of aero-engine model during multi-disk rub-impact

The stability of the system is analyzed using the Floquet theory as described in Sec. 2.2.4. Figure 5.13 shows the stability diagrams of the single and multi-disk rub-impact problems calculated at HPC-7 compressor position. It is found that for the multi-disk rub-impact

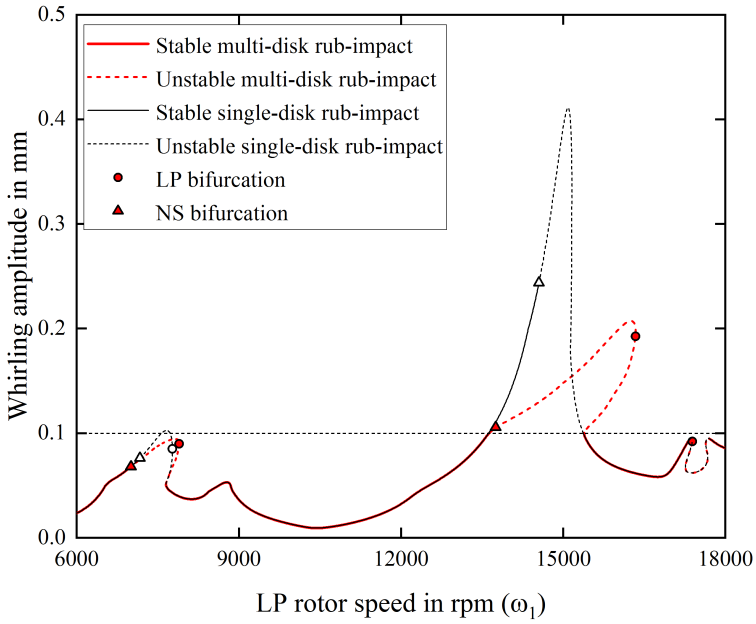


Fig. 5.13 Stability diagram calculated at HPC-7 compressor position during single and multi-disk rub-impact problems, obtained for the same set of system parameters. Stable responses are shown by a continuous line, while the dashed line shows the unstable part. The NS and LP bifurcations are indicated by triangle and circle markers, respectively.

problem, the response is stable till 7010 rpm, and then, it is subjected to the NS bifurcation. However, for the single-disk rub-impact problem, the response becomes unstable through the NS bifurcation at a speed of 7140 rpm. It means that the stable periodic response is changed into the unstable part so early due to the multi-disk rub-impact. Beyond the NS bifurcation point, the periodic response is unstable and is determined using the parametric continuation. A dashed line indicates the unstable response in Fig. 5.13.

Later, an LP bifurcation is observed at 7895 rpm, which is denoted by a circle marker in Fig. 5.13. The next rub-impact happens in the speed range of 8443-8890 rpm. During this period, the HPT disk alone undergoes contact. While analyzing the stability, it is found that the rubbing response is stable within this speed range, and no NS and LP bifurcations are observed. Moreover, the nature of stability is similar for both the single and multi-disk rub-impact problems. In the case of the third resonance peak, the NS bifurcation has happened at 13750 rpm for the multi-disk rub-impact problem, while it occurred at 14540 rpm for the single-disk rub-impact problem. It again proves that the multi-disk rub-impact results in an early loss of stability than the single-disk rub-impact problem.

### 5.3.3 Verification with numerical integration

To verify the results obtained using the ATVM, they are compared with the outputs of numerical integration. It is shown in Fig. 5.14. The responses at stable regimes are only compared and are found perfectly matching.

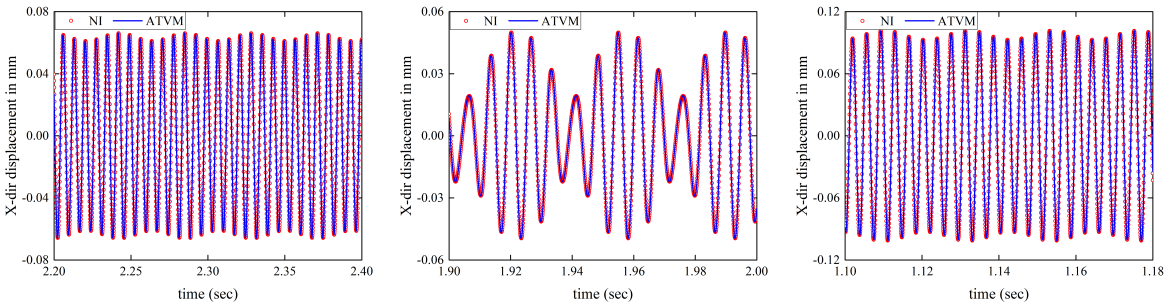


(a) (b) (c)

Fig. 5.14 X-dir displacements calculated at HPC-7 disk position when the rotor speed is (a) 6960 rpm, (b) 8630 rpm, and (c) 13660 rpm under multi-disk rub-impact using the ATVM and numerical integration.

Later, the orbit plots and Poincaré maps of the HPC-7 disk are analyzed at different speeds for verifying the existence of the NS bifurcation. They are shown in Fig. 5.15. It is seen that a period-5 motion is noticed in the response before the NS bifurcation, representing the stable response. During this motion, the orbit is fully circular, and the rotors undergo full annular rub as shown in Fig. 5.15a. Beyond the NS bifurcation point, the orbit plots and Poincaré maps are obtained using numerical integration. It is observed that the motion is completely quasi-periodic, indicated by the closed curves in the Poincaré maps. During this motion, the rotors bounce inside the stator. Thus, the detection of the NS bifurcation using the proposed method is verified using numerical integration.

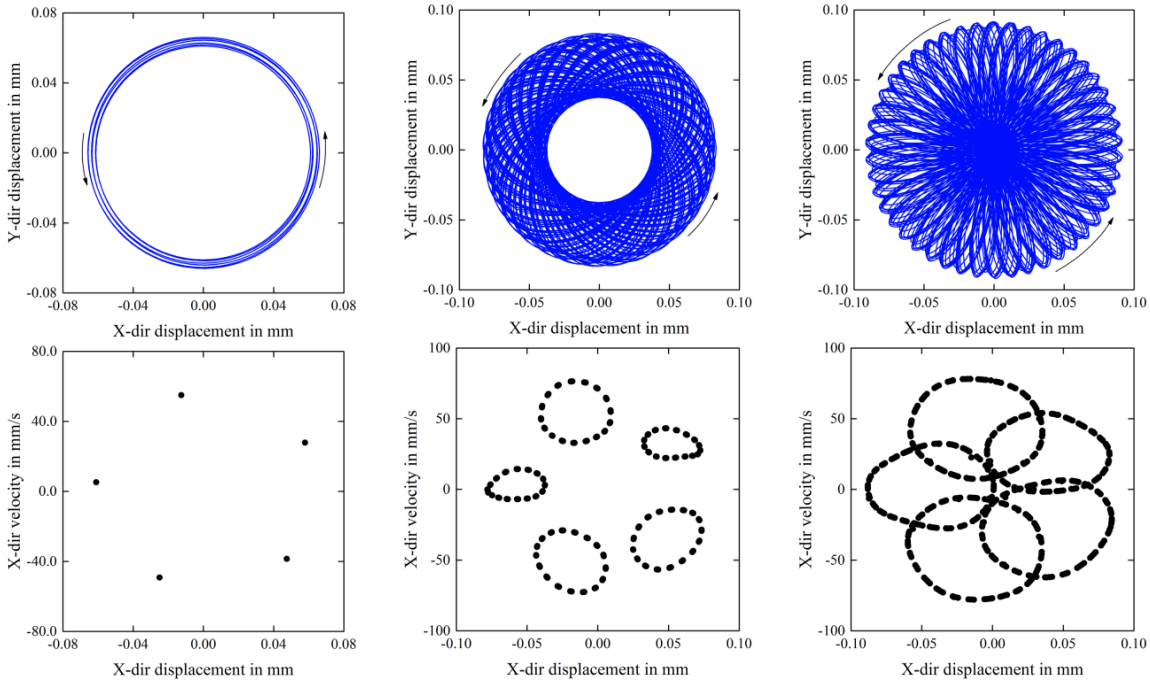


Fig. 5.15 Orbit plots and Poincaré maps calculated at HPC-7 disk position during multi-disk rub-impact when the rotor speed is (a) 6960 rpm, (b) 7150 rpm, and (c) 7390 rpm. Before the NS bifurcation, the response is period-5 motion indicated by five points in the Poincaré map. After the NS bifurcation, the response is quasi-periodic in nature, indicated by the closed curves in the Poincaré map.

In order to find out the frequency contents in the rub-impact response, the FFT spectra of the X-dir displacements are plotted for different values of the rotational speeds as shown in Fig. 5.16. When the rotor is undergoing synchronous full annular rub, the frequency components such as (1,-2), (2,-1), (2,-3), and (3,-2) appear in the response. They are the linear combinations of the excitation frequency components (1,0) and (0,1). However, when the response becomes quasi-periodic, some unknown fractional frequency components such as $0.716\omega_1$, $0.766\omega_1$, $0.916\omega_1$ and $0.964\omega_1$ are coming in the response, and the proposed ATVM technique can't detect them. Moreover, the dry friction backward whirl is observed beyond 14450 rpm, and it continues to exist as the rotating speed increases. The orbit plots and FFT spectra of the model during the dry friction backward whirl are shown in Fig. 5.17. The rotors are orbiting in the clockwise direction, which is opposite to the rotor spin direction; hence it is said to be a backward whirl. The amplitude of whirling is of the order of 2, which is very large, causing the destruction of the rotor system. From the FFT spectra, it is noticed that a superharmonic frequency component is alone appearing in the model.

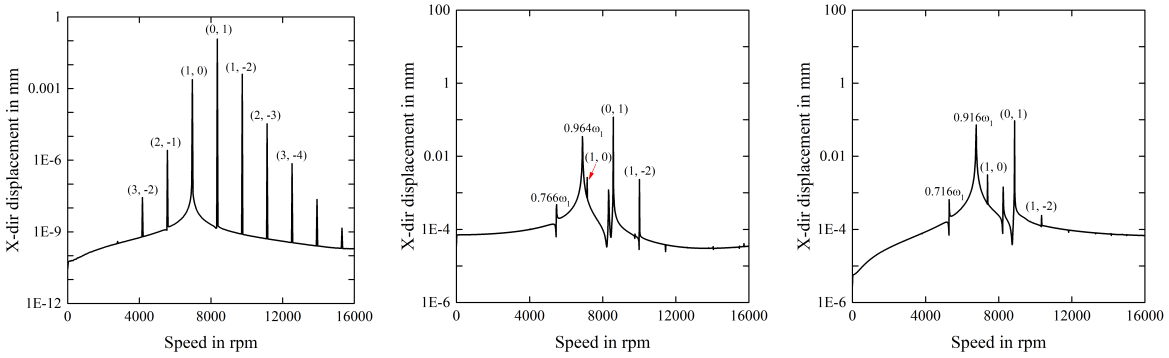


(a) (b) (c)

Fig. 5.16 The FFT spectra of the X-dir displacements calculated at HPC-7 disk position when the rub-impact has happened for different rotational speeds of (a) 6960 rpm, (b) 7150 rpm, and (c) 7390 rpm. For the full annular rub response, the frequency components are the linear combinations of the excitation frequencies, while for the quasi-periodic response, some unknown components are coming in the response.

## 5.4 Parametric analysis

It is obvious that the response of the rotor will vary according to the rubbing parameters, such as the coefficient of friction and contact stiffness. A parametric analysis needs to be conducted to understand their effects on the model dynamics. It helps to analyze the variations in the response characteristics and the stability when a parameter is altered. Generally, the parametric analysis is performed by varying a parameter while keeping the others constant. This understanding will assist the designers in selecting the suitable parameters of the model such that undesirable working conditions are avoided.

### 5.4.1 Effect of coefficient of friction

Figure 5.18 shows the variations in the model response when the friction coefficient is varied. The contact stiffness is assumed as a constant, and its value is taken as $k_c = 0.5\times10^8 N/m$ for the analysis.

It is found that the amplitude of rightward bending is shortened as the value of $\mu$ is increased. This is because the increased friction offers resistance to the whirling, thereby reducing its amplitude. While analyzing the stability of the response, it is found that for lower values of $\mu$ ($0 \leq \mu \leq 0.05$), no NS bifurcation is observed, and the complete response contains period-5 vibrations. However, as the friction coefficient increases, the model loses its stability through the NS bifurcation. For $\mu = 0.1$, the NS bifurcation happened at 7740

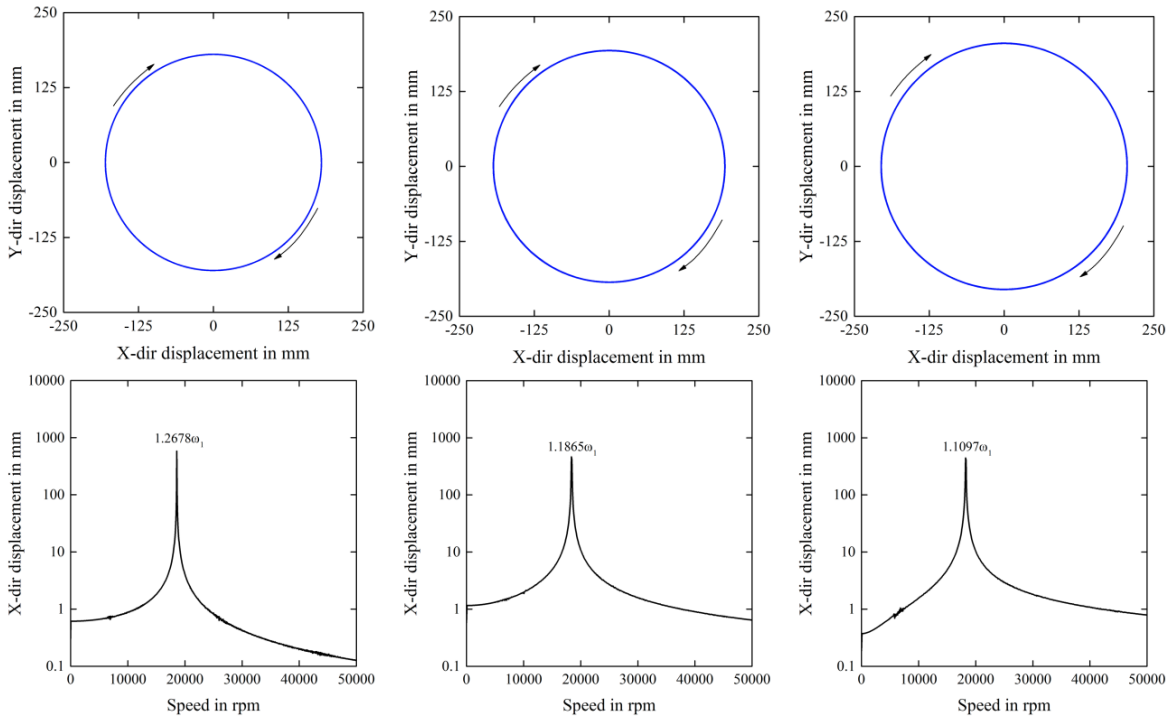


Fig. 5.17 The orbit plot and FFT spectra of the dual-rotor during the dry friction backward whirl at a rotating speed of (a) 14640 rpm, (b) 15550 rpm, and (c) 16410 rpm. The rotors are whirling in clockwise which is opposite to the direction of rotation. A superharmonic frequency component is noticed in the response while analyzing the FFT spectra.

rpm, whereas it occurred at 6615 rpm for $\mu = 0.5$. It indicates that the NS bifurcation is happening early for large values of $\mu$. An arrow mark indicates it in Fig. 5.18. As a result, the model enters into the quasi-periodic regime fastly as the friction coefficient increases, and the rotors will be bouncing inside the stator for a longer duration. It may destroy the rotor and stator surfaces. It is also noticed that there is no NS bifurcation observed for the second rub-impact peak, even for large values of $\mu$.

### 5.4.2 Effect of contact stiffness

Figure 5.19 shows the variations in the model response when the contact stiffness is altered. In this analysis, the coefficient of friction is assumed as a constant, and its value is taken as $\mu = 0.2$.

It is noticed that as the value of contact stiffness increases, the extent of rightward bending also increases. This is due to the modifications in the model stiffness when the value of $k_c$ is

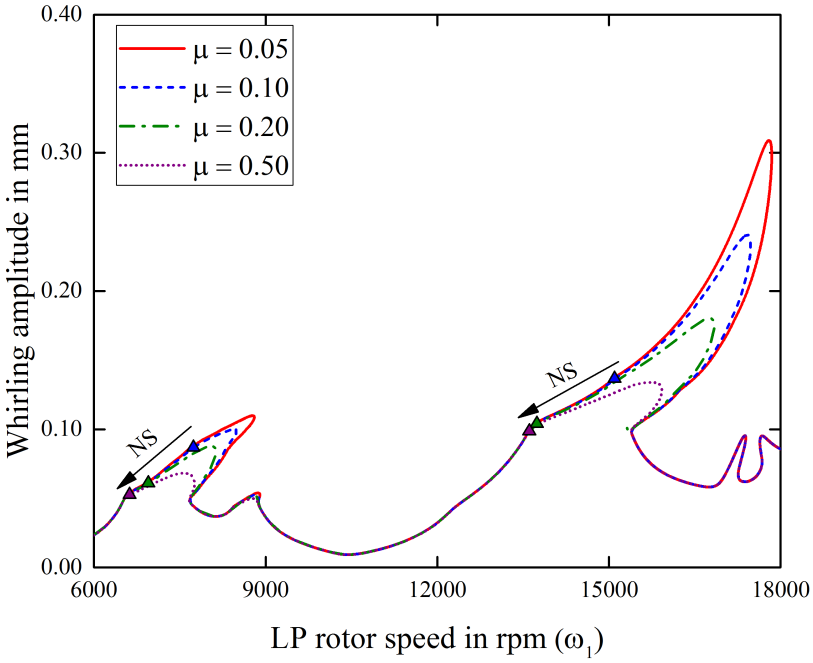


Fig. 5.18 Variations in the response when the coefficient of friction is increased. The amplitude of rightward bending is shortened as the value of $\mu$ increases. No NS bifurcation is observed for lower values of $\mu$ ($0 \leq \mu \leq 0.05$), and the complete response contains period-5 vibrations. As the friction coefficient increases, the model loses its stability through the NS bifurcation, and it happens early for large values of $\mu$. An arrow mark indicates it.

increased. In addition, the amplitude of whirling decreases for higher values of the contact stiffness. It indicates that the whirling of the rotor is prevented by the stator when its stiffness is increased. During the stability analysis, it is found that the response is completely periodic for smaller values of the contact stiffness (for $k_c < 0.1 \times 10^8$ N/m), and a period-5 motion is observed throughout the response. As the value of $k_c$ increases, the occurrence of the NS bifurcation is noticed. It happens at a speed of 7010 rpm for $k_c = 0.3 \times 10^8$ N/m and it occurs at 6810 rpm for $k_c = 0.9 \times 10^8$ N/m. It indicates that the NS bifurcation takes place early for larger values of the contact stiffness. Similar to the coefficient of friction, there is no NS bifurcation observed in the second rub-impact peak, even for large values of the contact stiffness.

## 5.5 Summary

In this chapter, the dynamic characteristics of an aero-engine under multi-disk rub-impact is investigated using a dual-rotor model consisting of multi-stage compressors and single-stage turbines. The rub nonlinearity is applied at all the disk positions, and it appears

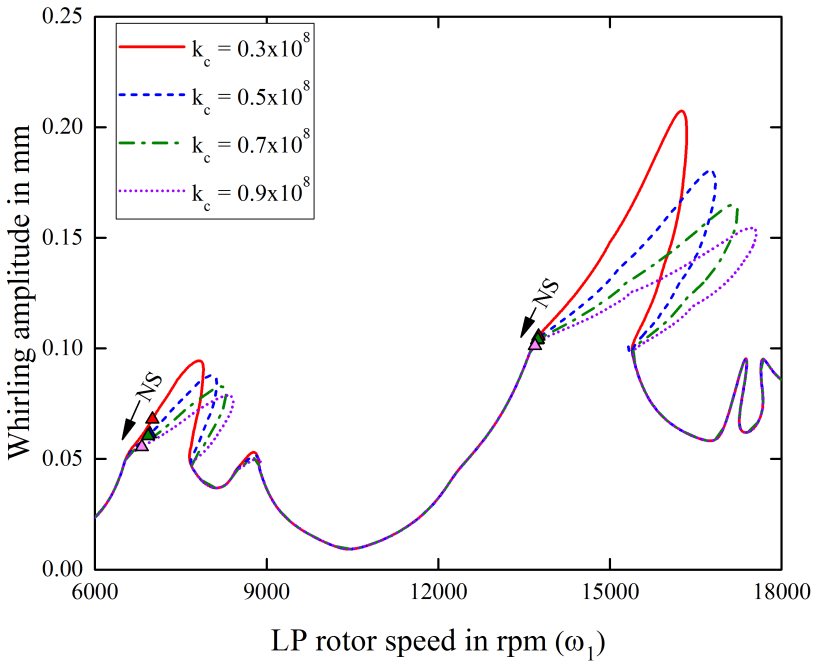


Fig. 5.19 Variations in the response when the contact stiffness is increased. The extent of rightward bending increases as the value of contact stiffness increases. The amplitude of whirling is decreasing for higher values of the contact stiffness. The response is completely periodic for smaller values of the contact stiffness. As the value of $k_c$ is increased, the occurrence of the NS bifurcation is noticed, and it happens early for larger values of the contact stiffness.

whenever the disks exceed the clearance space. The dual-rotor system is modelled using the tapered Timoshenko beam elements, rigid disks, and linear bearings. The total size of the FE model is reduced using the component mode synthesis method, based on the Craig-Bampton substructuring. The steady-state response of the model is calculated using the approximated time variational method by taking the discrete-time points $N_{pt}$ as 180. A hypersphere-based continuation technique is incorporated with ATVM to trace the unstable branches beyond bifurcation points. The model stability is determined by perturbing them from the equilibrium positions and monitoring the real parts of their eigenvalues. The effects of the rub parameters such as friction coefficient and contact stiffness are also investigated by performing a parametric analysis.

From the rub-impact analysis, it is observed that the model response is significantly affected by the multi-disk rub-impact. The total stiffness of the model is increased when more than two disks contact the stator simultaneously. It resulted in an increased rightward bending of the response compared to the single-disk rub-impact problem. The amplitude of whirling is also decreased due to the constraint effects of the casing. The bifurcations such

as the LP and NS bifurcations are observed in the response, indicating a sudden jump and the origin of a quasi-periodic branch, respectively. The responses such as full annular rub and partial rub are identified by analyzing the orbit plots and the Poincaré maps. Mainly, a period-5 motion is observed before the NS bifurcation, while a quasi-periodic motion is noticed after the NS bifurcation. During quasi-periodic motion, some unknown fractional components such as $0.716\omega_1$, $0.766\omega_1$, $0.916\omega_1$ and $0.964\omega_1$ are appeared in the response. Beyond the quasi-periodic regime, the model enters into the dry friction backward whirl in which the rotors orbit backwards with a huge amplitude. It is the most violent motion of the rotor, and it happens at a superharmonic frequency. The results are verified using numerical integration, and a good agreement is obtained. While performing the parametric analysis, it is found that the amplitude of forward-leaning is shortened, and the onset of NS bifurcation is happening early as the value of the coefficient of friction is increased. It happened mainly due to the increased friction resistance that intensified the nonlinearities in the model. Similarly, when the contact stiffness increases, the extent of forward-leaning increases, and the onset of NS bifurcation is happening early.

In the proposed dual-rotor model, the fan and the squeeze film dampers (SFD) aren't included. However, in an actual aero-engine, a heavy bypass ratio fan and SFDs are present at the front of the low-pressure compressor. The presence of such components completely changes the dynamics of the system. Hence, the influence of a heavy fan disk and the SFDs are discussed in the following chapter.

# Chapter 6

# The influence of squeeze film damper on rub-impact

This chapter is mainly intended to study the influence of squeeze film damper (SFD) on the rubbing response of an aero-engine dual-rotor model mounted on nonlinear bearing supports. The SFD is a device mainly employed to reduce the amplitude of vibrations in the aircraft rotor models. It is achieved by supplying a fluid film between the bearing and housing, thereby acquiring enough damping in the bearing support. The effects of SFD on the multi-disk rub-impact in aero-engines aren't studied so far; hence, it is the contribution of this work. For performing the numerical study, the dual-rotor models described in Chapters 4 & 5 have been modified by incorporating a heavy fan disk and nonlinear bearing support at specific locations of the model. The nonlinear bearing support includes rolling contact bearings, squirrel-cage elastic support, and squeeze film damper arrangements. Due to the presence of heavy fan disk and the SFD, the dynamics of both the models can be completely altered as compared to those described in Chapters 4 & 5. It is explained in detail as follows.

## 6.1 Dynamic modelling of nonlinear bearing support

The nonlinear bearing support generates ball bearing forces due to the Hertzian contact and SFD forces due to the wedging of the oil ($\mathbf{F}_{nl} = \mathbf{F}_{ball} + \mathbf{F}_{sfd}$). The details of rolling bearings are discussed in the previous chapter and the formulation of SFD is explained as follows.

### 6.1.1 Squeeze film damper model

A schematic diagram of the SFD arrangement is shown in Fig. 6.1. The rotating shaft and the ball bearing together constitute the damper's journal, and it whirls inside the SFD during

its motion. Meantime, the rotation of the ball bearing's outer ring is prevented by connecting it to the squirrel-cage elastic support. During the whirling motion, the oil is squeezed inside the annular clearance to produce radial and tangential oil film forces. They are derived from Reynold's equation based on short bearing approximation.

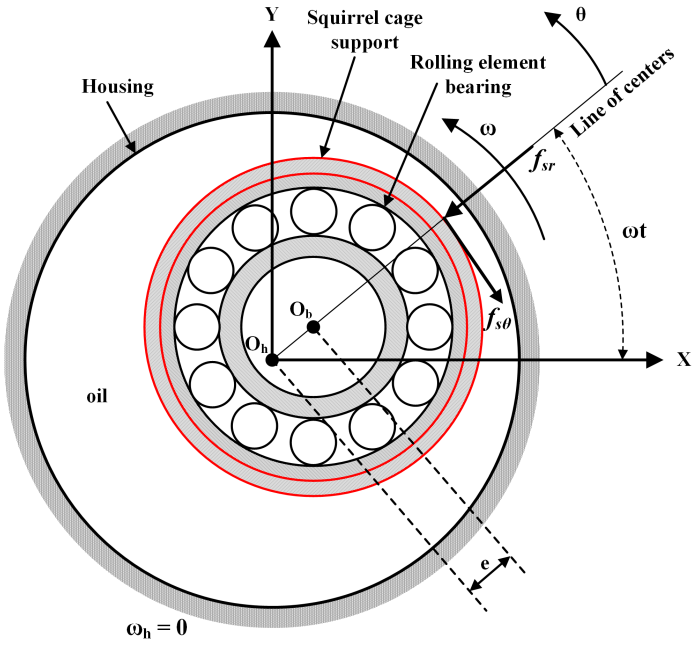


Fig. 6.1 Schematic diagram of the SFD arrangement including journal, squirrel-cage elastic support, and housing.

The pressure distribution inside a cavitated oil film is written in rotating coordinates (Chen et al. (2020)) as,

$$P(\theta,z) = \frac{6\eta}{c^2}\left(z^2 - \frac{L^2}{4}\right)\frac{(\varepsilon\omega\sin\theta + \dot{\varepsilon}\cos\theta)}{(1+\varepsilon\cos\theta)^3} \tag{6.1}$$

where $\varepsilon$ and $\dot{\varepsilon}$ are the eccentricity ratio ($\varepsilon = e/c$) and its first derivative respectively. Now, the force components in radial and tangential direction can be written as,

$$\begin{Bmatrix} f_{sr} \\ f_{s\theta} \end{Bmatrix} = -\int_{\theta_1}^{\theta_1+\pi}\int_0^L P(\theta,z)R\begin{Bmatrix} \cos\theta \\ \sin\theta \end{Bmatrix} dzd\theta \tag{6.2}$$

By expanding the Eq. 6.2, the radial and tangential force components can be rewritten as,

$$f_{sr} = -\frac{\eta RL^3}{c^2}[I_1\dot{\varepsilon} + I_2\varepsilon\omega] \qquad f_{s\theta} = -\frac{\eta RL^3}{c^2}[I_2\dot{\varepsilon} + I_3\varepsilon\omega] \tag{6.3}$$

where,

$$
\begin{aligned}
I_1 &= \int_{\theta_1}^{\theta_1+\pi} \frac{\cos^2\theta}{(1+\varepsilon\cos\theta)^3} d\theta \qquad & I_2 &= \int_{\theta_1}^{\theta_1+\pi} \frac{\sin\theta\cos\theta}{(1+\varepsilon\cos\theta)^3} d\theta \\
I_3 &= \int_{\theta_1}^{\theta_1+\pi} \frac{\sin^2\theta}{(1+\varepsilon\cos\theta)^3} d\theta \qquad & \theta_1 &= \tan^{-1}\left(-\frac{\dot{\varepsilon}}{\varepsilon\omega}\right)
\end{aligned}
\tag{6.4}
$$

The integrals $I_1$, $I_2$ and $I_3$ can be determined analytically by taking the integral interval as $[\pi, 2\pi]$. Finally, the nonlinear oil film forces in radial and tangential direction can be expanded as (Inayat-Hussain (2009)),

$$
\begin{aligned}
f_{sr} &= \frac{\eta R L^3}{c^2}\left[\frac{\pi\dot{\varepsilon}(1+2\varepsilon^2)}{2(1-\varepsilon^2)^{5/2}} + \frac{2\omega\varepsilon^2}{(1-\varepsilon^2)^2}\right] \\
f_{s\theta} &= \frac{\eta R L^3}{c^2}\left[\frac{2\varepsilon\dot{\varepsilon}}{(1-\varepsilon^2)^2} + \frac{\pi\omega\varepsilon}{2(1-\varepsilon^2)^{3/2}}\right]
\end{aligned}
\tag{6.5}
$$

For the numerical analysis, the radial and tangential squeeze film forces are transformed into the Cartesian coordinate system as,

$$
\begin{Bmatrix} f_{sx} \\ f_{sy} \end{Bmatrix} = \begin{bmatrix} \cos\theta & -\sin\theta \\ \sin\theta & \cos\theta \end{bmatrix} \begin{Bmatrix} f_{sr} \\ f_{s\theta} \end{Bmatrix} \tag{6.6}
$$

The oil-film force vector $\mathbf{F}_{sfd}$ is formed by inserting $f_{sx}$ and $f_{sy}$ in the respective positions corresponding to the SFD location. In this study, two dual-rotor models are utilized to investigate the influence of SFD on the rub-impact responses. They are explained in detail as follows.

## 6.2 Simplified dual-rotor with overhung fan and SFD

The simplified dual-rotor model described in Chapter 4 has been modified by attaching an overhung fan at the front of disk 1 and incorporating an SFD near the fan disk as shown in Fig. 6.2. Both the rotors are supported on ball bearings except the inter-shaft bearing, which is assumed as a linear spring-damper model. The SFD is incorporated with bearing 1 since the deflection of the rotor at the bearing 1 location may be significant due to the heavy unbalanced forces in the fan. The physical parameters of the fan disk, ball bearings and SFD are listed in Tab. 6.1-6.3. A Rayleigh damping is also accommodated in the model with its parameters as listed in Tab. 6.1.

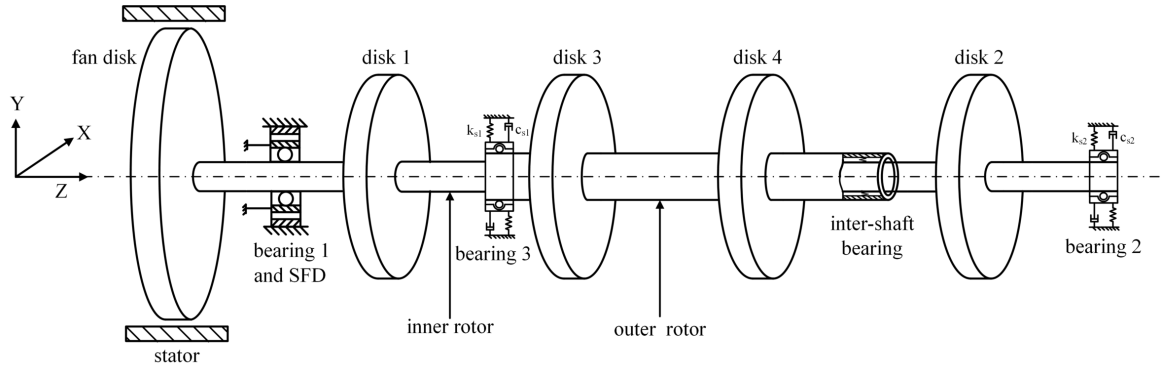


Fig. 6.2 Schematic diagram of a simplified dual-rotor model consisting of an overhung fan and SFD arrangement.

Table 6.1 Physical properties of the fan disk and elastic support

| Physical property | Value |
|---|---|
| Mass of fan disk (kg) | 16.2 |
| Diametral moment of inertia of fan disk (kg.m$^2$) | 0.255 |
| Polar moment of inertia of fan disk (kg.m$^2$) | 0.509 |
| Rayleigh Damping Coeff. (Mass) | 11.63 |
| Rayleigh Damping Coeff. (Stiffness) | 2.55e-6 |
| Elastic support stiffness $k_{s1}$ (N/m) | 36e6 |
| Elastic support damping $c_{s1}$ (Ns/m) | 100 |
| Elastic support stiffness $k_{s2}$ (N/m) | 36e6 |
| Elastic support damping $c_{s2}$ (Ns/m) | 100 |
| Mass unbalance in fan disk (kgm) | 4e-5 |
| Mass unbalance in disk 3 (kgm) | 6e-5 |

Table 6.2 Parameters used in the ball bearing models

| Bearing order | $R_b$ (mm) | $r_b$ (mm) | $N_b$ | $C_b$ (N/m$^{\frac{3}{2}}$) | $c_0$ ($\mu$m) |
|---|---|---|---|---|---|
| Bearing 1 | 22.746 | 15.246 | 18 | 6.58e8 | 10 |
| Bearing 2 | 22.746 | 15.246 | 33 | 13.25e8 | 12 |
| Bearing 3 | 31.196 | 30.126 | 24 | 11.58e8 | 16 |

Table 6.3 Parameters of the SFD used in the modified dual-rotor model

| Parameter | Description | Value |
|---|---|---|
| R (mm) | Journal radius | 22.746 |
| L(mm) | Width of damper | 11.000 |
| c (mm) | Clearance | 0.1 |
| $\eta$ (Pa.s) | Viscosity | 5.66e-3 |
| $K_a$ (N/m) | Squirrel-cage stiffness | 52e6 |

Initially, the mode shapes and Campbell diagrams of the modified dual-rotor model are determined. The first two mode shapes are shown in Fig. 6.3 in which the first mode represents the pitching vibration of the fan disk about the bearing 1 position. Fig. 6.4 shows the Campbell diagrams of the model when the speed ratio is 1.2. Due to the presence of overhanging fan disk, the gyroscopic effect becomes very significant. As a result, the separation between the forward and backward whirl frequencies is large compared to Fig. 4.4, especially for the first mode of vibration. It indicates that the dynamics of the dual-rotor model is remarkably altered by the addition of an overhanging fan disk.

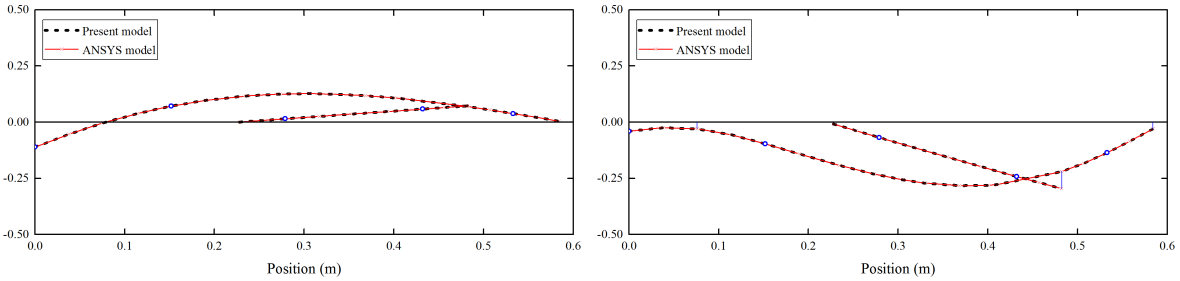


(a) (b)

Fig. 6.3 The first two mode shapes of the modified dual-rotor model at (a) 47.18 Hz and (b) 123.94 Hz.

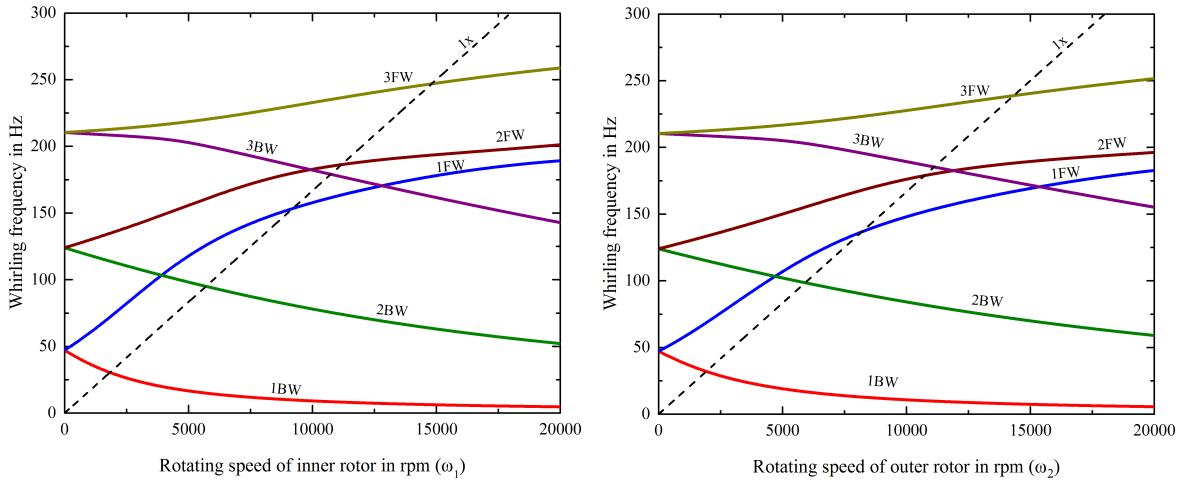


(a) excited by inner rotor (b) excited by outer rotor

Fig. 6.4 Campbell diagrams of the modified dual-rotor model

In order to understand the effects of SFD, a frequency response analysis is performed by applying mass unbalances at the fan and disk 3 locations. The magnitudes of unbalance forces are listed in Tab. 6.1. The analysis is performed using the numerical integration

technique. Figure 6.5 shows the comparison of rotor responses for different values of the SFD clearance and oil viscosity. Due to the presence of ball bearings, a jump-down phenomenon is noticed in the frequency response diagram. It is mainly due to the hard spring nature of the ball bearings. When an SFD has been introduced in the model significant reduction in the amplitude is happened. The percentage reduction in the amplitudes of model responses for different values of SFD parameters is listed in Tab. 6.4. It is noticed that as the value of the clearance decreases, the amplitude of the model response also decreases. In contrast, a reduction in the oil viscosity increases amplitude. It implies that an SFD with low clearance and moderately high oil viscosity can significantly reduce vibration amplitude. However, reducing the clearance below a certain value may result in contact nonlinearity, and increasing the viscosity above a particular value may result in locking. Hence, it is the designer's responsibility to calculate the optimum SFD parameters for the effective reduction of vibration.

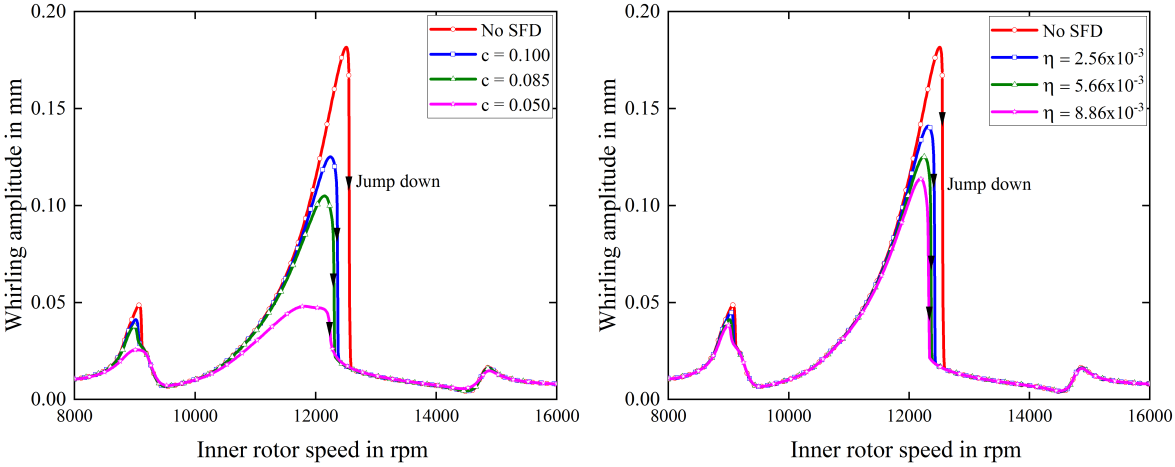


Fig. 6.5 Comparison of the unbalance responses of the modified dual-rotor model determined at fan disk location for different values of (a) SFD clearance and (b) oil viscosity.

Table 6.4 Percentage reduction in the amplitudes compared to no SFD response

| Parameter | SFD Clearance (mm) | | SFD oil viscosity (Pa.s) | | |
|---|---|---|---|---|---|
| | c = 0.10 | c = 0.05 | $\eta = 2.56 \times 10^{-3}$ | $\eta = 5.66 \times 10^{-3}$ | $\eta = 8.86 \times 10^{-3}$ |
| % of reduction | 31.12 | 73.57 | 22.37 | 31.12 | 37.46 |

### 6.2.1 Rub-impact response of dual-rotor in the presence of SFD

In order to study the influence of SFD on the rub-impact response, a stator is introduced at the fan disk location. When the deflection of the fan disk exceeds the clearance value, it contacts the stator. The value of rotor-stator contact stiffness, clearance and coefficient of friction are taken as $k_c = 0.3\times10^8$ N/m, $\delta = 0.1$ mm, $\mu = 0.01$. When the rotor-stator contact has happened, a forward-leaning of the response curve is observed due to the increase in the model stiffness. The analysis is carried out using numerical integration to obtain the nature of the rub-impact response. The graphs showing the comparison of rub-impact responses with respect to the SFD clearance and oil viscosity are given in Fig. 6.6. It shows the response at the fan location. The introduction of the SFD in the model made significant variations in the response. From Fig. 6.6, it is seen that by decreasing the clearance and by increasing the oil viscosity, the range of speed for which the rub-impact happens can be reduced remarkably. For low clearance and high viscosity, the jump-down phenomenon happens so early that the model shifts to no rub region fastly. This is the main advantage of incorporating the SFD into the model.

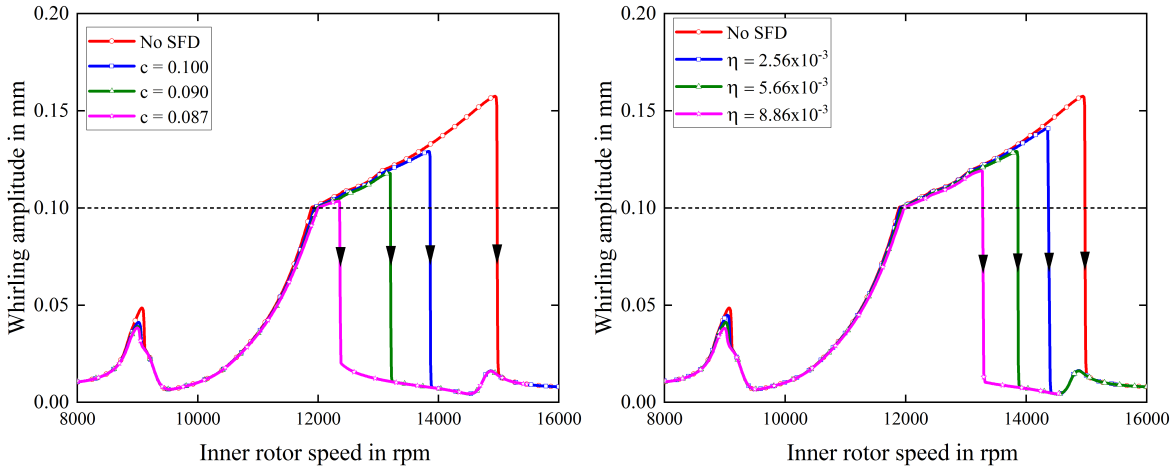


Fig. 6.6 Comparison of the model response during rub-impact for different values of (a) SFD clearance and (b) oil viscosity determined at the fan disk location; $k_c = 0.3\times10^8$ N/m, $\delta = 0.1$ mm, $\mu = 0.01$.

Figure 6.7 shows the variations in the response when the contact stiffness is altered. The values of SFD viscosity and clearance are taken as $\eta = 5.66\times10^{-3}$ Pa.s and c = 0.1 mm respectively. As observed earlier, the extend of rightward bending is increased as the value of contact stiffness is increased. For large values of $k_c$, some irregularities are noticed during a certain speed range. In order to understand more about them, the Poincaré maps and FFT

spectra are determined at different rotating speeds as shown in Fig. 6.8-6.9. The contact stiffness is taken as $k_c$ = 1.025 $\times 10^8$ N/m. A period-5 motion is noticed before the initial rub-impact, which is verified by checking the Poincaré map at a speed of 11800 rpm as shown in Fig. 6.8a. While observing the FFT spectrum, it is seen that in addition to the excitation frequency components, additional components such as (1, -2), (2, -1), (2, -3), (3, -2) and (4, -3) are also noticed in the response. This is mainly due to the presence of nonlinearity in the ball bearings.

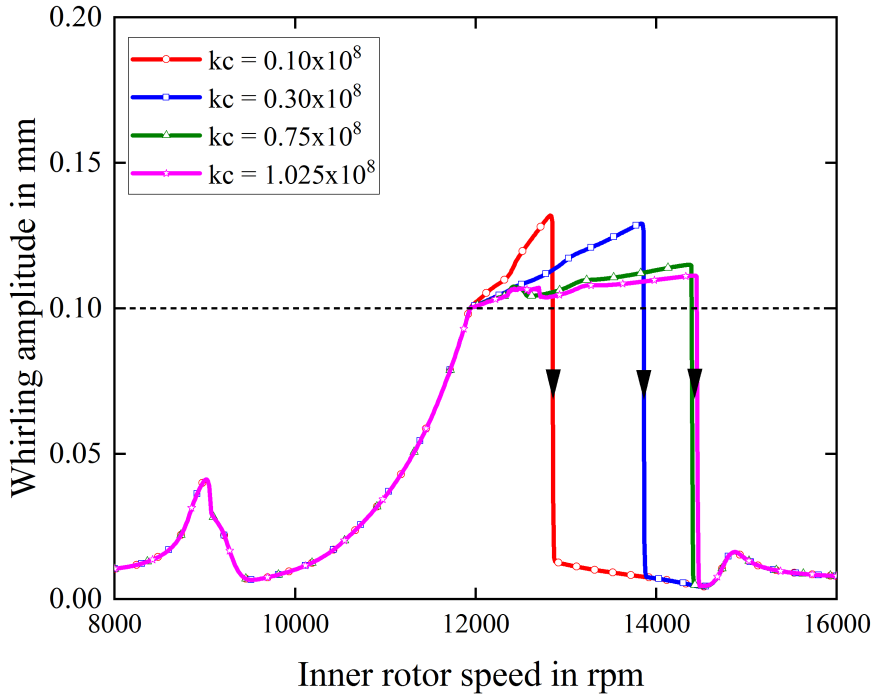


Fig. 6.7 Variations in the response when the contact stiffness is altered; $\eta$ = 5.66$\times 10^{-3}$ Pa.s, c = 0.1 mm

Once the contact has happened, a chaotic nature is observed in the speed range of 11940-12940 rpm that can be identified by looking at the Poincaré map and the FFT spectrum at 12100 rpm and 12600 rpm. The Poincaré map contains multiple scattered points, and the FFT diagram shows unknown frequency components, indicating the chaotic behaviour. Beyond 12940 rpm, a period-5 motion is again noticed in the spectrum, which can be verified from the Poincaré map at 13400 rpm and 14200 rpm. At 14410 rpm, a jump-down phenomenon has happened, and the motion is transferred to no rub region. While analyzing the FFT spectrum at 15500 rpm, it is seen that only excitation frequency components are coming in the response, indicating that the effects of ball bearings are negligible. When the SFD parameters are varied, there are no variations observed in the nature of the responses as

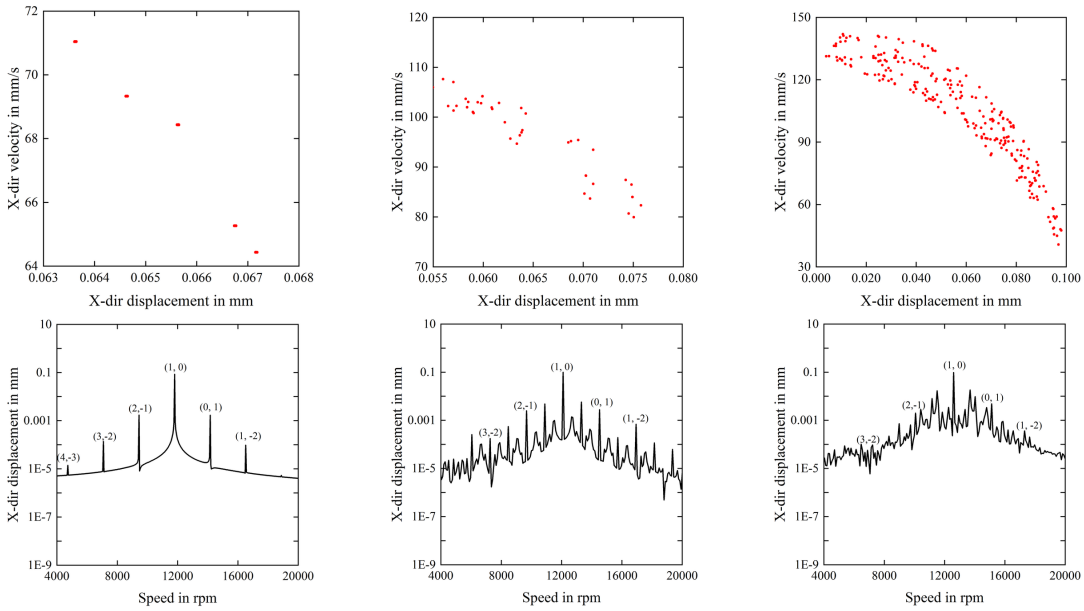


(a) (b) (c)

Fig. 6.8 Poincaré map and FFT spectrum of the model during rub-impact at a) 11800 rpm b) 12100 rpm and c) 12600 rpm, obtained using numerical integration; $k_c$ = 1.025 $\times 10^8$ N/m, $\eta$ = 5.66$\times 10^{-3}$ Pa.s, c = 0.1 mm

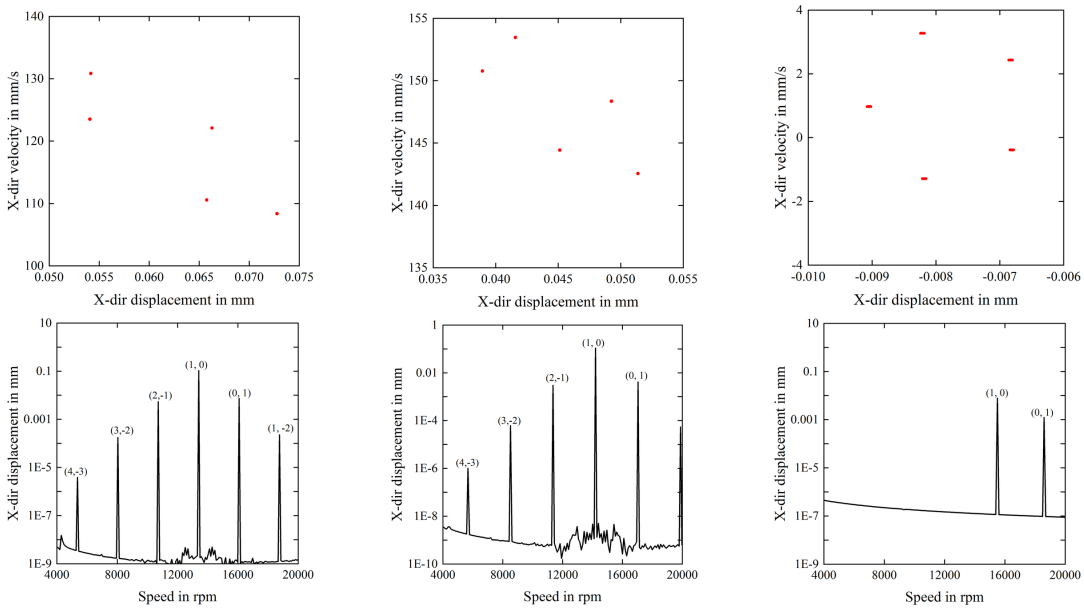


(a) (b) (c)

Fig. 6.9 Poincaré map and FFT spectrum of the model during rub-impact at a) 13400 rpm b) 14200 rpm and c) 15500 rpm, obtained using numerical integration; $k_c$ = 1.025 $\times 10^8$ N/m, $\eta$ = 5.66$\times 10^{-3}$ Pa.s, c = 0.1 mm

shown in Fig. 6.10. For all values of the SFD parameters, a period-5 motion is observed before the initial rub-impact, and a chaotic motion is noticed after the rub-impact. Later, the rotor undergoes a period-5 motion beyond a certain speed, and finally, a jump down happens to no-rub motion. As described earlier, the presence of SFD made the jump-down phenomenon early and reduced the speed range for which the rub-impact has happened.

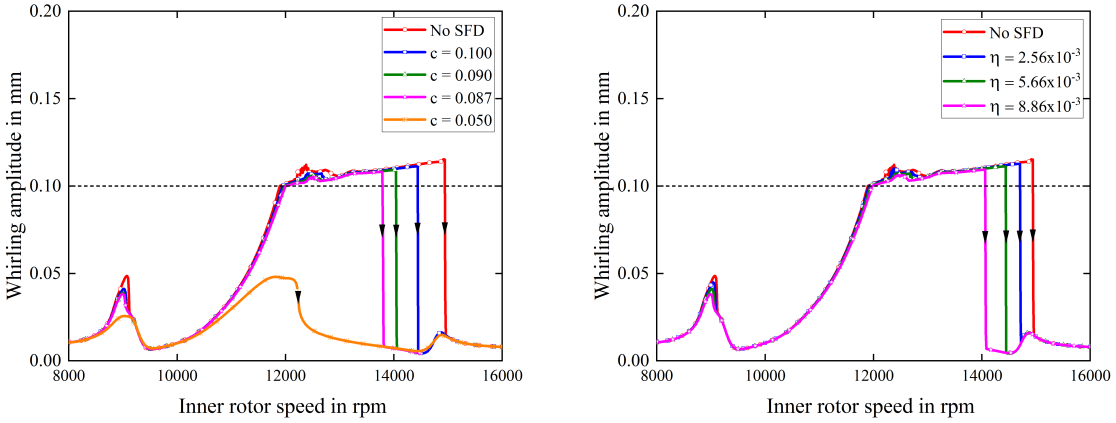


(a) (b)

Fig. 6.10 Comparison of the responses when contact stiffness is $k_c = 1.025 \times 10^8$ N/m for different values of (a) SFD clearance and (b) oil viscosity. Irregularities in the response are still there, even though the SFD parameters are altered.

## 6.3 Aero-engine model with an overhung fan and SFD

The aero-engine dual-rotor model described in Chapter 5 has been modified by adding a high bypass ratio fan at the front of the low-pressure compressor and an SFD at bearing 1 location. The schematic diagram of the modified aero-engine model is shown in Fig. 6.11. The parameters of the SFD are listed in Tab. 6.5 and the properties of fan disk are provided in Tab. A. The range of allowable eccentricities for which no rub happens is determined using the unbalance response analysis as $1.684 \times 10^{-3}$ kg m. Hence, in this work, the fan eccentricity is taken as $2.2642 \times 10^{-3}$ kg m to study the effects of rub-impact.

Table 6.5 Parameters of the SFD used in the modified aero-engine model

| Parameter | Description | Value |
|---|---|---|
| R (mm) | Journal radius | 59.314 |
| L(mm) | Width of damper | 28.7 |
| c (mm) | Clearance | 0.03 |
| $\eta$ (Pa.s) | Viscosity | 5.66e-3 |
| $K_a$ (N/m) | Squirrel-cage stiffness | 1.22e9 |

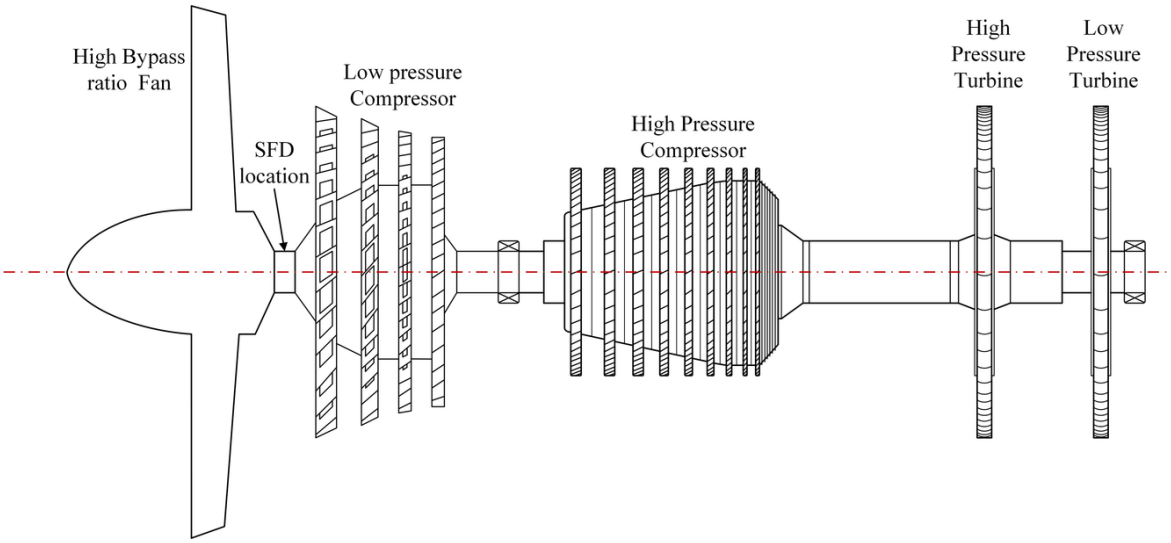


Fig. 6.11 Schematic diagram of the aero-engine dual-rotor model consisting of an overhung fan and SFD arrangement

Figure 6.12 shows the Campbell diagrams of the modified aero-engine model. Due to the presence of a heavy fan disk, pitching happens about the bearing 1 location during the first mode of vibration. As a result, the separation between forward and backward frequencies is increased, as shown in Fig. 6.12. The presence of the heavy fan disk made significant variations in the dynamics of the model compared to that described in Chapter 5. The critical speeds of the modified aero-engine model are listed in Tab. 6.6.

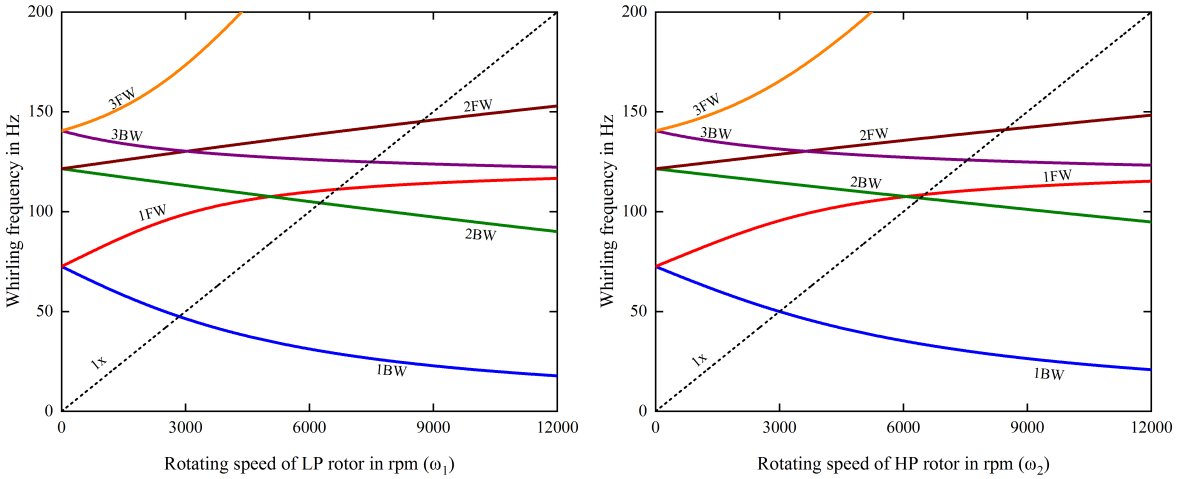


(a) excited by inner rotor (b) excited by outer rotor

Fig. 6.12 Campbell diagrams of the modified aero-engine dual-rotor model

Table 6.6 Critical speeds of the modified aero-engine model

| Order | Excited by low pressure rotor (rpm) | | Excited by high pressure rotor (rpm) | |
|---|---|---|---|---|
| | (BW) | (FW) | (BW) | (FW) |
| 1 | 2850 | 6675 | 2998 | 6520 |
| 2 | 6260 | 8710 | 6408 | 8462 |

The unbalance responses of the model with and without rolling contact bearings are plotted at the fan disk location as shown in Fig. 6.13. It is obtained using the ATVM technique by taking $N_{pt}$ as 150. The four peaks corresponding to the first two modes of vibrations are seen in the response, in which the resonance peak corresponding to the first critical speed (speed = 6675 rpm) is significant at the fan disk location. Other resonance amplitudes are small due to the damping in the model. A forward-leaning is observed in the response because of the hard spring characteristics of the contact bearings.

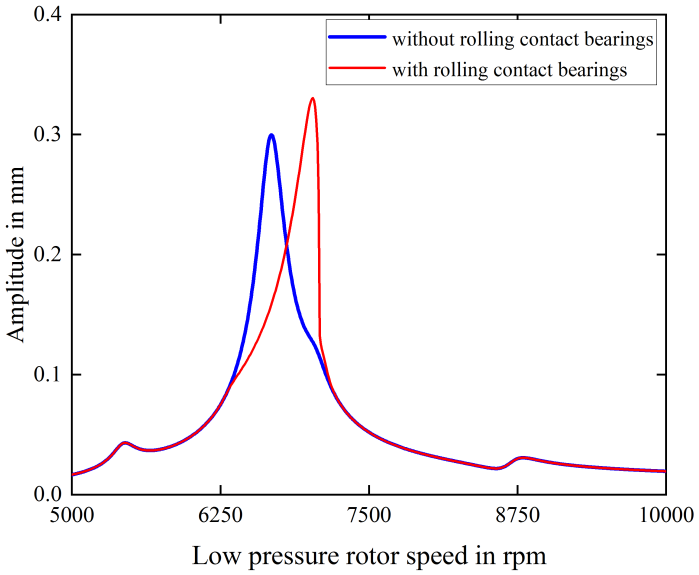


Fig. 6.13 Unbalance response of the modified aero-engine determined at the fan disk. The responses of the model when supported on linear and rolling contact bearings are compared.

The unbalance responses are plotted at other disk locations as well. It is shown in Fig. 6.14. Similar to the fan disk, the LPC disks also have large displacements during the first critical speed. However, the LPT, HPC and HPT disks are displaced more during the second vibration mode (Speed = 7051 and 8710 rpm). In Fig. 6.14b-6.14d, the first peak corresponds to the resonance when the rotor speed is 1/1.2 times the critical speed of the system with respect to the high-pressure rotor excitation, whereas the second peak corresponds to the resonance when the rotor speed is equal to the critical speed of the model with respect to the

low-pressure rotor excitation. When the SFD is incorporated, the amplitudes of vibrations are reduced remarkably, as shown in Fig. 6.15. The percentage of reduction in amplitudes compared to the no SFD response is listed in Tab. 6.7.

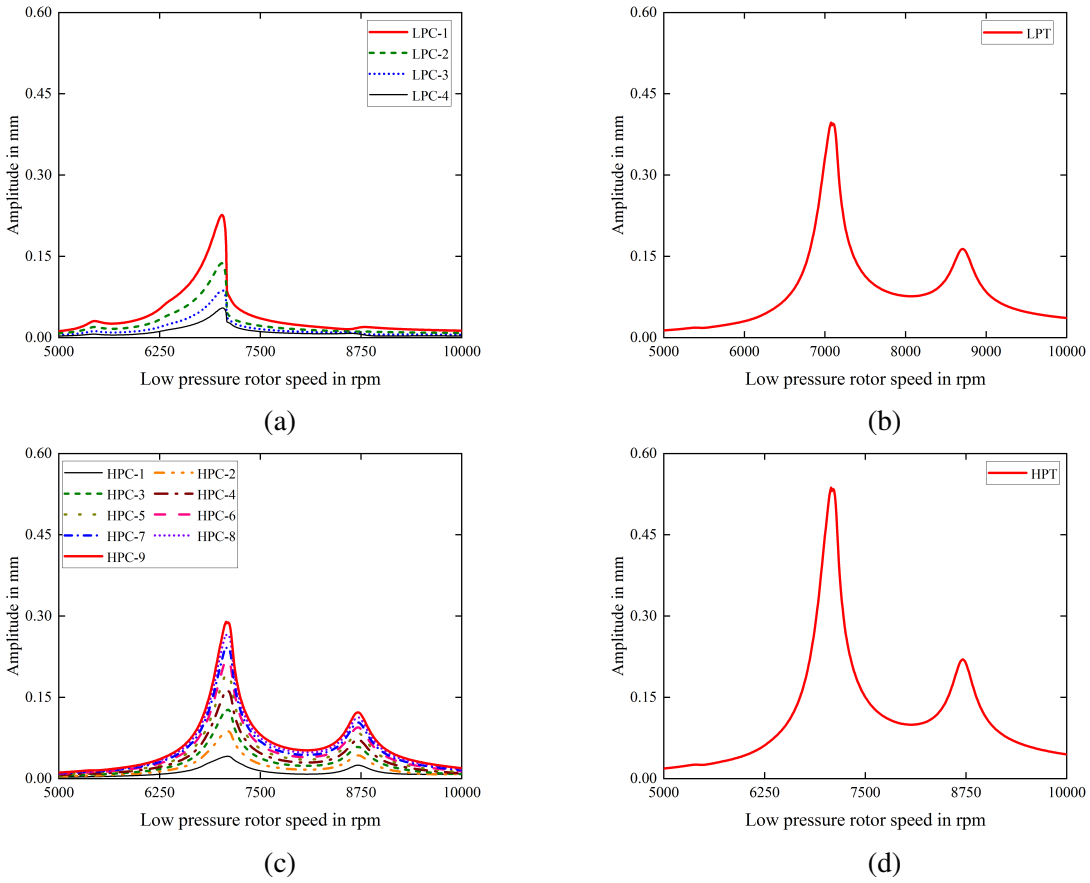


Fig. 6.14 Unbalance responses calculated at (a) LPC (b) LPT (c) HPC and (d) HPT disk positions. LPC disks have large displacements during the first critical speed. However, the LPT, HPC and HPT disks are displaced more during the second mode of vibration.

Table 6.7 Percentage reduction in the amplitudes of aero-engine vibration compared to no SFD response

| Parameter | SFD Clearance (mm) | | SFD oil viscosity (Pa.s) | | |
|---|---|---|---|---|---|
| | c = 0.40 | c = 0.25 | $\eta = 5.66 \times 10^{-3}$ | $\eta = 8.13 \times 10^{-3}$ | $\eta = 10.85 \times 10^{-3}$ |
| % of reduction | 11.44 | 53.08 | 30.6 | 43.31 | 55.72 |

### 6.3.1 Rub-impact response of the modified aero-engine model

For the rub-impact analysis, the rotor-stator contact stiffness, clearance and coefficient of friction are taken as $k_c = 0.3 \times 10^8$ N/m, $\delta = 0.1$ mm and $\mu = 0.2$. The analysis is carried

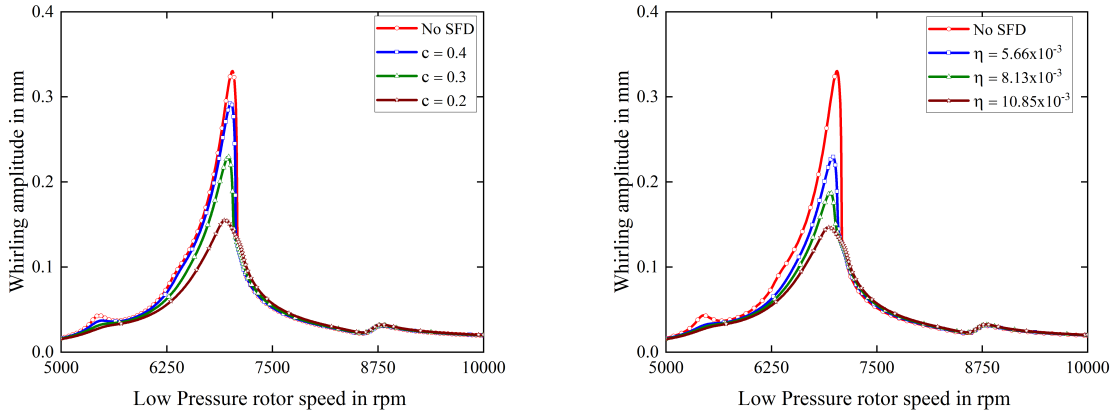


Fig. 6.15 Comparison of unbalance responses of the aero-engine model determined at fan disk location when SFD (a) clearance and (b) viscosity are varied.

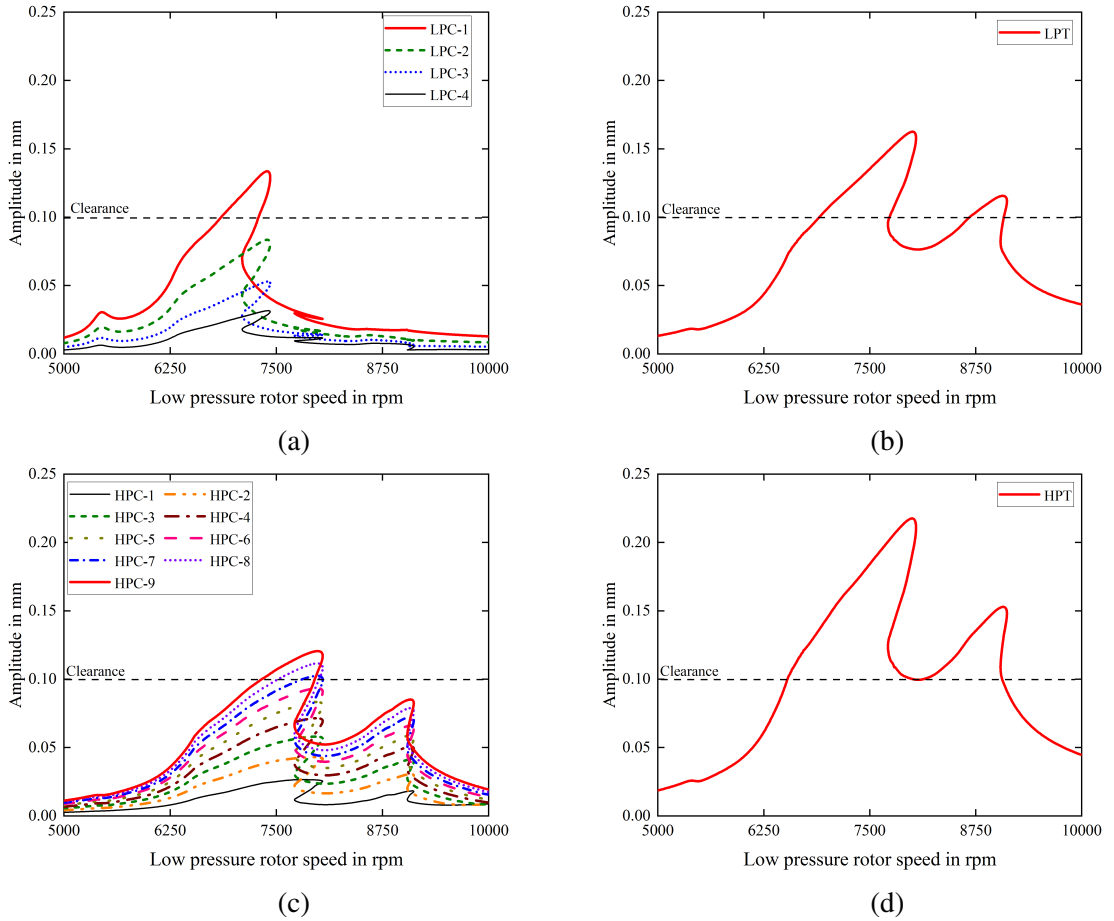


Fig. 6.16 Rub-impact responses calculated at (a) LPC (b) LPT (c) HPC and (d) HPT disk positions when no SFD is incorporated into the model

out using the ATVM technique by taking $N_{pt}$ as 180. Figure 6.16 shows the rub-impact responses of the aero-engine model, determined at different disk locations when no SFD is incorporated at bearing 1 location. It is observed that in addition to the fan disk, LPC-1, LPT, HPC-7, HPC-8, HPC-9, and HPT disks are also undergoing rub-impact at different rotating speeds as shown in Fig. 6.16. Hence, it can be stated that the multi-disk rub-impact is happening in the model.

Later, the stability of the model is analyzed, and it is plotted at the fan disk location as shown in Fig. 6.17. An NS bifurcation is noticed at a speed of 6900 rpm, which is verified by checking the orbit plot and Poincaré map at different speeds, before and after NS bifurcation as shown in Figs. 6.18-6.19. A period-5 motion is observed before the NS bifurcation at 6650 rpm, while a chaotic motion is noticed after the NS bifurcation at a speed of 6980 rpm. In Fig. 6.17, a small peak is observed in the response curve between the speed range of 7700-8100 rpm as circled. It actually happens due to the rub-impact of LPT, HPT and HPC disks during the second vibration mode. Because of the coupling of rotors, such behaviour appears in the response of the fan and LPC disks as well. It can be seen from Fig. 6.20 in which the rub-impact curves of LPT and HPT disks are compared with that of the fan disk.

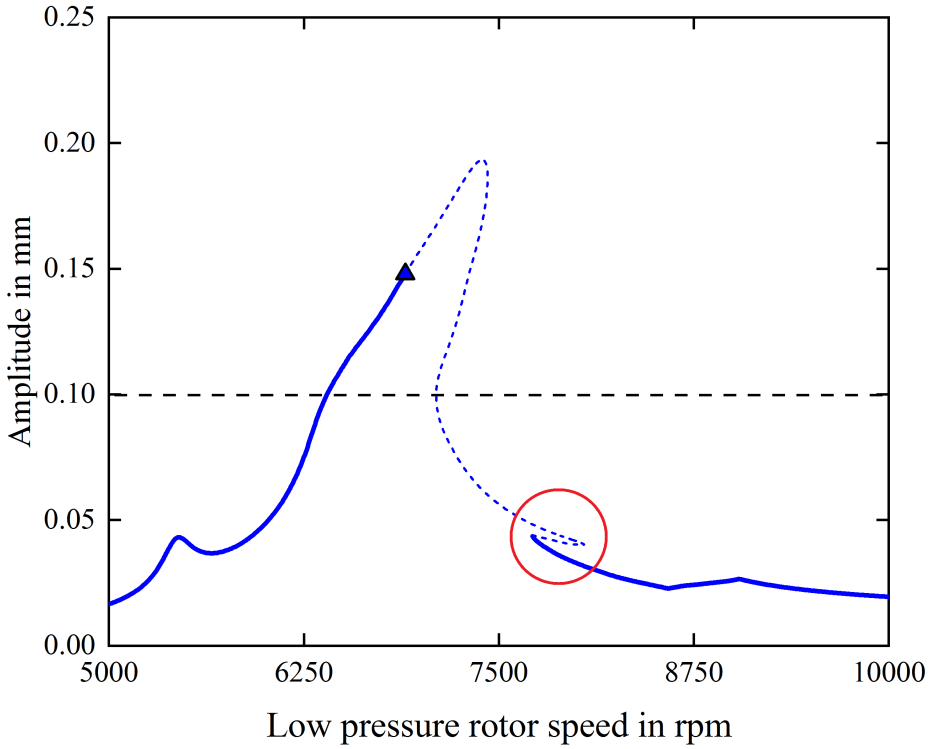


Fig. 6.17 Stability diagram plotted at the fan disk location without considering the presence of SFD. The circled part shows the small peak appearing due to rub-impact.

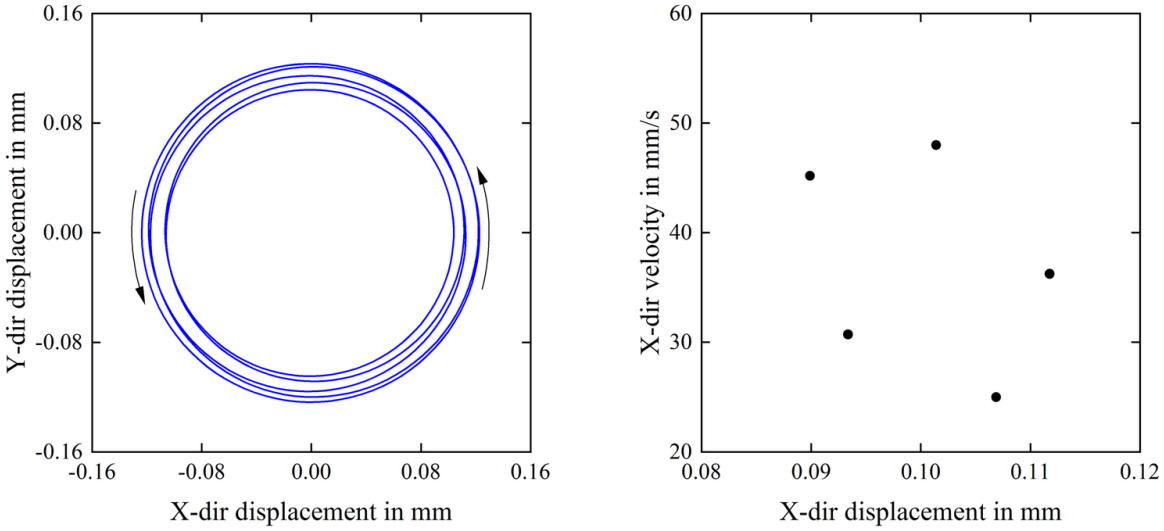


Fig. 6.18 Orbit plot and Poincaré map plotted at the fan location when the rotating speed is 6650 rpm which is before the NS bifurcation. A period-5 motion is observed in the response.

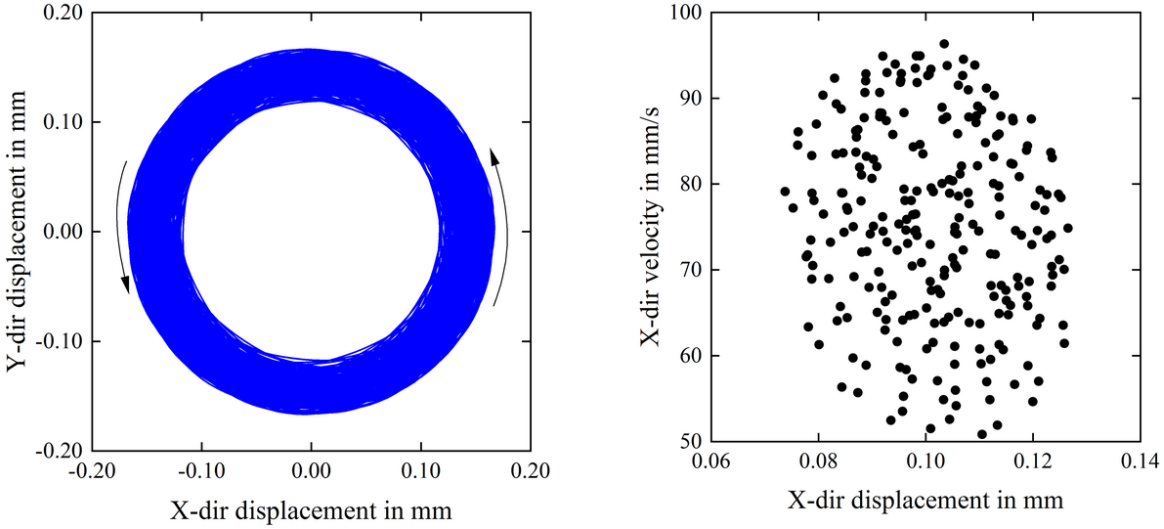


Fig. 6.19 Orbit plot and Poincaré map plotted at the fan location when the rotating speed is 6980 rpm which is after the NS bifurcation. A chaotic motion is observed in the response.

In order to understand the influence of SFD, the model responses during different values of the SFD clearance and oil viscosity are compared at the fan disk location as shown in Fig. 6.21. In the absence of the SFD, the initial rub-impact has happened at a speed of 6400 rpm. The NS bifurcation is noticed at a speed of 6900 rpm, and the maximum amplitude of whirling is reached up to 0.193 mm. When an SFD with clearance $c$ = 0.025 mm is introduced, the initial rub-impact is delayed to 6632 rpm. However, the NS bifurcation is

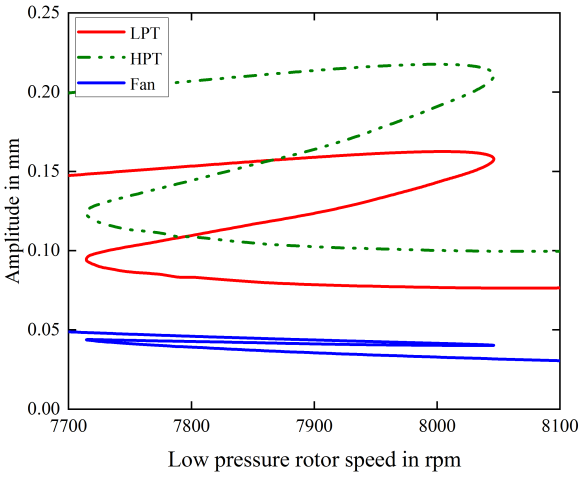


Fig. 6.20 The small peak observed in the fan response is compared against the rub-impact response of the LPT and HPT disks during the second mode of vibration (between the speed range of 7700-8100 rpm). It is the second resonance curve and it is amplified in the fan response due to the rub-impact at other disks.

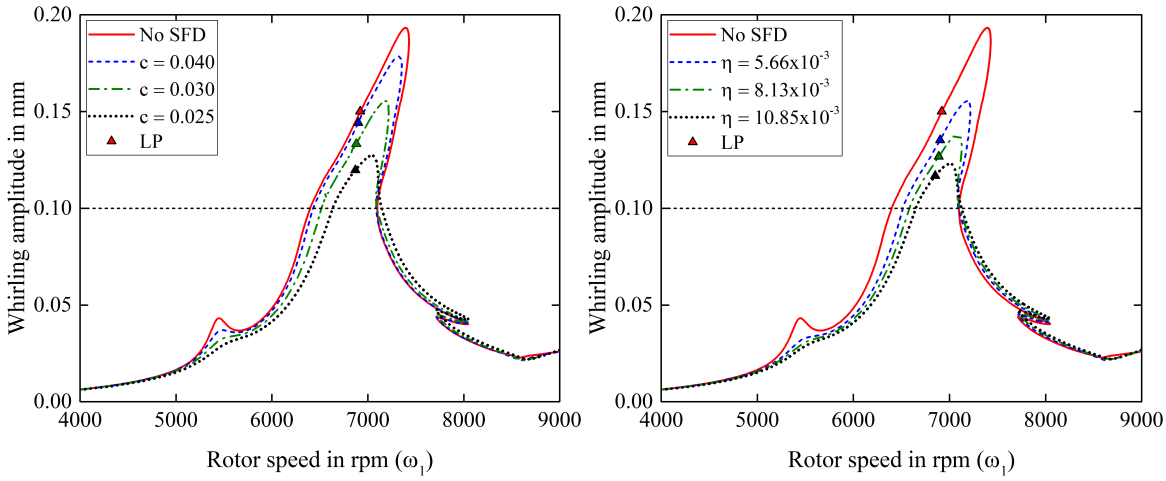


Fig. 6.21 Comparison of the system response during rub-impact for different values of (a)SFD clearance and (b) SFD oil viscosity. Clearance is varied between $c$ = 0.025-0.04 mm and oil viscosity is varied between $\eta = 5.66 \times 10^{-3}$- $10.85 \times 10^{-3}$ Pa.s

noticed at the same speed as that of the model with no SFD. The maximum amplitude of whirling is significantly reduced to 0.127 mm that proves the importance of the SFD. When the oil viscosity of the SFD is increased to $\eta$ = 10.85 $\times 10^{-3}$ Pa.S, the initial rub-impact is delayed to 6651 rpm, and the maximum amplitude is reduced to 0.123 rpm. Hence, it can be stated that due to the presence of SFD, the initial rub-impact is delayed, and the range of

rub-impact is also reduced. The amplitudes of vibrations are significantly reduced, and it is listed in Tab. 6.8. Figure 6.22 shows the rub-impact responses at other disk locations when the SFD is incorporated at the bearing location. In addition to the fan disk, the vibrations of the LPC disks are also reduced due to the SFD. However, there are no variations in the responses of LPT, HPC and HPT disks. This is mainly happening because the SFD is incorporated at bearing 1 location, which is far away from LPT, HPC and HPT disks.

Table 6.8 Percentage of reduction in rub-impact amplitudes of the aero-engine for different values of the SFD parameter

| Parameter | SFD Clearance (mm) | | SFD oil viscosity (Pa.s) | | |
|---|---|---|---|---|---|
| | c = 0.040 | c = 0.025 | $\eta = 5.66 \times 10^{-3}$ | $\eta = 8.13 \times 10^{-3}$ | $\eta = 10.85 \times 10^{-3}$ |
| % of reduction | 7.46 | 34.19 | 19.68 | 27.97 | 36.27 |

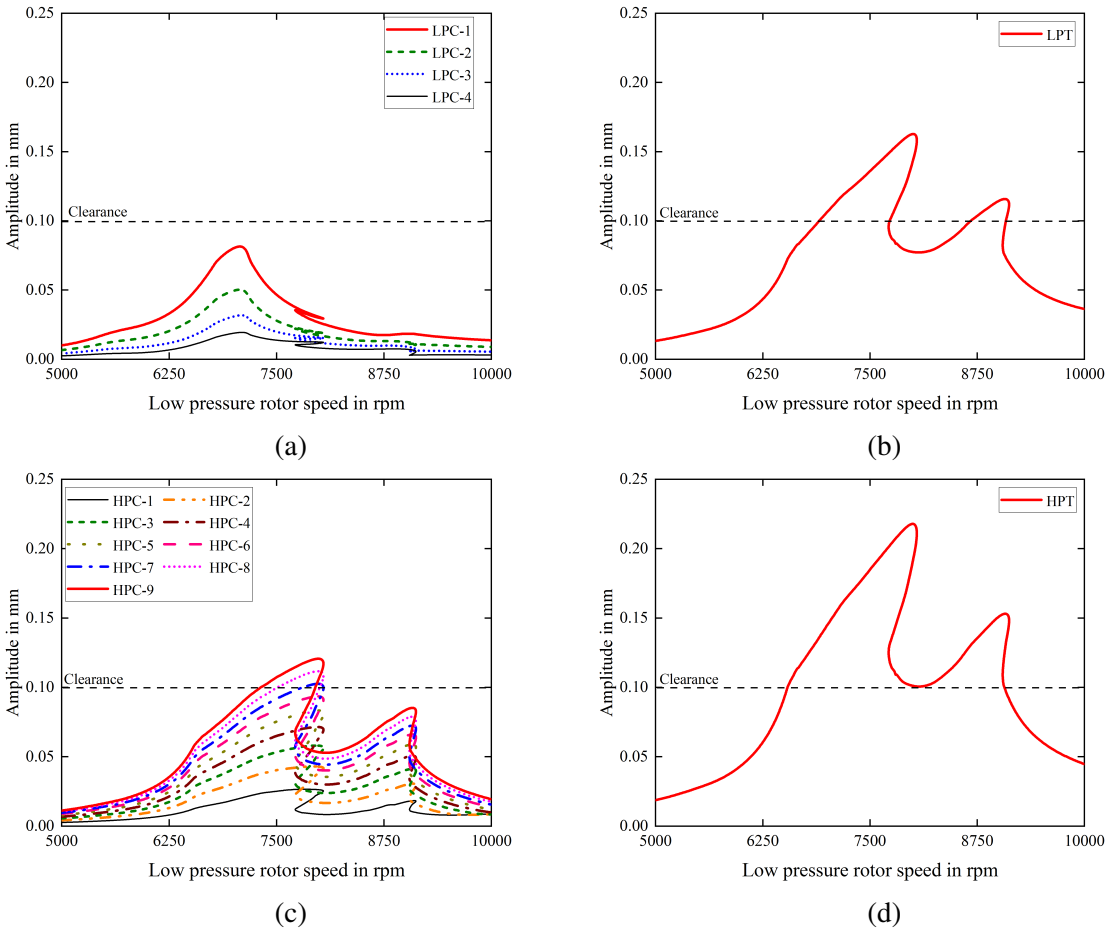


Fig. 6.22 Rub-impact responses calculated at (a) LPC (b) LPT (c) HPC and (d) HPT disk positions when SFD is incorporated into the model. In addition to the fan disk, the vibrations of the LPC disks are also reduced due to the SFD.

## 6.4 Summary

In this chapter, the influence of SFD parameters on the rub-impact response of a dual-rotor model mounted on the nonlinear bearing support is investigated. Mainly two rotor models, namely, a simplified dual-rotor model and a two-spool aero-engine model, are utilized to perform the analysis. The nonlinear bearing support includes the rolling contact bearings, SFD and squirrel-cage elastic support. The rolling contact bearing is modelled using the Hertz contact theory, while the SFD is modelled based on Reynold's equation. Due to the presence of rolling contact bearings, the frequency components such as (1, -2), (2, -1), (2, -3), (3, -2) and (4, -3) are seen in the response in addition to the excitation frequency components. Due to the hard spring characteristics of the ball bearing, a jump-down phenomenon has happened to a low amplitude orbit. In the presence of SFD, the amplitude of rotor vibrations are significantly reduced. It is observed that by decreasing the clearance and increasing oil viscosity, the range of speed for which the rub-impact happens can be reduced remarkably. The initial rub-impact is also delayed due to the introduction of the SFD in the model. Thus, an SFD with proper parameters can significantly reduce the consequences of the multi-disk rub-impact occurring due to the FBO and windmilling action.

# Chapter 7

# Conclusions

In this study, the dynamic analysis of an aero-engine undergoing the multi-disk rub-impact is investigated in detail. The aircraft engine is made up of a multi-disk rotor system; hence, the possibility of multi-disk rub-impact is high during the FBO and windmilling action. Since the conduction of the experimental tests to analyze the FBO is very expensive, it is necessary to carry out the numerical analysis of rub-impacts. In literature, most of the researchers have examined the single-disk rub-impact problem happening in a simplified dual-rotor models. However, the study of multi-disk rub-impact occurring in an aero-engine is necessary to reduce the consequences of the FBO and windmilling. As a result, the main contribution of the work is to study the multi-disk rub-impact happening in an aero-engine by developing a dual-rotor model consisting of multiple disks, rolling contact bearings and dampers.

A dual-rotor model similar to CFM56-5B engine is utilized to carry out the analysis, which consists of multi-stage compressors and turbines in both rotors. The dynamic modelling of the dual-rotor is performed using the FE method, including the tapered Timoshenko beam elements. However, the FE modelling resulted in a very large DOF model that will consume much computation time during the solution process. Hence, a proper model reduction technique needs to be used. It should be noted that the rotordynamic analysis includes asymmetric matrices and frequency-dependent gyroscopic effects. As a result, the model reduction techniques that are effective in structural dynamic problems won't be suitable for rotordynamic problems. In this work, a modified model reduction technique has been developed that can reduce the models with asymmetric matrices using quadratic eigenvalue decomposition. The method is based on the CMS technique coupled with the Craig-Bampton substructuring. A Nelson-McVaugh rotor model is used to verify the effectiveness of the model reduction technique. It is observed that the computation time for the reduced model is decreased by 50% of that of the complete model with the results exactly matching to each other, underlining the efficiency of the reduction technique.

Under the action of unbalaced forces and external excitations, the aero-engine model is subjected to multi-frequency excitation, with the frequency components being fractional multiples of each other. Generally, the MHBM-AFT technique is employed to solve the multi-frequency excitation problems. However, its formulation is very complicated for more than two-frequency excitation problems since the formulation of the higher dimensional FFT is very complex during the AFT procedure. Moreover, the alternate transformation between the time and frequency domain during the calculation of the nonlinear Jacobian is cumbersome. The ATVM technique overcomes this difficulty and performs the complete analysis in the time domain alone. In this technique, the multi-frequency excitation is expressed in terms of a fundamental frequency which is the common divisor of the excitation frequency components. If the frequency ratio is irrational, it is approximated to the nearest rational number, and then the greatest common divisor of the approximated frequency components is calculated. As a result, the response is approximate, and its accuracy is highly dependent on how close the approximated ratios are with the actual ones. It is achieved by an optimization procedure that will find an optimum frequency ratio that minimizes the error between the actual and approximated responses. The modified method is called the approximate time variational method.

The effectiveness of the ATVM technique is validated using three nonlinear mechanical models subjected to the multi-frequency quasi-periodic excitations. The results are compared with that of the MHBM-AFT and numerical integration techniques. An excellent match is obtained when proper approximated frequency ratios are taken after the optimization procedure. However, the time taken for getting the solution is large for the ATVM compared to the MHBM-AFT technique, and it increases with the extent of nonlinearity. But, the easiness of the ATVM in extending the analysis beyond the two-frequency excitation problems validates its usefulness.

After validating the proposed methodology, it is applied in the nonlinear dynamic analysis of a simplified dual-rotor models undergoing a single-disk rub-impact. Two modes of rotor operations, namely co-rotation and counter-rotation, are included in the analysis to study their effects on the response behaviour. The Campbell diagrams and the unbalance responses of the dual-rotor model are determined for both modes of rotor operations. From the Campbell diagrams, it is observed that the critical speeds are different for both co and counter rotations. For counter-rotation, the forward critical speeds are smaller, and backward critical speeds are larger compared to that of co-rotation. This is mainly due to the cancellation of the gyroscopic moments in the case of counter-rotation. Moreover, during the counter-rotation, the whirling direction depends on the value of rotating speed. When contact is initiated, a rightward bending of the response curve is observed as it touches the stator. Due to the

presence of inter-shaft bearing, the coupling of the inner and outer rotor vibrations has happened. As a result, the outer rotor also showed a similar rightward bending, although it didn't undergo any rub-impact. The stability of the model is assessed using a technique based on the Floquet theory. The Floquet exponents are monitored during the continuation procedure to detect the bifurcation points. Mainly, LP and NS bifurcations are observed in the responses when the rotor touches the stator. It is observed that the direction of rotor rotation has a significant effect on the onset of NS bifurcation and dry friction backward whirl. For the same set of model parameters, the onset of NS bifurcation and dry friction backward whirl happened early for the counter-rotating model compared to the co-rotating model. As a result, a co-rotating model will be preferable in a dual-rotor when considering the stability of the model during rub-impact.

Finally, the proposed numerical technique is employed for obtaining the dynamic characteristics of an aero-engine under multi-disk rub-impact. From the rub-impact analysis, it is observed that the response of the model is significantly affected by the multi-disk rub-impact. The total stiffness of the model is increased when more than two disks contact the stator simultaneously. It resulted in an increased rightward bending of the response compared to the single-disk rub-impact problem. The amplitude of whirling is also decreased due to the constraint effects of the casing. The bifurcations such as the LP and NS bifurcations are observed in the response, indicating a sudden jump and the origin of a quasi-periodic branch, respectively. The responses such as full annular rub and bouncing motion are identified by analyzing the orbit plots and the Poincaré maps. Mainly, a period-5 motion is observed before the NS bifurcation, while a quasi-periodic motion is noticed after the NS bifurcation. During quasi-periodic motion, some unknown fractional components such as $0.716\omega_1$, $0.766\omega_1$, $0.916\omega_1$ and $0.964\omega_1$ are appeared in the response. Beyond the quasi-periodic regime, the model enters into the dry friction backward whirl in which the rotors orbit backwards with a huge amplitude. It is the most violent motion of the rotor, and it happens at a superharmonic frequency. A parametric analysis is also conducted to understand the effects of rub and SFD parameters on the model response. It is found that the amplitude of rightward bending is shortened, and the onset of NS bifurcation is happening early as the value of the friction coefficient is increased. As a result, the model quickly enters into the quasi-periodic motions for large values of $\mu$. Similar nature is observed for the rotor-stator contact stiffness as well. When an SFD has been introduced in the model significant reduction in the amplitude has happened. It is seen that by decreasing the clearance and increasing oil viscosity, the range of speed for which the rub-impact happens can be reduced remarkably. For low clearance and high oil viscosity, the jump-down phenomenon occurs so early that the model quickly shifts to no rub region.

From the complete analysis, it can be concluded that the study of multi-disk rub-impact in the aero-engines is critical in avoiding the consequences of FBO and windmilling. However, there are certain limitations in the current work. The proposed ATVM technique can't capture the quasi-periodic branches beyond bifurcation points since it involves unknown irrational frequency components. The numerical integration is required to get the quasi-periodic branches beyond the NS bifurcation. This is a major limitation of the proposed ATVM, and it needs to be modified in future. Moreover, the experimental validation of the multi-disk rub-impact is lacking in this work. Although the numerical procedure is experimentally validated, the results of the multi-disk rub-impact in the aero-engine model need to be verified experimentally. Hence, the possible research extensions of this work are listed as follows.

- The extension of the TVM in capturing the quasi-periodic motions and dry friction backward whirl will be a challenging topic in the future. The TVM can be modified by introducing the concept of hypertime in the formulation as in the MHBM. Then, the response will be periodic for each of the dimensions, even though it contains irrational frequency components. The technique may be termed as the multi-time variational method, and its development in the quasi-periodic excitation problems will be an exciting area.
- An experimental study of the multi-disk rub-impact in an aero-engine model will be an interesting topic in the future. The development of the experimental setup will be a massive task since the aero-engine model has a complex structure. Hence, the analysis can be started with a simplified dual-rotor model consisting of a single-stage compressor and turbine in each rotor. The results of the present numerical study can be validated with the experimental results for further clarifications of the multi-disk rub-impact phenomenon.

# Appendix A

# Physical properties and geometrical dimensions of the model

Table A.1 Physical properties of the model (Jin et al. (2019))

| Physical property | Value | Physical property | Value |
|---|---|---|---|
| Mass of LPC-1 disk (kg) | 6.386 | Moment of inertia of LPC-1 disk (kg.m$^2$) | 0.143 |
| Mass of LPC-2 disk (kg) | 5.723 | Moment of inertia of LPC-2 disk (kg.m$^2$) | 0.122 |
| Mass of LPC-3 disk (kg) | 5.397 | Moment of inertia of LPC-3 disk (kg.m$^2$) | 0.115 |
| Mass of LPC-4 disk (kg) | 4.511 | Moment of inertia of LPC-4 disk (kg.m$^2$) | 0.101 |
| Mass of HPC-1 disk (kg) | 1.727 | Moment of inertia of HPC-1 disk (kg.m$^2$) | 0.035 |
| Mass of HPC-2 disk (kg) | 2.002 | Moment of inertia of HPC-2 disk (kg.m$^2$) | 0.038 |
| Mass of HPC-3 disk (kg) | 3.075 | Moment of inertia of HPC-3 disk (kg.m$^2$) | 0.048 |
| Mass of HPC-4 disk (kg) | 2.922 | Moment of inertia of HPC-4 disk (kg.m$^2$) | 0.053 |
| Mass of HPC-5 disk (kg) | 3.424 | Moment of inertia of HPC-5 disk (kg.m$^2$) | 0.068 |
| Mass of HPC-6 disk (kg) | 3.774 | Moment of inertia of HPC-6 disk (kg.m$^2$) | 0.073 |
| Mass of HPC-7 disk (kg) | 4.003 | Moment of inertia of HPC-7 disk (kg.m$^2$) | 0.081 |
| Mass of HPC-8 disk (kg) | 4.098 | Moment of inertia of HPC-8 disk (kg.m$^2$) | 0.083 |
| Mass of HPC-9 disk (kg) | 4.005 | Moment of inertia of HPC-9 disk (kg.m$^2$) | 0.086 |
| Mass of LPT-disk (kg) | 18.257 | Moment of inertia of LPT-disk (kg.m$^2$) | 0.749 |
| Mass of HPT-disk (kg) | 26.331 | Moment of inertia of HPT-disk (kg.m$^2$) | 0.86 |
| Mass of fan disk (kg) | 254.40 | Moment of inertia of fan disk (kg.m$^2$) | 10.86 |
| Elastic modulus of Ti alloy $E_{Ti}$ (GPa) | 105 | Elastic modulus of Ni alloy $E_{Ni}$ (GPa) | 206 |
| Density of Ti alloy $\rho_{Ti}$ (Kg/m$^3$) | 4350 | Density of Ni alloy $\rho_{Ni}$ (Kg/m$^3$) | 8200 |
| Poisson ratio of Ti alloy $\nu_{Ti}$ | 0.26 | Poisson ratio of Ni alloy $\nu_{Ni}$ | 0.3 |
| Stiffness of bearing-1 (N/m) | $1.22\times10^9$ | Damping of bearing-1 (Ns/m) | 2750 |
| Stiffness of bearing-2 (N/m) | $1.00\times10^9$ | Damping of bearing-2 (Ns/m) | 4200 |
| Stiffness of bearing-3 (N/m) | $1.18\times10^9$ | Damping of bearing-3 (Ns/m) | 5500 |
| Stiffness of bearing-4 (N/m) | $2.04\times10^8$ | Damping of bearing-4 (Ns/m) | 4700 |
| Stiffness of bearing-5 (N/m) | $1.37\times10^9$ | Damping of bearing-5 (Ns/m) | 5000 |
| Eccentricity of LPC-3 disk (mm) | 0.08 | Eccentricity of HPC-7 disk (mm) | 0.14 |
| Eccentricity of LPT disk (mm) | 0.03 | Eccentricity of HPT disk (mm) | 0.05 |
| Rayleigh Damping Coeff. (Mass) | 27.3374 | Rayleigh Damping Coeff. (Stiffness) | $5.5848\times10^{-6}$ |

Table A.2 Geometrical dimensions of the shaft elements (Jin et al. (2019))

| Element length (m) | Value | Element radius | Value | | | |
|---|---|---|---|---|---|---|
| | | | $r_{Li}$ (m) | $r_{Lo}$ (m) | $r_{Ri}$ (m) | $r_{Ro}$ (m) |
| $l_1$ | 2×0.025 | elements in $l_1$ | 0.0355 | 0.0475 | 0.0355 | 0.0475 |
| $l_2$ | 3×0.016 | elements in $l_2$ | 0.0405 | 0.0475 | 0.1100 | 0.1180 |
| $l_3$ | 2×0.065 | elements in $l_3$ | 0.1100 | 0.1180 | 0.1740 | 0.1820 |
| $l_4$ | 2×0.047 | elements in $l_4$ | 0.1740 | 0.1820 | 0.1980 | 0.2060 |
| $l_5$ | 2×0.033 | elements in $l_5$ | 0.1980 | 0.2060 | 0.1980 | 0.2060 |
| $l_6$ | 3×0.041 | elements in $l_6$ | 0.1280 | 0.1380 | 0.0405 | 0.0475 |
| $l_7$ | 5×0.079 | elements in $l_7$ | 0.0355 | 0.0405 | 0.0355 | 0.0405 |
| $l_8$ | 1×0.018 | elements in $l_8$ | 0.0355 | 0.0475 | 0.0355 | 0.0405 |
| $l_9$ | 1×0.066 | elements in $l_9$ | 0.0355 | 0.0405 | 0.0355 | 0.0405 |
| $l_{10}$ | 2×0.029 | elements in $l_{10}$ | 0.0355 | 0.0405 | 0.0355 | 0.0440 |
| $l_{11}$ | 3×0.025 | elements in $l_{11}$ | 0.0355 | 0.0440 | 0.0395 | 0.0460 |
| $l_{12}$ | 6×0.045 | elements in $l_{12}$ | 0.0395 | 0.0460 | 0.0565 | 0.0625 |
| $l_{13}$ | 11×0.043 | elements in $l_{13}$ | 0.0565 | 0.0625 | 0.0565 | 0.0625 |
| $l_{14}$ | 2×0.048 | elements in $l_{14}$ | 0.0565 | 0.0625 | 0.0480 | 0.0625 |
| $l_{15}$ | 2×0.048 | elements in $l_{15}$ | 0.0480 | 0.0625 | 0.0570 | 0.0650 |
| $l_{16}$ | 2×0.052 | elements in $l_{16}$ | 0.0570 | 0.0650 | 0.0415 | 0.0495 |
| $l_{17}$ | 4×0.062 | elements in $l_{17}$ | 0.0415 | 0.0495 | 0.0415 | 0.0495 |
| $l_{18}$ | 1×0.026 | elements in $l_{18}$ | 0.0530 | 0.0590 | 0.0530 | 0.0590 |
| $l_{19}$ | 1×0.065 | elements in $l_{19}$ | 0.0530 | 0.0590 | 0.0540 | 0.0600 |
| $l_{20}$ | 1×0.028 | elements in $l_{20}$ | 0.0540 | 0.0600 | 0.0540 | 0.0610 |
| $l_{21}$ | 1×0.036 | elements in $l_{21}$ | 0.0540 | 0.0610 | 0.0550 | 0.0620 |
| $l_{22}$ | 1×0.036 | elements in $l_{22}$ | 0.0550 | 0.0620 | 0.0870 | 0.0920 |
| $l_{23}$ | 1×0.050 | elements in $l_{23}$ | 0.0870 | 0.0920 | 0.1630 | 0.1680 |
| $l_{24}$ | 1×0.072 | elements in $l_{24}$ | 0.1520 | 0.1580 | 0.1650 | 0.1710 |
| $l_{25}$ | 1×0.062 | elements in $l_{25}$ | 0.1650 | 0.1710 | 0.1840 | 0.1900 |
| $l_{26}$ | 1×0.050 | elements in $l_{26}$ | 0.1840 | 0.1900 | 0.2000 | 0.2060 |
| $l_{27}$ | 1×0.044 | elements in $l_{27}$ | 0.2000 | 0.2060 | 0.2160 | 0.2210 |
| $l_{28}$ | 1×0.038 | elements in $l_{28}$ | 0.2160 | 0.2210 | 0.2300 | 0.2350 |
| $l_{29}$ | 1×0.036 | elements in $l_{29}$ | 0.2300 | 0.2350 | 0.2410 | 0.2460 |
| $l_{30}$ | 1×0.036 | elements in $l_{30}$ | 0.2410 | 0.2460 | 0.2500 | 0.2540 |
| $l_{31}$ | 1×0.036 | elements in $l_{31}$ | 0.2500 | 0.2540 | 0.2570 | 0.2600 |
| $l_{32}$ | 1×0.035 | elements in $l_{32}$ | 0.2570 | 0.2600 | 0.2320 | 0.2370 |
| $l_{33}$ | 1×0.036 | elements in $l_{33}$ | 0.2130 | 0.2180 | 0.1280 | 0.1330 |
| $l_{34}$ | 1×0.036 | elements in $l_{34}$ | 0.1280 | 0.1330 | 0.1220 | 0.1280 |
| $l_{35}$ | 1×0.036 | elements in $l_{35}$ | 0.1220 | 0.1280 | 0.1220 | 0.1280 |
| $l_{36}$ | 1×0.035 | elements in $l_{36}$ | 0.1220 | 0.1280 | 0.1220 | 0.1280 |
| $l_{37}$ | 2×0.043 | elements in $l_{37}$ | 0.1220 | 0.1280 | 0.1020 | 0.1070 |
| $l_{38}$ | 6×0.060 | elements in $l_{38}$ | 0.1020 | 0.1070 | 0.1020 | 0.1070 |
| $l_{39}$ | 1×0.048 | elements in $l_{39}$ | 0.1020 | 0.1070 | 0.1080 | 0.1170 |
| $l_{40}$ | 1×0.074 | elements in $l_{40}$ | 0.1080 | 0.1170 | 0.0720 | 0.0800 |
| $l_{41}$ | 2×0.046 | elements in $l_{41}$ | 0.0720 | 0.0800 | 0.0720 | 0.0800 |

Table A.3 Parameters used in the rolling contact bearing models (Jin et al. (2019))

| Bearing order | Type | $R_b$ (mm) | $r_b$ (mm) | $N_b$ | $C_b$ (N/m$^n$) | $c_0$ ($\mu$m) |
|---|---|---|---|---|---|---|
| Bearing 1 | Roller | 59.314 | 51.786 | 18 | 6.58e9 | 10 |
| Bearing 2 | Ball | 101.832 | 85.857 | 33 | 13.25e9 | 12 |
| Bearing 3 | Roller | 65.858 | 55.126 | 24 | 11.58e9 | 16 |
| Bearing 4 | Ball | 101.832 | 85.857 | 33 | 13.25e9 | 22 |

# Appendix B

# Dynamic matrices of a conical element

$L =$ length of the element

$\rho =$ mass density

$\nu =$ Poisson ratio

$r_{Li} =$ inner radii of the element at first node

$r_{Lo} =$ outer radii of the element at first node

$r_{Ri} =$ inner radii of the element at second node

$r_{Ro} =$ outer radii of the element at second node

$E =$ Young's modulus

$G =$ Shear modulus

Since the cross-section parameters of the conical element vary with the section position, they are expressed in terms of their mean values by assuming the section is very short. Hence, the shear deformation coefficient can be calculated using the expression given below,

$$\varphi_s = \frac{12EI_m\chi}{GA_mL^2}$$

where $A_m = \pi(r_{mo}^2 - r_{mi}^2)$, $I_m = \frac{\pi}{4}(r_{mo}^4 - r_{mi}^4)$ and $\chi = \frac{7+6\nu}{6(1+\nu)}\left[1 + \frac{20+12\nu}{7+6\nu}\left(\frac{r_{mo}r_{mi}}{r_{mo}^2+r_{mi}^2}\right)^2\right]$. Here, $r_{mo}$ and $r_{mi}$ are the mean values of outer and inner radii respectively. Let, $A$ and $I$ are the section area and second moment of area of the element at the left end.

Now, the dynamic matrices of a conical shaft element can be written as,

$$\left[\mathbf{M}_e^t\right]_{con} = \frac{\rho AL}{1260(1+\varphi_s)^2}\begin{bmatrix} m_1 & 0 & 0 & m_2 & m_3 & 0 & 0 & -m_4 \\ 0 & m_1 & -m_2 & 0 & 0 & m_3 & m_4 & 0 \\ 0 & -m_2 & m_5 & 0 & 0 & -m_6 & -m_7 & 0 \\ m_2 & 0 & 0 & m_5 & m_6 & 0 & 0 & -m_7 \\ m_3 & 0 & 0 & m_6 & m_8 & 0 & 0 & -m_9 \\ 0 & m_3 & -m_6 & 0 & 0 & m_8 & m_9 & 0 \\ 0 & m_4 & -m_7 & 0 & 0 & m_9 & m_{10} & 0 \\ -m_4 & 0 & 0 & -m_7 & -m_9 & 0 & 0 & m_{10} \end{bmatrix}$$

$$\left[\mathbf{M}_e^r\right]_{con} = \frac{\rho I}{210L(1+\varphi_s)^2}\begin{bmatrix} m_{11} & 0 & 0 & m_{12} & -m_{11} & 0 & 0 & m_{13} \\ 0 & m_{11} & -m_{12} & 0 & 0 & -m_{11} & -m_{13} & 0 \\ 0 & -m_{12} & m_{14} & 0 & 0 & m_{12} & -m_{15} & 0 \\ m_{12} & 0 & 0 & m_{14} & -m_{12} & 0 & 0 & -m_{15} \\ -m_{11} & 0 & 0 & -m_{12} & m_{11} & 0 & 0 & -m_{13} \\ 0 & -m_{11} & m_{12} & 0 & 0 & m_{11} & m_{13} & 0 \\ 0 & -m_{13} & -m_{15} & 0 & 0 & m_{13} & m_{16} & 0 \\ m_{13} & 0 & 0 & -m_{15} & -m_{13} & 0 & 0 & m_{16} \end{bmatrix}$$

$$\left[\mathbf{G}_e\right]_{con} = -\frac{\rho I}{105L(1+\varphi_s)^2}\begin{bmatrix} 0 & -m_{11} & m_{12} & 0 & 0 & m_{11} & m_{13} & 0 \\ m_{11} & 0 & 0 & m_{12} & -m_{11} & 0 & 0 & m_{13} \\ -m_{12} & 0 & 0 & -m_{14} & m_{12} & 0 & 0 & m_{15} \\ 0 & -m_{12} & m_{14} & 0 & 0 & m_{12} & -m_{15} & 0 \\ 0 & m_{11} & -m_{12} & 0 & 0 & -m_{11} & -m_{13} & 0 \\ -m_{11} & 0 & 0 & -m_{12} & m_{11} & 0 & 0 & -m_{13} \\ -m_{13} & 0 & 0 & m_{15} & m_{13} & 0 & 0 & -m_{16} \\ 0 & -m_{13} & -m_{15} & 0 & 0 & m_{13} & m_{16} & 0 \end{bmatrix}$$

$$\left[\mathbf{K}_e\right]_{con} = \frac{EI}{105L^3(1+\varphi_s)^2}\left[\mathbf{K}_a\right] + \frac{GA\varphi_s^2}{12\chi L(1+\varphi_s)^2}\left[\mathbf{K}_b\right]$$

$$\left[\mathbf{K}_a\right] = \begin{bmatrix} k_1 & 0 & 0 & k_2 & -k_1 & 0 & 0 & k_3 \\ 0 & k_1 & -k_2 & 0 & 0 & -k_1 & -k_3 & 0 \\ 0 & -k_2 & k_4 & 0 & 0 & k_2 & k_5 & 0 \\ k_2 & 0 & 0 & k_4 & -k_2 & 0 & 0 & k_5 \\ -k_1 & 0 & 0 & -k_2 & k_1 & 0 & 0 & -k_3 \\ 0 & -k_1 & k_2 & 0 & 0 & k_1 & k_3 & 0 \\ 0 & -k_3 & k_5 & 0 & 0 & k_3 & k_6 & 0 \\ k_3 & 0 & 0 & k_5 & -k_3 & 0 & 0 & k_6 \end{bmatrix}$$

$$\left[\mathbf{K}_b\right] = \begin{bmatrix} k_7 & 0 & 0 & k_8 & -k_7 & 0 & 0 & k_8 \\ 0 & k_7 & -k_8 & 0 & 0 & -k_7 & -k_8 & 0 \\ 0 & -k_8 & k_9 & 0 & 0 & k_8 & k_9 & 0 \\ k_8 & 0 & 0 & k_9 & -k_8 & 0 & 0 & k_9 \\ -k_7 & 0 & 0 & -k_8 & k_7 & 0 & 0 & -k_8 \\ 0 & -k_7 & k_8 & 0 & 0 & k_7 & k_8 & 0 \\ 0 & -k_8 & k_9 & 0 & 0 & k_8 & k_9 & 0 \\ k_8 & 0 & 0 & k_9 & -k_8 & 0 & 0 & k_9 \end{bmatrix}$$

where,

$$\begin{aligned}
m_1 &= (468 + 882\varphi_s + 420\varphi_s^2) + a_1(108 + 210\varphi_s + 105\varphi_s^2) + b_1(38 + 78\varphi_s + 42\varphi_s^2) \\
m_2 &= [(66 + 115.5\varphi_s + 52.5\varphi_s^2) + a_1(21 + 40.5\varphi_s + 21\varphi_s^2) + b_1(8.5 + 18\varphi_s + 10.5\varphi_s^2)]L \\
m_3 &= (162 + 378\varphi_s + 210\varphi_s^2) + a_1(81 + 189\varphi_s + 105\varphi_s^2) + b_1(46 + 111\varphi_s + 63\varphi_s^2) \\
m_4 &= [(39 + 94.5\varphi_s + 52.5\varphi_s^2) + a_1(18 + 40.5\varphi_s + 21\varphi_s^2) + b_1(9.5 + 21\varphi_s + 10.5\varphi_s^2)]L \\
m_5 &= [(12 + 21\varphi_s + 10.5\varphi_s^2) + a_1(4.5 + 9\varphi_s + 5.25\varphi_s^2) + b_1(2 + 4.5\varphi_s + 3\varphi_s^2)]L^2 \\
m_6 &= [(39 + 94.5\varphi_s + 52.5\varphi_s^2) + a_1(21 + 54\varphi_s + 31.5\varphi_s^2) + b_1(12.5 + 34.5\varphi_s + 21\varphi_s^2)]L \\
m_7 &= [(9 + 21\varphi_s + 10.5\varphi_s^2) + a_1(4.5 + 10.5\varphi_s + 5.25\varphi_s^2) + b_1(2.5 + 6\varphi_s + 3\varphi_s^2)]L^2 \\
m_8 &= (468 + 882\varphi_s + 420\varphi_s^2) + a_1(360 + 672\varphi_s + 315\varphi_s^2) + b_1(290 + 540\varphi_s + 252\varphi_s^2) \\
m_9 &= [(66 + 115.5\varphi_s + 52.5\varphi_s^2) + a_1(45 + 75\varphi_s + 31.5\varphi_s^2) + b_1(32.5 + 52.5\varphi_s + 21\varphi_s^2)]L \\
m_{10} &= [(12 + 21\varphi_s + 10.5\varphi_s^2) + a_1(7.5 + 12\varphi_s + 5.25\varphi_s^2) + b_1(5 + 7.5\varphi_s + 3\varphi_s^2)]L^2 \\
m_{11} &= 252 + 126a_2 + 72b_2 + 45g_2 + 30d_2 \\
m_{12} &= [21 - 105\varphi_s + a_2(21 - 42\varphi_s) + b_2(15 - 21\varphi_s) + g_2(10.5 - 12\varphi_s) + d_2(7.5 - 7.5\varphi_s)]L \\
m_{13} &= [21 - 105\varphi_s + a_2(-63\varphi_s) - b_2(6 + 42\varphi_s) - g_2(7.5 + 30\varphi_s) - d_2(7.5 + 22.5\varphi_s)]L
\end{aligned}$$

$$
\begin{aligned}
m_{14} =&[(28+35\varphi_s+70\varphi_s^2)+a_2(7-7\varphi_s+17.5\varphi_s^2)+b_2(4-7\varphi_s+7\varphi_s^2)....\\
&+g_2(2.75-5\varphi_s+3.5\varphi_s^2)+d_2(2-3.5\varphi_s+2\varphi_s^2)]L^2\\
m_{15} =&[(7+35\varphi_s-35\varphi_s^2)+a_2(3.5+17.5\varphi_s-17.5\varphi_s^2)+b_2(3+10.5\varphi_s-10.5\varphi_s^2)....\\
&+g_2(2.75+7\varphi_s-7\varphi_s^2)+d_2(2.5+5\varphi_s-5\varphi_s^2)]L^2\\
m_{16} =&[(28+35\varphi_s+70\varphi_s^2)+a_2(21+42\varphi_s+52.5\varphi_s^2)+b_2(18+42\varphi_s+42\varphi_s^2)....\\
&+g_2(16.25+40\varphi_s+35\varphi_s^2)+d_2(15+37.5\varphi_s+30\varphi_s^2)]L^2
\end{aligned}
$$

$$
\begin{aligned}
k_1 =&1260+630a_2+504b_2+441g_2+396d_2\\
k_2 =&[630+210a_2+147b_2+126g_2+114d_2-\varphi_s(105a_2+105b_2+94.5g_2+84d_2)]L\\
k_3 =&[630+420a_2+357b_2+315g_2+282d_2+\varphi_s(105a_2+105b_2+94.5g_2+84d_2)L\\
k_4 =&[420+210\varphi_s+105\varphi_s^2+a_2(105+52.5\varphi_s^2)+b_2(56-35\varphi_s+35\varphi_s^2)....\\
&+g_2(42-42\varphi_s+26.25\varphi_s^2)+d_2(36-42\varphi_s+21\varphi_s^2)]L^2\\
k_5 =&[210-210\varphi_s-105\varphi_s^2+a_2(105-105\varphi_s-52.5\varphi_s^2)+b_2(91-70\varphi_s-35\varphi_s^2)....\\
&+g_2(84-52.5\varphi_s-26.25\varphi_s^2)+d_2(78-42\varphi_s-21\varphi_s^2)]L^2\\
k_6 =&[420+210\varphi_s+105\varphi_s^2+a_2(315+210\varphi_s+52.5\varphi_s^2)+b_2(266+175\varphi_s+35\varphi_s^2)....\\
&+g_2(231+147\varphi_s+26.25\varphi_s^2)+d_2(204+126\varphi_s+21\varphi_s^2)]L^2\\
k_7 =&12+6a_1+4b_1\\
k_8 =&(6+3a_1+2b_1)L\\
k_9 =&(3+1.5a_1+b_1)L^2
\end{aligned}
$$

In the above expressions, $a_1$, $b_1$, $a_2$, $b_2$, $g_2$, and $d_2$ are the geometrical constants and can be obtained as,

$$
\begin{aligned}
a_1 &= \frac{2\pi}{A}(r_{Lo}\Delta r_o - r_{Li}\Delta r_i) & b_1 &= \frac{\pi}{A}(\Delta r_o^2 - \Delta r_i^2)\\
a_2 &= \frac{\pi}{I}(r_{Lo}^3\Delta r_o - r_{Li}^3\Delta r_i) & b_2 &= \frac{3\pi}{2I}(r_{Lo}^2\Delta r_o^2 - r_{Li}^2\Delta r_i^2)\\
g_2 &= \frac{\pi}{I}(r_{Lo}\Delta r_o^3 - r_{Li}\Delta r_i^3) & d_2 &= \frac{\pi}{4I}(\Delta r_o^4 - \Delta r_i^4)
\end{aligned}
$$

where $\Delta r_o = r_{Ro} - r_{Lo}$ and $\Delta r_i = r_{Ri} - r_{Li}$.

# References


Al-bedoor, B. O. (2000). Transient torsional and lateral vibrations of unbalanced rotors with rotor-to-stator rubbing. *Journal of Sound and Vibration*, 229(3):627–645.

ATSB (2008). In-flight engine failure: Sydney, Boeing Company 747-438, VH-OJM, 03 February 2007. Technical report, 200700356, Australian Transport Safety Bureau.

Bahree, R., Sharan, A., and Rao, J. (1989). The design of rotor blades taking into account the combined effects of vibratory and thermal loads. *Journal of Engineering for Gas Turbines and Power*, 111:610–618.

Bai, Z. (2002). Krylov subspace techniques for reduced-order modeling of large-scale dynamical systems. *Applied numerical mathematics*, 43(1-2):9–44.

Balaji, N. N. and Krishna, I. P. (2018). Coupled simulation of rotor systems supported by journal bearings. In *Proceedings of the 10th International Conference on Rotor Dynamics–IFToMM, Mechanisms and Machine Science*, volume 60, pages 411–421. Springer.

Banerjee, S. and Rao, J. (1976). Coupled bending-torsion vibrations of rotating blades. In *Turbo Expo: Power for Land, Sea, and Air*, volume 79740, page V01AT01A043. American Society of Mechanical Engineers.

Bartha, A. R. (2000). *Dry friction backward whirl of rotors*. PhD thesis, ETH No. 13817, Swiss Federal Institute of Technology Zurich.

Bently, D. E. (1974). Forced sub-rotative speed dynamic action of rotating machinery. In *Petroleum Mechanical Engineering Conference, Dallas, Texas, ASME paper No. 74-PET-16*.

Bently, D. E., Yu, J. J., Goldman, P., and Muszynska, A. (2002). Full annular rub in mechanical seals, part I: Experimental results. *International Journal of Rotating Machinery*, 8(5):319–328.

Besselink, B., Tabak, U., Lutowska, A., van de Wouw, N., Nijmeijer, H., Rixen, D. J., Hochstenbach, M., and Schilders, W. (2013). A comparison of model reduction techniques from structural dynamics, numerical mathematics and systems and control. *Journal of Sound and Vibration*, 332(19):4403–4422.

Bhat, R., Rao, J., and Sankar, T. (1982). Optimum journal bearing parameters for minimum rotor unbalance response in synchronous whirl. *Journal of Mechanical Design*, 104(2):339–344.

Black, H. (1968). Interaction of a whirling rotor with a vibrating stator across a clearance annulus. *Journal of Mechanical Engineering Science*, 10(1):1–12.

Black, H. F. (1966). Paper 4: Synchronous whirling of a shaft within a radially flexible annulus having small radial clearance. In *Proceedings of the Institution of Mechanical Engineers, Conference Proceedings*, volume 181, pages 65–73. SAGE Publications.

Buza, G., Jain, S., and Haller, G. (2021). Using spectral submanifolds for optimal mode selection in nonlinear model reduction. *Proceedings of the Royal Society A*, 477(2246):20200725.

Cameron, T. and Griffin, J. H. (1989). An alternating frequency/time domain method for calculating the steady-state response of nonlinear dynamic systems. *Journal of Applied Mechanics*, 56:149–154.

CFMI (2000). Training manual CFM56-5B basic engine. Technical report, CFM International.

Chatterjee, A. (2000). An introduction to the proper orthogonal decomposition. *Current science*, 78(7):808–817.

Chen, X., Gan, X., and Ren, G. (2020). Nonlinear responses and bifurcations of a rotor-bearing system supported by squeeze-film damper with retainer spring subjected to base excitations. *Nonlinear Dynamics*, 102(4):2143–2177.

Childs, D. W. (1979). Rub-induced parametric excitation in rotors. *Journal of Mechanical Design*, 101(4):640–644.

Childs, D. W. (1982). Fractional-frequency rotor motion due to nonsymmetric clearance effects. *Journal of Engineering for Power*, 104(3):533–541.

Choi, Y.-S. and Noah, S. T. (1987). Nonlinear steady-state response of a rotor-support system. *Journal of Vibration, Acoustics, Stress, and Reliability in Design*, 109(3):255–261.

Christie, C. A. (1996). Task14-Engine windmilling imbalance loads. Technical report, FR Doc. 96-16960, Aviation Rulemaking Advisory Committee, Federal Aviation Administration.

Christopher, A, H., Robert, L, S., Bella, Dinh-Zarr, T., and Earl, F, W. (2017). Safety recommendation report: Preventing catastrophic failure of Pratt & Whitney Canada JT15D-5 engines following birdstrike or foreign object ingestion. Technical report, ASR-17-003, National Transportation Safety Board.

Chu, F. and Lu, W. (2005). Experimental observation of nonlinear vibrations in a rub-impact rotor system. *Journal of Sound and Vibration*, 283(3-5):621–643.

Chu, F. and Zhang, Z. (1997). Periodic, quasi-periodic and chaotic vibrations of a rub-impact rotor system supported on oil film bearings. *International Journal of Engineering Science*, 35(10-11):963–973.

Chu, F. and Zhang, Z. (1998). Bifurcation and chaos in a rub-impact Jeffcott rotor system. *Journal of Sound and Vibration*, 210(1):1–18.

Craig Jr, R. R. and Bampton, M. C. (1968). Coupling of substructures for dynamic analyses. *AIAA Journal*, 6(7):1313–1319.

Dimarogonas, A. (1973). Newkirk effect: thermally induced dynamic instability of high-speed rotors. In *Turbo Expo: Power for Land, Sea, and Air*, volume 79801, page V001T01A026. American Society of Mechanical Engineers.

Dimarogonas, A. (1974). A study of the Newkirk effect in turbomachinery. *Wear*, 28(3):369–382.

Ehrich, F. (1992). Observations of subcritical superharmonic and chaotic response in rotordynamics. *Journal of Vibration and Acoustics*, 114(1):93–100.

Ehrich, F. F. (1966). Subharmonic vibration of rotors in bearing clearance. In *Design Engineering Conference and Show, Chicago, III., May 9-12, ASME Paper 66-MD-l.*

Ehrich, F. F. (1988). High order subharmonic response of high speed rotors in bearing clearance. *Journal of Vibration, Acoustics, Stress, and Reliability in Design*, 110(1):9–16.

Ehrich, F. F. (1991). Some observations of chaotic vibration phenomena in high speed rotordynamics. *Journal of Vibration and Acoustics*, 113(1):50–57.

Ehrich, F. F. and O'Connor, J. J. (1967). Stator whirl with rotors in bearing clearance. *Journal of Engineering for Industry*, 89(3):381–389.

El-Shafei, A. (1991). Stability analysis of intershaft squeeze film dampers. *Journal of Sound and vibration*, 148(3):395–408.

Flowers, G. T. and Ryan, S. G. (1991). Development of a set of equations for incorporating disk flexibility effects in rotordynamical analyses. In *ASME 1991 International Gas Turbine and Aeroengine Congress and Exposition, Orlando, Florida, USA, June 3–6, Paper No: 91-GT-075*. American Society of Mechanical Engineers Digital Collection.

Flowers, G. T. and Wu, F. (1996). Disk/shaft vibration induced by bearing clearance effects: analysis and experiment. *Journal of Vibration and Acoustics*, 118(2):204–208.

Flowers, G. T. and Wu, F. S. (1993). A study of the influence of bearing clearance on lateral coupled shaft/disk rotordynamics. *Journal of Engineering for Gas Turbines and Power*, 115(2):279–286.

Friswell, M., Garvey, S., and Penny, J. (1995). Model reduction using dynamic and iterated irs techniques. *Journal of sound and vibration*, 186(2):311–323.

Friswell, M., Garvey, S., and Penny, J. (1998). The convergence of the iterated irs method. *Journal of Sound and Vibration*, 211(1):123–132.

Friswell, M., Penny, J., and Garvey, S. (1996). The application of the irs and balanced realization methods to obtain reduced models of structures with local non-linearities. *Journal of Sound and Vibration*, 196(4):453–468.

Friswell, M. I. and Inman, D. J. (1999). Reduced-order models of structures with viscoelastic components. *AIAA journal*, 37(10):1318–1325.

Friswell, M. I., Penny, J. E., Garvey, S. D., and Lees, A. W. (2010). *Dynamics of rotating machines*. Cambridge University Press, 1$^{st}$ edition, New York.

Gao, P., Chen, Y., and Hou, L. (2020). Nonlinear thermal behaviors of the inter-shaft bearing in a dual-rotor system subjected to the dynamic load. *Nonlinear Dynamics*, 101(1):191–209.

Gao, P., Hou, L., Yang, R., and Chen, Y. (2019). Local defect modelling and nonlinear dynamic analysis for the inter-shaft bearing in a dual-rotor system. *Applied Mathematical Modelling*, 68:29–47.

Ghosh, M., Majumdar, B., and Rao, J. (1979). Steady-state and dynamic behaviour of multi-recess hybrid oil journal bearings. *Journal of Mechanical Engineering Science*, 21(5):345–351.

Gilardi, G. and Sharf, I. (2002). Literature survey of contact dynamics modelling. *Mechanism and Machine Theory*, 37(10):1213–1239.

Gildin, E. (2006). *Model and controller reduction of large-scale structures based on projection methods*. PhD thesis, The University of Texas at Austin.

Goldman, P. and Muszynska, A. (1994). Chaotic behavior of rotor/stator systems with rubs. *Journal of Engineering for Gas Turbines And Power*, 116(3):692–701.

Goldman, P. and Muszynska, A. (1995). Rotor-to-stator, rub-related, thermal/mechanical effects in rotating machinery. *Chaos, Solitons & Fractals*, 5(9):1579–1601.

Goldman, P., Muszynska, A., and Bently, D. E. (2000). Thermal bending of the rotor due to rotor-to-stator rub. *International Journal of Rotating Machinery*, 6(2):91–100.

Gonsalves, D., Neilson, R., and Barr, A. (1995). A study of the response of a discontinuously nonlinear rotor system. *Nonlinear Dynamics*, 7(4):451–470.

Gunter, E., Barrett, L., and Allaire, P. (1977). Design of nonlinear squeeze-film dampers for aircraft engines. *Journal of Lubrication Technology*, 99(1):57–64.

Gupta, S., Tiwari, R., and Nair, S. B. (2007). Multi-objective design optimisation of rolling bearings using genetic algorithms. *Mechanism and Machine Theory*, 42(10):1418–1443.

Guskov, M. and Thouverez, F. (2012). Harmonic balance-based approach for quasi-periodic motions and stability analysis. *Journal of Vibration and Acoustics*, 134(3).

Guyan, R. J. (1965). Reduction of stiffness and mass matrices. *AIAA journal*, 3(2):380–380.

Haller, G. and Ponsioen, S. (2016). Nonlinear normal modes and spectral submanifolds: existence, uniqueness and use in model reduction. *Nonlinear dynamics*, 86(3):1493–1534.

Hou, L., Chen, H., Chen, Y., Lu, K., and Liu, Z. (2019). Bifurcation and stability analysis of a nonlinear rotor system subjected to constant excitation and rub-impact. *Mechanical Systems and Signal Processing*, 125:65–78.

Hou, L., Chen, Y., Fu, Y., Chen, H., Lu, Z., and Liu, Z. (2017). Application of the HB–AFT method to the primary resonance analysis of a dual-rotor system. *Nonlinear Dynamics*, 88(4):2531–2551.

Humes, B. and Holmes, R. (1978). The role of subatmospheric film pressures in the vibration performance of squeeze-film bearings. *Journal of Mechanical Engineering Science*, 20(5):283–289.

Hurty, W. C. (1960). Vibrations of structural systems by component mode synthesis. *Journal of the Engineering Mechanics Division*, 86(4):51–69.

Inayat-Hussain, J. I. (2009). Bifurcations in the response of a flexible rotor in squeeze-film dampers with retainer springs. *Chaos, Solitons & Fractals*, 39(2):519–532.

Ivanov, I., Blinnik, B., and Myasnikov, V. (2019). Nonlinear reduced dynamic model of turbofan engine for investigation of engine structural frame vibrations after fan blade out event. In *Turbo Expo: Power for Land, Sea, and Air*, volume 58684, page V07AT33A003. American Society of Mechanical Engineers.

Jiang, J. (2007). The analytical solution and the existence condition of dry friction backward whirl in rotor-to-stator contact systems. *Journal of Vibration and Acoustics*, 129(2):260–264.

Jiang, J. (2009). Determination of the global responses characteristics of a piecewise smooth dynamical system with contact. *Nonlinear Dynamics*, 57(3):351–361.

Jiang, J., Shang, Z., and Hong, L. (2010). Characteristics of dry friction backward whirl—a self-excited oscillation in rotor-to-stator contact systems. *Science China Technological Sciences*, 53(3):674–683.

Jiang, J. and Ulbrich, H. (2001). Stability analysis of sliding whirl in a nonlinear Jeffcott rotor with cross-coupling stiffness coefficients. *Nonlinear Dynamics*, 24(3):269–283.

Jiang, J. and Ulbrich, H. (2005). The physical reason and the analytical condition for the onset of dry whip in rotor-to-stator contact systems. *Journal of Vibration and Acoustics*, 127(6):594–603.

Jin, Y., Lu, K., Huang, C., Hou, L., and Chen, Y. (2019). Nonlinear dynamic analysis of a complex dual rotor-bearing system based on a novel model reduction method. *Applied Mathematical Modelling*, 75:553–571.

John, H, R., Francis, H, M., Louts, M, T., Isabel, A, B., and William, R, H. (1975). Aircraft accident report: National Airlines, Inc. DC-10-10, N60NA, near Albuquerque, New Mexico, November 3, 1973. Technical report, NTSB-AAR-75-2, National Transportation Safety Board.

Ju, R., Fan, W., Zhu, W., and Huang, J. (2017). A modified two-timescale incremental harmonic balance method for steady-state quasi-periodic responses of nonlinear systems. *Journal of Computational and Nonlinear Dynamics*, 12(5):051 007.1–12.

Karpenko, E. V., Pavlovskaia, E. E., and Wiercigroch, M. (2003). Bifurcation analysis of a preloaded Jeffcott rotor. *Chaos, Solitons & Fractals*, 15(2):407–416.

Karpenko, E. V., Wiercigroch, M., and Cartmell, M. P. (2002). Regular and chaotic dynamics of a discontinuously nonlinear rotor system. *Chaos, Solitons & Fractals*, 13(6):1231–1242.

Khanlo, H., Ghayour, M., and Ziaei-Rad, S. (2011). Chaotic vibration analysis of rotating, flexible, continuous shaft-disk system with a rub-impact between the disk and the stator. *Communications in Nonlinear Science and Numerical Simulation*, 16(1):566–582.

Kim, Y., Noah, S., and Choi, Y. (1991). Periodic response of multi-disk rotors with bearing clearances. *Journal of Sound and Vibration*, 144(3):381–395.

Kim, Y. B. and Noah, S. T. (1991). Response and bifurcation analysis of a mdof rotor system with a strong nonlinearity. *Nonlinear Dynamics*, 2(3):215–234.

Koutsovasilis, P. and Beitelschmidt, M. (2008). Comparison of model reduction techniques for large mechanical systems. *Multibody System Dynamics*, 20(2):111–128.

Krishna, I. P. and Padmanabhan, C. (2011). Improved reduced order solution techniques for nonlinear systems with localized nonlinearities. *Nonlinear Dynamics*, 63(4):561–586.

Krishna, I. P. and Padmanabhan, C. (2018). Experimental and numerical investigations on rotor–stator rub. *Proceedings of the Institution of Mechanical Engineers, Part C: Journal of Mechanical Engineering Science*, 232(18):3200–3212.

Kumar, D. S., Sujatha, C., and Ganesan, N. (1997). Disc flexibility effects in rotor bearing systems. *Computers & structures*, 62(4):715–719.

Lankarani, H. and Nikravesh, P. (1990). A contact force model with hysteresis damping for impact analysis of multibody systems. *Journal of Mechanical Design*, 112(3):369–376.

Leung, A. Y.-T. (1978). An accurate method of dynamic condensation in structural analysis. *International Journal for Numerical Methods in Engineering*, 12(11):1705–1715.

Li, Q., Yan, L., and Hamilton, J. (1986). Investigation of the steady-state response of a dual-rotor system with intershaft squeeze film damper. *Journal of Engineering for Gas Turbines and Power*, 108(4):605–612.

Liesen, J. and Strakos, Z. (2013). *Krylov subspace methods: principles and analysis*. Oxford University Press.

Liu, J., Wang, C., and Luo, Z. (2020a). Research nonlinear vibrations of a dual-rotor system with nonlinear restoring forces. *Journal of the Brazilian Society of Mechanical Sciences and Engineering*, 42(9):1–20.

Liu, J., Wang, C., and Luo, Z. (2020b). Research of the internal resonances on a nonlinear dual-rotor based on the energy tracks shifting. *Journal of Sound and Vibration*, 481:115429.

Liu, J., Wang, C., and Luo, Z. (2021). High dimensional nonlinear spring characteristic modelling and vibration analyses of subharmonic resonance of a dual-rotor system based on energy tracks. *Applied Mathematical Modelling*, 91:390–411.

Lu, K., Jin, Y., Chen, Y., Yang, Y., Hou, L., Zhang, Z., Li, Z., and Fu, C. (2019). Review for order reduction based on proper orthogonal decomposition and outlooks of applications in mechanical systems. *Mechanical Systems and Signal Processing*, 123:264–297.

Lu, W. and Chu, F. (2014). Radial and torsional vibration characteristics of a rub rotor. *Nonlinear Dynamics*, 76(1):529–549.

Lu, Z., Zhong, S., Chen, H., Wang, X., Han, J., and Wang, C. (2021). Nonlinear response analysis for a dual-rotor system supported by ball bearing. *International Journal of Non-Linear Mechanics*, 128:103627.

Luo, Z., Wang, J., Tang, R., and Wang, D. (2019). Research on vibration performance of the nonlinear combined support-flexible rotor system. *Nonlinear Dynamics*, 98(1):113–128.

Ma, H., Lu, Y., Wu, Z., Tai, X., and Wen, B. (2016a). Vibration response analysis of a rotational shaft–disk–blade system with blade-tip rubbing. *International Journal of Mechanical Sciences*, 107:110–125.

Ma, H., Yin, F., Guo, Y., Tai, X., and Wen, B. (2016b). A review on dynamic characteristics of blade–casing rubbing. *Nonlinear Dynamics*, 84(2):437–472.

Mohan, S. and Hahn, E. (1974). Design of squeeze film damper supports for rigid rotors. *Journal of Engineering for Industry*, 96(3):976–982.

Mokhtar, M. A., Darpe, A. K., and Gupta, K. (2017). Investigations on bending-torsional vibrations of rotor during rotor-stator rub using Lagrange multiplier method. *Journal of Sound and Vibration*, 401:94–113.

Moon, F. C. (2008). *Chaotic and fractal dynamics: introduction for applied scientists and engineers*. John Wiley & Sons, Second Edition.

Moreira, R. V. and Paiva, A. (2018). The influence of friction in rotor-stator contact nonlinear dynamics. In *Proceedings of the 10th International Conference on Rotor Dynamics–IFToMM, Mechanisms and Machine Science*, volume 61, pages 428–441. Springer.

Muszynska, A. (2005). *Rotordynamics*. CRC Press, $1^{st}$ edition, Taylor & Francis Group, Boca Raton, Florida.

Muszynska, A. and Goldman, P. (1995). Chaotic responses of unbalanced rotor/bearing/stator systems with looseness or rubs. *Chaos, Solitons & Fractals*, 5(9):1683–1704.

Nelson, H. and McVaugh, J. (1976). The dynamics of rotor-bearing systems using finite elements. *Journal of Engineering for Industry*, 98(2):593–600.

Newkirk, B. L. (1927). Shaft rubbing. *Journal of the American Society for Naval Engineers*, 39(1):114–120.

O'Callahan, J. (1989a). A procedure for an improved reduced system (irs) model. *Proceedings of 7th IMAC, Las Vegas, NV., Jan. 30-Feb. 2 1989*.

O'Callahan, J. C. (1989b). System equivalent reduction expansion process. In *Proceedings of 7th IMAC, Las Vegas, NV., Jan. 30-Feb. 2 1989*.

Patel, T. H. and Darpe, A. K. (2009). Coupled bending-torsional vibration analysis of rotor with rub and crack. *Journal of Sound and Vibration*, 326(3-5):740–752.

Patel, T. H., Zuo, M. J., and Zhao, X. (2012). Nonlinear lateral-torsional coupled motion of a rotor contacting a viscoelastically suspended stator. *Nonlinear Dynamics*, 69(1-2):325–339.

Peletan, L., Baguet, S., Torkhani, M., and Jacquet-Richardet, G. (2014). Quasi-periodic harmonic balance method for rubbing self-induced vibrations in rotor–stator dynamics. *Nonlinear Dynamics*, 78(4):2501–2515.

Pennacchi, P., Bachschmid, N., and Tanzi, E. (2009). Light and short arc rubs in rotating machines: Experimental tests and modelling. *Mechanical Systems and Signal Processing*, 23(7):2205–2227.

Petrov, E. (2012). Multiharmonic analysis of nonlinear whole engine dynamics with bladed disc-casing rubbing contacts. In *ASME Turbo Expo 2012: Turbine Technical Conference and Exposition, Copenhagen, Denmark, June 11–15, Paper No: GT2012-68474*, pages 1181–1191. American Society of Mechanical Engineers Digital Collection.

Petrov, E. (2016). Analysis of bifurcations in multiharmonic analysis of nonlinear forced vibrations of gas turbine engine structures with friction and gaps. *Journal of Engineering for Gas Turbines and Power*, 138(10):102 502.1–11.

Ponsioen, S., Jain, S., and Haller, G. (2020). Model reduction to spectral submanifolds and forced-response calculation in high-dimensional mechanical systems. *Journal of Sound and Vibration*, 488:115640.

Popprath, S. and Ecker, H. (2007). Nonlinear dynamics of a rotor contacting an elastically suspended stator. *Journal of Sound and Vibration*, 308(3-5):767–784.

Qu, Z.-Q. (2004). *Model Order Reduction Techniques with Applications in Finite Element Analysis*. 1st edition, Springer Science & Business Media, London.

Rao, B. R. and Tiwari, R. (2007). Optimum design of rolling element bearings using genetic algorithms. *Mechanism and machine theory*, 42(2):233–250.

Rao, J. (1982). Conditions for backward synchronous whirl of a flexible rotor in hydrodynamic bearings. *Mechanism and Machine Theory*, 17(2):143–152.

Rao, J. (1983). Instability of rotors in fluid film bearings. *Journal of Vibration and Acoustics*, 105(3):274–279.

Rao, J. (1985). Instability of rotors mounted in fluid film bearings with a negative cross-coupled stiffness coefficient. *Mechanism and Machine Theory*, 20(3):181–187.

Rao, J. (1996). *Rotor dynamics*. New Age International, Third edition, New Delhi.

Rao, J. (2011). *History of rotating machinery dynamics*, volume 20. Springer Science & Business Media.

Rao, J. (2013). Transient forward and backward whirl of beam and solid rotors with stiffening and softening effects. *Advances in Vibration Engineering*, 12(1):59–74.

Rao, J. and Banerjee, S. (1977). Coupled bending-torsional vibrations of rotating cantilever blades—method of polynomial frequency equation. *Mechanism and Machine Theory*, 12(4):271–280.

Rao, J., Bhat, R., and Sankar, T. (1980). A theoretical study of the effect of damping on the synchronous whirl of a rotor in hydrodynamic bearings. *Transactions of the Canadian Society for Mechanical Engineering*, 6(3):155–161.

Rao, J. and Carnegie, W. (1970). Solution of the equations of motion of coupled-bending bending torsion vibrations of turbine blades by the method of ritz-galerkin. *International Journal of Mechanical Sciences*, 12(10):875–882.

Rao, J. and Sreenivas, R. (2003). Dynamics of asymmetric rotors using solid models. In *Proceedings of the International Gas Turbine Congress Tokyo*, pages 2–7. Citeseer.

Rao, J. and Vyas, N. (1990). Transient stress response of a turbine blade under non-linear damping effects. In *Turbo Expo: Power for Land, Sea, and Air*, volume 79085, page V005T14A017. Citeseer.

Rook, T. (2002). An alternate method to the alternating time-frequency method. *Nonlinear Dynamics*, 27(4):327–339.

Rouch, K. and Kao, J. (1980). Dynamic reduction in rotor dynamics by the finite element method. *Journal of Mechanical Design*, 102(2):360–368.

Saad, Y. (2003). *Iterative methods for sparse linear systems*. SIAM, Second edition, Philadelphia.

Shang, Z., Jiang, J., and Hong, L. (2011). The global responses characteristics of a rotor/stator rubbing system with dry friction effects. *Journal of Sound and Vibration*, 330(10):2150–2160.

Sharan, A. and Rao, J. (1985). Unbalance response of rotor disks supported by fluid film bearings with a negative cross coupled stiffness using influence coefficient method. *Mechanism and machine theory*, 20(5):415–426.

Subrahmanyam, K., Kulkarni, S., and Rao, J. (1981). Coupled bending-torsion vibrations of rotating blades of asymmetric aerofoil cross section with allowance for shear deflection and rotary inertia by use of the reissner method. *Journal of Sound and Vibration*, 75(1):17–36.

Sun, C., Chen, Y., and Hou, L. (2016). Steady-state response characteristics of a dual-rotor system induced by rub-impact. *Nonlinear Dynamics*, 86(1):91–105.

Sun, C., Chen, Y., and Hou, L. (2018). Nonlinear dynamical behaviors of a complicated dual-rotor aero-engine with rub-impact. *Archive of Applied Mechanics*, 88(8):1305–1324.

Taylor, H. (1924). Rubbing shafts above and below resonant speed. *General Electric Technical Information Series*, R-16709:Schenectady, New York.

Tiwari, R. (2017). *Rotor systems: analysis and identification*. Taylor & Francis Group, CRC press, First Edition.

Tiwari, R. and Chakravarthy, V. (2006). Simultaneous identification of residual unbalances and bearing dynamic parameters from impulse responses of rotor–bearing systems. *Mechanical systems and signal processing*, 20(7):1590–1614.

Tiwari, R. and Chakravarthy, V. (2009). Simultaneous estimation of the residual unbalance and bearing dynamic parameters from the experimental data in a rotor-bearing system. *Mechanism and Machine Theory*, 44(4):792–812.

Tiwari, R., Lees, A., and Friswell, M. I. (2004). Identification of dynamic bearing parameters: a review. *The Shock and Vibration Digest*, 36(2):99–124.

Tiwari, R. and Vyas, N. (1995). Estimation of non-linear stiffness parameters of rolling element bearings from random response of rotor-bearing systems. *Journal of Sound and Vibration*, 187(2):229–239.

Torkhani, M., May, L., and Voinis, P. (2012). Light, medium and heavy partial rubs during speed transients of rotating machines: Numerical simulation and experimental observation. *Mechanical Systems and Signal Processing*, 29:45–66.

Urabe, M. and Reiter, A. (1966). Numerical computation of nonlinear forced oscillations by Galerkin's procedure. *Journal of Mathematical Analysis and Applications*, 14(1):107–140.

Vania, A., Pennacchi, P., Chatterton, S., and Cangioli, F. (2018). Intermittent rub caused by carbonized oil in a steam turbine. In *Proceedings of the 10th IFToMM International Conference on Rotor Dynamics, Mechanisms and Machine Science*, volume 61, pages 290–304. Springer.

Verma, S. K. and Tiwari, R. (2021). Robust design of ball bearings for an improved performance using genetic algorithm. *International Journal for Computational Methods in Engineering Science and Mechanics*, 22(6):514–537.

Wagner, M. B., Younan, A., Allaire, P., and Cogill, R. (2010). Model reduction methods for rotor dynamic analysis: a survey and review. *International Journal of Rotating Machinery*, 2010.

Wang, F., Luo, G.-H., Yan, S., and Cui, H.-T. (2018). A comparison study on co-and counterrotating dual-rotor system with squeeze film dampers and intermediate bearing. *Shock and Vibration*, 2017.

Wang, N., Jiang, D., and Behdinan, K. (2017). Vibration response analysis of rubbing faults on a dual-rotor bearing system. *Archive of Applied Mechanics*, 87(11):1891–1907.

Wang, N., Jiang, D., and Xu, H. (2020a). Effects of rub-impact on vibration response of a dual-rotor system-theoretical and experimental investigation. *Experimental Techniques*, 44:1–13.

Wang, N., Jiang, D., and Xu, H. (2020b). Effects of rub-impact on vibration response of a dual-rotor system-theoretical and experimental investigation. *Experimental Techniques*, 44:299–311.

Wang, N., Liu, C., Jiang, D., and Behdinan, K. (2019). Casing vibration response prediction of dual-rotor-blade-casing system with blade-casing rubbing. *Mechanical Systems and Signal Processing*, 118:61–77.

Xiang, H.-J., Zhang, Z.-W., Shi, Z.-F., and Li, H. (2018). Reduced-order modeling of piezoelectric energy harvesters with nonlinear circuits under complex conditions. *Smart Materials and Structures*, 27(4):045004.

Xinxing, M., Hui, M., Haiqin, Q., Xumin, G., Chenguang, Z., and Mingyue, Y. (2021). Nonlinear vibration response characteristics of a dual-rotor-bearing system with squeeze film damper. *Chinese Journal of Aeronautics*, 34(10):128–147.

Xu, H., Wang, N., Jiang, D., Han, T., and Li, D. (2016). Dynamic characteristics and experimental research of dual-rotor system with rub-impact fault. *Shock and Vibration, Article ID 6239281*, 2016.

Yamamoto, T. and Ishida, Y. (1977). Theoretical discussions on vibrations of a rotating shaft with nonlinear spring characteristics. *Ingenieur-Archiv*, 46(2):125–135.

Yang, Y., Cao, D., Wang, D., and Jiang, G. (2017). Response analysis of a dual-disc rotor system with multi-unbalances–multi-fixed-point rubbing faults. *Nonlinear Dynamics*, 87(1):109–125.

Yang, Y., Cao, D., Yu, T., Wang, D., and Li, C. (2016). Prediction of dynamic characteristics of a dual-rotor system with fixed point rubbing–theoretical analysis and experimental study. *International Journal of Mechanical Sciences*, 115:253–261.

Yang, Y., Ouyang, H., Wu, X., Jin, Y., Yang, Y., and Cao, D. (2019). Bending-torsional coupled vibration of a rotor-bearing-system due to blade-casing rub in presence of non-uniform initial gap. *Mechanism and Machine Theory*, 140:170–193.

Yang, Y., Ouyang, H., Yang, Y., Cao, D., and Wang, K. (2020). Vibration analysis of a dual-rotor-bearing-double casing system with pedestal looseness and multi-stage turbine blade-casing rub. *Mechanical Systems and Signal Processing*, 143:106845.

Yu, J., Muszynska, A., and Bently, D. (1998). Dynamic behavior of rotor with full annular rub. *Bently Rotor Dynamics Research Corporation, BRDRC Report, Minden, Nevada*, 7.

Yu, J., Muzynska, A., Goldman, P., and Bently, D. (2002). Rotor/seal experimental and analytical study on full annular rub. *Journal of Engineering for Gas Turbines and Power*, 124(2):340–350.

Yu, P., Zhang, D., Ma, Y., and Hong, J. (2018). Dynamic modeling and vibration characteristics analysis of the aero-engine dual-rotor system with fan blade out. *Mechanical Systems and Signal Processing*, 106:158–175.

Zhang, G. F., Xu, W. N., Xu, B., and Zhang, W. (2009). Analytical study of nonlinear synchronous full annular rub motion of flexible rotor–stator system and its dynamic stability. *Nonlinear Dynamics*, 57(4):579–592.

Zhao, Q., Yao, H., Xu, Q., and Wen, B. (2015). Prediction method for steady-state response of local rubbing blade-rotor systems. *Journal of Mechanical Science and Technology*, 29(4):1537–1545.

Zuo, Y. and Wang, J. (2015). A component mode synthesis method for 3-d finite element models of aero-engines. *Journal of Mechanical Science and Technology*, 29(12):5157–5166.

# List of Publications

## Peer-Reviewed International Journals

- **K. Prabith, I. R. Praveen Krishna**, “A Time Variational Method for the Approximate Solution of Nonlinear Systems Undergoing Multiple-Frequency Excitations", ***Journal of Computational and Nonlinear Dynamics***, vol 15(3), 2020, pp. 031006.1-11, American Society of Mechanical Engineers, Impact factor: 2.085 (2020).
- **K. Prabith, I. R. Praveen Krishna**, “The stability analysis of a two-spool rotor system undergoing rub-impact", ***Nonlinear Dynamics***, vol 104(2), 2021, pp. 941-969, Springer, Impact factor: 5.022 (2020).
- **K. Prabith, I. R. Praveen Krishna**, “Response and stability analysis of a two-spool aero-engine rotor system undergoing multi-disk rub-impact", ***International Journal of Mechanical Sciences***, vol 213, 2022, pp. 106861.1-24, Elsevier, Impact factor: 5.329 (2020).
- **K. Prabith, I. R. Praveen Krishna**, “The numerical modeling of rotor-stator rubbing in rotating machinery: a comprehensive review", ***Nonlinear Dynamics***, vol 101, 2020, pp. 1317-1363, Springer, Impact factor: 5.022 (2020).
- **K. Prabith, I. R. Praveen Krishna**, “The influence of squeeze film damper on the response characteristics of a two-spool aero-engine rotor system undergoing multi-disk rub-impact"(Manuscript under preparation).

## Conference Proceedings

- **K. Prabith, I. R. Praveen Krishna**, “A modified model reduction technique for the dynamic analysis of rotor-stator rub", Proceedings of the 10th IFToMM International Conference on Rotor Dynamics, Mechanisms and Machine Science, Vol 62, pp 400-411, Springer 2018. (Book Chapter)

- **K. Prabith., I. R. Praveen Krishna**, “An optimum frequency ratio calculation for the quasi-periodic response analysis of nonlinear systems", 27th International Congress on Sound and Vibration (ICSV27), Prague, Czech Republic, 2021.

- **K. Prabith., I. R. Praveen Krishna**, “Bifurcation studies of a nonlinear mechanical system subjected to multi-frequency-quasi-periodic excitations, Second International Nonlinear Dynamics Conference (NODYCON), Advances in Nonlinear Dynamics, Vol 1, pp 735-745, Springer

- **K. Prabith, I. R. Praveen Krishna**,“Influence of squeeze film damper on the rub-impact response of a dual-rotor model", XVI Vibration Engineering & Technology of Machinery Conference (VETOMAC), Bengaluru, India, 2021.